SECTION A

JOURNAL OF RESEARCH

of the NATIONAL BUREAU OF STANDARDS

JNBAAR 79A(6) 671-812 Nov.-Dec. 1975

U.S. DEPARTMENT OF COMMERCE / National Bureau of Standards

Physics and Chemistry

Journal of Research

of the

National Bureau of Standards

A. Physics and Chemistry

Nov.–Dec. • 1975

VOLUME • 79A

NUMBER • 6

Editor: C. W. Beckett

Associate Editor: D. D. Wagman

Publication dates:
Feb. 1, Apr. 1, June 1, Aug. 1, Oct. 1, Dec. 1, 1975

J. Res. Nat. Bur. Stand. (U.S.), A

JOURNAL OF RESEARCH

The National Bureau of Standards Journal of Research reports research and development in the fields of activity shown at right. Also included from time to time are survey articles on topics closely related to the Bureau's scientific and technical program.

The Journal is published in two separate sections as follows:

A. Physics and Chemistry

Contains papers of interest primarily to scientists working in these fields. Issued six times a year. Annual subscription: domestic, $17.00; foreign, $21.25. Single copy, varies.

B. Mathematical Sciences

Presents studies and compilations designed mainly for the mathematician and the theoretical physicist. Issued quarterly. Annual subscription: domestic, $9.00; foreign, $11.25. Single copy, $2.25.

The National Bureau of Standards[1] was established by an act of Congress March 3, 1901. The Bureau's overall goal is to strengthen and advance the Nation's science and technology and facilitate their effective application for public benefit. To this end, the Bureau conducts research and provides: (1) a basis for the Nation's physical measurement system, (2) scientific and technological services for industry and government, (3) a technical basis for equity in trade, and (4) technical services to promote public safety. The Bureau consists of the Institute for Basic Standards, the Institute for Materials Research, the Institute for Applied Technology, the Institute for Computer Sciences and Technology, and the Office for Information Programs.

THE INSTITUTE FOR BASIC STANDARDS provides the central basis within the United States of a complete and consistent system of physical measurement; coordinates that system with measurement systems of other nations; and furnishes essential services leading to accurate and uniform physical measurements throughout the Nation's scientific community, industry, and commerce. The Institute consists of the Office of Measurement Services, the Office of Radiation Measurement and the following Center and divisions:

Applied Mathematics — Electricity — Mechanics — Heat — Optical Physics — Center for Radiation Research: Nuclear Sciences; Applied Radiation — Laboratory Astrophysics[2] — Cryogenics[2] — Electromagnetics[2] — Time and Frequency[2].

THE INSTITUTE FOR MATERIALS RESEARCH conducts materials research leading to improved methods of measurement, standards, and data on the properties of well-characterized materials needed by industry, commerce, educational institutions, and Government; provides advisory and research services to other Government agencies; and develops, produces, and distributes standard reference materials. The Institute consists of the Office of Standard Reference Materials, the Office of Air and Water Measurement, and the following divisions:

Analytical Chemistry — Polymers — Metallurgy — Inorganic Materials — Reactor Radiation — Physical Chemistry.

THE INSTITUTE FOR APPLIED TECHNOLOGY provides technical services to promote the use of available technology and to facilitate technological innovation in industry and Government; cooperates with public and private organizations leading to the development of technological standards (including mandatory safety standards), codes and methods of test; and provides technical advice and services to Government agencies upon request. The Institute consists of the following divisions and Centers:

Standards Application and Analysis — Electronic Technology — Center for Consumer Product Technology: Product Systems Analysis; Product Engineering — Center for Building Technology: Structures, Materials, and Life Safety; Building Environment; Technical Evaluation and Application — Center for Fire Research: Fire Science; Fire Safety Engineering.

THE INSTITUTE FOR COMPUTER SCIENCES AND TECHNOLOGY conducts research and provides technical services designed to aid Government agencies in improving cost effectiveness in the conduct of their programs through the selection, acquisition, and effective utilization of automatic data processing equipment; and serves as the principal focus within the executive branch for the development of Federal standards for automatic data processing equipment, techniques, and computer languages. The Institute consists of the following divisions:

Computer Services — Systems and Software — Computer Systems Engineering — Information Technology.

THE OFFICE FOR INFORMATION PROGRAMS promotes optimum dissemination and accessibility of scientific information generated within NBS and other agencies of the Federal Government; promotes the development of the National Standard Reference Data System and a system of information analysis centers dealing with the broader aspects of the National Measurement System; provides appropriate services to ensure that the NBS staff has optimum accessibility to the scientific information of the world. The Office consists of the following organizational units:

Office of Standard Reference Data — Office of Information Activities — Office of Technical Publications — Library — Office of International Relations — Office of International Standards.

[1] Headquarters and Laboratories at Gaithersburg, Maryland, unless otherwise noted; mailing address Washington, D.C. 20234.
[2] Located at Boulder, Colorado 80302.

U.S. DEPARTMENT OF COMMERCE
Elliot L. Richardson, Secretary

NATIONAL BUREAU OF STANDARDS
Ernest Ambler, Acting Director

Order all publications from the Superintendent of Documents
U.S. Government Printing Office, Washington, D.C. 20402.

The Secretary of Commerce has determined that the publication of this periodical is necessary in the transaction of the public business required by law of this Department. Use of funds for printing this periodical has been approved by the Director of the Office of Management and Budget through June 30, 1976.

JOURNAL OF RESEARCH of the National Bureau of Standards—A. Physics and Chemistry
Vol. 79A, No. 6, November–December 1975

On the Growth Rate of Spherulites and Axialites from the Melt in Polyethylene Fractions: Regime I and Regime II Crystallization

John D. Hoffman, Lois J. Frolen, Gaylon S. Ross, and John I. Lauritzen, Jr.

Institute for Materials Research, National Bureau of Standards, Washington, D.C. 20234

(September 3, 1975)

The growth rate G of the crystalline bodies appearing in each of a set of 35 characterized polyethylene fractions ranging from 3600 to 807,000 in molecular weight has been measured as a function of the undercooling ΔT. In isothermal crystallization, only axialites were found from $M_w = 3600$ to 18,000. (For these runs, $\Delta T < 17.5$ °C.) From $M_w = 18{,}000$ to $M_w \cong 115{,}000$ coarse-grained non-banded spherulites were found for $\Delta T > 17.5$ °C, and axialites for $\Delta T < 17.5$ °C; a rather sharp break occurred in the $\log_{10} G$ versus T data at $\Delta T \cong 17.5$ °C. The morphological changes were more gradual. Above $M_w \cong 115{,}000$, only nearly structureless "irregular" spherulites were found at all undercoolings corresponding to isothermal growth. Typical ringed spherulites were obtained only on quenching. Wide-angle x-ray data showed that the usual orthorhombic subcell predominated in all the morphologies encountered. Low-angle x-ray data showed that the specimens exhibited lamellar crystallization irrespective of the particular gross morphology involved. The growth rate data on each fraction were analyzed using

$$G = G_0 \exp\left[-U^*/R(T-T_\infty)\right] \exp\left[-K_g/T(\Delta T) f\right]$$

where $f \cong 1$ to obtain values of K_g and G_0. The value of Y in $K_g = Yb\sigma\sigma_e/(\Delta h_f)k$ was obtained for each morphology by applying the "Z" test of Lauritzen. $Y = 4$ for regime I crystallization (single surface nucleus leads to completion of substrate) and $Y = 2$ for regime II crystallization (numerous surface nuclei involved in substrate completion). It was found that the axialites obeyed regime I kinetics ($Y = 4$), the coarse-grained spherulites regime II kinetics ($Y = 2$), and the irregular spherulites "mixed" kinetics ($Y \sim 3$). The assumption that the substrate length L in Lauritzen's regime theory was $\sim 5\ \mu$m led to the prediction of a rather sharp regime I → regime II transition (corresponding to a break in the $\log_{10} G$ versus T data) at $\Delta T \cong 17.5$ °C, in accord with experiment. The $\sigma\sigma_e$ value calculated from K_g and Y for $M_w \geq 20{,}000$ was approximately constant with molecular weight and independent of morphology; the limiting value of $\sigma\sigma_e$ from kinetic measurements was about 1285 erg^2/cm^4, corresponding to $\sigma_{e(\infty)} = 90.5$ erg/cm^2 and $\sigma = 14.2$ erg/cm^2. (This value of $\sigma_{e(\infty)}$ compares favorably with $\sigma_{e(eq)} = 93 \pm 8$ erg/cm^2 from melting point experiments.) The increase of $\sigma\sigma_e$ and σ_e that took place at low molecular weights on up to $\sim 20{,}000$ was treated using an expression given by Hoffman, viz, $\sigma_e = \sigma_{e(\infty)}[(\nu+\beta_i)/(\nu+1)]$ where ν = number of folds per molecule, $\beta_i = \sigma_{e(\text{cilium})}/\sigma_{e(\infty)}$. Intermittent high and low values of σ_e were found experimentally in this region, showing that β_i varied with increasing molecular weight between 0.15 and ~ 0.7. Theoretical estimates of these upper and lower bounds for β_i are given. The variation of σ_e between its upper and lower bounds was tentatively explained in terms of the alternate appearance of short and long terminal cilia. Estimates of the initial lamellar thickness l_g^* were made from σ_e, and compared with the appropriate low-angle x-ray spacings. A theoretical estimate of the ratio of the pre-exponential factors $G_{0(\text{I})}$ and $G_{0(\text{II})}$ for regimes I and II was compared with experiment with satisfactory results. The value of G_0 is not strongly dependent upon the viscosity of the melt. The work of chain folding deduced from the growth rate data is close to 4.1 kcal/mol, which is in good agreement with other estimates.

Keywords: Axialite; chainfolds; crystallization rate; molecular weight dependence; nucleation theory; polyethylene; spherulite; regime I; regime II.

Contents

	Page
1. Introduction	672
2. Experimental detail	673
3. Results: Growth rate and morphology	676
3.1. Growth rate curves and determination of T_b and ΔT_b	676
3.2. Morphology	678
3.3. Birefringence and x-ray studies	679
4. Analysis of data to obtain K_g and G_0	681
5. Regime I and regime II growth: calculation of $\sigma\sigma_e$ from K_g	684
5.1. Relationship between surface nucleation rate i and regime I and regime II crystal growth rate laws	684
5.2. Regime I (single surface nucleus causes completion of substrate)	684
5.3. Regime II (numerous surface nuclei involved in formation of substrate)	685
5.4. Criteria for regimes I and II	687
5.5. Application of regime test to spherulites and axialites in Polyethylene	687
5.6. Sharpness of regime I→regime II transition: an estimate of L	688
5.7. Calculation of $\sigma\sigma_e$ as a function of molecular weight from K_g values for various fractions	689
5.8. The pre-exponential factors for regime I and II	690
6. The variation of σ_e with molecular weight	691
6.1. Experimental evaluation of σ_e	691
6.2. Theory for variation of σ_e with molecular weight	692
7. Work of chain folding	698
8. Discussion	697
8.1. Relationship to earlier work: growth rate and morphology	697
8.2. Regime I and regime II in other polymers: morphological implications	697
8.3. Overview	698
9. References	699

1. Introduction

The primary objective of this study was to determine the nucleation constants that describe the rate of growth of polyethylene crystals from the subcooled melt as a function of undercooling and molecular weight, and to interpret these in terms of predictions arising from the kinetic theory of nucleation-controlled growth with chain folding. Characterized fractions of linear polyethylene ranging in molecular weight from $M_w = 3600$ to $M_w = 807{,}000$ were used in the investigation. An analysis of the experimentally determined nucleation constant K_g allows the surface free energy product $\sigma\sigma_e$ to be obtained for each fraction. This product can be separated into its components σ, the lateral surface free energy, and σ_e, the fold surface free energy. The value of σ_e obtained in this way may be called a "kinetic" value, since it is determined from growth rate data. One of our primary interests was to determine the dependence of $\sigma\sigma_e$, and therefore the effective value of σ_e, on molecular weight.

According to certain current theories [1–3][1] the effective value of σ_e should be nearly independent of molecular weight if the folded surface nuclei leading to growth contain enough folds to be essentially free of the effects of chain ends. At low molecular weights, some chain end effects must be expected to be included in the effective value of σ_e. The present study was designed in part to determine where the value of σ_e leveled off and became approximately constant with increasing molecular weight. The initial upswing of σ_e and the leveling off in this quantity that occurs as the molecular weight is increased is treated in terms of a simple model that allows extension of the theory of nucleation with chain folds from quite high molecular weights to cases where the surface nuclei have only a few folds per molecule.

As the work progressed, a somewhat surprising richness of morphology appeared, the details of which did not seem to have been foretold in the literature in a systematic manner. Several types of spherulites and one type of axialite were found. Except at large undercoolings accessible only by quenching, none of the spherulites seemed to closely correspond in any detail to the usual "ringed" type with numerous concentric bands so commonly reported in other investigations (see for example [4]). Meanwhile, it was discovered that axialites and spherulites sometimes occurred in different temperature regions in the same specimen, and that in these two regions the growth rate data gave decidedly different nucleation constants. Therefore, a secondary objective became the searching out of the regions of undercooling and molecular weight where these particular morphological entities occurred.

[1] Figures in brackets indicate the literature references at the end of this paper.

Part of the method of preparation of the specimens involved removal by filtration in solution of a very substantial fraction of the heterogeneities that initiated crystallization, with the result that each spherulite or axialite grew to relatively large size as it crystallized from the melt, thus allowing its morphology to be clearly revealed in an optical microscope. By this technique we were able to obtain large spherulites or axialites without heating the specimen far above the melting point prior to crystallization. Excessive heating can cause oxidation or degradation (see later).

It will prove useful to be more specific concerning the significance of the nucleation constants that were determined. By so doing, an important issue regarding the interpretation of not only the present data but also other growth rate data in the literature may be brought out. According to the kinetic theory of crystallization with chain folding, the growth rate G at a temperature T near the equilibrium melting temperature T_m° relevant to the molecular weight under consideration depends on the undercooling $\Delta T = T_m^\circ - T$ in a manner that is proportional to [1, 2][2] $\exp[-K_g/T(\Delta T)f]$ where K_g is the nucleation constant. (The quantity f is a factor that is close to unity near T_m° that corrects for the change in heat of fusion with temperature.) Accordingly, a measurement of G as a function of ΔT allows K_g to be determined experimentally with considerable precision, and it is this parameter that was obtained from the growth data on the polyethylene fractions as a function of molecular weight and morphology.

An important point concerning K_g is that its theoretical interpretation, which affects the value of $\sigma\sigma_e$ and the resultant value of σ_e, depends critically on the assumptions used in relating the flux describing the surface nucleation rate i to the actual lineal growth rate G. The theory of the flux for chain-folded surface nuclei gives $i \propto \exp[-4b\sigma\sigma_e T_m^\circ/(\Delta h_f)(\Delta T)kTf]$, where b is the layer thickness and (Δh_f) the heat of fusion. In one limit (*regime* I, single surface nucleus causes substrate completion), G is directly proportional to i, and K_g is to be interpreted correctly as $4b\sigma\sigma_e T_m^\circ/(\Delta h_f)k$. In the other limit (*regime* II, numerous surface nuclei involved in substrate completion), G varies as $i^{1/2}$ as was pointed out by Sanchez and DiMarzio [7], and K_g is $2b\sigma\sigma_e T_m^\circ/(\Delta h_f)k$. Thus, a question arises in analyzing experimental K_g data as to whether they should be used with regime I or regime II kinetics to estimate $\sigma\sigma_e$.

Criteria delineating where regime I or regime II kinetics should be applied have been developed by Lauritzen [8], and discussed in detail elsewhere [1]. In the present work, application of these criteria suggested that the axialites followed regime I behavior and that most of the coarse-grained non-banded spherulites appearing in the same specimens at different undercoolings followed regime II behavior. The result was that, despite a difference of a factor of approximately two in the K_g values observed for spherulites and axialites, respectively, the resultant $\sigma\sigma_e$ values were very similar in the intermediate molecular weight range where both types of objects appeared in the same specimen. High molecular weight specimens exhibited "irregular" spherulites where mixed regime I and II behavior was suggested by the criteria. When analyzed in this light, they indicated a $\sigma\sigma_e$ rather similar to the axialites or coarse-grained non-banded spherulites. The regime effect is discussed in some detail for the polyethylene fractions, and an indication is given of the importance of correctly identifying the regime of crystallization in other polymers.

Attention is given to an experimental determination of the pre-exponential factors G_0 that govern the absolute growth rates of the axialites and spherulites. Theoretical predictions suggest that the G_0 value for regime I should be very much larger than that for regime II [1, 2].

A number of other topics are discussed briefly. These include: (1) some details of the different morphological entities that were encountered, i.e., axialites, coarse-grained non-banded spherulites, and "irregular" spherulites; (2) a discussion of the birefringence and lamellar nature of the aforementioned objects, including some information on the so-called "L_1" and "L_2" low angle x-ray spacings for certain of the fractions; (3) the work of chain folding q obtained from the kinetic estimate of σ_e; (4) the crystallization behavior of "whole" polymer polyethylene; and (5) the relationship between this work and earlier work on the growth rate of crystallites in polyethylene and other polymers as a function of molecular weight.

2. Experimental Detail

Because the results obtained here are more extensive and somewhat different than those reported in the literature for polyethylene, both as regards K_g and morphology, we consider it of importance to describe the basic elements of our procedures and the reasons for employing them.

Most of the samples used in this investigation were prepared by column elution (CE) or preparative gel permeation chromatography (PGPC) of NBS Standard Reference Material (SRM) 1475 linear polyethylene. This SRM is a linear polyethylene that has the following molecular weight distribution characteristics: $M_n = 18{,}310 \pm 360$, $M_w = 53{,}070 \pm 620$, $M_z = 138{,}000 \pm 3{,}700$, and $M_w/M_n = 2.90$. Full details of the characterization of this source material have been published elsewhere [9].

The sample designation that will be used throughout this paper is based on the weight average molecular weight, M_w. Thus the sample with the weight average

[2] See also Price [5], and Lauritzen and Hoffman [6] for early derivations applicable to crystallization with chain folding corresponding to the case $f = 1$.

molecular weight of $M_w = 3600$ is designated "3.6 K", that with $M_w = 30{,}600$ as "30.6 K", and so on.[3]

The source, method of preparation, and characterization parameters of the fractions are shown in table 1. Some of the fractions were prepared from SRM 1475 by the Waters Corporation[4] in PGPC columns 12.2 m in length, achieving an M_w/M_n ratio in a few cases in the vicinity of 1.05. The samples fractionated by the Waters Corporation are marked (W) in table 1. All specimens denoted CE were fractionated at NBS. Three samples were prepared by the PGPC method and supplied by the Monsanto Chemical Company, and these are denoted (M) in table 1. The latter were not prepared from SRM 1475.

All of the specimens listed in table 1 were characterized in a Waters Model 200 (analytical scale) gel permeation chromatographic (GPC) apparatus. Each column was 1.22 m long and 0.953 cm in diameter, and consisted of a stainless steel tube packed with beads of rigid cross-linked polystyrene gel. The gel was prepared and packed in the columns by the manufacturer. Five such columns having nominal exclusion limits of 10^7, 10^6, 10^5, 10^4, and 10^3 Å were connected in series to form the set used for analysis.[5]

[3] Note that an upright K is used to mean "thousand" in denoting the molecular weight. In accordance with international convention, an italic *K* is used later in this paper to indicate temperature in kelvins.

[4] Certain company names and commercial products are identified in order to adequately specify the experimental procedure. In no case does such identification imply recommendation or endorsement by the National Bureau of Standards, nor does it imply that the products identified are necessarily the best available for the purpose.

[5] One angstrom unit (Å) is equal to 10^{-10} m.

TABLE 1. *Method of preparation and characterization parameters for the polyethylene fractions*

Sample designation	M_w	M_n	M_w/M_n[a]	T_m° (°C) (calculated)[b]	Method of[c] preparation
Low molecular weight region					
3.6 K	3,600	3,190	1.13	133.3	PGPC (W)
4.2 K	4,200	3,330	1.26	135.0	CE
5.10 K	5,100	4,640	1.10	137.0	PGPC (W)
5.62 K	5,620	5,350	1.05	137.7	PGPC (W)
6.15 K	6,150	5,640	1.09	138.3	PGPC (W)
6.29 K	6,290	5,380	1.17	138.5	CE
6.35 K	6,350	5,990	1.06	138.7	PGPC (W)
7.84 K	7,840	7,610	1.03	139.9	PGPC (W)
8.06 K	8,060	7,200	1.12	140.1	CE
8.56 K	8,560	7,850	1.09	140.4	PGPC (W)
8.59 K	8,590	7,740	1.11	140.5	CE
9.70 K	9,700	9,150	1.06	141.1	PGPC (W)
11.4 K	11,370	10,430	1.09	141.8	PGPC (W)
11.67 K	11,670	10,710	1.09	141.9	CE
11.74 K	11,740	10,970	1.07	142.0	PGPC (W)
17.0 K	16,950	15,690	1.08	143.2	CE
Intermediate molecular weight region					
18.1 K	18,120	13,040	1.39	143.4	PGPC (M)
19.8 K	19,830	19,530	1.07	143.7	CE
23.7 K	23,680	22,130	1.07	144.1	CE
24.6 K	24,640	23,030	1.07	144.2	CE
30.0 K	30,020	26,800	1.12	144.6	PGPC (W)
30.6 K	30,600	25,710	1.19	144.6	PGPC (W)
37.6 K	37,630	34,210	1.10	144.9	PGPC (W)
42.6 K	42,580	34,900	1.22	145.1	PGPC (W)
62.8 K	62,770	45,820	1.37	145.5	CE
68.6 K	68,570	58,610	1.17	145.6	PGPC (W)
74.4 K	74,440	66,460	1.12	145.7	CE
115.0 K	114,500	71,120	1.61	145.9	PGPC (M)
High molecular weight region					
119 K	119,200	94,600	1.26	145.9	PGPC (W)
134 K	134,300	79,000	1.70	146.0	CE
210 K	210,000	146,900	1.43	146.2	CE
266 K	265,500	146,700	1.81	146.3	PGPC (M)
323 K	323,200	200,700	1.61	146.3	CE
500 K	500,400	313,000	1.60	146.4	CE
807 K	807,400	507,800	1.59	146.4	CE

[a] Corrected for instrumental broadening effects (see text).
[b] Calculated using equation given later in the text.
[c] PGPC = preparative gel permeation chromatography; CE = column elution.

The apparatus was calibrated using fractions whose M_w and M_n values were known to about ± 5 percent from light scattering and osmotic pressure measurements. GPC instrumental broadening effects were estimated by measuring nearly pure samples of n-$C_{32}H_{66}$ and n-$C_{94}H_{190}$ for which M_w/M_n was known to be about 1.00. These samples gave $M_w/M_n \cong 1.05$ in the GPC analytical apparatus. Therefore, a correction of -0.05 was applied to the original M_w/M_n data for the fractions characterized with the analytical GPC columns. Detailed studies carried out on some specimens suggested that the distribution of molecular weights $P(M)$ was closely approximated by the customary "log normal" function.

We turn now to the topics of the removal of heterogeneities, and other items that relate to obtaining consistent morphological and growth rate data.

Polyethylene "as received" usually contains an extremely large number of heterogeneities ($\geq 10^9/cm^3$) that initiate growth centers and cause any crystalline bodies that are formed in a subsequent crystallization to impinge on one another before they attain sufficient size to be critically examined in an optical microscope. Frequently, all that is seen with an optical microscope with crossed polarizers in such material is something that may be described as a grainy fog. Samples prepared directly from SRM 1475 are no exception to this. The usual procedure used to obtain large spherulites is to inactivate most of the heterogeneities by raising the specimen to a temperature T_1 that is far above the melting point prior to cooling down to the isothermal crystallization temperature T. The procedure of heating to a high T_1 to inactivate most of the heterogeneities is well suited to polymers of high thermal stability such as poly(chlorotrifluoroethylene), where this technique was successfully applied [10]. In the case of polyethylene, the use of a high T_1 is successful in inactivating many of the heterogeneities, allowing large spherulites to form in a subsequent crystallization, but the sample is degraded or otherwise deteriorated at the same time, often even showing a distinct brown coloration. (GPC studies on specimen 30.6 K showed no deterioration when stored at $T_1 = 160$ °C for long periods of time between cover slips, but definite changes were noted when the specimen was held at a high T_1 (190 °C) for two hours, again between glass cover slips.) The result is that the spherulites seen at the usual isothermal crystallization temperatures (*circa* 122 to 127 °C) in specimens where high T_1 values were used are almost certainly characteristic of polymer that is degraded. A T_1 of 155 °C was generally used in the present study, which avoided difficulties resulting from degradation.

In order to avoid the problem of heating to an excessively high T_1 to obtain large spherulites or axialites, each of the fractions was dissolved in xylene at ~ 135 °C (0.1 % solution by weight) and filtered hot three times through a 0.2 μm micropore filter to remove a considerable portion of the heterogeneities. The filtrate was then cooled to ~ 85 °C and the polyethylene crystals precipitated and filtered off. The precipitate was then treated by heating in vacuum at 100 °C for 24 hours or more to remove the xylene. Tests using a gas chromatograph showed that the resultant crystal mats contained less than 10 ppm of xylene. Specimens after filtration generally showed less than 10^4 heterogeneous nuclei per cm^3, which allowed the formation of large spherulites or axialites.

The aforementioned step of crystallization from solution certainly removed a considerable portion of any extremely low molecular weight material that might have been present in the fractions. We also mention that the characterization of the specimens by analytical GPC was carried out subsequent to the filtration and crystallization from solution steps noted above.

A dried and characterized sample was prepared for examination in an optical microscope by lightly pressing 100 to 300 mg of the fraction between glass cover slips at a temperature close to 150 °C in a vacuum oven to make a sandwich where the polymer layer was roughly 40 μm thick. The central region of the specimens was thus protected against oxidation. The cleaning of the cover slips was important, since if they were used as supplied, excessive crystallization began at the polymer-glass interface. The cover slips were first cleaned in chromic acid solution, rinsed thoroughly in distilled water, and then cleaned further in distilled water using conventional ultrasonic scrubbing techniques. After drying, the cover slips were ready for use. When treated as noted above, the cover slips caused little or no nucleation at the polymer-glass interface.

The actual observation of the growth rates were made by heating the specimen in a specially designed microscope hot stage [11] to $T_1 = 155$ °C, which is above the equilibrium melting temperature, and then quickly cooling to a predetermined isothermal crystallization temperature T, usually somewhere in the range of about 118° to 131 °C, and controlling this temperature to ± 0.001 °C. Photomicrographs (with the sample between crossed nicol prisms) were made at suitable intervals as the crystallization proceeded at T, and these were analyzed to obtain the growth rates as $G = dx/dt$ where t is the time, and x the radius of a spherulite, or alternatively, one-half the longest dimension of an axialite (see photomicrographs shown later). In practice, the value of G at a given temperature was obtained by analysis of typically 10 points on an x versus t plot constructed from the photomicrographs taken during the isothermal growth process.

The following comments are pertinent to the reliability of the observations of the rate of growth. First, repeated heating to $T_1 \cong 155$ °C (or any T_1 within 5 °C of this value) never caused any noticeable degradation or oxidation of the central part of glass-enclosed specimens. Some discoloration was occasionally noticed at the extreme edge of the cover slips where air could come in contact with the polyethylene, but optical measurements were always confined to regions where

this did not occur. Second, the growth rates obtained at various T values on a given fraction were highly reproducible no matter what the T of the previous run. Third, the growth rate G did not depend on the residence time at T_1, or the number of times it had been heated to T_1. Fourth, the growth rates at any selected temperature were independent of the thickness of the specimen. Finally, we mention that care was taken to assure that the heat of crystallization did not influence the actual temperature of crystallization by restricting the measurements to growth rates that did not exceed about 5×10^{-5} cm/s.

Measurements of the sign of the birefringence were carried out using well-known techniques for various specimens to determine the orientation of the polymer chains with respect to the growth direction. Wide angle x-ray (WAXR) measurements on specimens of suitable dimensions were made using fractions in the low, intermediate, and high molecular weight ranges to determine if the usual orthorhombic subcell appeared. Low-angle x-ray (LAXR) measurements were made with a Kratky camera to determine if the crystalization in selected fractions of widely different molecular weights was basically lamellar in character, and to find the values of the various lamellar spacings that were present.

3. Results: Growth Rate and Morphology

3.1. Growth Rate Curves and Determination of T_b and ΔT_b

Typical growth rate data for certain fractions between 3.60 and 17.0 K are shown in figure 1A. For convenience, we refer to samples in this general category as being in the "low" molecular weight range. In this region only axialites are seen in the temperature range where isothermal growth can be reliably measured, and the slopes of the growth rate curves change rather markedly with molecular weight. The apparently irregular variations in slope seen in figure 1A as a function of molecular weight are real and reproducible, and will be dealt with in detail after the K_g and σ_e values have been reported for each specimen. Data for a number of other specimens in the low molecular weight range have been omitted to avoid cluttering the diagram.

Data are shown for fractions 18.1 to 74.4 K in figure 1B. These specimens are typical of what we term the "intermediate" molecular weight range, which extends from 18.1 to 115 K. It is seen that a definite break occurs in the $\log_{10} G$ versus T data at a temperature that we denote T_b (fig. 1B). Somewhat above T_b, axialites are formed, and somewhat below it only spherulites are seen. (Details of the morphology will be given subsequently.) In the region of intermediate molecular weight, the slopes of the $\log_{10} G$ versus T plots for the axialites are more nearly constant with molecular weight than they were in the low molecular weight range. As in the case of the low molecular weight region, data for a number of other samples were obtained, but are not shown.

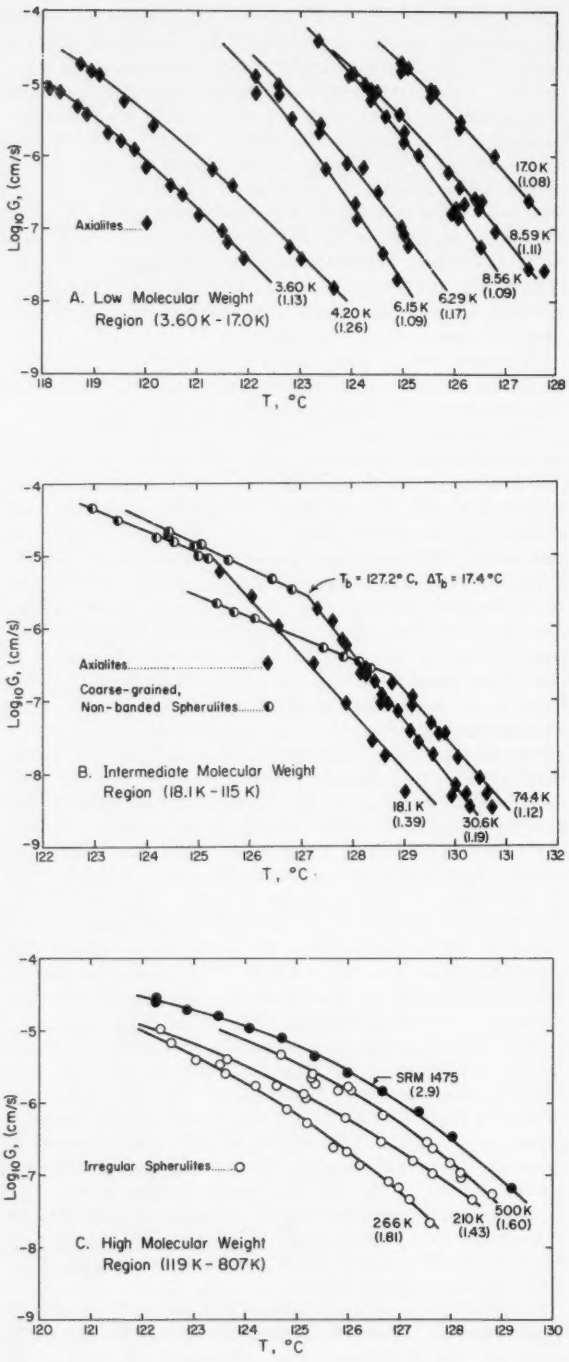

FIGURE 1. *Logarithm of spherulite or axialite growth rate as a function of isothermal growth temperature for low, intermediate and high molecular weight specimens.*

Numbers in parentheses ( ) indicate M_w/M_n for the specimen.

In this paper we adhere to the convention of showing axialite data as solid diamonds (◆), coarse-grained non-banded spherulites as half-filled circles (◐), and "irregular" spherulites (see below) as open circles (○).

Before discussing the growth rate data for the "irregular" spherulites that appear in the high molecular weight region, it is advantageous to show that the *undercooling* at which crystallization is carried out determines whether axialites or spherulites appear in the low and intermediate molecular weight regions.

The variation of T_b with molecular weight as determined from plots of $\log_{10} G$ versus T is shown in figure 2A. It is seen that the break in the growth curves can be clearly detected for samples in the intermediate molecular weight range of $M_w = 18{,}100$ to $M_w = 114{,}500$. This feature is clarified if the undercooling ΔT_b at which the transition takes place is plotted as a function of molecular weight. The result is that the transition occurs at essentially a fixed undercooling of 17.5 ± 1 °C as is shown in figure 2B. Although the rate transitions at T_b are sharper than the corresponding morphological changes (see below), it is nevertheless found that if the undercooling is about 1 °C or more lower than ΔT_b, axialites are formed, and if it is about 1 °C or more greater than this, spherulites are formed. On the basis of this finding, we surmised that spherulites might be found in the specimens with a molecular weight below $M_w \cong 18{,}000$ if crystallization with an undercooling larger than 17.5 °C could be achieved. Runs could not be made on samples lower in molecular weight than 18,000 at $\Delta T > 17.5$ °C because the growth rates became too rapid to measure with any certainty and there is some question as to whether the growth is isothermal under such conditions, but quenching of specimens of such low molecular weight from the melt to room temperature did in fact lead to (nonisothermal) growth of spherulites. The finding that $\Delta T_b \cong 17.5$ °C approximately separates the axialitic and spherulitic growth modes does not apply to samples exceeding about 115 K in molecular weight. At these high molecular weights, a different type of morphology appears over the entire range where isothermal growth can be effected ("irregular" spherulites), and there is no break in the $\log_{10} G$ versus T curve.

The values of T_m° as a function of molecular weight used to estimate ΔT_b for the various specimens shown in figure 2B can be obtained from a modified Broadhurst [12] or Flory-Vrij [13] equation (discussed later).

The growth rate of the axialites and coarse-grained non-banded spherulites studied in the low and intermediate range of molecular weight was in every case lineal, i.e., dx/dt at a given temperature is a constant regardless of the size of the spherulite or axialite up to the point of impingement. (The measurements leading to values of G were generally confined to values of x far short of actual impingement.) There was no significant induction period—the x, t data passed through the origin on an x versus t plot within acceptable statistical limits.

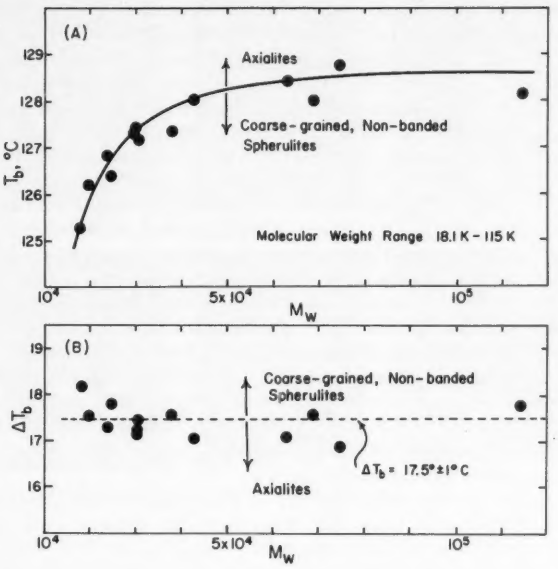

FIGURE 2. *Growth temperature and undercooling corresponding to break in log G versus T data.*

T_b and ΔT_b correspond within about 1 °C to the temperatures and undercoolings that separate the axialitic and spherulitic growth modes.

Typical growth rate data for the "irregular" spherulites that appear in the high molecular weight region (119 to 807 K) are shown in figure 1C.

A notable feature of the irregular spherulites is that no break is found in the $\log_{10} G$ versus T data near $\Delta T_b = 17.5$ °C. Instead, each $\log_{10} G$ versus T plot exhibits considerable curvature and has an average slope that is between that for the axialities and the coarse-grained nonbanded spherulites (compare figs. 1B and 1C).

It is possible that the absence of a relatively sharp break in the $\log_{10} G$ versus T data for the specimens of high molecular weight exhibiting "irregular" spherulites may be associated in part with a broad distribution of molecular weights. This can be seen from a comparison of the data in figure 1 and table 1. Most of the specimens in the "intermediate" range in table 1 possess an M_w/M_n ratio of ~ 1.1 to ~ 1.4 and virtually all exhibit a clear-cut break in the $\log_{10} G$ versus T data of the type shown in the examples depicted in figure 1B. On the contrary, most of the specimens in the high molecular weight range where irregular spherulites appear have an M_w/M_n ratio of ~ 1.4 to ~ 1.8, and specimens of this class show an overall large curvature rather than a distinct break in a plot of $\log_{10} G$ versus T. One possible implication is that a broad distribution of molecular weights may cause the break at T_b to become quite diffuse in the high molecular weight specimens. Note in figure 1C that the SRM from which the fractions were made, for which $M_w \cong 53{,}000$ and $M_w/M_n \cong 2.90$, exhibits a

distinct curvature rather than a break. It may be recalled that a narrow molecular weight fraction with $M_w = 53{,}000$ would be expected to have a distinct break in the $\log_{10}G$ versus T curve (fig. 1B). However, it must be pointed out that specimen 119 K, which has a moderately narrow distribution ($M_w/M_n = 1.26$), shows no break in $\log_{10}G$ versus T, while specimen 115 K with a broad distribution of molecular weight ($M_w/M_n = 1.61$) exhibits the break. This suggests as an alternative that the onset of the appearance of irregular spherulites and the absence of a rather sharp break in the $\log_{10}G$ versus T data may be an inevitable result of increasing molecular weight rather than mainly a function of the distribution. The question concerning how high in molecular weight the sharp break at T_b actually occurs and where irregular spherulites appear will probably only be answered when fractions with $M_w/M_n \sim 1.1$ to 1.2 are available in the high molecular weight range, and measurements made over a considerable temperature range.

The overall radial growth of the irregular spherulites is lineal with time, but possesses an apparent small scale (*circa* 10 μm) sporadic character in that small sectors at the outer boundary of the irregular spherulite appear to grow for a time, stop, and then begin again. This is possibly a result of the details of the extinction pattern that accompany the outward growth of the lamellae rather than an actual starting and stopping of the growth process.

3.2. Morphology

We first examine the question of morphology for samples in the low and intermediate ranges of molecular weight. Figure 3 shows representative axialites in specimens 7.84, 18.1, 30.6, and 42.6 K.[6] Note that in each case the undercooling is less than 17.5 °C. Although differences are detectable, it is clear that these structures are rather similar. Figure 4A, 4B, and 4C depicts typical coarse-grained non-banded spherulites in specimens 18.1, 30.6, and 62.8 K. Observe that the undercooling exceeds 17.5 °C in each case. The "maltese cross" effect is present in the extinction pattern, but the spherulites exhibit a coarse texture and are either non-banded or alternatively, have a few very coarse bands. Typical banded spherulites with many concentric rings can be formed by strong quenching from the melt of the samples in the intermediate molecular weight range. An example is shown in figure 4D for specimen 30.6 K, which crystallizes by formation of such spherulites when quenched rapidly from $T_1 = 155°$ to 25 °C. The distinctive feature of the present work resides in the fact that both axialites and spherulites were found in different temperature

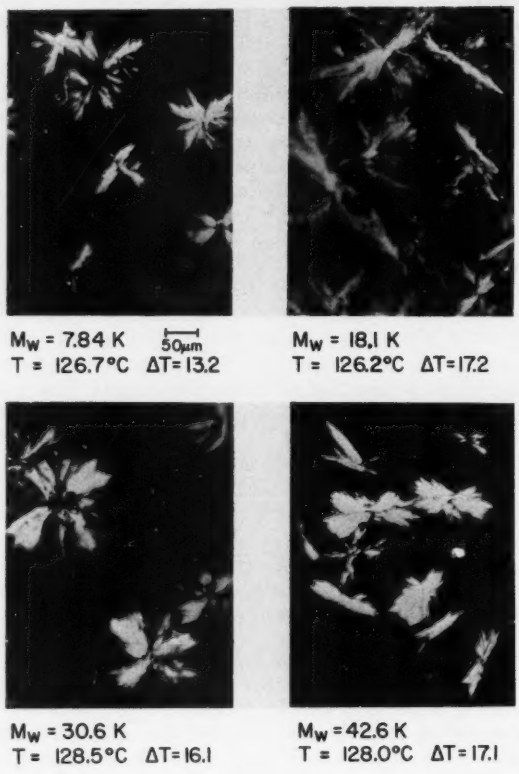

FIGURE 3. *Axialites in specimens of low and intermediate molecular weight at $\Delta T < 17.5$ °C (optical micrographs, crossed nicol prisms).*
The axialites were grown under isothermal conditions.

ranges in the same specimen in the intermediate molecular weight range, together with the fact that these objects exhibited significantly different growth rate constants.

From a morphological standpoint, the transitions from axialitic to spherulitic structures observed in the intermediate molecular weight range are not completely abrupt as the undercooling at which the crystallization occurs passes through ΔT_b. However, there are sufficient differences in the appearance of the crystallizing objects 1 °C above and below T_b to warrant classification as a spherulite or axialite. There are smaller variations in the details of structure within each morphology, with the result that the appearance of the spherulites or axialites in an optical microscope can actually be used by an experienced viewer to estimate the crystallization temperature within a degree or so. A set of photomicrographs illustrating the changes of structure with temperatures and degree of undercooling are shown in figure 5 for specimen

[6] In its strictest definition, the term "axialite" refers to a crystalline object that is highly asymmetrical. The large rather open and sometimes roughly spherical structures that we have loosely called "axialites" in this paper are true axialites in their early stages of growth. In many cases the strictly axialitic mode persists up to rather large values of x (see for example, specimen 42.6 K in fig. 3).

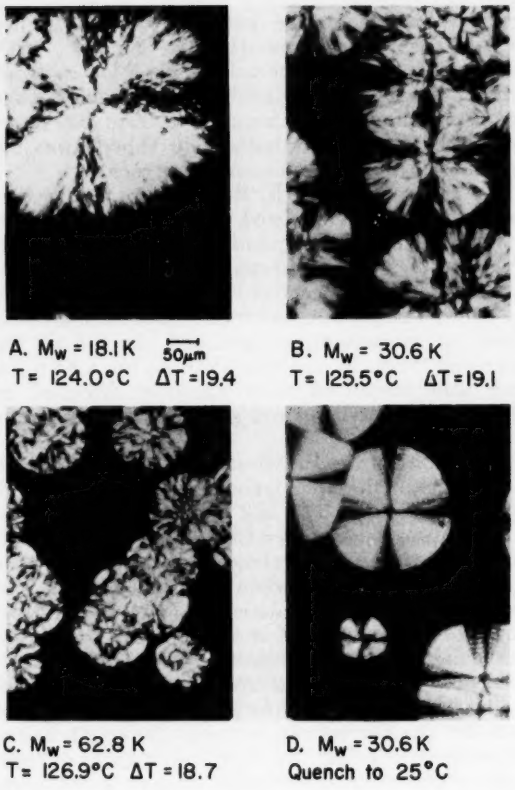

FIGURE 4. *Spherulites in specimens of intermediate molecular weight at* $\Delta T > 17.5$ °C *,optical micrographs, crossed nicol prisms).*

A, B_2 and C show coarse-grained non-banded spherulites resulting from isothermal growth. $\Delta T > 17.5$ °C. Micrograph D shows typical banded spherulites obtained in specimen 30.6 K by rapid quenching, from $T_1 = 155$ to 25 °C.

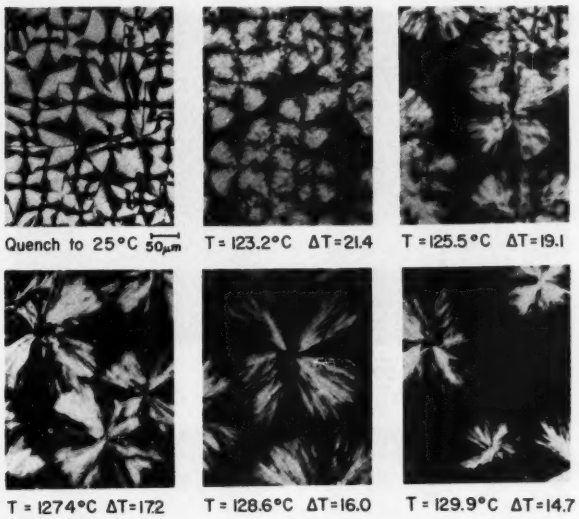

FIGURE 5. *Transition from spherulitic to axialitic morphology in specimen 30.6 K with decreasing undercooling (optical micrographs, crossed nicol prisms).*

Normal banded spherulites are formed at the large undercoolings effected by quenching. In the $\Delta T = 21.4$ °C run there is some evidence of coarse bands. Typical coarse-grained non-banded spherulities are formed at $\Delta T = 19.1$ °C. The object formed at $\Delta T = 17.2$ °C is close to the transition at T_b (see fig. 1B). Axialites are formed at $\Delta T = 16.0$ °C. and $\Delta T = 14.7$ °C. Isothermal growth applies in all cases except that denoted quench.

30.6 K. The steady change from the coarse-grained non-banded spherulitic morphology at $\Delta T > 17.5$ °C to the axialitic morphology at $\Delta T < 17.5$ °C is clearly apparent. (At the lowest isothermal growth temperature ($T = 123.2$ °C, $\Delta T = 21.4$ °C) the spherulites show a few coarse bands.) Samples ranging from 18.1 to 74.4 K show rather similar variations of morphology with decreasing undercooling.

It is worth noting the somewhat unusual structures and phenomena that occur in the specimens in the "high" molecular weight range, i.e., those from 119,000 to near 807,000 in molecular weight. Figure 6 shows the crystalline objects that appear in specimens 119, 210, 323, and 807 K. The clear-cut axialitic morphology characteristic of somewhat lower molecular weights does not appear at undercoolings less than 17.5 °C, and the type of coarse-grained non-banded spherulite seen at intermediate molecular weights at undercoolings greater than 17.5 °C is also absent. Instead, somewhat irregular objects with either a weak or nonexistent "maltese cross" extinction effect appear that in many respects resembles a cauliflower (fig. 6). Some of them show evidence of being banded. We refer to these objects as "irregular" spherulites. The unusual spherulites found for specimen 119 K seem to be a transitional type; the optical micrographs seen in figure 6 for specimens 210, 323, and 807 K are more typical of the "high" molecular weigh. range.

Some very high molecular weight specimens where $M_w > 10^6$ were prepared and examined (not listed). No objects clearly identifiable in an optical microscope with crossed nicol prisms appeared at all despite the fact that differential thermal analysis (DTA) measurements clearly showed that significant crystallization had taken place. Heating of such specimens even for long periods of time to $T_1 = 155$ °C or even $T_1 = 190$ °C failed to remove the birefringence so that any crystalline object that appeared on subsequent cooling was impossible to observe properly with an optical microscope. The highest available molecular weight specimen showing any object whose growth rate could be measured was 807 K.

3.3. Birefringence and X-Ray Studies

Birefringence measurements were made on speci mens 11.67 K (axialites), 30.6 K (both axialitic and spherulitic regions), and 500 K (irregular spherulites).

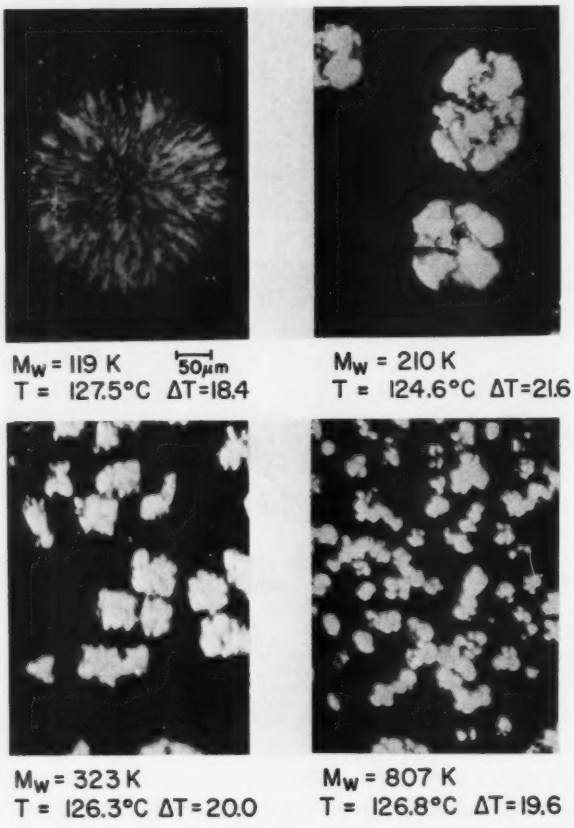

FIGURE 6. *Irregular spherulites in specimens of high molecular weight (optical micrographs, crossed nicol prisms).*

The spherulite in 119 K appears to represent a transition between the intermediate and high molecular weight types. The irregular spherulites in 210 and 323, and 807 K are typical of those found in the high molecular weight region. Growth is under isothermal conditions in all cases.

In each case the sign of the birefringence showed that the polymer chain axes were approximately perpendicular to the direction of growth. This result has been adduced previously for spherulites in polyethylene.

An investigation of sample 30.6 K was made in both the axialitic and spherulitic regions using wide-angle x-ray (WAXR) techniques. The WAXR studies of specimen 30.6 K showed that both the axialitic and spherulitic forms consisted principally of crystals with the usual orthorhombic subcell. The WAXR lines of the axialitic and spherulitic specimens were almost indistinguishable even when examined in detail. The transition from axialitic to spherulitic growth centering around T_b therefore does not involve crystallization into different unit subcells above and below T_b.

Each specimen showed weak extra WAXR lines that have been assigned to either the monoclinic or the triclinic subcell by various authors [14–16]. These weak "extra" lines are commonly found in melt-crystallized polyethylene [14–16]. Similar WAXR studies were made on the axialites in a low molecular weight specimen (11.74 K) and on the irregular spherulites in a high molecular weight specimen (500 K) with the finding that the orthorhombic subcell was by a wide margin the predominant one present.

Low-angle x-ray (LAXR) studies were also made on sample 30.6 K crystallized at undercoolings corresponding to the axialitic and spherulitic regions. For LAXR studies on specimens 11.74 K and 500 K, the samples were crystallized in 1 to 1.5 mm capillary tubes at a known temperature to a high degree of crystallinity, cooled to room temperature, and the LAXR lines measured there. In one case (30.6 K) the LAXR lines were also measured in a specially designed and thermostated beryllium cell at the actual temperature of crystallization.

The results of the LAXR studies are shown in table 2. In general, the specimens showed two categories of LAXR spacings. The first and most prominent was L_1 (which was usually *circa* 400 to 600 Å), and its higher orders. The L_1 line is relatively narrow and intense, and its higher orders, when reported in table 2, are also distinct and easily detected. (We note, however, that the L_1 line for 500 K is considerably broader than that found in the specimens of lower molecular weight.) In sample 30.6 K, crystallized at 128.3 °C and cooled to 30.2 °C, four orders of L_1 could be clearly identified (table 2). The second category was the very broad and rather weak so-called "L_2" line, which does not appear to be a higher order of L_1 [17]. Later we will tentatively identify L_2 with the initial lamellar thickness. Melting point data on the specimens discussed here suggest that lamellar thickening (approximately a doubling and sometimes more) occurs in the fractions during crystallization, so it is not surprising that evidence of two different thickness ranges for the lamellae is found in a given specimen (see L_1 and L_2 values in table 2). (In brief, we postulate that L_1 represents thickened (i.e., aged) stacks of lamellae, while L_2 represents the younger unthickened lamellae characteristic of the initial thickness.) Observe that the values of L_2 are mostly in the range of ~ 180 to ~ 220 Å. We note that this is quite close to the theoretical value of the initial lamellar thickness of $l_g^* = \{2\sigma_e T_m^\circ/(\Delta h_f)(\Delta T)\} + C_2$ calculated using the effective value of σ_e obtained from the growth rate data (see later).

From the LAXR studies noted in table 2 it is seen that both the axialites and coarse-grained non-banded spherulites in the molecular weight range noted (and probably somewhat outside it) are basically lamellar in character. It is also apparent that the irregular spherulites have a lamellar texture.

It has been demonstrated that the spherulites in rather broad molecular weight distribution samples of melt-crystallized polyethylene possess a birefringence consistent with the chain axes in the crystal being

TABLE 2 *Low angle x-ray spacings for selected fractions*

Specimen	Crystallization temp. °C	Measurement temp. °C	Morphology	X-ray spacings [a]	
				L_1(Å)	L_2(Å)[b]
11.74 K	122.0	30.2	Axialites	[c] 368(1)	186(1)
30.6 K	128.3	128.3	Axialites	670(1)	258(1)
30.6 K	128.3	30.2	Axialites	454(4)	195(1)
30.6 K	124.8	124.8	Coarse-grained nonbanded spherulites	396(2)	199(1)
30.6 K	124.8	30.2	Coarse-grained nonbanded spherulites	367(1)	194(1)
500 K	124.0	30.2	Irregular spherulites	470(1)	210(1)

[a] The numbers in parentheses ( ) indicate the number of orders that were detected.
[b] The error in L_2 is rather large, since the line is broad and its value somewhat sensitive to the method used to subtract out the base line.
[c] A weak shoulder at $\sim 1200 \pm 200$ Å was observed for this specimen. This appears to correspond to an extended chain structure, and probably results from thickening.

perpendicular to the direction of growth [18]. (This same orientation is shown by microbeam x-ray data [19, 20].) Further, it is known that the spherulites in broad distribution material are basically lamellar in character [21], and the same appears to hold for certain fractions [22]. The axialites and spherulites found in the fractions used in the present study show these same general characteristics, which are thus consistent with lamellar crystallization with chain-folding. In order for the argument for chain-folding to be logically complete, it would be necessary to show that the lamellae in each of the morphological variations were parallel to the direction of growth, or to in some other manner demonstrate that the chain axes in the crystal were perpendicular to the large surfaces of the thin lamellae. This has been shown for spherulitic structures in bulk polyethylene with a rather broad molecular weight distribution [23, 24]. Also, Bank and Krimm indicate that the usual type of spherulites in polyethylene exhibit mostly adjacent reentry type chain folding [25]. (For a full discussion of these topics, see the recent review by Khoury and Passaglia [26].)

Because of the parallelism of the optical behavior and lamellar character of the axialites and spherulites found in the present investigation of fractions with the optical and lamellar nature of spherulites where chain folding has been substantiated for broader distribution material, we proceed with some confidence under the assumption that the fractions exhibit chain-folding with mostly adjacent reentry.

4. Analysis of Data to Obtain K_g and G_0

The kinetic theory of nucleation-controlled polymer crystal growth with chain folds leads to the expression [1–3]

$$G = G_0 \exp\left[-U^*/R(T-T_\infty)\right] \exp\left[-K_g/T(\Delta T)f\right] \quad (1)$$

for the growth rate G. Here U^* is the activation energy for transport of segments to the site of crystallization, R the gas constant, T the crystallization temperature, T_∞ a temperature somewhat below the glass transition temperature T_g, ΔT the undercooling $T_m^\circ - T$, and f a factor near unity that accounts for the slight diminution of the heat of fusion Δh_f as the temperature falls below T_m°.[7] By plotting $\log_{10}G + U^*/2.303R(T-T_\infty)$ against $1/T(\Delta T)f$, the numerical value of the nucleation constant K_g can be obtained from the slope, and the pre-exponential factor G_0 can be determined from the intercept on the $\log_{10}G + U^*/2.303R(T-T_\infty)$ coordinate.

It has been demonstrated by Suzuki and Kovacs [27] that eq (1) quantitatively fits the growth rate data for isotactic polystyrene for a range of 100 °C. In a recent review [1], this result has been confirmed, and it was shown further that eq (1) can be used to fit data on a number of polymers crystallized from the melt over a wide range of temperature with considerable accuracy, including nylon 6, poly(tetramethyl-*p*-silphenylene) siloxane (hereafter denoted TMPS) fractions, and poly(chlorotrifluoroethylene), correlation coefficients ranging from 0.985 to 0.999 being found. In the afore-

[7] The following customary units are used in this paper: G and G_0 in cm/s, U^* in cal/mol, with $R = 1.987$ cal mol^{-1}K^{-1}, T and T_∞ in kelvins (K), K_g in kelvins squared (K^2). The quantity K_g in customary usage contains surface free energies σ and σ_e in units of erg/cm^2, the heat of fusion in erg/cm^3, a molecular layer thickness b in cm, and Boltzmann's constant in erg K^{-1}. The conversion factors to SI units are 1 erg/cm^2 = 1 mJ/m^2, 1 erg/cm^3 = 0.1 J/m^3, 1 cal/mol = 4.184 J/mol, and $R = 8.314$ J mol^{-1}K^{-1}.

mentioned review, and in the work of Suzuki and Kovacs, it was found that $U^* \cong 1500$ cal/mol and $T_\infty \cong T_g - 30$ °C, with one exception, allowed the best fit of the rate of crystallization data at low temperatures. (The values of U^* and T_∞ that describe bulk viscous flow in polymers between T_g and $T_g + 100$ °C are $U^* \cong 4100$ cal/mol and $T_\infty \cong T_g - 51.6$ °C. The fact that $U^* \cong 1500$ cal and $T_\infty \cong T_g - 30$ °C for crystallization has been interpreted in terms of segmental motions in an adsorbed polymer layer on the lateral face of the crystal [1].) In the case of the present analysis to obtain K_g and G_0 for various polyethylene fractions, the crystallization rate is controlled much more strongly by the variation with temperature of the term involving $K_g/T(\Delta T)f$ than that involving $U^*/R(T - T_\infty)$, since the region of observable crystallization rates in polyethylene is near the melting point. The variation of $U^*/R(T - T_\infty)$ is small and that of $K_g/T(\Delta T)f$ quite large in this region. Therefore in the case of polyethylene, little error in K_g results from rather large variations in the assumed value of U^* or T_∞, and we proceed on the basis of $U^* = 1500$ cal/mol and $T = T_g - 30$ °C, where $T_g = -40$ °C $= 233.2$ K [28]. (The assumption that T_g was -80 °C or 193.2 K would lower K_g for a given set of data by only about 2 percent, and the use of $U^* = 4120$ cal instead of 1500 cal would raise K_g by only 5 percent.) The value of f is approximated [1] by $f = 2T/(T_m^\circ + T)$. This correction is also quite small for polyethylene, again because the observable isothermal crystallization occurs so near the melting point.

One important parameter that requires discussion is the equilibrium melting temperature T_m°, which is a function of molecular weight. This must be known with the best possible accuracy, since K_g, through its relationship to the undercooling $T_m^\circ - T$, is rather sensitively dependent upon it. In figure 7 is shown a plot of T_m° against molecular weight M calculated using a modified form of Broadhurst's equation [12]. The expression used to calculate the curve is

$$T_m^\circ = \frac{T_m^\circ(\infty)(n - 0.542)}{n + 0.46\{7.667 + 1.987 \ln n + (5.6/n) - (0.25n - 7)[1 - (T_m^\circ/T_m^\circ(\infty))]\}} \quad (2)$$

where T_m° is in kelvins (K), and $n = M/14.026$ is the number of carbon atoms in the polymer chain. This equation was derived from Broadhurst's work by setting T_m° at $n \to \infty$ at $T_m^\circ(\infty) = 419.7K = 146.5$ °C, and adjusting the constants accordingly. The curve calculated with eq (2) passes through the melting point data for the short chain hydrocarbons in the orthorhombic form with acceptable accuracy. Therefore, if the value of $T_m(\infty)$ can be justified within certain limits, considerable confidence can be placed on the interpolated values of interest here. Broadhurst's equation is based on a treatment due to Flory and Vrij [13], and the two treatments differ only in minor details.

The experimental justification for selecting $T_m^\circ(\infty) = 146.5$ °C is as follows: (1) Huseby and Bair [29] found $T_m^\circ = 145.8$ °C ± 1 from a plot of T_m versus $1/l$ where l is the lamellar thickness for polyethylene single crystals with $M_w \sim 20{,}000$ to 100,000, implying a $T_m^\circ(\infty)$ that is about 0.5 to 1 °C higher, (2) a plot of T_m versus T_x obtained by Weeks [30] for melt crystallized polymer suggests $T_m^\circ = 145.5 \pm 1$ °C for a specimen of finite molecular weight, again suggesting that $T_m^\circ(\infty)$ for polyethylene of very high molecular weight is slightly higher, and (3) Rijke and Mandelkern [31] have found a melting point for fibrillar polyethylene of $T_m^\circ = 146.0$

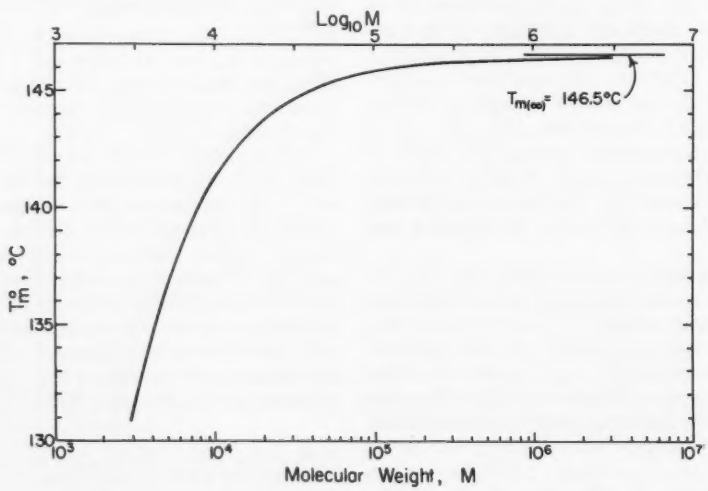

FIGURE 7. *Variation of T_m° with molecular weight according to equation (2).*

± 0.5 °C. We note also that our suggested value for $T_m^\circ(\infty)$ lies within the limits given by Flory and Vrij, who give $T_m^\circ(\infty) = 145.5 \pm 1$ °C. In any event, it seems reasonable on the basis of the above to assume that $T_m^\circ(\infty)$ is within about 1 °C or so of 146.5 °C. No basic conclusion of this paper would be changed if a different value of $T_m^\circ(\infty)$ in this range were used or even a value somewhat outside of it. The melting point T_m° for each fraction was estimated using the assumption that the M value implicit in eq (2) corresponds to M_w. Numerical values of T_m° calculated using eq (2) are given for each of the fractions in table 1.

Typical plots of $\log_{10}G + U^*/2.303R(T-T_\infty)$ against $1/T(\Delta T)f$ constructed from low molecular weight data of the type shown in figure 1A are shown in figure 8A. As noted earlier, only axialites are found in low molecular weight samples in the range of undercooling where isothermal runs can be made. Similar plots for a number of the samples of intermediate molecular weight based on data of the type shown in figure 1B are depicted in figure 8B. Both axialites and coarse-grained non-banded spherulites appear in this molecular weight region at the undercoolings noted. It is clear from the slopes that the axialites and spherulites have different nucleation constants. Finally, a plot is shown for some of the irregular spherulites found at high molecular weight in figure 8C.

Values of the nucleation constants K_g obtained from plots such as those shown in figure 8 are shown for all specimens studied in figure 9A. Values of K_g and $\log_{10} G_0$ are given in table 3. The error in the K_g for a given fraction was generally about 3 to 5 percent (calculated as one standard deviation), depending on the number of points and the temperature range involved. To test the reproducibility of our procedures, a portion of the original supply of sample 30.0 K was rerun, including all filtration, optical sample preparation, and growth rate measurement steps. The K_g for the axialites was within 1.7 percent of the previous run, while that for the coarse-grained non-banded spherulites was within 2.6 percent (table 3). Based on this and other reruns (table 3) it is believed that the K_g values are in general correct to within about 3 to 5 percent. In a few cases the error is larger, and these values of K_g are enclosed in parentheses in table 3.

Attention is specifically drawn to the apparent scatter of the K_g data in figure 9A and table 3 at closely spaced molecular weight values at low molecular weights, especially near $M_w = 6200$ and $M_w = 8600$. Note particularly specimen pairs (6.15, 6.29 K) and (8.56, 8.59 K), together with the confirmatory reruns of the high points, 6.15(R) and 8.56(R). This "scatter" is definitely outside the estimated experimental error of the K_g data. The large variation in K_g at these low molecular weights is believed to be associated with cilium length effects, and will be discussed in section 6.

For the axialites, the value of K_g generally rises at first and then tends toward a limiting value at about $M_w = 20{,}000$, and remains approximately constant

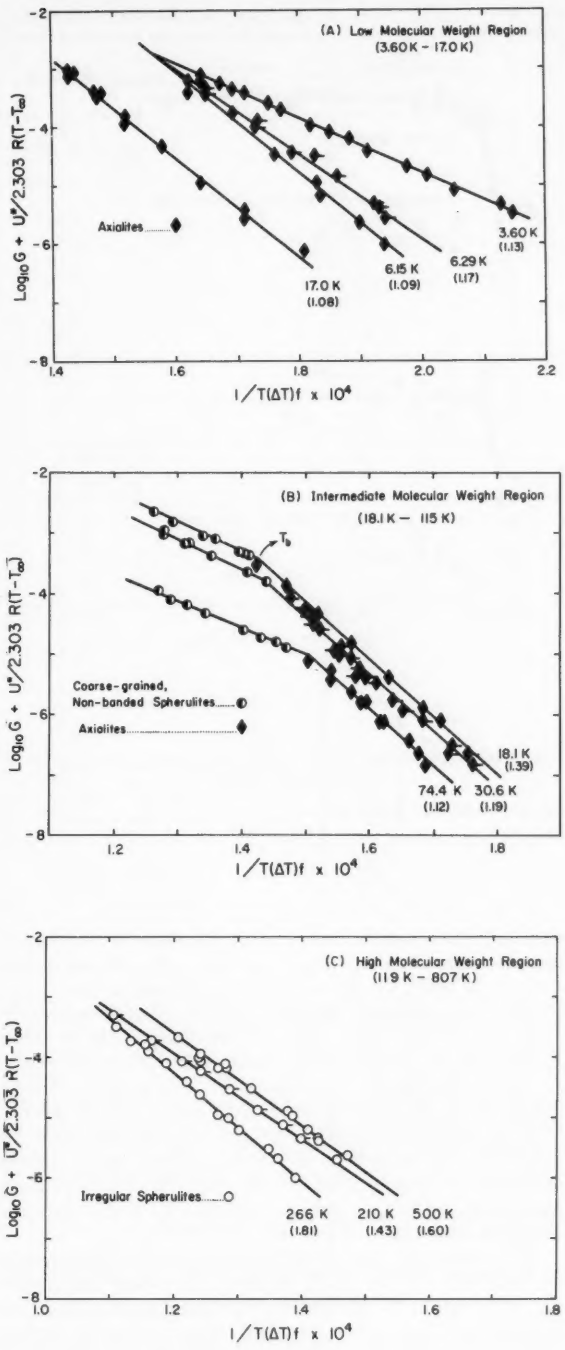

FIGURE 8. *Typical plots of* $\log_{10} G + U^*/R(T-T_\infty)$ *versus* $1/T(\Delta T)f$ *in low, intermediate, and high molecular weight regions.*

Numbers in parentheses ( ) indicate M_w/M_n. The growth rate G is in units of cm/s.

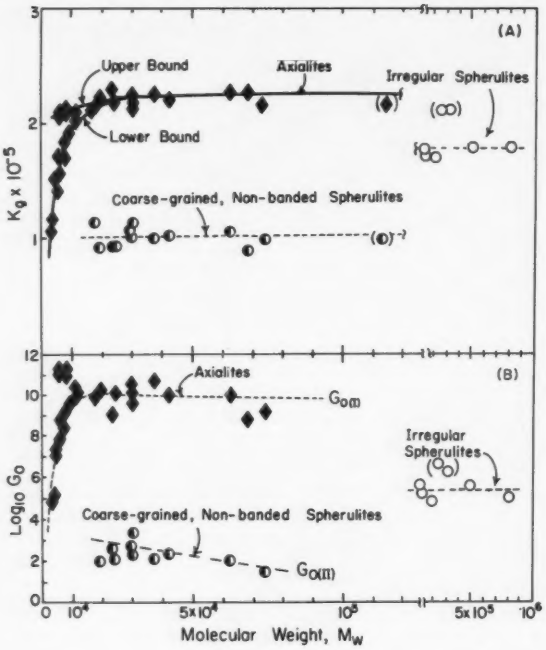

FIGURE 9. *Experimental values of K_g and $\log_{10}G_0$ as a function of molecular weight.*

G_0 is in cm/s and K_g is in units of K^2.

within experimental error up to the highest molecular weight where an accurate axialite run can be made ($M_w \sim 72{,}400$). In the case of the coarse-grained non-banded spherulites, the K_g values are approximately constant in the molecular weight range where their growth can be observed ($M_w \cong 18{,}000$ to $M_w \cong 115{,}000$). From an experimental standpoint, the most accurate values of K_g for the coarse-grained non-banded spherulites lie between M_w=30,000 and M_w=62,800. The K_g value for the axialites in sample 115 K shows some evidence of being affected by the transition to high molecular weight behavior; sample 119 K exhibits no axialites and has no T_b at all.

The values of $\log_{10}G_0$ obtained from the intercepts on the ordinate of plots of the type shown in figure 8C are shown in figure 9B. Because of the long extrapolation, the scatter in the $\log_{10}G_0$ data is rather large. It is estimated that each G_0 value is correct to within about one order of magnitude. However, there are differences between the results for axialites, non-banded spherulites, and irregular spherulites that are far outside this error limit, and which are amenable to theoretical interpretation (see sec. 6).

5. Regime I and Regime II Growth: Calculation of $\sigma\sigma_e$ from K_g

5.1. Relationship Between Surface Nucleation Rate i and Regime I and Regime II Crystal Growth Rate Laws

The rate of deposition i of chain-folded nuclei on a unit length of a substrate is given by nucleation theory as [1, 2]

$$i(\text{surface nuclei} \cdot \sec^{-1} \cdot \text{cm}^{-1}) = C\beta \exp\left[-4b\sigma\sigma_e/(\Delta f)kT\right] \qquad (3)$$

where β is a retardation factor measured in units of "events" or "nuclei" per second that has a temperature dependence of the form $\exp\left[-U^*/R(T-T_\infty)\right]$, C is a constant, in units of cm^{-1}, that is essentially independent of temperature, and (Δf) the free energy difference between the subcooled liquid and the crystal. In general, (Δf) is given by $(\Delta h_f)(\Delta T)f/T^\circ_m$, where for a number of polymers including polyethylene, $f \cong 2T/(T^\circ_m + T)$. (In the case of crystallization of polyethylene from the melt, the factor f never differs more than 3 percent from unity. However, in the case of homogeneous nucleation, where ΔT is typically 60 °C, this factor is of considerable importance in obtaining correct estimates of $\sigma^2\sigma_e$.) Thus the surface nucleation rate may be written [1, 2][8].

$$i = \beta(z/a) \exp\left[-4b\sigma\sigma_e T^\circ_m/(\Delta h_f)(\Delta T)kTf\right]. \qquad (4)$$

where for polyethylene z is the number of $-CH_2-$ units corresponding to the initial lamellar thickness l^*_g. In rough calculations we may take l^* as 200 Å, giving $z \sim 158$; the quantity a is the molecular width, which is 4.55 Å for polyethylene for growth where folds form along the (110) planes (i.e., the long diagonal) of the unit cell. This corresponds to a layer thickness b of 4.15 Å.[9]

With such a surface nucleation rate, one can imagine two limiting cases for the rate of growth normal to the substrate which depend on the nucleation rate itself and the rate g that the folded nucleus spreads on the substrate. It is important to examine these possibilities, since it will be found that both occur in polyethylene.

5.2. Regime I (Single Surface Nucleus Causes Completion of Substrate)

The customary assumption is that each nucleation act causes the substrate or "persistence" length L to be completed before a new surface nucleus appears, leading to the accession of a new layer of thickness b

[8] The factor z in eq (4) was omitted in our previous formulations [2], but its presence is noted in a review [1]

[9] It is assumed in making the calculations here and elsewhere in this paper that (110) type folds prevail at the leading growth front no matter which particular morphology is under consideration. This does not necessarily imply that other types of folds, e.g., (200), may not be present at other parts of the lamellae in some cases. Points related to this issue are mentioned later in the paper, particularly in section 7.

TABLE 3. *Values of K_g, $\log_{10}G_0$ and $\sigma\sigma_e$ for various polyethylene fractions*

Sample designation	M_w/M_n	Temperature range	$K_g \times 10^{-5}$	$\text{Log}_{10}\, G_0$	$\sigma\sigma_e$ calc. with $b=4.15$ Å using $K_{g(1)}=4b\sigma\sigma_e T_m^\circ/\Delta h_f k$
A. Low molecular weight region (axialites)					erg²/cm⁴
		°C	K^2	(G_0 *in* $cm \cdot s^{-1}$)	
3.6 K	1.13	117.6–121.9	1.069	4.97	611
4.2 K	1.26	118.7–123.7	1.172	5.14	668
5.10 K	1.10	119.9–124.3	1.516	7.37	861
5.62 K	1.05	119.8–124.7	1.434	7.15	812
6.15 K	1.09	122.1–124.9	2.101	11.28	1188
[a] 6.15 K(R)	1.09	122.1–124.9	2.078	11.10	1176
6.29 K	1.17	122.6–125.1	1.725	8.81	976
6.35 K	1.06	120.0–125.2	1.578	7.86	892
7.84 K	1.03	121.7–126.7	1.714	8.41	966
8.06 K	1.12	122.7–126.3	1.830	9.07	1031
8.56 K	1.09	123.4–126.5	2.127	11.23	1197
[a] 8.56 K(R)	1.09	123.4–126.5	2.098	11.01	1181
8.59 K	1.11	124.3–127.8	1.822	9.30	1025
9.70 K	1.06	124.3–127.5	1.935	9.56	1087
11.4 K	1.09	124.2–127.7	2.078	10.39	1166
11.67 K	1.09	125.0–127.6	2.096	10.01	1175
11.74 K	1.07	125.3–128.5	2.036	10.17	1142
17.0 K	1.08	125.0–128.9	2.098	9.75	1173
B. Intermediate molecular weight region (axialites, $\Delta T < 17.5$ °C)					$\sigma\sigma_e$ calc. with $b=4.15$ Å using $K_{g(1)}=4b\sigma\sigma_e T_m^\circ/\Delta h_f k$ erg²/cm⁴
18.1 K	1.39	125.2–129.1	2.152	9.88	1202
19.8 K	1.07	126.2–129.1	2.231	10.23	1246
23.7 K	1.07	126.8–130.0	2.296	9.04	1281
24.6 K	1.07	126.4–129.6	2.195	10.07	1224
30.0 K	1.12	127.4–128.9	2.230	10.50	1243
[a] 30.0 K(R)	1.12	127.4–129.4	2.192	10.12	1221
30.6 K	1.19	127.2–130.3	2.150	9.60	1198
37.6 K	1.10	127.3–130.0	2.263	10.70	1260
42.6 K	1.22	128.0–129.8	2.202	10.00	1225
62.8 K	1.37	128.4–130.5	2.280	9.98	1268
68.6 K	1.17	128.0–129.7	2.268	8.77	1261
74.4 K	1.12	128.8–130.8	2.175	9.21	1209
115 K	1.16	128.1–130.7	(1.883)	(6.76)	(1046)

$\langle\sigma\sigma_e\rangle_{av}=1236$ (1202, 1246, 1281, 1224, 1243, 1221, 1198) $\langle\sigma\sigma_e\rangle_{av}=1236$ (1260, 1225, 1268, 1261, 1209)

(fig. 10). The growth rate G normal to the substrate is in this case given by $G=biL$. The quantity L is given by $n_s a$, where n_s is the number of available stems where crystallization may begin on the substrate (fig. 10).[10] In any event, one readily finds in cases where $G \propto i$ that [1, 2]

$$G_1 = G_{0(1)} \exp\,[-U^*/R(T-T_\infty)] \exp\,[-4b\sigma\sigma_e T_m^\circ/(\Delta h_f)\,(\Delta T)kTf]. \quad (5)$$

To a sufficient approximation the pre-exponential factor is given by

$$G_{0(1)} \cong b(kT/h)n_s z J_1 = b(kT/h)\,(L/a)zJ_1, \quad (6)$$

where J_1 is a factor that was anticipated in previous work [1, 2] to be within perhaps two orders of magnitude of 10^{-3}. Observe that $G_{0(1)}$ contains the factor n_s which depends on the mean substrate or "persistence" length L. In previous work n_s was estimated to be 10^3 to 10^6 [2]. Note that $n_s z$ is the number of $-CH_2-$ units on the substrate, i.e., the number of "sites" where crystallization of a new layer can be initiated.

By comparison with eq (1) and eq (5), it is seen that

$$K_{g(1)} = 4b\sigma\sigma_e T_m^\circ/(\Delta h_f)k. \quad (7)$$

5.3. Regime II (Numerous Surface Nuclei Involved in Formation of Substrate)

Under certain circumstances to be discussed shortly, it is not reasonable to suppose that the substrate will be completed before many other nuclei impinge on it (fig. 10). Thus we consider the other limit where the surface nucleation rate i is very large compared to the spreading rate g for a specified L. Sanchez and DiMarzio [7] and more recently Lauritzen [8] have

[10] Note that a and b refer to the width and thickness respectively of the polymer molecule on the substrate as shown in figure 10, and not to the dimensions of the unit cell. The dimensions of the unit cell mentioned later in this paper are denoted with the bold face letters **a** and **b**.

TABLE 3. *Values of K_g, $\log_{10}G_0$ and $\sigma\sigma_e$ for various polyethylene fractions*—Continued

Sample designation	M_w/M_n	Temperature range	$K_g \times 10^{-5}$	$\text{Log}_{10}\, G_0$	$\sigma\sigma_e$ calc. with $b=4.15$Å using $K_{g(II)}=2b\sigma\sigma_e T_m^\circ/\Delta h_f k$ erg²/cm⁴
C. Intermediate molecular weight region (coarse-grained non-banded spherulites, $\Delta T > 17.5$ °C)					
18.1 K	1.39	122.9–125.2	1.142	3.63	1277
19.8 K	1.07	125.8–126.2	0.932	2.00	1041
23.7 K	1.07	124.6–126.8	.942	2.60	1051
24.6 K	1.07	124.8–126.4	.925	2.12	1032
30.0 K	1.12	124.8–127.4	1.065	2.71	1187
[a]30.0 K (R)	1.12	125.0–127.4	1.038	2.34	1157
30.6 K	1.19	124.4–127.2	1.141	3.33	1272 } $\langle\sigma\sigma_e\rangle_{av}=1177$
37.6 K	1.10	124.6–127.3	1.008	2.13	1123
42.6 K	1.22	124.8–128.0	1.028	2.36	1145
62.8 K	1.37	125.9–128.4	1.061	2.06	1180
68.6 K	1.17	125.6–128.0	(0.896)	(0.51)	(996)
74.4 K	1.12	125.4–128.8	0.998	1.49	1110
115 K	1.61	125.6–128.1	1.042	1.66	1158
D. High molecular weight region (irregular spherulites)					$\sigma\sigma_e$ calc. with $b=4.15$ Å using $K_{g(I,\,II)}=3b\sigma\sigma_e T_m^\circ/\Delta h_f k$ erg²/cm⁴
119 K	1.26	125.3–129.4	1.777	5.64	1316
134 K	1.70	123.1–128.5	1.725	5.21	1278
210 K	1.43	122.4–128.4	1.710	4.86	1266
266 K	1.81	122.6–127.6	2.113	(6.63)	[b]1162 } $\langle\sigma\sigma_e\rangle_{av}=1263$
323 K	1.61	120.3–126.3	2.113	(6.31)	[b]1162
500 K	1.60	125.0–129.1	1.795	5.61	1328
807 K	1.59	124.5–129.3	1.800	5.08	1331

[a] (R) denotes complete rerun.
[b] Calculated with regime I kinetics. (See text.)

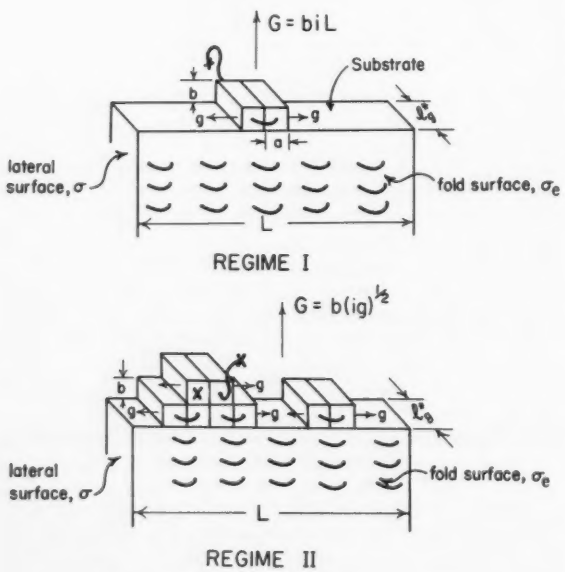

FIGURE 10. *Regime I and regime II growth (schematic).*

The quantity L is equal to $n_s a$, where n_s is the number of stems of length l_g^* comprising the substrate, and a the width of each molecule.

shown that the growth rate normal to the substrate in this case is (omitting a numerical factor of the order of unity) given by $G=b(ig)^{1/2}$. Noting that the spreading rate is to a sufficient approximation given by [2]

$$g=a\beta \exp\,[-2ab\sigma_e/kT] \tag{8}$$

it can be shown that

$$G_{II}=G_{0(II)} \exp\,[-U^*/R(T-T_\infty)] \exp\,[-2b\sigma\sigma_e T_m^\circ/(\Delta h_f)(\Delta T)kTf] \tag{9}$$

where to the same approximation that was used for $G_{0(I)}$,

$$G_{0(II)}=b(kT/h)z^{1/2}J_1 \exp\,[-ab\sigma_e/kT]. \tag{10}$$

Note that $G_{0(II)}$ does not contain the factor L or n_s. The ratio

$$\frac{G_{0(I)}}{G_{0(II)}}=n_s z^{1/2} \exp\,(ab\sigma_e/kT) \tag{11}$$

shows that $G_{0(I)}$ must under comparable conditions always be larger than $G_{0(II)}$.

The value of K_g for regime II has the value

$$K_{g(II)}=2b\sigma\sigma_e T_m^\circ/(\Delta h_f)k \tag{12}$$

which differs from that for regime I by a factor of two. This arises fundamentally from the fact that $G_I \propto i$, while $G_{II} \propto i^{1/2}$.

We turn now to the question of which formula, eq (7) or eq (12), should be used to estimate $\sigma\sigma_e$ from an experimentally known value of K_g.

5.4. Criteria for Regimes I and II

Lauritzen [8] has shown that when the dimensionless quantity

$$Z = iL^2/4g \tag{13}$$

is 0.01 or less that regime I holds with high precision, in which case eqs (5–7) apply. If $Z = 0.1$, the K_g for regime I is correct to within about 10 percent. Conversely, we estimate that when $Z \geq 1$ that regime II is entered, and is closely followed when $Z >> 1$. Thus for a given substrate length L, the ratio i/g determines which regime of crystallization is applicable. When i/g is large, regime II kinetics hold, and when i/g is small, regime I kinetics obtain. The principal variation of Z with temperature is a result of the large variation of i with undercooling.

The test for regime I and regime II behavior is as follows. We consider the experimental value of K_g as obtained by analysis of data with eq (1) to be known. We may now write [1, 2]

$$Z = iL^2/4g \approx z\mathcal{W}(L/2a)^2 \exp\left[-X/T(\Delta T)\right] \tag{14a}$$

where

$X = K_g$ (experimental) for test of regime I

with $Z \leq 0.1$ (14b)

and

$X = 2K_g$ (experimental) for test of regime II with $Z \geq 1$. (14c)

In the above expression for Z, it is found in one approximation that [1, 2]

$$\mathcal{W} = \exp(2ab\sigma_e/kT). \tag{14d}$$

With these expressions, it is possible to estimate the range of L values that are consistent with regime I or regime II behavior. What frequently happens is that such a procedure suggests a reasonable value of L for one regime, and an impossible one for the other, allowing the correct choice of regime to be made by *reductio ad absurdum*. Examples that illustrate this are cited below. The value of L cannot exceed the dimensions of a small spherulite, which places an upper limit of perhaps 25 to 50 μm on this quantity. The lower limit is at present a matter of speculation, but values of L below about 0.1 μm or 1000 Å are suspect: a predicted value of L that is on the order of the molecular width a is clearly inadmissable.

5.5. Application of Regime Test to Spherulites and Axialites in Polyethylene

We select K_g values for the test that correspond to the molecular weight in the intermediate range of ~ 30,000 to ~ 70,000 where K_g is reasonably near its limiting value (fig. 9 and table 3). Values of the parameters useful in the calculations to follow have been collected in table 4 in the appropriate units.[11]

For the coarse-grained non-banded spherulites in the range 30,000 to 70,000 we use $\Delta T = 20$ °C, $T = 400$ K, and $X = K_g = 1.05 \times 10^5$ K². Then for these objects to obey regime I, it is found with eqs (14a) and (14b) that $L \leq 2$Å, which must be regarded as completely unrealistic—no growth could occur on such a substrate. The test for regime II using eqs (14a) and (14c) for these spherulites indicates with $X = 2K_g = 2.1 \times 10^5$ K² that regime II applies when $L \geq 1.4$ μm, which is an entirely

[11] Note that a, b, and l are in cm in eqs (3) through (14) even though for convenience they are often quoted elsewhere in the text in other units such as Å or μm.

TABLE 4. *Input data for calculations on polyethylene*

Quantity	Value	Remarks
Heat of fusion, Δh_f	2.80×10^9 erg/cm³	See [1] for original reference
Molecular width, a	4.55×10^{-8} cm	Valid at 125 °C for (110) type growth face [a]
Layer thickness, b	4.15×10^{-8} cm	
Cross-sectional area of chain, $ab = A_0$	18.9×10^{-16} cm²	Valid at 125 °C
Fold surface free energy, $\sigma_{e(eq)}$ from T_m vs $1/l$ plot	93 erg/cm²	Ref. [29]
Number of —CH_2— units in stem, z		
(calc. for $l = 200$ Å)	158	
(calc. for $l = 190$ Å)	150	
Product $z \exp(2ab\sigma_e/kT) = z\mathcal{W}$ in eq (14a)	8.96×10^4	

[a] If the growth corresponds to (200) type layers, $b = 3.82 \times 10^{-8}$ cm and $a = 4.95 \times 10^{-8}$ cm at 125 °C.

594-051 O - 76 - 2

reasonable substrate length. It is therefore possible to draw the definite conclusion that the coarse-grained non-banded spherulites in the molecular weight region mentioned grow according to regime II kinetics, in which case K_g is given by $2b\sigma\sigma_e T_m^\circ/(\Delta h_f)k$.

Consider now the corresponding calculations for the axialites in the intermediate molecular weight range, where we may use $K_g = 2.2\times10^5\ K^2$, $\Delta T = 16$ °C and $T = 400$ K to make estimates. It is found that for these objects to obey regime I kinetics ($Z \leqslant 0.01$) then $L \leqslant \sim 8.1\ \mu$m. If the condition $Z = 0.1$ is used then $L \leqslant \sim 26\ \mu$m. Either way, these are reasonable substrate lengths. A test for regime II behavior with $X = 2K_g = 4.4\times10^5$ and $Z \geqslant 1$ gives $L \geqslant \sim 10^5$ cm, which is absurd. We conclude that the axialites grow according to regime I kinetics, so that $K_g = 4b\sigma\sigma_e T_m^\circ/(\Delta h_f)k$ must apply.

It is of special interest to comment on the regime that applies to the axialites in the low molecular weight range where K_g falls significantly below the value $\sim 2.2\times10^5\ K^2$ typical of the intermediate molecular weight range. Recall that in the intermediate range that the axialites follow regime I kinetics. Theoretically, the low K_g at low molecular weights could be a result of two quite different causes. The first hypothesis is that regime I applies as it does at higher molecular weights and that it is σ_e (viewed as the average surface free energy of cilia and folds) that actually falls, leading to the low K_g value. The second hypothesis is that K_g falls at low molecular weight because regime II is entered, this process taking place in such a way that σ_e is approximately constant. These hypotheses are easily checked using the most extreme axialite case, sample 3.6 K, for which $K_g = 1.069\times10^5\ K^2$. A simple calculation using $Z \geqslant 1$ shows that L would have to be larger than 0.14 cm for regime II kinetics to apply. This is clearly impossible, so pure regime II behavior can be discounted. A test for regime I kinetics using $Z \leqslant 0.1$ indicates that regime I is applicable if L is 1250 Å or less. (In making this estimate, it was assumed in calculating W in eq (14d) that σ_e had fallen to a value of 45 erg/cm².) This may be regarded as perhaps a borderline case of regime I behavior, but specimens of somewhat higher molecular weight give results that clearly imply the applicability of regime I kinetics for the axialites. In all these instances, the occurrence of regime I can be traced to the low undercooling at which axialites grow in specimens of low molecular weight. The average undercooling ΔT for specimen 3.6 K is only 13.6 °C. Thus, in the expression for Z, a low K_g is compensated for by a low value of ΔT. It is our conclusion that the falling off of the value of K_g for the axialites in the low molecular weight region is not a result of any serious variation of regime with molecular weight, but is instead caused mostly by a genuine lowering of σ_e as the molecular weight falls. The subject of the variation of σ_e with molecular weight will be dealt with in more detail in subsequent sections.

The case of the "irregular" spherulites that appear from 119 to 807 K is of interest. Using the test value $K_g \cong 1.75\times10^5\ K^2$ from table 3 as X in eqs (14), it is found that the substrate length L is such as to suggest that the samples are crystallizing between regimes I and II. At $\Delta T = 20$, for regime I to apply exactly ($Z \leqslant 0.01$), then L would have to be less than 150 Å. This is too small a substrate to be fully credible. Under the same conditions of undercooling, L would have to be 0.83 cm or larger to have regime II kinetics. This is much too large to be acceptable. The true value of L almost certainly lies between these extremes, and the samples therefore behave in a manner intermediate between regimes I and II. In this situation we apply the approximate formula

$$K_{g(\mathrm{I,II})} \cong 3b\sigma\sigma_e T_m^\circ/(\Delta h_f)k \qquad (15)$$

where the subscript (I, II) means mixed regime I and II behavior, and where it is understood that the factor of 3 contains an inherent uncertainty of perhaps $\pm\frac{1}{2}$.

Two of the irregular spherulite specimens (266 and 323 K) are close to regime I. The rest all fall between regimes I and II as noted above.

5.6. Sharpness of the Regime I → Regime II Transition: An Estimate of L

The relative sharpness of the transition between regimes I and II is evident in figures 1B and 8B, and requires comment. This effect can be understood by plotting Z versus ΔT using

$$Z = iL^2/4g \cong zW(L/2a)^2 \exp[-4b\sigma\sigma_e/(\Delta h_f)(\Delta T)kT] \qquad (16)$$

with the constants appropriate to polyethylene given in table 4. As noted earlier, the temperature dependence of Z is controlled principally by the nucleation rate i, which according to eqs (3), (4) and (16) depends on $\sigma\sigma_e$. Taking $\sigma\sigma_e$ to have the nominal value of 1250 erg²/cm⁴, which corresponds to $K_{g(\mathrm{I})} \cong 2.2\times10^5 K^2$, it is easy to calculate Z versus ΔT for various assumed values of L. The results are shown in figure 11 for L values between 1 and 30 μm.

Consider the curve for $L = 5\mu$m. It crosses the line $Z = 0.1$ at $\Delta T = 17.6$ °C, and intersects $Z = 1$ at $\Delta T = 19.2$ °C. Regime I is valid within 10 percent for $Z = 0.1$, and regime II is substantially obeyed for $Z = 1$, and obeyed with considerable precision for $Z \geqslant 10$. Thus, we estimate that the bulk of the transition takes place in a temperature range no larger than ~ 1.6 °C. It is also interesting to note that the treatment outlined above suggests that for a fixed value of L the transition should take place at a fixed undercooling, which is what is observed for specimens of different molecular weight ($\Delta T_b = 17.5 \pm 1$ °C, fig. 2B). Assuming that ΔT_b corresponds to $Z \sim 0.3$, it is found that ΔT_b is about 17.5 °C for $L = 10\ \mu$m, which is in good accord with the experimental value of $\Delta T_b = 17.5 \pm 1$ °C.

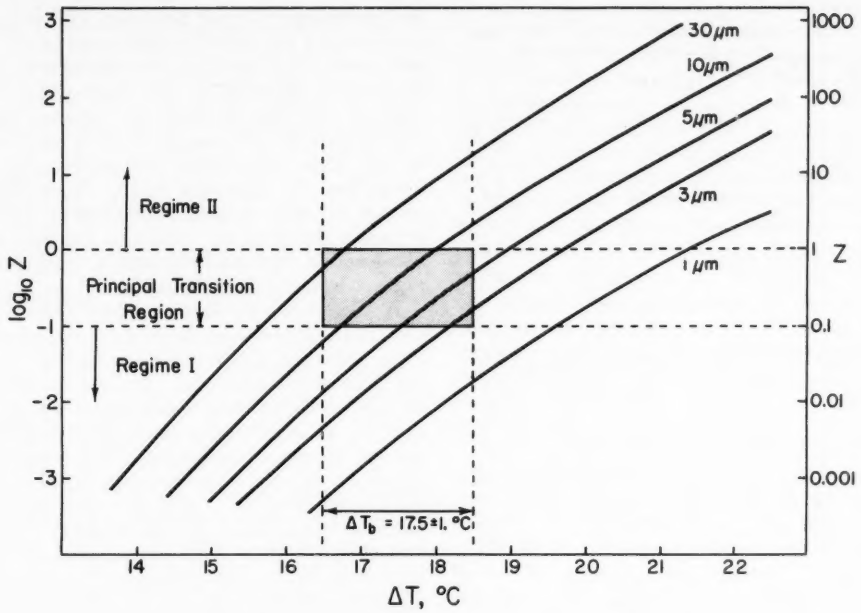

FIGURE 11. *Plot of Z versus ΔT for polyethylene for various substrate or persistence lengths L (theoretical).*

Calculated with $\sigma\sigma_e = 1230$ erg²/cm⁴, $z = 158$ and other data from table 4 using eq (16). Regime I kinetics are substantially in effect for $Z \leq 0.1$; and regime II kinetics are approximately obeyed for $Z = 1$ and are fully in effect for $Z \geq 10$. The shaded area shows region of Z and ΔT where the bulk of regime I → regime II transition takes place.

It may be surmised from the above that the value of L near the regime I→ regime II transition is within about a factor of about three or so of 5 μm for polyethylene in the intermediate molecular weight range. The width of the fibrils in polyethylene crystallized from the melt has been reported to be of about this magnitude [22, 32].[12] The value of L may be connected with the existence of a fibrillar habit in polyethylene spherulites—in such a case the width of the fibrils might be governed by L interpreted as a persistence length. Possibly this conception deserves further consideration, but we shall not pursue it further here.

5.7. Calculation of $\sigma\sigma_e$ as a Function of Molecular Weight from the K_g Values for Various Fractions

The K_g data for the axialites in the low and intermediate range have been analyzed using regime I kinetics according to eq (7) to obtain $\sigma\sigma_e$, and the results given in table 3 and plotted in figure 12A. For the axialites, the value of b in the expression for $K_{g(I)}$ was taken to be equal to $b_{(110)}$, i.e., 4.15 Å (table 4). (The symbol $b_{(110)}$ refers to the thickness of the layer growing along the (110) planes; this is $d_{(110)}$ in the customary crystallographic notation.) This tentative assignment is based mostly on the physical appearance of the axialites, inasmuch as they at least superficially resemble aggregates of single crystals of the type grown from solution. By the use of a linear molecular weight scale, figure 12A emphasizes those results that correspond to the molecular weight range 18,100 to 72,400 where K_g and hence $\sigma\sigma_e$ is nearly constant with molecular weight. Because of the logarithmic molecular weight scale, figure 12B stresses detailed values of $\sigma\sigma_e$ calculated for the axialites in the region of low molecular weight where K_g increases noticeably with increasing molecular weight, and where a large variation in $\sigma\sigma_e$ occurs because of the variation in K_g.

The K_g data for the coarse-grained non-banded spherulites in the region $M_w = 18{,}100$ to 115,000 were analyzed to obtain $\sigma\sigma_e$ using regime II kinetics with eq (12). These results are shown in table 3 and in figure 12A. For these spherulites, the value of b in the expression for $K_{g(II)}$ was taken to be equal to $b_{(110)}$, i.e., 4.15 Å (table 4). This assignment of b might seem to contradict the work of Bank and Krimm [25] who found predominantly (200) type folds for spherulites grown at $\Delta T > 17.5$ °C in polyethylene with a broad molecular weight distribution. Actually these folds are parallel to the direction of overall growth, the latter being colinear with the ***b*** axis of the unit cell. This leaves open the

[12] The value $L \sim 5$ μm refers to polymer crystallized at an undercooling of ~ 17.5 °C. Actually, L is probably a function of temperature, and may vary in such a way as to cause a further sharpening of the regime I → regime II transition.

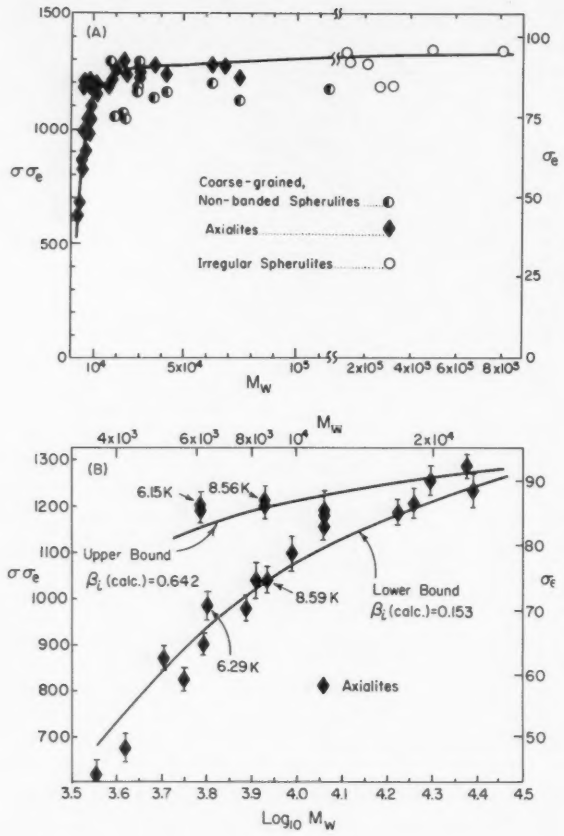

FIGURE 12. *$\sigma\sigma_e$ and σ_e as a function of molecular weight.*

definite possibility that the leading growth front is really of the (110) type. The work of Bank and Krimm does not preclude the existence of a certain fraction of (110) type folds.[13]

It is evident from figure 12A and table 3 that the $\sigma\sigma_e$ values for the axialites and coarse-grained non-banded spherulites that occur in the same specimens between 18.1 and 72.4 K are approximately the same despite the fact that the experimental K_g values from which these results were calculated differ by a factor of about two. This is mostly a result of correctly identifying the regime of crystallization in the two cases. In addition, it is clear from figure 9 and table 3 that, in qualitative accord with expectation, the G_0 values for the axialites (regime I) are very much larger than those for the spherulites (regime II) in the same specimens.

With the two exceptions, the K_g data for the irregular spherulites found between 119 and 807 K were analyzed for the approximate value of $\sigma\sigma_e$ using eq (15) with b=4.15 Å and the results given in table 3 and plotted in figure 12A. The exceptions to the use of "mixed" regime kinetics are samples 266 and 323 K, which approximate regime I. Note that the $\sigma\sigma_e$ values for all these specimens are quite close to what was found for the axialites above $M_w \cong 20{,}000$. The G_0 values for the irregular spherulites are in all cases between those of the axialites and the coarse-grained non-banded spherulites, again suggesting a mixed regime I and II growth mode.

It should be recalled that the numerical value 3 in eq (15) possesses an inherent uncertainty of up to 15 to 20 percent, so the $\sigma\sigma_e$ values for the "mixed" regime irregular spherulites are not as accurate as they are for the axialites and non-banded spherulites. Nevertheless, it is perhaps somewhat surprising that the advent of interlamellar links on a fairly large scale, which is thought to occur between $M_w = 10^5$ and 10^6, does not affect $\sigma\sigma_e$ and the corresponding average value of σ_e in a more obvious manner. (An interlamellar link of substantial length must be expected to exhibit a high local surface free energy.) Polyethylene exhibits a marked reduction in degree of crystallinity in this range [33, 34] which has been interpreted partly in terms of the occurrence of a considerable amount of "amorphous" material consisting at least partly of interlamellar links [1]. One possible implication of the above is that the number of such links is small and the amount of material in each one rather large at high molecular weights.

To a fair approximation, the various ranges of K_g values shown in figure 9 for the different morphologies lead to a single master curve for $\sigma\sigma_e$ for $M_w \geq \sim 20{,}000$ when K_g is analyzed by taking proper account of the regime of crystallization (fig. 12A). This is especially true of the data for the axialites and the irregular spherulites. The results for the coarse-grained non-banded spherulites appear to be slightly lower than those for the axialites. However, it may be noted that a statistical analysis of the "best" data, which lie between 30.0 and 62.8 K, shows that the coarse-grained spherulites and axialites have slightly overlapping values calculated as one standard deviation: coarse-grained non-banded spherulites, $\langle \sigma\sigma_e \rangle_{av} = 1177 \pm 53$ erg^2/cm^4; axialites in the same range, $\langle \sigma\sigma_e \rangle_{av} = 1236 \pm 26$ erg^2/cm^4. The value of $\langle \sigma\sigma_e \rangle_{av}$ for the irregular spherulites is 1263 ± 58 erg^2/cm^4.

5.8. The Pre-exponential Factors for Regimes I and II

Before proceeding to analyze $\sigma\sigma_e$ to get the molecular weight dependence of σ_e, it is worthwhile to briefly examine the pre-exponential factors for regime I and II. The ratio $G_{0(I)}/G_{0(II)}$ as given by eq (11) is independent of J_1, and will be dealt with first. The best data on this ratio encompasses specimens 30.0 to 62.8 K. Here regime I and regime II crystallization occur in the same specimen over a reasonable temperature range for each regime, and the data exhibit good internal con-

[13] Keith has devised a scheme whereby he explains the shape of the overall growth front in polyethylene lamellae in spherulitic structures crystallizing from concentrated solution in long chain hydrocarbons as alternate and intersecting (200) and (110) growth fronts, the latter occurring at the leading tip. The subject of (110) and (200) growth is again taken up in section 7.

TABLE 5. *Estimates of pre-exponential factors*

A. The ratio $G_{0(I)}/G_{0(II)}$	Log $[G_{0(I)}/G_{0(II)}]$	
Experimental value (30.0 to 62.8 K)	7.66 ± 1.0	
Theoretical value for $L = 10$ μm (eq 11)	6.86	
B. Absolute values [a] of $G_{0(I)}$ and $G_{0(II)}$	$G_{0(I)}$, cm/s	$G_{0(II)}$, cm/s
Theoretical value (with $\Delta F^{\dagger} = 4.5$ kcal/mol; $J_1 = 3.6 \times 10^{-3}$)	0.52×10^{10}	0.72×10^{3}
Experimental value (30.0 to 62.8 K)	1.4×10^{10}	0.3×10^{3}

[a] $G_{0(I)}$ calculated with $L = 10$ μm.

sistency within each regime. The ratio $\log_{10}[G_{0(I)}/G_{0(II)}]$ obtained from the data in table 3 is shown in table 5A, together with the theoretical value calculated using eq (11) for the case $L = 10^{-3}$ cm (10 μm). The result may be regarded as satisfactory in view of the fact that the value of the ratio $G_{0(I)}/G_{0(II)}$ is from an experimental standpoint probably not reliable to better than an order of magnitude. In any event, the theory certainly predicts the bulk of the difference in the pre-exponential factors in regimes I and II. Most of this difference is a result of the factor n_s, which occurs only in the expression for $G_{0(I)}$.

The absolute values of $G_{0(I)}$ and $G_{0(II)}$ depend on $J_1 = \exp(-\Delta F^{\dagger}/RT)$ (see eqs (6) and (10)). For the choice $L \cong 10$ μm, which is within the range estimated previously, the most consistent results are obtained when J_1 is set equal to 3.6×10^{-3}, which corresponds to $\Delta F^{\dagger} = 4500$ cal/mol. Then the absolute values of $G_{0(I)}$ and $G_{0(II)}$ are predicted within a factor of no worse than three (table 5B). The factor J_1 was inserted in $\beta = (kT/h)\, J_1 \exp[-U^*/R(T - T_\infty)] -$ from which position it enters the absolute growth rate – to account for any orientational or "parking" problem effects that might occur as polymer segments migrate across the substrate to the site of crystallization [1, 2]. The value of $\Delta F^{\dagger} \sim 4500$ cal/mol is undoubtedly subject to considerable uncertainty. From a theoretical standpoint little can be said of J_1 without a much more detailed model of the surface segmental motions involved in crystallization except to note that it should be substantially less than unity. In the case of the crystallization of copolymers or partially atactic polymers, a "parking" problem arises which should cause J_1 to become considerably smaller than was estimated for polyethylene.

Finally, we comment on the dependence of G_0 on molecular weight. If the absolute growth rate depended on the melt viscosity, one would expect G_0 to vary as $M^{-3.4}$. Between $M_w \cong 8500$ and $M_w = 74{,}400$, the value of $G_{0(I)}$ for the axialites shows some scatter, but no persistent trend with molecular weight (see fig. 9B and table 3). In this region the melt viscosity increases as $M^{3.4}$, i.e., it rises by a factor of $(74{,}400/8500)^{3.4}$ or about 1600 times. It is therefore possible to state with considerable certainty that the absolute growth rate of the axialites, as reflected in the value of $G_{0(I)}$, is not markedly affected by changes in the macroscopic viscosity. (Recall also that K_g and $\sigma\sigma_e$ are approximately constant over much of this range.) The theory for β was constructed in such a way as to refer to the "segmental" or "local jump" rate, which depends but little on molecular weight, and this accounts for the fact that G_0 is not predicted to vary strongly with molecular weight [1, 2]. Evidently this assumption was a good one for axialites in the molecular weight range cited. Specimen 115 K shows a low value of $\log_{10} G_0$ in the axialitic region (see table 3), but this sample is very close to the transition region where irregular spherulites appear, and has rather broad distribution.

The situation with the molecular weight dependence of G_0 for the coarse-grained non-banded spherulites that occur between 18.1 and 115 K is not so clear-cut because of the large scatter (fig. 9B). On examination of the data, one nevertheless gains the impression that G_0 for these structures falls as the molecular weight increases. A statistical analysis of all the points suggests that $G_0 \propto M_w^{-1.5 \pm 0.5}$. It is extremely unlikely that the variation can be as large as $M_w^{-3.4}$, which again means that the melt viscosity does not play the dominant role in the molecular weight dependence of G_0.

The pre-exponential factor for the irregular spherulites is insensitive to changes in molecular weight from 119 to 807 K. It is evident that the macroscopic viscosity does not lead to a change of G_0 in the high molecular weight region.

Our overall conclusion is that the theory gives a reasonable explanation of the order of magnitude of the ratio of the pre-exponential factors for regime I and regime II crystallization in the intermediate molecular weight range, and provides some insight into the factors that control the absolute magnitude of the pre-exponential. Another conclusion is that the macroscopic viscosity does not directly govern the pre-exponential factor or the absolute crystallization rate.

6. The Variation of σ_e With Molecular Weight

6.1. Experimental Determination of σ_e

Our first objective in this section is to extract the average value of σ_e from the product $\sigma\sigma_e$ for each fraction, and thereby establish the "kinetic" value of σ_e as a function of molecular weight. Then a simple theoretical treatment will be given which elucidates the variation of σ_e with molecular weight, and thereby allows the theory of chain folding to be applied over practically the entire range of molecular weight studied.

Basically what we shall do is establish a reasonable value of σ, and find the σ_e relevant to each molecular weight by calculating it as $\sigma\sigma_e/\sigma$.

In the first method of obtaining σ, we estimate the value of $\sigma\sigma_{e(\infty)}$ by noting that $\langle \sigma\sigma_e \rangle_{av}$ for the axialites in the intermediate molecular weight range (30.0 to

TABLE 6. *Values of* $\langle\sigma\sigma_e\rangle_{av}$ *and estimates of* $\sigma\sigma_{e(\infty)}$, σ *and other parameters*

A. Input Data	Value[a]	Estimated value of $\sigma\sigma_{e(\infty)}$ ($\nu \to \infty$)	
	erg^2/cm^4	erg^2/cm^4	
1. $\langle\sigma\sigma_e\rangle_{av}$, axialites (30.0 to 62.8 K; $\bar{\nu} \cong 22$)	1236 ± 26	1285	
2. $\langle\sigma\sigma_e\rangle_{av}$, coarse-grained non-banded spherulites (30.0 to 62.8 K; ($\bar{\nu} \cong 22$)	1177 ± 53	1224	
3. $\langle\sigma\sigma_e\rangle_{av}$, irregular spherulites (119 to 807 K)	1263 ± 58	1263	
B. Estimates of σ and σ_e	σ	σ_e	$\sigma_{e(\infty)}$
	erg/cm^2	erg/cm^2	erg/cm^2
1. Calculate σ as $\sigma\sigma_{e(\infty)}$ axialites/$\sigma_{e(eq)} = 1285/93$	13.8	—	—
2. Calculate σ for polyethylene using $\alpha = 0.12$ obtained from homogeneous nucleation in *n*-octadecane using $\sigma = \alpha(\Delta h_f)(ab)^{1/2}$	14.6	—	—
3. Combine $\langle\sigma\sigma_e\rangle_{av} = 1236$ erg/cm² (axialites 30.0 to 62.8 K) with $\sigma^2\sigma_e = 18{,}000$ erg³/cm⁶ from homogeneous nucleation data on polyethylene in same M.W. range [35].	14.6	84.9	88.3[b]
C. Best values—summary			
Value	*Remarks*		
1. $\sigma = 14.2 \pm 0.4$ erg/cm²	Mid-range value for B.1, B.2, and B.3 above.		
2. $\alpha = 0.117 \pm 0.006$	Calc. from $\alpha = \sigma/(\Delta h_f)(ab)^{1/2}$		
3. $\sigma_{e(\infty)} \cong 90.5$ erg/cm²	Calc. as 1285/14.2		

[a] Errors quoted as one standard deviation.

[b] Calculated as $\sigma_e \times 1.04$.

62.8 K), which corresponds to an average of $\nu \cong 22$ folds per molecule, is 1236 ± 26 erg²/cm⁴. We then correct this value slightly upward by the factor $(\nu+1)/(\nu+\beta_i) = 1.04$ with $\beta_i = 0.15$ (see later) to get the estimated limiting value at high molecular weights, $\sigma\sigma_{e(\infty)} = 1285$ erg²/cm⁴ (table 6, item A.1). The value of $\sigma = 13.8$ erg/cm² is then estimated from $\sigma\sigma_{e(\infty)}$ using $\sigma_{e(eq)}$ as shown in table 6, item B.1. In making this estimate of σ, axialite data have been emphasized because of their rather low standard deviation, and because the explanation of the large variation of $\sigma\sigma_e$ and σ_e in the axialites at low molecular weights is our main objective. However, we note that no basic conclusion of this paper would be altered if one of the other estimates of $\sigma\sigma_{e(\infty)}$ in table 6A were employed in the estimation of σ.

The second estimate of σ is made by using the empirical relation [1, 2]

$$\sigma = \alpha\,(\Delta h_f)\,(ab)^{1/2} \tag{17}$$

where α was determined by homogeneous nucleation studies on n-$C_{18}H_{38}$ (table 6, item B.2). (For details see reference [1].)

Finally we obtain another estimate of σ by combining $\sigma^2\sigma_e$ from homogeneous nucleation data on polyethylene fractions [35] and $\sigma\sigma_e$ from growth data (table 6, item B.3). Notice that this calculation also gives a value of $\sigma_{e(\infty)}$ in reasonable accord with the equilibrium value. The homogeneous nucleation data were confined to the same molecular weight range as the axialite data in A.1 in table 6, e.g., 30.0 to 62.8 K.

From these results it is found that $\sigma = 14.2 \pm 0.4$ erg/cm² (mid-range value for the three estimates). A very similar estimate of σ was given in a recent review [1]. Values of σ_e calculated by dividing the $\sigma\sigma_e$ value for each fraction by 14.2 erg/cm² are shown in figure 12.

The foregoing procedure involves the implicit assumption that σ does not depend on molecular weight, and that the variation of $\sigma\sigma_e$ is due to changes in the average value of σ_e. Combination of $\sigma^2\sigma_e$ from homogeneous nucleation data of Ross and Frolen [35] and $\sigma\sigma_e$ from growth data taken on the fractions studied here at low molecular weights suggests that σ_e is the quantity that varies with molecular weight.

The existence of a master curve at moderate to high molecular weights for the variation of $\sigma\sigma_e$ with molecular weight that is approximately independent of morphology implies of course that there is a similarly shaped master curve for σ_e versus M_w (see fig. 12A, right-hand scale).

6.2. Theory for Variation of σ_e With Molecular Weight

Insofar as the variation of $\sigma\sigma_e$ or σ_e is concerned, it is seen in figure 12 that it is only at fairly low molecular weights—say from about 20,000 or so downward for the axialites—that we need seriously concern ourselves with a theoretical treatment for the variation of σ_e. Above this molecular weight, the theory of growth with chain folds appears to be applicable with a nearly constant value of σ_e or $\sigma\sigma_e$. Three morphologically distinct species appear from a molecular weight of 20,000 and upward, but the temperature dependence of their growth is in each case governed by practically the same value of $\sigma\sigma_e$ in the expression for the surface

nucleation rate i. As the "regime" analysis showed, the temperature dependence of the axialite growth rate varies as i, the growth of non-banded spherulites varies as $i^{1/2}$, and the growth of the irregular spherulites changes with temperature as $i^{3/4}$, but the $\sigma\sigma_e$ or σ_e value that controls i is about the same for each modification at moderate and high molecular weights.

We turn now to the low molecular weight region, and ask two questions: (1) why does the value of $\sigma\sigma_e$ and σ_e generally fall at low molecular weights and (2) why do the data show such strong variations for samples of practically the same molecular weight (fig. 12B)? That these variations are real and far outside experimental error can be traced through the analysis beginning with the $\log_{10}G$ versus T data in figure 1A. (See for example specimen pairs (6.15, 6.29 K) and (8.56, 8.59 K) in fig. 1A and note how these data lead through the K_g values in table 3, to high and low points at nearly the same molecular weight in fig. 12B.) Note also that the reruns of the high points 6.15 and 8.56 K, denoted 6.15 K(R) and 8.56 K(R) in table 3, gave practically identical results for $\sigma\sigma_e$.

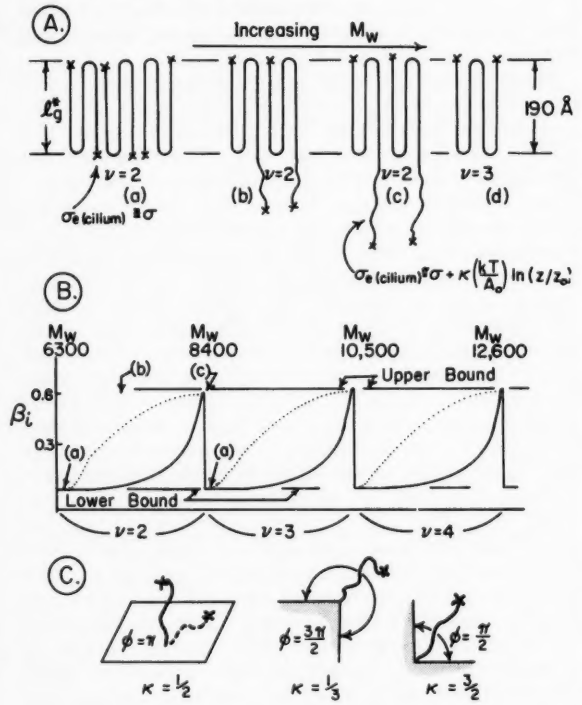

FIGURE 13. *Model for variation of σ_e with molecular weight.*

Item B calculated for case $l_g^* = 190$ Å.

The simple model shown in figure 13A will be helpful in discussing the change of σ_e with molecular weight and the intermittent high and low values of σ_e shown in fig. 12B. (Note curves denoted "upper bound" and "lower bound" in fig. 12B.)

Treating the observed surface free energy of the surface nucleus (and subsequent steps) as the sum of the effects of cilia and folds we may write [3]

$$\sigma_e = \sigma_{e(\infty)}[(\nu+\beta_i)/(\nu+1)] \tag{18}$$

where $\sigma_{e(\infty)}$ is the limiting value of σ_e at high molecular weights corresponding to a strictly folded surface, and ν the number of folds per molecule on a substrate of width l_g^*. The quantity β_i is

$$\beta_i = \sigma_{e(\text{cilium})}/\sigma_{e(\infty)} \tag{19}$$

where $\sigma_{e(\text{cilium})}$ is the local contribution associated with a cilium (or chain end in the surface) to the average surface free energy. We will take $\sigma_{e(\infty)}$ to be 93 erg/cm² for preliminary calculations. This will prove to be within a few percent of the "best" value.

Specific attention is drawn to the fact that eq (18) was derived [3] on the assumption that the first chain end is situated essentially flush with the fold surface as shown schematically in figure 13A. One basic reason for making this assumption (entirely apart from its simplicity) is that it minimizes the local surface free energy associated with a molecule that is forming a nucleus on the substrate. This assumption involves the implication that the molecule to be attached has time to sample various configurations before it becomes a surface nucleus, or participates in the subsequent strip completion process. Evidence exists suggesting that molecules are physically adsorbed to some extent prior to crystallization, and crystallize after transport across the surface [1, 2]. Such a process would allow ample opportunity for the assumed configuration to occur. In practice, it is sufficient that the first chain end be associated with a quite short cilium rather than one that is always exactly flush with the fold surface.

As a useful simplification, we will assume that the width of the substrate, l_g^*, is approximately constant in the region of interest. (It is apparent in table 2 that L_2 generally has a value in the range of 200 ± 20 Å; later we shall calculate that l_g^* is within the same limits.) In the case of a nearly constant substrate width, it is seen in figure 13A that as the molecular weight is increased (a) through (d) that the pendant cilium at first gets longer as the molecular weight increases [(a) through (c)]. Then as the cilium becomes as long as l_g^*, a new fold appears at $\nu+1$ with a short cilium, and the process repeats itself, (d). This process will cause $\sigma_{e(\text{cilium})}$, and hence β_i, to vary in some manner (solid and dotted lines in fig. 13B) between the lower and upper bounds of β_i.

The experimental σ_e data in figure 12B exhibit rather definite upper and lower bounds. This shows that β_i in eqs (18) and (19) has a corresponding upper and lower bound. Let us now attempt on a theoretical basis to estimate the upper and lower bounds of β_i. We obtain the lower bound by setting $\sigma_{e(\text{cilium})} \cong \sigma = 14.2$ erg/cm², which with $\sigma_{e(\infty)} = 93$ erg/cm², gives $\beta_i = 0.153$. This leads to

$$\sigma_{e(\text{lower bound})} = 93\{(\nu+0.153)/(\nu+1)\}. \tag{20a}$$

Assuming that $l_g^* = 190$ Å, each stem has a molecular weight close to 2100. The molecular weight M at each integral ν value is 2100 $(\nu+1)$, which leads to

$$\sigma_{e(\text{lower bound})} = 93[(M-1779)/M]. \quad (20b)$$

This function is plotted in figures 12B and 14. It is seen to give a reasonable description of the lower bound of the data from $M_w \cong 5{,}000$ upwards.

Consider now the upper bound. We have heretofore introduced the concept that the initial surface nucleus (and subsequent molecules in the strip completion process) may exhibit a pendant cilium (fig. 13A). There is considerable independent justification for the assumption that cilia can exist in unthickened crystals. (For example, Keller and Priest have demonstrated that a substantial fraction of the end groups in polyethylene single crystals are external to the body of the crystal [36].) With this concept, we proceed by assuming that the upper bound of σ_e corresponds to a surface containing the largest cilium that can occur, which has a length closely approaching l_g^*; a cilium that is any longer will fold over, giving a chain end in the surface at $\nu+1$. Lauritzen and DiMarzio [37] (LD) have devised an expression for the surface free energy contribution of a long cilium where, in its entropic wandering, configurations outside of a wedge angle ϕ are excluded (fig. 13C). Taking account of the fact that a "zero" length cilium has a surface free energy of approximately σ, the LD expression may be written

$$\sigma_{e(cilium)} \cong \sigma + \kappa(kT/ab)\ln(z/z_0) \quad (21a)$$

where

$$\kappa = \pi/2\phi. \quad (21b)$$

In this expression z_0 is the "effective" or "statistical" segment length, which is about 6.7 for polyethylene [38], z the number of $-CH_2-$ units in the cilium, and ab the cross-sectional area A_0 of the chain. The quantity kT/ab is 29.3 erg/cm² at $T = 400\,K$ for polyethylene. The expression is only valid for values of z/z_0 that are in excess of about 5. (It also gives the correct result $\sigma_{e(\text{cilium})} = \sigma$ for $z/z_0 = 1$.) Equation (21a) is a more general case which extends the earlier calculations of DiMarzio [39] demonstrated only for the situations where $\phi = \pi/2$ and $\phi = \pi$.

Assuming that the cilium emanates from a plane, i.e., $\phi = \pi$, which gives $\kappa = 1/2$, we calculate using $\sigma = 14.2$ erg/cm² and $l_g^* = 190$ Å ($z \cong 150$) in eqs (19) and (21a) that

$$\beta_{i(\text{upper bound})} \cong 0.642. \quad (22)$$

Because of the uncertainty in ϕ, and other factors, this must be regarded as only a rough estimate. Also, the effect of the volume excluded by nearby cilia is not considered. Nevertheless, the point remains that it is reasonable that a long cilium has a high local surface free energy associated with it, which leads to a β_i that is much higher than that of a short cilium or chain end in a surface.

Using the above estimate, we may calculate

$$\sigma_{e(\text{upper bound})} = 93[(\nu+0.642)/(\nu+1)] \quad (23a)$$

or, using $M = 2100\ (\nu+1)$:

$$\sigma_{e(\text{upper bound})} = 93[(M-752)/M]. \quad (23b)$$

A plot of this function is shown in figure 12B. The agreement is such as to suggest that the surface nuclei that are associated with the high values of σ_e (e.g., 6.15, 6.15 K(R) and 8.56, 8.56 K(R)) possess long terminal cilia approximating l_g^* in length. Meanwhile, it appears highly probable to us that those data points that lie near the lower bound are associated with quite short initial and terminal cilia, or initial and terminal chain ends actually in or nearly in the same plane as the folds (see fig. 13A). An analysis of the high points in figure 12B indicates that the best experimental fit is obtained if $\beta_i = 0.74$ (fig. 14).

The "best" value of $\sigma_{e(\infty)}$ is close to 90.5 erg/cm² (table 6, item C.3). The foregoing analysis could be repeated with this value instead of our original estimate of 93 erg/cm², but the change in both the theoretical and experimental estimates of β_i (upper bound) and β_i (lower bound) would be insignificant.

Sanchez and DiMarzio have developed a theory of crystallization with chain folding that deals with the variation of growth rate with molecular weight and polymer concentration [40, 41]. They employ the assumption that the initial chain end is rather long—about one-third to one-sixth of the whole molecule forms the initial cilium—in contrast to our simplified assumption that the initial chain end is practically flush with the fold surface (fig. 13A). If their assumption were to be used in the present work, a large effective value of β_i would be calculated with eq (21) for the initial cilium that would give σ_e values that greatly exceeded our calculated and experimentally determined lower bound ($\beta_i \cong 0.15$) and which would possibly even exceed the upper bound. While we thus have good reason for holding to our particular assumption regarding the nature of the placement of the initial chain end in bulk crystallization, it must be remembered that other aspects of the treatment of Sanchez and DiMarzio confine its validity to rather dilute solution. Nevertheless, an extension or revision of their theory using the assumption that the first chain end is quite short is probably worth some consideration.

The experimental values of σ_e and β_i vary intermittently between rather definite upper and lower bounds at low molecular weights, and it is shown above that these bounds can be reasonably explained in terms of the length of the terminal cilia associated with the molecules comprising the surface nuclei and growth strip. We now ask why the values for σ_e intermittently vary between the upper and lower bounds. The explanation suggested below implies that β_i and σ_e actually alternate between their upper and lower bounds. Despite the large number of samples studied, the data are insufficient to show actual alternation over a wide range of molecular weights. However, there is some evidence for a regular variation over a

restricted range of molecular weight. Accordingly, the explanation offered below for the variation of σ_e and β_i between their upper and lower bounds must be regarded as somewhat tentative.

For a given value of ν, say $\nu=2$, the terminal cilium length in the model shown in figure 13A increases uniformly as the molecular weight increases. Then the cilium reaches a length of l_g^* where $\nu \rightarrow \nu+1$, and the cilium length again becomes very small. This will lead β_i to alternate between the lower and upper bounds as the molecular weight increases as shown in figure 13B. We emphasize again that this holds only if l_g^* does not vary strongly with molecular weight as the molecular weight changes. The details of the variation of β_i with molecular weight (increasing cilium length) with a given ν is a matter of considerable uncertainty. Equation (21) suggests a situation as shown by the dotted lines in figures 13B and 14. This assumes an extremely sharp fraction. If it is arbitrarily assumed that the variation of β_i with increasing cilium length is as shown in the solid line in figure 13B, the estimates of the rather abrupt variation of σ_e with molecular weight seem appropriately predicted at $\nu=1 \rightarrow \nu=2$ and $\nu=2 \rightarrow \nu=3$, as shown in figure 14.

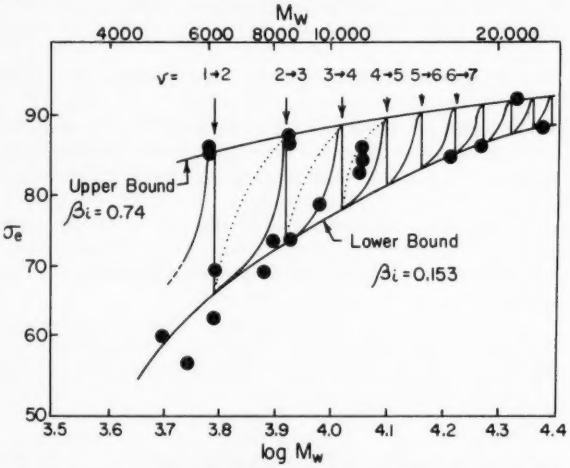

FIGURE 14. *σ_e as a function of molecular weight for axialites showing effects of long and short cilia as $\nu \rightarrow \nu+1$.*

The solid and dotted lines are due to variation of β_i within a given ν as shown in figure 13B.

It is possible that the tendency for many of the experimental points that lie between ν and $\nu+1$ that imply a lower β_i than that given by eq (21) [dotted lines in figures 13B and 14] is a result of the existence of the distribution of molecular weight in the samples. There should be a natural tendency in the presence of a distribution for the nucleus to select out chains with short cilia (low β_i) leading to σ_e values near the lower bound. Then when just the appropriate molecular weight corresponding to a long cilium is reached, the search for molecules leading to short cilia is too difficult, and the system shows a high β_i and enhanced σ_e. At a slightly higher molecular weight, the long cilia folds over, and a low β_i and σ_e is rather abruptly recovered.

Our overall conclusions are as follows. The upper and lower bounds exhibited by σ_e and β_i at low molecular weights are a result of cilium length effects in the growth nucleus. A terminal cilium in or near the fold surface is associated with a low β_i and σ_e, and a terminal cilium that approximates l_g^* in length leads to a high β_i and a σ_e near the upper bound. The increase and decrease of cilium length shown in figure 13A with increasing molecular weight is probably the cause of the existence of a rather definite upper and lower bound to σ_e at low molecular weights. This model implies that β_i and σ_e should alternate in a regular way between their respective upper and lower bounds. The data are insufficient to show this in detail, but abrupt changes in β_i and σ_e occur in two regions of molecular weight that are consistent with the model. Many more good fractions—and possibly much sharper ones—than were available to us would be required to obtain experimentally the shape of the β_i curve within a given ν.

Attention is now drawn to the question of the constancy of l_g^*, which approximation was used in the foregoing analysis. The value of the initial lamellar thickness l_g^* for single crystals of polyethylene of high molecular weight can be accurately calculated as a function of undercooling with the expression [1]

$$l_g^* = 2\sigma_e T_d^\circ/(\Delta h_f)(\Delta T) + C_2 \qquad (24)$$

where $C_2 = 4.3 \times 10^{-7}$ cm or 43 Å. This expression, which has a general theoretical basis, is quantitative for a thickness range of ~100 Å to near 200 Å for crystals formed from dilute solution [1]. We adapt this expression to the present case, and calculate l_g^* for each of the fractions using σ_e from figures 12 or 14, the T_m° relevant to the fraction, and the average undercooling $\overline{\Delta T}$ used in the growth rate runs (table 3)[14]. The results are shown in figure 15. It is seen that l_g^* is predicted to be in the range 200 ± 20 Å from $M_w \simeq 6000$ upwards, which covers the cases $\nu=1 \rightarrow 2$, and all higher ν. Also shown are the LAXR "L_2" data for several of the fractions. In general, these lie within the same range as the l_g^* values calculated with eq (24). This confirms the validity of the assumption concerning the approximate constancy and magnitude of l_g^* that was used in the calculations cited above for $M_w \geq 6000$. At very low molecular weights, the low value of σ_e causes l_g^* as calculated by eq (24) to fall well below 200 ± 20 Å.

It is of interest to comment on why l_g^* was so nearly constant in the particular case of polyethylene fractions of $M_w \sim 6000$ and higher. We may write the expression for the growth rate in the form

$$G \cong G_0 \exp[-U^*/R(T-T_\infty)] \exp[-2b\sigma l_g^*/kT] \qquad (25)$$

to a good approximation. Then if G were measured within the restricted range of $\sim 10^{-5}$ cm/s to $\sim 10^{-8}$

[14] It is worth noting that the value of l_g^* calculated with eq (24) does not depend on the regime in which the crystallization occurs [1, 2].

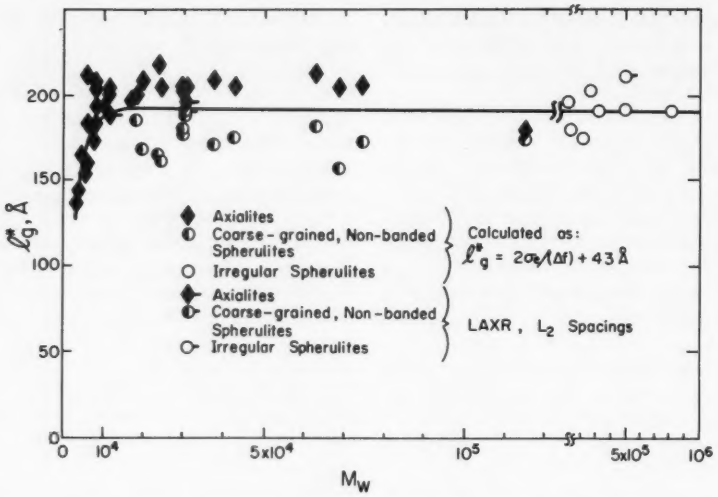

FIGURE 15. *Experimental and theoretical values of the initial lamellar thickness l^*_g as a function of molecular weight.*

cm/s, it is easy to show that l^*_g will increase by only about 10 percent or so as G goes from 10^{-5} cm/s to 10^{-8} cm/s. What happens is that l^*_g increases with temperature according to eq (24) in accord with theory and experiment, but this increase for any given specimen is small compared to l^*_g (or the maximum cilium length) because of the restricted temperature range allowed by the practical matter of the slowest and fastest rates that are feasible to measure.

With the analysis given in this section, it is justified to say that we have gained some insight into the factors that govern the growth rate of polyethylene from the melt from a molecular weight corresponding to but two folds per molecule (*circa* $M_w \sim 6000$) up to a molecular weight in excess of 800,000.

7. Work of Chain Folding

The "best" value of $\sigma_{e(\infty)}$ given in table 6 (item C.3) is 90.5 erg/cm². While there are various ways to estimate this quantity, this value represents a reasonable compromise and is consistent with the growth rate data within rather narrow limits. This can be used to calculate a "kinetic" value of the work of chain folding q as

$$\sigma_{e(\infty)}\,(\text{kinetic}) = (q/2ab) + \sigma_{e0} \tag{26}$$

where σ_{e0}, which is the surface free energy in the absence of any work of chain folding, may be taken as equal to $\sigma = 14.2$ erg/cm² (table 6, item C.1). This leads to the estimate

$$q\,(\text{kinetic}) = 4.09 \pm 0.4 \text{ kcal/mol.} \tag{27}$$

The corresponding estimate of q from equilibrium data on single crystals of polyethylene (i.e., $\sigma_{e(eq)} = 93 \pm 9$ erg/cm² from a T_m versus $1/l$ plot) gives with $\sigma_{e0} = 14.2$ erg/cm² the value [1]

$$q\,(\text{equilibrium}) = 4.23 \pm 0.4 \text{ kcal/mol.} \tag{28}$$

The agreement between the "kinetic" and "equilibrium" estimates of q in polyethylene is sufficient to support our particular application of nucleation theory to the problem of chain folding. The folds are kinetically formed continuously during the crystallization process, and exhibit the same properties whether their free energy of formation is measured by kinetic or thermodynamic means.

It is of interest in connection with the foregoing estimates that theoretical calculations by Corradini and co-workers using inter- and intra-potential energy functions have suggested that

$$q\,(\text{theoretical}) = 4.26 \text{ kcal/mol} \tag{29}$$

for (110) type folds [42]. It may be recalled that our analysis in which we find q (kinetic) $= 4.09 \pm 0.4$ kcal/mol is based on the assumption that (110) type folds control the growth kinetics; we also observe that the experimental value of q (equilibrium) $= 4.23 \pm 0.4$ kcal/mol is based on melting data on single crystals with mostly (110) folds.

Corradini and co-workers estimate a q value close to 3.1 kcal/mol for (200) folds. The accuracy of these calculations is difficult to assess. Nevertheless, in view of the agreement attained between q(kinetic), q(equilibrium), and the q(theoretical) estimated by Corradini et al., in the case of (110) type folding, it is reasonable to assume that their theoretical estimate of q from potential energy functions for the (200) folds is basically correct. This then raises the question of why the lower energy (200) folds, known to occur in ordinary

polyethylene spherulites [25], do not make themselves more apparent in the kinetics.

If two types of folds of different q were present in a given morphology, it is by no means certain that the low one would be clearly observed in kinetic measurements. Circumstances occur where both (110) and (200) type folds appear on the same overall growth front. For example, Keith [43] has shown that the overall growth front of polyethylene spherulites forming from concentrated solutions of pure hydrocarbons are serrated, with alternate and intersecting traverses of (110) and (200) folds, the latter being in the direction of overall growth, which is along the $\boldsymbol{b}$ axis of the unit cell. The polymer lamella resembles a laurel leaf with serrated edges, with the growth direction corresponding to the long axis of the leaf. The (110) folds occur at the growth tip, and at each serration. In this case—which we consider to be reasonable in a spherulitic morphology in bulk polyethylene—the kinetics of radial growth would tend to be dominated by the higher energy (110) folds until the (200) runs became quite long in comparison with the (110) runs. Possibly the presence of (200) folds is the reason that $\sigma\sigma_{e(\infty)}$ for the coarse-grained non-banded spherulites is slightly lower than it is for the axialites (table 6). However, it must be noted again that the difference between the $\sigma\sigma_{e(\infty)}$ in these two cases has a somewhat doubtful statistical significance. In any case it appears that (110) type folds generally dominate the kinetics of overall growth in axialites and irregular spherulites, and have the largest effect in the case of the coarse-grained non-banded spherulites.

8. Discussion

8.1. Relationship to Earlier Work: Growth Rate and Morphology

The principal previous research on the rate of growth of crystals from the melt in polyethylene appears to be that of Lindenmeyer and Holland [4]. They used five specimens ranging from $M_v = 3900$ to 135,000 in molecular weight. They mention the presence of banded spherulites only, whereas we found axialites over most of this molecular weight range at low undercoolings, and coarse-grained non-banded spherulites at higher undercoolings. There is no evidence of a break in log G versus T in their data, but this is explained by the relatively low growth temperatures used in their investigation. The quantitative agreement in absolute growth rates between our work and theirs is not particularly good. This can be traced in part to the fact that some of their runs were made at temperatures low enough to produce crystallization that was apparently sufficiently rapid to cause some self-heating. Also we infer from their paper that they may have used very high T_1 values which might have degraded the samples somewhat. Nevertheless, their data, when plotted as log G versus $1/T(\Delta T)$ (see their fig. 3), show changes in slope in the low molecular weight region very similar in broad aspect to that shown in our figure 8A. This implies that K_g increases and then levels off, as we found in the present research. No intermittent high and low values at low molecular weights were observed, but this may have resulted from the relatively few samples used.

It is of considerable interest to compare what we have found for polyethylene fractions with the results reported for a systematic study of TMPS fractions by Magill [44]. In this work, it was found that $\sigma\sigma_e$ rose rapidly at first and then tended to level off at high molecular weights, and Magill interpreted this as meaning that σ_e behaved with increasing molecular weight in the same manner. Moreover, Magill noted some variations of σ_e at low molecular weights (but still well within the region where folding occurs) that are strongly reminiscent of the intermittent high and low data for σ_e for polyethylene fractions near $M_w = 6200$ and $M_w = 8500$ as seen in figures 12 and 14. In particular, one of the low TMPS fractions ($M = 8700$) has a σ_e that is substantially higher than that of neighboring points. (Recall that in polyethylene we have tentatively attributed this type of behavior to the occasional appearance of a terminal cilium close to l_g^* in length on the growth nucleus.)

Most of the data points on TMPS were taken at rather high undercoolings, corresponding, in our estimation, to regime II or mixed regime I and regime II [1]. It is therefore not surprising that Magill did not observe a regime I → regime II transition. Our analysis of the growth data, given elsewhere [1], suggests that $\sigma_{e(\infty)}$ for TMPS is 34 ± 11 erg/cm^2, which is in fair accord with the value $\sigma_{e(eq)} = 39$ erg/cm^2 obtained from a T_m *versus* $1/l$ plot.

Devoy and Mandelkern [45] have discussed polymers where $\sigma\sigma_e$ rises and then levels off with increasing molecular weight. Their analysis differs in a number of significant respects from that given in this work.

8.2. Regime I and Regime II in Other Polymers: Morphological Implications

Definite evidence for the existence of regime I and regime II crystallization was found for polyethylene fractions in the intermediate molecular weight range. The regime tests gave clear-cut results in this region, and the K_g values differed by a factor of about two. Also, the ratio of the pre-exponential factors was very large and of approximately the magnitude expected.

We must now raise the question as to why no such effect was seen by previous investigators for polyethylene or any other polymer crystallizing from the melt. In the case of polyethylene the answer is fairly straightforward. Few measurements, if any, were previously made at undercoolings sufficiently low to enter regime I. For example, Lindenmeyer and Holland carried out the main body of their investigations at temperatures below 127 °C, and the transition between regimes I and II occurs near or above this temperature. This same point probably accounts in part for the failure to observe the transition in other polymers—at high growth temperatures where regime I is entered, the growth rate tends to be extremely slow and the

region is therefore quite inconvenient to survey from an experimental standpoint.

It has already been pointed out that the regime I → regime II transition is smeared out in polyethylene with a broad distribution of molecular weight. This is particularly clear in the case of the whole polymer SRM 1475 sample. On this basis, one might not expect to find the transition in other polymers where the distribution was broad. It will be a matter of interest to see if fractions of other polymers exhibit the transition.

It is of special interest to note that Cooper and Manley [46] have found some evidence for the existence of a regime I → regime II transition in polyethylene fractions crystallized from dilute solution. We observe that the transition, though not as well-defined in the dilute solution case as in the case of crystallization from the melt, appears to occur at approximately the same undercooling in both cases. We also observe that at a specified concentration, $\sigma\sigma_e$ as calculated with $K_g = 3b\sigma\sigma_e T_d^\circ/(\Delta h_f)k$, where T_d° is the dissolution temperature, tends to rise and then level off with increasing molecular weight when the variation of T_d° with molecular weight is taken into account (see their table 6). They find a $\sigma\sigma_e$ at high molecular weights comparable to that which we have found for melt-crystallized polyethylene.

In the case of polyethylene fractions in the low and intermediate molecular weight range, a good correlation exists between morphology and regime. Regime II kinetics could in general be identified with the existence of coarse-grained non-banded spherulites, (or spherulites with a few coarse bands at the lowest isothermal growth temperatures), and the appearance of axialites at high growth temperatures is, broadly speaking, associated with regime I kinetics. Also, the existence of irregular spherulites at high molecular weights seems to mostly involve mixed regime I and II kinetics. While these identifications seem reasonably definite for polyethylene fractions crystallized from the melt, it is not known how widely applicable the general idea of the relationship between regime and morphological characteristics really is for fractions in other polymers.

8.3. Overview

The following summarizes the basic picture of crystallization that has evolved.

The rate of crystallization of polyethylene fractions from the melt is governed by the rate of deposition of folded surface nuclei on the previously formed substrate. The nucleus is formed by a molecule (probably already associated with the substrate by physical adsorption [1]) that apparently arranges its first chain end in such a way as to keep the free energy near a minimum, i.e., the initial chain end is flush or nearly so with the fold surface. Then the rest of the molecule comes into crystallographic register with the substrate in a sequential process, leaving a dangling terminal cilium if the contour length of the molecule does not correspond to an integral multiple of the fold period l_g^*. On the average, the pendant cilium does not exceed the fold period; if it is longer than l_g^* a new fold is formed, and the long cilium goes down on the substrate. A sufficiently short terminal chain end has a low effective surface free energy $\sigma_{e(\text{cilium})} \cong \sigma$, and a long terminal cilium has a $\sigma_{e(\text{cilium})}$ that is proportional to the natural logarithm of the effective chain length z/z_0, giving a $\sigma_{e(\text{cilium})}$ value that is many times larger than σ. The value of $\sigma_{e(\text{cilium})}$ for a long terminal cilium of length l_g^* is roughly comparable to, but probably not in excess of, σ_e. Since the average terminal cilium length is such that its local surface free energy $\sigma_{e(\text{cilium})}$ is less than that associated with a chain fold, the total average surface free energy (cilia plus folds) is rather low for material of low molecular weight where the fraction of cilia is rather high. As the molecular weight is increased, the fraction of folds likewise increases, and the average value of the surface free energy σ_e tends toward a limiting value, $\sigma_{e(\infty)}$.

For a given number of folds and a fixed substrate width l_g^*, a surface nucleus can have either a very short cilium, one of intermediate size, or one closely approaching l_g^* in length, depending on the contour length of the molecule forming the nucleus. Since the local surface free energy of a long cilium is greater than that of a short one, alternating values of σ_e are to be expected in very sharp fractions at low molecular weights as with increasing molecular weight a molecule goes through the sequence: short cilium → intermediate length cilium → cilium approaching l_g^* in length → formation of additional fold with short cilium. This effect is believed on a tentative basis to be the source of the intermittent low and high values of σ_e observed at low molecular weights in the particular fractions employed in the work reported here.

The surface nucleation rate i, which is proportional to $\exp[-4b\sigma\sigma_e T_m^\circ/(\Delta h_f)(\Delta T)kTf]$, leads to overall observable growth of two types. At high growth temperatures (low undercoolings) the nucleation rate is low, and each nucleus causes the completion of the substrate of length L. Then a new nucleus forms, and the process is repeated forming a lamellar crystal. In this case, regime I, the growth rate G is proportional to the nucleation rate i. At lower growth temperatures, (high undercoolings) the nucleation rate becomes quite high, and many surface nuclei are formed on the substrate. Then regime II is entered, and G is proportional to $i^{1/2}$, again with the formation of a lamellar crystal. The transition between regimes I and II is experimentally quite sharp in good fractions, and the undercooling where it occurs can be explained in terms of a value of L that is roughly 5 μm. The sharpness of the transition is fundamentally a result of the rapid change of i with undercooling.

At moderate to high molecular weight, the nucleation rate and the concomitant overall growth rate are not strongly dependent on changes of viscosity of the melt from which the various crystalline bodies are formed. Also, the nucleation rate, as measured by $\sigma\sigma_e$, appears to be nearly independent of such factors as the presence of interlamellar links at high molecular weights. The absolute value of the pre-exponential for regime I is much greater than that for regime II, principally

because that for regime I contains the factor L, whereas that for regime II does not.

The observed value of the initial lamellar thickness l_g^* is in general close to that predicted from the undercooling and the σ_e relevant to the molecular weight under consideration. Because the growth rate G is related to l_g^* according to $G \propto \exp(-2b\sigma l_g^*/kT)$, and because the experimental range of G is limited, l_g^* is itself restricted in polyethylene crystallizing isothermally from the melt to a rather narrow range close to 200 Å.

The work of chain folding q can be deduced from strictly kinetic measurements. The value so obtained is in close agreement with that from equilibrium measurements on polyethylene single crystals, and with certain theoretical calculations. There appear to be no inconsistencies of an energetic character in the picture of crystallization presented here.

The authors thank Esmund Drott of the Monsanto Chemical Company for supplying some of the fractions, and J. J. Weeks, Jr., for his considerable assistance in carrying out the WAXR and LAXR measurements. We also gratefully acknowledge a number of discussions with E. A. DiMarzio and F. Khoury. We are indebted to H. D. Keith for pointing out the significance of his work on crystallization of polyethylene from pure hydrocarbons, and for a number of timely discussions.

9. References

[1] Hoffman, J. D., Davis, G. T., and Lauritzen, J. I., Jr., *in* Treatise on Solid State Chemistry, N. B. Hannay, Ed. (Plenum Press, New York, Vol. **3,** 1976).
[2] Lauritzen, J. I., Jr., and Hoffman, J. D., J. Appl. Phys. **44,** 4340 (1973).
[3] Hoffman, J. D., Soc. Plastics Eng. Trans. **4,** 315 (1964).
[4] Lindenmeyer, P. H., and Holland, V. F., J. Appl. Phys. **35,** 55 (1964).
[5] Price, F. P., J. Polymer Sci. **42,** 49 (1960).
[6] Lauritzen, J. I., Jr., and Hoffman, J. D., J. Res. Nat. Bur. Stand. (U.S.), **64A** (Phys. and Chem.), No. 1, 73–102 (Jan.–Feb. 1960).
[7] Sanchez, I. D. and DiMarzio, E. A., J. Res. Nat. Bur. Stand. (U.S.), **76A** (Phys. and Chem.), No. 3, 213–223 (May–June 1972).
[8] Lauritzen, J. I., Jr., J. Appl. Phys. **44,** 4353 (1973).
[9] NBS Special Publication 260–42, The Characterization of Linear Polyethylene SRM 1475, H. L. Wagner and P. H. Verdier, Eds. (1972). Reprinted from J. Res. Nat. Bur. Stand. (U.S.), **76A** (Phys. and Chem.), No. 2, 137–170 (Mar.–Apr. 1972).
[10] Hoffman, J. D., and Weeks, J. J., J. Chem. Phys. **37,** 1723 (1962).
[11] Ross, G. S., and Frolen, L. J., to be published.
[12] Broadhurst, M. G., J. Res. Nat. Bur. Stand. (U.S.), **70A** (Phys. and Chem.), No. 4, 481–486 (Nov.–Dec. 1966).
[13] Flory, P. J. and Vrij, A., J. Am. Chem. Soc. **85,** 3548 (1963).
[14] Gieniewski, C. and Moore, R. S., Macromolecules **2,** 385 (1969).
[15] Tearè, P. W., and Holmes, D. R., J. Polymer Sci. **24,** 496 (1957).
[16] Niegisch, W. D., and Swan, P. R., J. Appl. Phys. **31,** 1906 (1960).
[17] Geil, P. H., Polymer Single Crystals, (Interscience Publishers, New York, 1963).
[18] Bunn, C. W., and Alcock, T. C., Trans. Faraday Soc. **41,** 317 (1945).
[19] Point, J. J., Bull. Acad. Roy. Belg. **41,** 982 (1955).
[20] Point, J. J., and Homès, G. A., Compt. Rend. **242,** 2557 (1956).
[21] Fischer, E. W., Z. Naturforsch. **12a,** 753 (1957).
[22] Anderson, F. R., J. Appl. Phys. **35,** 64 (1964).
[23] Palmer, R. P., and Cobbold, A. J., Macromol. Chem. **74,** 174 (1964).
[24] Keller, A., and Sawada, S., ibid., 190 (1964).
[25] Bank, M. I., and Krimm, S., J. Polymer Sci. **A27,** 1785 (1969).
[26] Khoury, F., and Passaglia, E., *in* Treatise on Solid State Chemistry, N. B. Hannay, Ed. (Plenum Press, New York, Vol. **3,** 1976).
[27] Suzuki, T., and Kovacs, A., Polymer J. **1,** 82 (1970).
[28] Davis, G. T., and Eby, R. K., J. Appl. Phys. **44,** 4274 (1973).
[29] Huseby, T. W., and Bair, H. E., J. Appl. Phys. **39,** 4969 (1968).
[30] Weeks, J. J., J. Res. Nat. Bur. Stand. (U.S.), **67A,** (Phys. and Chem.), No. 5, 441–451 (Sept.–Oct. 1963).
[31] Rijke, A. M., and Mandelkern, L., J. Polymer Sci. A–2, **8,** 225 (1970).
[32] Private communication from H. D. Keith, Bell Telephone Laboratories.
[33] Ergöz, E., Fatou, J. G., and Mandelkern, L., Macromolecules **5,** 147 (1972).
[34] Elban, W., and Hoffman, J. D., manuscript in preparation.
[35] Ross, G. S., and Frolen, L. J., J. Res. Nat. Bur. Stand. (U.S.), **79A,** (Phys. and Chem.), No. 6 (Nov.–Dec. 1975).
[36] Keller, A., and Priest, D. J., J. Macromol. Sci. **B2,** No. 3, 479 (1969).
[37] Lauritzen, J. I., Jr., and DiMarzio, E. A., manuscript in preparation.
[38] Flory, P. J., *in* Statistical Mechanics of Chain Molecules, (Interscience, New York, 1969).
[39] DiMarzio, E. A., XXIII International Congress of Pure and Applied Chemistry, **8,** 239 (1971).
[40] Sanchez, I. C., and DiMarzio, E. A., Macromolecules, **4,** 677 (1971).
[41] Sanchez, I. C., and DiMarzio, E. A., J. Chem. Phys. **55,** 893 (1971).
[42] Corradini, P., Petraccone, V., and Allegra, G., Macromolecules **4,** 770 (1971).
[43] Keith, H. D., J. Appl. Phys. **35,** 3115 (1964).
[44] Magill, J. H., J. Polymer Sci. Part A–2, **5,** 89 (1967).
[45] Devoy, C., and Mandelkern, L., J. Polymer Sci. Part A–2, **7,** 1883 (1969).
[46] Cooper, M., and Manley, R. St. J., Macromolecules **8,** No. 2, 219 (1975).

(Paper 79A6–867)

JOURNAL OF RESEARCH of the National Bureau of Standards—A. Physics and Chemistry
Vol. 79A, No. 6, November–December 1975

Homogeneous Nucleation in Polyethylene: Molecular Weight Dependence

Gaylon S. Ross and Lois J. Frolen

Institute For Materials Research, National Bureau of Standards, Washington, D.C. 20234

(September 18, 1975)

The droplet technique was used to obtain estimates of the isothermal rate of homogeneous crystal nucleation in highly supercooled melts of 8 characterized fractions of linear polyethylene (weight average molecular weights from 3,100 to 249,000). The data obtained from these experiments were analyzed in accord with current theories of homogeneous nucleation of chain folded crystals. Values for the quantity $\sigma^2\sigma_e$, where σ and σ_e are the lateral and end-surface free energies of the crystal, were estimated as a function of molecular weight.

Sample 3.2 K was found to be anomalous in its nucleation behavior. When we assume that this sample crystallizes in the extended chain form and calculate σ^3 instead of $\sigma^2\sigma_e$ the value for σ is found to be 10.57 ergs/cm^2 which is in reasonable agreement with the value 9.6 ergs/cm^2 found by other investigators for linear hydrocarbons. However, there remains the question as to whether sample 3.2 K ever underwent homogeneous nucleation.

For samples 9.70, 11.74, and 23.0 K, $\sigma^2\sigma_e$ was found to increase rapidly due to a decrease in the number of cilia per chain fold as the molecular weight increases. For higher molecular weights the value for $\sigma^2\sigma_e$ levels off and the average value of $\sigma^2\sigma_e$ for samples 23.0 to 249 K was found to be 19,000 ergs^3/cm^6.

The experimental value of the absolute nucleation frequency I_0, was found to differ from the theoretical value by approximately 1×10^{12}. If one assumes that the surface free energies are temperature dependent [i.e., $\sigma=\sigma_1(1+\overline{x}\Delta T)$ and $\sigma_e=\sigma_{e1}(1+\overline{y}\Delta T)$ where $\overline{x}=-0.0073$ and $\overline{y}=0.014$] the average value of $\sigma^2\sigma_e$ changes only slightly (to 19,800 ergs^3/cm^6) due to the compensating effects in the signs of the temperature corrections and I_0 is close to the theoretical value, 1×10^{34} nuclei/cm^3/s.

Key words: Chain folds; fractions; homogeneous nucleation; molecular weight; nucleation theory; polyethylene; surface free energies.

1. Introduction

For more than a decade there has been considerable interest in determining the magnitude of the lateral, σ, and end, σ_e, surface free energies for chain-folded polymer crystals. Measurements of spherulitic growth rates as a function of temperature provide values for the product, $\sigma\sigma_e$, at temperatures near the melting point of the polymer. Studies of homogeneous nucleation provide important additional information concerning the surface free energies because the process depends on the product, $\sigma^2\sigma_e$, at temperatures well below those accessible for growth studies. The temperature dependence of σ_e has been estimated [1][1] from growth studies and the temperature dependence of σ can be estimated from the present homogeneous nucleation rate studies.

The original homogeneous nucleation rate studies for polyethylene were performed by Cormia, Price, and Turnbull, (CPT) [2] in 1962. The technique employed to suppress the effect of heterogeneities was that first used by Vonnegut [3], namely the bulk sample was subdivided into small droplets so that the heterogeneities were confined to a portion of the droplets, the remaining droplets being free to nucleate at rates governed by the molecular characteristics of the sample. CPT studied an unfractionated polyethylene sample (Marlex–50)[2] using a slow cooling technique. In 1967, Gornick, Ross, and Frolen (GRF) [4] repeated the nucleation studies on Marlex 50 under isothermal conditions, using essentially the same droplet preparation technique as CPT. In a later paper (1969) by Hoffman et al. [5] the nucleation studies on a fairly narrow fraction of polyethylene having a $M_w=50{,}000$ were reported. The results of all three studies were quite similar when calculated on the same basis, i.e., using the same melting point. In addition, in this later paper [5], the effect of a temperature dependence of the surface free energies was first explored.

In the present work, eight narrow molecular weight distribution linear polyethylene fractions were investi-

[1] Figures in brackets indicate the literature references at the end of this paper.

[2] Certain trade names and company names are mentioned in this paper in order to adequately specify the experimental procedure. In no case does such identification imply recommendation or endorsement by the National Bureau of Standards, nor does it imply that the product identified is necessarily the best available for the purpose.

gated using improved techniques for sample preparation. The goals of this study were threefold: (1) To determine the effects of molecular weight on the product, $\sigma^2\sigma_e$, (2) To estimate the temperature dependence of σ and, (3) To investigate the effect of the temperature dependencies of σ and σ_e on the absolute nucleation rate constant, I_0.

2. Theory

Each determination of isothermal nucleation frequency was obtained by counting spots (i.e., crystallized frozen polethylene droplets) on successive frames of film exposed at known time intervals as discussed in section 3 of this paper. The nucleation rate, I, (nuclei $cm^{-3}s^{-1}$) is related to the observed frequency of droplet freezing by the relationship,

$$n/n_0 = \sum_{v=0}^{\infty} N_D \exp(-K_D t) \tag{1}$$

where $K_D = v_D I$ and v_D is the volume of a droplet of diameter D. Since for each fraction of polyethylene, the droplets which are in the homogeneous population have a constant diameter within our ability to measure (i.e., ± 0.3 μm), the summation sign can be removed, resulting in the following expression:

$$n/n_0 = \exp(-Ivt). \tag{2}$$

The ratio (n/n_0) is the fraction of droplets of volume v, remaining unfrozen at time, t; n_0 is the total number of droplets which undergo the homogeneous nucleation act (population A) in any isothermal experiment. A plot of $\ln(n/n_0)$ versus time, t, results in a straight line having a slope of Iv. Since we can measure the value of v, the value of I for each isothermal experiment can be calculated.

The temperature dependence of I is reflected in the following generalized relationship for homogeneous nucleation [6]:

$$I = I_0' \exp\left[-\Delta\phi^*/kT\right] \tag{3}$$

where $\Delta\phi^*$ is defined as the free energy change accompanying the formation of a nucleus of critical size. Following Fisher and Turnbull [7], we approximate I_0' by

$$I_0' = I_0 \exp\left[-\Delta F^*/RT\right] \tag{4}$$

where ΔF^* is the activation energy for transport of the crystallizing molecules. Applying the reasoning of Hoffman et al. [5], we define

$$\Delta F^* = \frac{U^* T}{(T - T_\infty)} \tag{5}$$

where T_∞ is defined as:

$$T_\infty = T_g - 30 \tag{6}$$

and T_g is the glass transition temperature for the polymer. Now, combining eqs (3), (4), and (5), we have:

$$I = I_0 \exp\left[-U^*/R(T - T_\infty)\right] \exp\left(-\Delta\phi^*/kT\right). \tag{7}$$

Lauritzen and Hoffman [8] have shown that,

$$\Delta\phi^* = 30.2\ \sigma^2\sigma_e/(\Delta f)^2 \tag{8}$$

where σ and σ_e are respectively the lateral and end surface free energies of the nucleus and $-(\Delta f)$ is the thermodynamic driving force for the crystallization process. The factor 30.2 is obtained when one assumes that the homogeneous nucleus builds upon the orthorhombic unit cell. Hoffman and Weeks [9] have shown that (Δf) is best represented by

$$(\Delta f) = \Delta h_f \cdot \frac{\Delta T}{T_m} \cdot f \tag{9}$$

where f is the correction term to the free energy and is equal to $(2T/T_m + T)$. The correction factor, f, becomes increasingly important at high undercoolings. T_m is the equilibrium melting point, T is the experimental temperature and $\Delta T = T_m - T$. (Δh_f) is the heat of fusion per unit volume of crystal.

Combining eqs (7), (8), and (9) we obtain the following relationship

$$I = I_0 \exp\left[-U^*/R(T - T_\infty)\right] \exp\left[-30.2\sigma^2\sigma_e T_m^2/k(\Delta h_f)^2 f^2 T \Delta T^2\right]. \tag{10}$$

Equation (10) assumes that the surface free energies, σ and σ_e, are temperature independent. However, Hoffman, et al. [5] have shown that it is more reasonable to assume that σ and σ_e vary with temperature and they suggested a dependence of the form

$$\sigma = \sigma_1(1 + x\Delta T) \tag{11}$$

and

$$\sigma_{e(k)} = \sigma_{e1}(1 + y\Delta T) \tag{12}$$

where $\sigma_{e(k)}$ is the kinetic value of the fold surface free energy [10]. Incorporating the temperature dependencies into eq (10), we then obtain the general nucleation relationship

$$I = I_0 \exp\left[\frac{U^*}{R(T - T_\infty)}\right] \exp\left[\frac{-30.2\sigma_1^2\sigma_{e(k)}T_m^\circ}{k(\Delta h_f)^2}\right] \left[\frac{(1 + x\Delta T)^2\ (1 + y\Delta T)}{f^2 T(\Delta T)^2}\right] \tag{13}$$

According to Fisher and Turnbull [7], I_0 can be defined in the following way,

$$I_0 = (N/\bar{V}_m)\ (kT/h) \tag{14}$$

where N is Avogadro's number and $\bar{V}_m$ (for polymers) is the molar volume of a sequence of chain segments

whose length is approximately that of the crystal nucleus. (kT/h) is the usual frequency factor where k is Boltzman's constant, T the temperature, and h is Planck's constant. Assuming $\bar{V}_m$ is equal to 140 times the molar volume of a single $-CH_2-$ group, I_0 can be calculated and has a numerical value of approximately 1×10^{34}. It should be pointed out at this time that the theoretical value of I_0 differs from the experimentally determined I_0 by a factor of approximately 1×10^{12}. This discrepancy will be discussed in detail in the final section of this paper.

A careful analysis [1] of the crystal growth data for a number of polymers which crystallize by chain folding showed that the best value for U^* is about 1500 cal/mol.[3] and $T_\infty = Tg - 30$ °C, where T_g is the glass transition temperature. We assume these values for polyethylene. In addition for the particular case of polyethylene it was estimated that $\sigma_{e(k)}$ and y were 93 [4] ergs/cm^2 and 0.014 deg^{-1} respectively. The only other factor to be determined is the value of x and that can be established approximately with the homogeneous nucleation rate data. Lauritzen [11] has developed a theory for the behavior of σ based on a model where the presence of the lateral polymer crystal surface reduces the number of allowed configurations of the polymer molecule in the subcooled liquid adjacent to the crystal surface. In this treatment an entropy gradient exists in the surface zone whose magnitude increases with increasing temperature. Under these circumstances, one would expect σ to increase with increasing temperature and consequently would expect x to be negative and considerably smaller than unity. The actual values determined for x will be discussed in detail in section 4 of this paper.

[3] In SI units 1 cal · mol^{-1} = 4.184 J · mol^{-1}.
[4] In SI units 1 erg · cm^{-2} = 0.1 J · m^{-2}.

3. Experimental Detail

The nucleation behavior of eight fractions of linear polythylene was studied. Four of these (CE designation) were fractions from Marlex–50, which was obtained from the Phillips Petroleum Company. The fractions were prepared using a column extraction (CE) technique [12] with the solvent system described by Chiang [13]. The other four were fractions of the National Bureau of Standards linear polyethylene standard reference material, SRM 1475. These were fractioned by preparative gel permeation chromatography (GPC designation). GPC was used to analyze all of the fractions (table 1) using the column system and technique described in [14]. GPC instrumental broadening effects were estimated by measuring nearly pure samples of $n-C_{32}H_{66}$ and $n-C_{94}H_{190}$ for which M_w/M_n was known to be about 1.00. These samples gave $M_w/M_n \cong 1.05$ in the GPC analytical apparatus. Therefore, a correction of -0.05 was applied to the original data for the fractions characterized with the analytical GPC columns. In particular, the technique used in the preparation of samples 9.70 and 11.74 K was such that a true polydispersity of about 1.01 to 1.02 was to be expected.

TABLE 1

Sample designation	M_n	M_w	M_z	T_m°(°C) (calculated)[b]	Polydispersity (M_w/M_n)[c]	Method of Preparation [d]
3.2 K	2,140	3,160	4,530	131.7	1.43	CE
9.70 K	9,150	9,700	10,246	141.1	1.01	PGPC
11.74 K	10,970	11,740	12,431	142.0	1.02	PGPC
23.0 K	17,690	23,010	32,674	144.1	1.25	CE
30.6 K	25,710	30,600	36,659	144.6	1.14	PGPC
[a]49.9 K	36,370	49,890	69,850	145.2	1.32	CE
119 K	94,600	119,200	146,931	145.9	1.21	PGPC
249 K	178,500	248,560	348,000	146.2	1.34	CE

[a] This sample was treated as described in reference (4). The population of droplets which nucleated homogeneously contained 50–200 droplets as compared to present methods which produce 600–1000 droplets in the homogeneous population. Consequently, we feel that the results found for the other fractions are statistically more reliable than those obtained for Marlex–50 and CE–50.

[b] Calculated using the equation

$$T_m^\circ = \frac{T_m^\circ(\infty)\,(n-0.542)}{n + 0.46\{7.667 + 1.987 \ln n + (5.6/n) - (0.25n-7)\,[1-(T_m^\circ/T_m^\circ(\infty))]\}}$$

where $n = M/14.026$ is the number of carbon atoms in the polymer chain. This equation was derived from Broadhurst's work (J. Res. NBS. **70A**, 481 (1966)), by setting T_m° at $n \to \infty$ at $T_m^\circ(\infty) = 419.7$ K = 146.5 °C.

[c] Corrected for instrumental broadening effects (see text).

[d] PGPC = preparative gel permeation chromatography: CE = column elution.

594-051 O - 76 - 3

3.1. Droplet Preparation

In a crystallization process in the bulk there are two possible nucleation modes whereby a stable nucleus can be formed from the liquid phase. In heterogeneous nucleation the nucleus is formed on the surface of some extraneous solid existing in contact with the liquid, or at a liquid-liquid or liquid-solid interface. Homogeneous nucleation results from the spontaneous formation of a favorably oriented cluster of molecules (or a single molecule in the case of many polymers) without the aid of any substrate. Vonnegut [3] assumed that crystallization in bulk generally occurred by heterogeneous nucleation because of the large number of heterogenities per unit volume. However, he reasoned that by subdividing the bulk material into small particles, many of these particles would be free of heterogeneities (dirt). Therefore any nucleation occurring within such "clean" particles would occur via the homogeneous route. This is the rationale behind the droplet experiment.

Two ways for doing this subdivision are described in the literature. One method is to simply grind up the crystalline sample, using a grinder or blender. This technique was used by Turnbull and Cormia [15] in their homogeneous nucleation experiments with linear hydrocarbons. The other technique is to dissolve the sample in a suitable solvent, then to subdivide the solution into small portions, and subsequently to remove the solvent. Two different approaches have been used to achieve the latter. The first, described by Cormia, Price, and Turnbull (CPT) [2], made use of the consolute temperature portion of the polyethylene-nitrobenzene phase relationship. If a solution of polyethylene in nitrobenzene is first heated to the boiling point of nitrobenzene and then allowed to cool, a new polyethylene-enriched liquid phase is produced. This new phase occurs as liquid droplets, approximately 5 μm in diameter. If the two-phase mixture is further cooled before the droplets of the enriched phase coalesce, the polyethylene in the droplets crystallizes, expelling the nitrobenzene and forming fairly uniform spheres approximately 1 to 2 μm in diameter. These polyethylene spheres can be separated from the nitrobenzene by either centrifugation or filtration. These polyethylene spheres are subsequently dispersed in a suitable dispersive media.

The second method is that employed by Koutsky, Walton, and Baer (KWB) [16]. The cells used in these experiments were heated microscope slides having shallow concavities containing silicone oil (a nonsolvent) as a substrate. They sprayed a hot solution of polymer with atomizers onto the hot silicone oil substrate, volatilizing the solvent and leaving the finely divided polymer floating on or slightly below the silicone oil surface. No glass cover was used so the polyethylene droplets remained dispersed at the oil-air interface.

3.2. Sample Cleaning Techniques

The success of the homogeneous nucleation experiments is dependent upon producing a large number of polyethylene droplets which nucleate homogeneously and whose volumes are nearly identical. The CPT method of particle preparation was the one used, both in our previous work (GRF) [4], and the present studies. This method is only successful if all materials used are as free of extraneous matter as possible.

In order to render our starting solvents reasonably free of particulate matter, filtration, crystallization, distillation, and centrifugation were used. Starting materials were reagent grade xylene and nitrobenzene. First, each of these solvents was twice filtered through regenerated cellulose filters using only gravity flow; we had previously found that the higher flow rates which could be achieved by applying pressure to the filtration system were much less effective. Secondly, subatmospheric pressure distillation was used, wherein only the "center cut" was collected. This step was used both to chemically purify the solvent and to further reduce the concentration of particulates. After this treatment, analysis of both the nitrobenzene and xylene by gas-liquid chromatography indicated a purity in excess of 99.5 mol percent.

Crystallization was then used, not with the idea of further chemically purifying the solvents, but rather, as a means of further reducing the particulate count. The solutions were cooled somewhat below their melting point, and crystallization was induced. During this crystallization the solutions were vigorously stirred, producing a slurry of small crystals. These crystals were then removed from the remaining liquid by rapid filtration through a cooled filter. This crystallization process was performed twice, and analysis of both the nitrobenzene and xylene by light scattering indicated that suspended particulate matter was not present. This crystallization technique, sometimes referred to as "snowing out," is quite effective in that the suspended particles usually act as crystallization nuclei, and hence they are scavenged by the crystals and are removed when the crystals and the remaining liquid are separated by filtration.

Originally we also employed ultracentrifugation, using only the middle portion of the solvent in the centrifuge tubes. Since subsequent experiments indicated that this technique did not seem to further reduce the particulate concentration, ultracentrifugation was not used for xylene and nitrobenzene.

For the final dispersion of the polyethylene droplets we used isooctylphenoxy-poly(ethyleneoxy)ethanol, furnished by the General Aniline and Film Company under the trade name of IGEPAL CA–630, as a suspending medium. Both CPT and GRF have experimentally verified that liquid and solid polyethylene are insoluble in this material. The IGEPAL was cleaned using the vacuum distillation and filtration procedures described for xylene and nitrobenzene. However, since the IGEPAL could not be crystallized we continued the use of ultracentrifugation as a final step.

Preliminary cleaning of the polyethylene samples was accomplished by dissolving them in hot xylene and filtering through 0.2 micrometer pore size filters in a heated filter assembly. The polyethylene was then

allowed to crystallize and was separated from the xylene by filtration. This process was repeated three times per sample.

Initially we were of the opinion that all of the cleaning, preparation, and filling of the sample-containing cell should be done in clean-room facilities. In fact, while the procedures became much more difficult, no significant improvement was seen, and consequently we performed such experimental operations henceforth in a conventional laboratory area.

3.3. Sample Preparation

Each of the fractions of polyethylene was handled in an identical fashion. A concentrated solution of each was prepared by dissolving the previously cleaned fraction in hot, purified xylene. This solution was twice filtered through the 0.2 micrometer cellulose filters, and a small portion was then poured into nitrobenzene preheated to approximately 200 °C. Most of the zylene immediately boiled away, leaving solutions containing approximately 30 mg of polyethylene per 200 ml of nitrobenzene. Gas-liquid chromatography indicated that the amount of xylene left in the nitrobenzene solution was negligible.

With continuous shaking, the flask containing the hot polyethylene-nitrobenzene solution was immersed in tap water, ultimately producing a dispersion of frozen polyethylene droplets. The droplets were separated from the nitrobenzene by filtering through the cellulose filters. The nitrobenzene filtrate was saved, and the process of droplet preparation was repeated three times, each subsequent time using the same nitrobenzene. A small portion of the droplets collected in the fourth precipitation were redispersed in approximately 10 ml of the cleaned IGEPAL. The dispersion was achieved by ultrasonic agitation. One droplet of this dispersion was sufficient to fill the cell used for observation of homogeneous nucleation.

3.4. Preparation and Cleaning of the Cell

The cell used to contain the dispersion was formed by fusing a 0.2 mm thick glass washer with an inner diameter of 0.5 cm to an 18 mm square microscope cover glass. The sample was contained within the washer, and a disc made from a cover glass was used as the top. The cell and its cover were successively cleaned with chromic acid, distilled water, and ethanol. Prior to filling, the cell was ultrasonically scrubbed in distilled water. In a previous paper (GRF) [4], we described many treatments designed to change the nucleating effect of the glass surfaces of the cell, and came to the conclusion that little improvement could be made over the simple cleaning procedure just described.

3.5. Experimental Equipment

The disk-shaped cell containing the sample was fitted into an enclosed temperature environment on the stage of a polarizing microscope. This temperature stage was designed and constructed by us and will be described in a separate publication [17]. The cell temperature can be maintained to within ±0.02 °C for periods of weeks, and the absolute temperature in the cell is known to within ±0.1 °C. The temperatures are measured to ±0.005 °C, and temperature differences between a series of experiments on the same sample are accurate to ±0.01 °C.

The optics of the microscope were such that in a circular field of 200 μm radius, a 0.5 μm object could be identified from the resulting photographs. The experiments are conducted using crossed polarizers, and, in the liquid state, the droplets are invisible. Upon freezing they appear as small stars against the otherwise dark background. A xenon light source was used, and the sample was illuminated only during the actual film exposure.

Automatic time-lapse cinemicrophotography was used to record the nucleation, using a 16-mm motion picture camera. The camera framing rate was adjusted to obtain between 200 and 2000 pictures during a single experiment, but usally only 20 pictures were used in the actual analysis.

3.6. Preliminary Experiments

Prior to the final dispersion of the droplets, a small sample of droplets from each fraction was examined using both electron and optical microscopy. The electron micrographs were similar for all fractions, showing a few large diameter spheroids (diameters in excess of 20 μm), with the majority of the droplets having diameters between 2 and 1 μm. A peculiar characteristic of the droplet population was their occurrence in clusters, held together by a thin, veil-like webbing (see fig. 1A). We assume that this webbing is polyethylene formed when the residual polyethylene in the nitrobenzene solution (not that in the concentrated droplet second phase) precipitates. When a dispersion is made of these droplets, the clusters are not completely broken up by mechanical agitation. Only ultrasonic agitation seems effective (see figs. 1B and 1C).

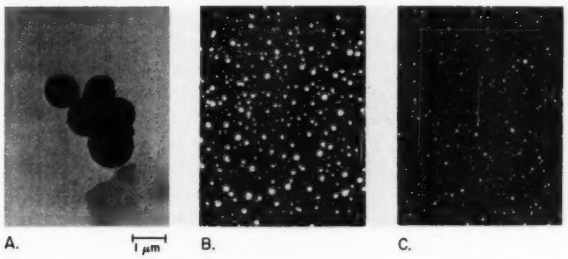

FIGURE 1. *Photographs of typical Polyethylene droplet populations.*

(A) Electron micrograph of droplets as they are precipitated from nitrobenzene showing size distribution and veil as discussed in text; (B) droplet population dispersed in Igepal using only mechanical (shaking) agitation; and (C) droplet population in Igepal using ultrasonic dispersion. Note better uniformity and smaller droplet size.

The diameters of these spheres have been measured using two microscopical techniques. Using the optical microscope and a calibrated image-splitting device similar to that described by Dyson [18], we found that each polyethylene fraction formed droplets such that in a population of 2000, over 1800 had apparent diameters between 2 and 1 μm. This is in agreement with the less extensive measurements made using electron microscopy. Unfortunately, as was elegantly demonstrated by Saylor [19], it is extremely difficult to determine the absolute size of small particles. In these experiments on homogeneous nucleation of droplets, the size of the droplet has a direct relationship to the nucleation frequency (usually expressed in nuclei $cm^{-3}s^{-1}$). We have attempted to minimize the effect of this uncertainty in absolute droplet radius by: (1) observing the same droplet population for a series of experiments with each fraction, and (2) by using the image-splitting device on each population to determine if there is a measurable difference between fractions. At best the apparent diameter can be determined to only ± 0.3 μm, and, we have found that all droplets assumed to be homogeneously nucleated in any given polyetnylene fraction have essentially the same diameter. Droplet size from fraction to fraction varies by no more than this same 0.3 μm limit. In general, it appears that the diameter of the droplet decreases slightly with increasing molecular weight.

Figure 1A is an electron micrograph of a small number of droplets. Figure 1B is an optical photomicrograph of droplets dispersed by mechanical stirring, and figure 1C shows the effect of dispersion by ultrasonic agitation on the same sample.

The reason for using only the polyethylene droplets prepared from nitrobenzene used for three previous preparations is shown in fig. 2. Here each of the four droplet preparations was dispersed in IGEPAL and its freezing (nucleating) behavior was recorded. The droplet size does not change, but the nucleating behavior changes dramatically. The first preparation produces droplets which freeze with relatively little supercooling. The succeeding preparations freeze at progressively lower temperatures, forming well-defined subgroupings in respect to temperature. After the fourth preparation little or no change is observed. This tendency of the droplets to freeze at certain temperatures, forming subpopulations of droplets, is a characteristic of all of the fractions, although each fraction is unique in its temperature profile. We only show the behavior for sample 23.0 K, but in this discussion we will refer to the subpopulation nucleating at the lowest temperature (usually around 85 °C) as population A (this is assumed to be the homogeneous nucleation population), the next lowest in nucleating temperature (usually around 95 °C) as B, and so on. In the particular case shown, population D would be those droplets which nucleate around 125 °C. It is in this first freezing population that the larger droplets are invariably found. In the final preparations this population represents 10 percent or less of the total number of droplets. One interesting point of difference between the work of KWB [16] and our own work is that while we always observe a relatively large percentage of our droplet populations nucleating at temperatures around 95 °C. KWB finds no droplets nucleating in this temperature region. A possible explanation for this marked difference in droplet behavior is to be found in the following melting and freezing experiments.

One of the more interesting things which can be done is to compare the nucleating character of the droplet population with that of its melting character. Examples of this type of experiment are shown in figures 3 and 4. In figure 3 we have shown the nu-

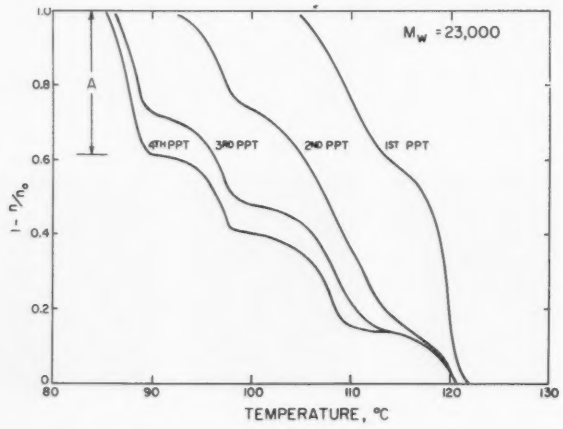

FIGURE 2. *Nucleation of polyethylene fraction 23.0 K showing the effect of repeated droplet preparation using the same solvent.*

$1 - n/n_o$ is the fraction of droplets nucleated as a function of temperature (cooling rate = 0.1 °C/min). Population A is the droplet population prepared from the 4th precipitation which is assumed to be homogeneously nucleated.

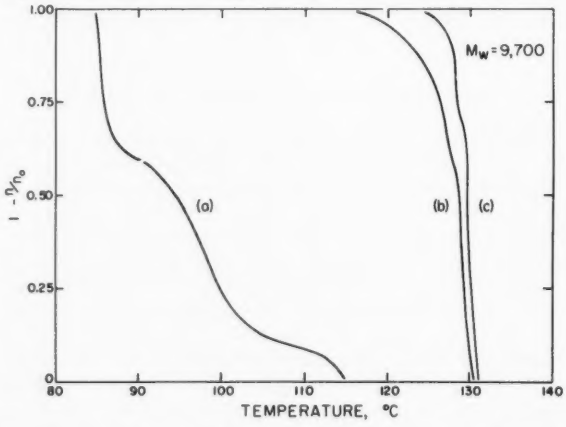

FIGURE 3. *Curve (a). Nucleation of polyethylene fraction 9.70 K (cooling rate = 0.1 °C/min.); Curve (b). Melting of the droplets whose crystallization profile is shown in curve (a) (warming rate 0.5 °C/min); Curve (c). The effect of annealing on the melting behavior of droplets whose crystallization profile is shown in curve (a).*

The sample was heated to 115 °C for 5 h then to 120 °C for 48 h, followed by warming at a constant rate of 0.5 °C/min.

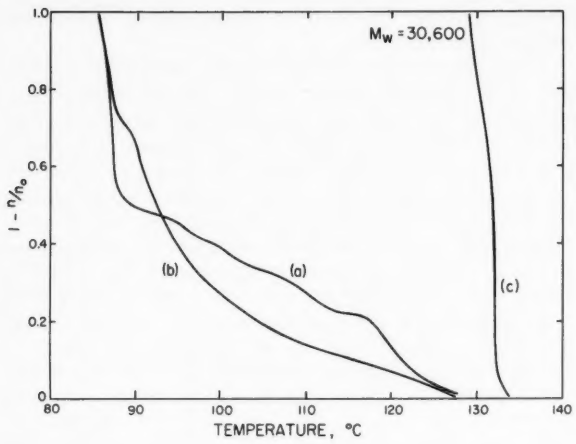

FIGURE 4. *Effect of heating the polyethylene droplet populations for sample 30.6 K to temperatures well above the melting point for long periods of time on nucleation and melting behavior.*

Curve (a): Nucleation distribution of the same droplet population after heating to 150 °C for 10 h (cooling rate = 0.1 °C/min). Curve (b): Nucleation distribution of the droplet population shown in curve (a) after heating to 170° for 2 h. Curve (c): Melting behavior of the droplets crystallized in curve (b) (warming rate = 0.5 °C/min).

cleating and melting curves of sample 9.70 K. The freezing (nucleating) curve shows only three populations (A, B, and C). The first melting curve was produced by warming the sample at a nearly constant rate starting from 80 °C. The second melting curve was produced by first heating the sample at 115 °C for 5 h and then at 120 °C for another 48 h, prior to warming at a nearly constant rate. In general, those droplets which froze at the lower temperature are the same as those which melted at the lower temperatures. This tendency is seen throughout the total droplet population. Thus, we note that in both melting experiments those droplets in population A melt first and melt over a much wider range of temperature than the other populations. In addition, the annealing process produces melting of all droplets at higher temperatures.

Figure 4 shows that the same type of behavior is exhibited by sample 30.6 K. Here we show the freezing behavior of the droplet population when melted and heated to 150 °C for approximately 10 min (the usual type of pretreatment prior to running an actual nucleation experiment). Approximately 50 percent of the total population is in the subpopulation A. There are, in addition, at least three other populations. The sample was then heated to 170 °C for 2 h, and the experiment repeated. The results of freezing this sample are shown in the second freezing curve. There are two important differences. (1) Some of the droplets formerly freezing at the higher temperatures now freeze at lower temperatures. (2) Population A is being depleted forming a new population B. While not shown here, more prolonged heating at 170 °C or higher will completely annihilate that population originally called A. This is true for all of the samples which we have investigated. The melting curve shown in figure 4 is that obtained from melting the sample after the 170 °C treatment. Again we see a difference between population A and the rest of the droplet population. Qualitatively, with the possible exception of sample 3.2 K, all the samples behave similarly, namely that population A melts first and over a wider range of temperature, and that the entire droplet population shows the usual effects of annealing.

We are able to positively identify individual droplets as various melting-freezing cycles are examined, excepting occasionally a droplet seems to change its position, i.e., one droplet disappears and another appears near the position of the original one. When this is observed, the "old" and the "new" droplets may change from population A to population B. Under normal thermal treatment only two or three droplets will make this change, but upon more severe thermal conditioning, many droplets will go from population A to B. From the paper of KWB, we find that the top surface of their dispersions are not in contact with glass, i.e., the cells have no top or cover. To a droplet 1 or 2 μm in diameter, the surface of the glass cover must appear to be far from smooth. It is therefore possible that our normal population B occurs as a result of heterogeneous nucleation by the glass surface of the cover, and that on occasion a droplet may move to a different position, either freeing itself from contact with the glass surface or becoming attached to it. Consequently, we could expect a large population of B, whereas KWB should not observe the phenomena.

4. Analysis of Data

From the 200 to 2000 pictures taken during an isothermal experiment, 20 pictures are selected with a time interval such that the homogeneous population (population A) is 80 percent frozen in the last frame. At the conclusion of each run the sample is cooled to 70 °C so that all droplets are frozen and the value for $n_{0_{exp}}$, the total homogeneous population can be established. Using the first picture as a blank, succeeding pictures are compared one by one, giving the number of newly crystallized droplets, n_{ij}, which appear during each time interval, t_i.

The next step in the analysis is to plot the data as $\ln(n/n_{0_{exp}})$ against t[(eq 2) in its logarithmic form]. This results in a linear plot having a slope equal to Iv. Figure 5 shows this type of analysis for sample 30.6 K at several isothermal temperatures. Since the volume, v, of the droplets is known, I, the nucleation rate can be calculated for each experimental temperature T_{exp}. n_0 is the total number of droplets in the homogeneous population A, i.e., the number of droplets which remain unfrozen at an arbitrarily chosen time, $t_i = 0$.

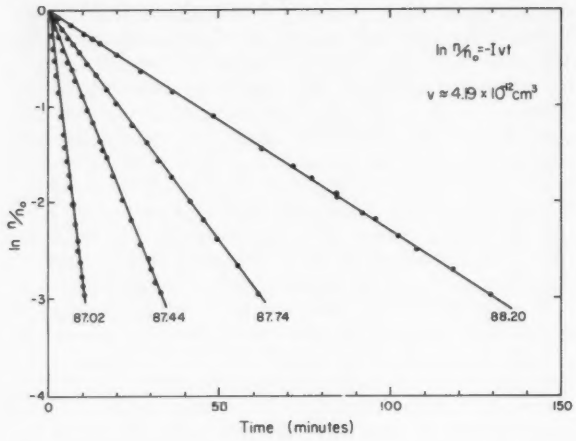

FIGURE 5. *Typical isothermal homogeneous nucleation experiments showing the temperature dependence of the nucleation rate for polyethylene fraction 30.6 K.*

n/n_0 is the fraction of droplets remaining not nucleated at any time, t.

A least squares analysis of $\ln (n_i/n_0)$, t_i pairs was done by first forcing the intercept through zero, using the experimentally determined n_0. Since the choice of $t_i=0$ is completely arbitrary, the slope Iv is calculated first using all 20 n_i,t_i pairs; then the slope was redetermined using only the first 10 pairs and then the last 10 pairs. If there are no temperature fluctuations in the experiment, the three calculated slopes are identical. Experiments not meeting this test were discarded. The purpose of this test was only to show that the run was made under isothermal conditions; it tells nothing in respect to the constancy of volume of the droplet population.

The absolute correlation coefficients for the least squares fitting operations were of the order of 0.998 or greater, indicating that the droplet population was statistically well-behaved. Because the degree of correlation was so high it was possible to perform a series of fitting tests.

First we refitted the data using the general relationship

$$\ln n/n_0 = a + bt \tag{15}$$

wherein the intercept a was calculated. Without exception the calculated value of a was nearly equal to zero.

The value, n_0, can also be calculated. Using the absolute value of the correlation coefficient as the fitting criterion, we varied the value of n_0 until we obtained the highest absolute value of the correlation coefficient, using eq (15). From this we obtained calculated values of Iv, n_0 and a.

Thus, there are two final gates for establishing internal experimental consistency, namely that $n_{0_{exp}}$ should nearly equal $n_{0_{calc}}$ and a should be nearly zero. If the calculated and experimental values of n_0 were not nearly equal, there would be strong evidence to suspect the validity of our basic assumption in regard to the constancy of droplet volume. As stated previously, the average number of droplets in the homogeneous population A was 600 and for all data used in this report $n_{0_{calc}}$ differed from $n_{0_{exp}}$ by no more than 2 percent and a differed from zero by no more than ± 0.01, (usually a was much smaller). It should be noted that the results reported for this current study are significantly more precise than those reported previously [5]. The actual values for I reported in this paper are those obtained using $n_{0_{calc}}$, although the results using $n_{0_{exp}}$ are not significantly different.

The sets of values of I's and T's obtained in the above manner were next analyzed using eq (13) to determine the values for the surface-free energy product, $\sigma^2\sigma_e$. In our original paper (GRF) [4] we assumed that these free energies were temperature independent, i.e., in eq (13) $x=y=0$. As a first step we again analyzed the data setting $x=y=0$. The values for $\sigma^2\sigma_e$ and I_0 were determined by performing a least squares fit of

$$\ln I + \frac{U^*}{R(T-T_\infty)} \text{ versus } \frac{(1+x\Delta T)^2(1+y\Delta T)}{f^2T(\Delta T)^2},$$

using a value for U^* of 1500 cal/mol. Plots of these functions for all the samples studied are shown in figure 6. Again we obtained values of nearly one for the absolute correlation coefficients. As in the previous work, the values obtained for $\sigma^2\sigma_e$ were reasonable but the values for I_0 differed from the theoretical value, 1×10^{34}, by approximately 1×10^{12}.

As discussed in section 2, it is reasonable to assume that the surface-free energies are temperature dependent; consequently using $y=0.014$ as the best value from crystallization studies, we sought a best value for x. This was done by reanalyzing the data with $y=0.014$. Remembering that x should be negative and small, x was varied until the highest correlation coefficient was obtained. The value for x obtained in this way was -0.002. Using this value for x, the $\sigma^2\sigma_e$ values were low, and the value for I_0 was even higher than before.

As a final step we assumed that the theoretical value for I_0 might well be used as input information, and a value for x was determined by the fitting operation. Since the value for x should be nearly the same, at least for the higher molecular weight fractions, the calculated values for x were averaged and the value

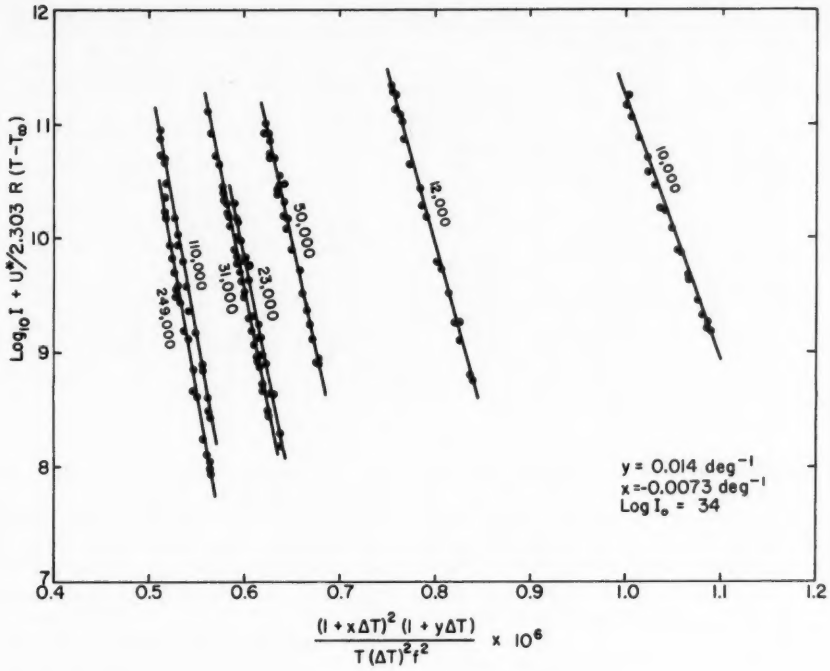

FIGURE 6. *Graphical summary of the homogeneous nucleation experiments for all the polyethylene fractions studied except fraction 3.2 K which is anomolous.*

See text for details.

obtained was $\bar{x}=-0.0073$. As a result of the compensating effects of the small positive and negative temperature dependencies of σ_e and σ, the values for $\sigma^2\sigma_e$ calculated in this way are nearly identical to the values obtained when x and y are set equal to zero, and the value for I_0 is very close to the theoretical value [1].

Since other workers have also reported extremely high values of I_0, the discrepancy between theory and experiment does not appear to be a question of input data, and the introduction of the proper temperature dependencies does seem to resolve the problem in a simple way.

5. Results and Discussion

The results of our experiments for eight fractions of linear polyethylene are summarized in table 2. These samples can be divided into three molecular weight regions. Fraction 3.2 K is little more than a collection of high molecular weight hydrocarbons. Fractions 9.70, 11.74, and 23.0 K represent a region wherein T_m is rapidly changing with molecular weight and $\sigma^2\sigma_e$ is expected to show strong molecular weight effects. The remaining samples are in a region where T_m changes slowly and $\sigma^2\sigma_e$ should show little molecular weight dependence [20].

First, let us examine the unique results obtained for fraction 3.2 K. This sample is the first cut from the column elution of Marlex–50. As such it has a higher polydispersity than any of the other fractions contains a much higher percentage of terminating end groups per $-CH_2-$ unit and although it was carefully purified, significant amounts of branched polymer, catalyst fragments, etc., might well remain.

For the moment, let us assume that homogeneous nucleation does occur in sample 3.2 K. The molecular weight of this sample is such that one might expect a stable nucleus containing one fold and two cilia to form. This nucleus would be expected to resemble an extended chain molecule more than a chain-folded nucleus. Assuming that one measures σ^3 rather than $\sigma^2\sigma_e$ the calculated value for σ is 10.57 ergs/cm^2 which is in good agreement although slightly higher than the 9.6 ergs/cm^2 value obtained by Turnbull and Cormia [15] for the linear hydrocarbons in their homogeneous nucleation experiments.

Although the calculated value for σ appears to be reasonable, there remains a question concerning the mechanism of nucleation in this sample. There is some evidence that the nucleation is heterogeneous rather than homogeneous. First, we note from table 2 that the lowest obtainable experimental temperature range is 15

TABLE 2

Sample	T_m^b °C	Experimental temperature range, °C	$x=y=0$		$y=0.014$ Log $I_0=34$		Correlation coefficient
			$\sigma^2\sigma_e$	Log I_0	$\sigma^2\sigma_e$	x	
3.2 K	131.74	98.2–101.8	1,180	15.6	719	0.033	0.972
[a]9.70 K	141.09	85.0–87.5	12,400	37.9	11,100	−.0047	.994
[a]11.74 K	141.95	85.4–87.9	15,000	43.2	14,500	−.0063	.998
23.0 K	144.14	86.4–88.1	18,610	48.5	19,100	−.0073	.976
30.6 K	144.60	86.3–88.6	18,600	48.8	19,300	−.0074	.999
49.9 K	145.17	86.9–88.9	17,400	46.5	17,500	−.0069	.986
119.0 K	145.96	87.1–89.1	20,000	50.8	21,120	−.0077	.993
249.0 K	146.21	87.6–89.4	20,500	51.5	21,800	−.0077	.990

Avg. 23,000–250,000 = 19,000 ergs^{3}cm^{-6} ($x=y=0$)
Avg. 23,000–250,000 = 19,800 ergs^{3}cm^{-6} ($y=0.014$ Log $I_0=34$)

[a]Special samples, estimated polydispersities between 1.01 and 1.02.
[b]Assuming $T_m^\circ = 146.5$ °C. See reference [1] for details.

degrees higher than that of 9.70 K although the calculated T_m is approximately 10 degrees lower. In addition, one notes that this is the temperature range in which the subpopulation B of all other fractions nucleate. When the kinetics of subpopulation B for the other fractions are analyzed the values for $\sigma^2\sigma_e$ and I_0 obtained are of the same magnitude as those calculated for 3.2 K.

We believe that the nucleation of population B is via a glass surface-polymer interaction. First of all, KWB [16], using no cover glass on their sample cell, do not obtain a B-type population. Second, if we subject our samples to harsh thermal treatment, there is an increase in population B at the expense of the homogeneous population. The lower molecular weight, thermally degraded sample has a lower viscosity than the original sample, consequently we postulate that the polymer wets the glass surface and henceforth nucleates heterogeneously on the glass surface of cell cover.

We therefore conclude that it is likely that the measurements on 3.2 K are really the results of heterogeneous rather than homogeneous nucleation.

Excluding fraction 3.2 K, table 2 shows a continuing increase in both $\sigma^2\sigma_e$ and log I_0 as the weight average molecular weight increases. For samples 9.70, 11.74, and 23.0 K one expects $\sigma^2\sigma_e$ to increase rapidly due to a decrease in the number of cilia per chain fold as the molecular weight increases [20]. This effect should be of much less importance in the higher molecular weight fractions. There is still a slight upward trend in $\sigma^2\sigma_e$ and I_0 even in the highest molecular weight fractions but in view of the experimental uncertainties the trend may not be statistically significant. One notes that the values of $\sigma^2\sigma_e$ and I_0 for fraction 49.9 K tend to be lower than those calculated for neighboring fractions. There are two reasons for this: (1) this fraction has a higher polydispersity than the other fractions, which may affect its nucleating character somewhat, and (2) this was the first fraction measured and the experimental techniques were greatly improved as the experiments progressed.

For the time being, if we regard $\sigma^2\sigma_e$ to be independent of temperature, the average value for the five highest molecular weight fractions is 19,000 erg^3/cm^6 and the value for $\log_{10}I_0$ is 49.4. The value of σ can be calculated in two ways from $\sigma^2\sigma_e$: (1) $\sigma^2\sigma_e$ (homogeneous nucleation)/$\sigma\sigma_e$ (growth) = 19,000/1280 = 14.8 ergs/cm^2, and (2) $\sigma^2\sigma_e$ (homogeneous nucleation)/σ_e (T_m versus $1/l$ plot. = 19,000/93 = σ^2 = 205 and σ = 14.3 ergs/cm^2 [20]. Hoffman et al. [1] have shown that from all the information available it is reasonably certain that σ for polyethylene lies between 12 and 15 ergs/cm^2.

The question of the experimental [2, 4] value of I_0 is a more complicated one and does not appear to be a question of the input data. As discussed previously (sec. 4), it is reasonable to assume that both σ and σ_e are temperature dependent. The assignment of $y = 0.014$ appears to be experimentally justified. If we assume that the theoretical value for I_0, (i.e., $\log_{10}I_0 = 34$) and calculate a value for x we obtain an average value of -0.0073. Applying these temperature dependencies to σ and σ_e we find that the average value of $\sigma^2\sigma_e$ for the higher molecular weight fractions changes only slightly (to 19,800 erg^3/cm^6) due to the compensating effects in the signs of the temperature corrections and I_0 is the theoretical value. From these results we conclude that the theoretical value for I_0 should be included as input data in the homogeneous nucleation studies on other polymers.

With the exception of sample 3.2 K, we are satisfied that the nucleation mechanism in the measured fractions is homogeneous. First, nucleation has not been observed in a lower temperature range; second, the nucleation of population A is truly sporadic in nature and finally, the values calculated for σ using $\sigma^2\sigma_e$ from these studies and the values for $\sigma\sigma_e$ from the growth studies lie in a reasonable range. Hoffman et al. [20] have estimated the best values of σ and $\sigma_{e(\infty)}$ for polyethylene from several methods to be 14.2 ± 0.4 ergs/cm^2 and 90.5 ergs/cm^2 respectively. The values obtained from the homogeneous nucleation studies presented here (i.e. $\sigma = 14.8$ ergs/cm^2 and $\sigma_e = 86.7$ ergs/cm^2) are in reasonable agreement.

6. References

[1] Hoffman, J. D., Lauritzen, J. I., Jr., and Davis, G. T., A chapter *in* Treatise on Solid State Chemistry, N. B. Hannay, Editor. In press.

[2] Cormia, R. L., Price, F. P., and Turnbull, D., J. Chem. Phys., **37,** 1333 (1962).

[3] Vonnegut, B. J., J. Colloid Sci. **3,** 563 (1948).

[4] Gornick, F., Ross, G. S., and Frolen, L. J., J. Polymer Sci., Part C, No. 18, 70 (1967).

[5] Hoffman, J. D., Lauritzen, J. I., Jr., Passaglia, E., Ross, G. S., Frolen, L. J., and Weeks, J. J., Kolloid-Z. Z. Polymere **231,** 564 (1969).

[6] Becker, R., and Döring, W., Ann. Physik **24,** 719 (1935).

[7] Fischer, J. and Turnbull, D., J. Chem. Phys. **17,** 71 (1949).

[8] Lauritzen, J. I., Jr., and Hoffman, J. D., J. Res. Nat. Bur. Stand. (U.S.), **64A** (Phys. and Chem.), No. 1, 73–102 (Jan.–Feb. 1960).

[9] Hoffman, J. D., and Weeks, J. J., J. Chem. Phys. **37,** 1723 (1962).

[10] Lauritzen, J. I., Jr., and Passaglia, E., J. Res. Nat. Bur. Stand. (U.S.), **71A,** (Phys. and Chem.), No. 4, 261–275 (July–Aug. 1967).

[11] Lauritzen, J. I., Jr., private communication.

[12] Desreux, V., Rec. Trav. Chim. **68,** 789 (1949).

[13] Chiang, R. J., Polymer **36,** 91 (1959).

[14] Ross, G. S., and Frolen, L. J., J. Res. Nat. Bur. Stand. (U.S.), **76A** (Phys. and Chem.), No. 2, 163–170 (Mar.–Apr. 1972).

[15] Turnbull, D., and Cormia, R. L., J. Chem. Phys. **34,** 820 (1961).

[16] Koutsky, J. A., Walton, A. G., and Baer, L., J. Appl. Phys. **38,** 1831 (1967).

[17] Ross, G. S., and Frolen, L. J., to be published.

[18] Dyson, J., and Noble, P. J. W., J. Royal Micro, Soc. **81,** Pt. 2, 95 (1962).

[19] Saylor, C. P., Applied Optics, **4,** 477 (1965).

[20] Hoffman, J. D., Frolen, L. J., Ross, G. S., and Lauritzen, J. I., Jr., J. Res. Nat. Bur. Stand. (U.S.) **79A,** (Phys. and Chem.), No. 6, (Nov.–Dec. 1975).

(Paper 79A6–868)

JOURNAL OF RESEARCH of the National Bureau of Standards—A. Physics and Chemistry
Vol. 79A, No. 6, November–December 1975

Absolute Isotopic Abundance Ratios and the Atomic Weight of a Reference Sample of Potassium

E. L. Garner, T. J. Murphy, J. W. Gramlich, P. J. Paulsen, and I. L. Barnes

Institute for Materials Research, National Bureau of Standards, Washington, D.C. 20234

(August 27, 1975)

Solid sample, thermal ionization, mass spectrometry has been used to obtain absolute values for the isotopic abundance ratios of a reference sample of potassium. Standards of known isotopic composition, prepared by gravimetrically mixing nearly isotopically and chemically pure separated isotopes of ^{39}K and ^{41}K, were used for calibration. The absolute isotopic abundance ratios are $^{39}K/^{41}K = 13.8566 \pm 0.0063$ and $^{40}K/^{41}K = 0.0017343 \pm 0.0000061$ which yield atom percent compositions of $^{39}K = 93.2581 \pm 0.0029$, $^{40}K = 0.01167 \pm 0.00004$, and $^{41}K = 6.7302 \pm 0.0029$. The calculated atomic weight for potassium is 39.098304 ± 0.000058. The indicated uncertainties are overall limits of error which are the sum of the uncertainty components for ratio determinations and the components covering the effects of known sources of possible systematic error.

Key words: Absolute ratios; atomic weight; isotopic abundance; potassium; reference standard.

1. Introduction

The Analytical Spectrometry Section of the National Bureau of Standards is conducting a long term program of absolute isotopic abundance ratio and atomic weight determinations using the mass spectrometric method. Previous atomic weight determinations include silver [1],[1] chlorine [2], copper [3], bromine [4], chromium [5], magnesium [6], lead [7], boron [8], rubidium [9], rhenium [10], and silicon [11]. The present work extends the study to potassium.

A mass spectrometric determination of the atomic weight of an element requires a determination of the absolute isotopic abundance of a reference standard and also the establishment of limits for natural variations. The essential criteria for obtaining absolute isotopic abundances from relative or observed isotopic ratios is calibration of the instrument for the effects of bias using calibration standards of the analyte element with accurately known isotopic ratios. Accurately known calibration standards are prepared by gravimetrically mixing nearly isotopically and chemically pure separated isotopes of the analyte element. The uncertainty in the absolute ratio of the reference standard due to the assay and mixing of the separated isotopes must be within ± 0.02 percent to obtain the desired high accuracy atomic weight results. Mass spectrometric analysis of the reference standard and the calibration standard under nearly identical analytical conditions provides the means of calculating correction factors (calculated isotopic ratio of calibration standard/observed isotopic ratio of calibration standard) which when applied to the observed ratios of the reference standard being calibrated yield absolute isotopic abundance ratios for the standard. The atomic weight of the reference standard can then be calculated from the absolute abundances and the nuclidic masses reported by Wapstra and Gove [12]. Establishing the limits of natural variability requires a sampling of minerals from different geographic and geological origins on a world-wide basis. The uncertainty components due to possible natural variations, the ratio determination and other known sources of possible systematic error are summed to obtain an overall limit of error for the atomic weight of the element. A more detailed discussion of the mass spectrometric determination of the atomic weights of the elements is given by Cameron [13].

Naturally occurring potassium consists of stable isotopes ^{39}K and ^{41}K, and a radioactive isotope ^{40}K. With a half-life of approximately 1.4×10^9 years, ^{40}K is changing by beta emission to ^{40}Ca and by orbital electron capture to ^{40}Ar. Since the stable isotopes are 99.988 percent of the total number of potassium atoms present, the effect of the total amount of ^{40}K on the atomic weight is only 2.6 parts-per-million. During the course of a 10^9 year half-life the decay of ^{40}K will decrease the atomic weight by 1.5 parts-per-million (ppm).

Prior to 1951 the International Commission on

[1] Figures in brackets indicate the literature references at the end of this paper.

Atomic Weights used data from the chemical combining weight method as the source for establishing the potassium atomic weight. All of the mass spectrometric isotopic abundance data available at that time were relative measurements, which could not be corrected for bias effects because of insufficient information. Secondly, there were conflicting reports which indicated both large natural variations [14, 15, 16, 17, 18, 19, 20, 21], and a high degree of constancy [22, 23] in the isotopic abundances of potassium. These two factors weighed heavily against the use of mass spectrometric data as a source of information for the atomic weight of potassium.

In what was considered a benchmark in analytical mass spectrometry at the time of the measurement in 1950, Nier [24] calibrated for the effects of bias with standards of known isotopic composition prepared from high purity separated isotopes of argon. Reuterswärd [25], in an extensive effort to identify and correct for bias in the mass spectrometric measurement, discussed the risk of accepting a calibration which did not use potassium separated isotopes. Although extensive in scope, the calibration of Reuterswärd did not include calibration with standards of known isotopic composition. The atomic weight calculated from his abundance data was 39.101 and did not provoke any serious misgivings about the 1951 report of the International Commission on Atomic Weights [26] which accepted the 1950 isotopic abundance measurements of Nier as the basis for calculating the atomic weight of potassium.

Since 1951, the values recommended for the atomic weight of potassium by the International Commission on Atomic Weights have fluctuated between 39.098, obtained from the chemical method, and 39.102, obtained from the mass spectrometric method. Much of the indecision was due to an apparent difference of 0.01 percent between the methods and the lack of new sources of data or a high accuracy measurement to resolve the discrepancy. Tables 1 and 2 give a detailed summary of atomic weight ($^{12}C = 12$) data by these methods. The mass spectrometric data is not inclusive of all published isotopic data but is representative of the measurements published since 1930. Where investigators reported natural variations, the $^{39}K/^{41}K$ value for the standard or mineral most representative of terrestrial potassium was used for the atomic weight calculation. Examining the data from a point of view that none of the measurements satisfy the criteria for an absolute abundance determination, the average and range obtained is similar to the chemical data. The new source of information which eventually produced the revision to 39.098 ± 0.003 as the accepted value by the International Commission on Atomic Weights was Marinenko's [36] discussion of the data of Bates and Wichers [37], obtained from potentiometric titration of acids.

The primary purpose of the research reported here was a high accuracy determination of the atomic weight of potassium which would resolve the apparent discrepancy between the chemical and mass spectrometric data. To accomplish this goal, six calibration standards of known isotopic composition were prepared by gravimetrically blending isotopically and chemically pure separated isotopes of ^{39}K and ^{41}K. A secondary purpose was to provide an isotopic standard of accurately known composition which can serve as a stabilizer in geochemistry where the search for potassium variations has produced a collection of diverse and conflicting relative isotopic measurements. The material chosen for the isotopic standard was a potassium chloride (Standard Reference Material 985) obtained from the J. T. Baker Chemical Company[2], Phillipsburg, New Jersey.

[2] Company names are identified in this paper. Such identification does not imply recommendation or endorsement by the National Bureau of Standards.

TABLE 1. *Recalculation of atomic weight of potassium* ($^{12}C = 12$)

Year	Investigator	Method		Atomic weight
1906	Richards and Staehler [27]	$\frac{KCl}{Ag}$	$=0.691072$	39.092
		$\frac{KCl}{AgCl}$	$=0.0520118$	39.091
1907	Richards and Müeller [28]	$\frac{KCl}{Ag}$	$=0.69107$	39.091
		$\frac{KCl}{AgCl}$	$=0.52012$	39.091
1928	Hönigschmid and Gaubeau [29]	$\frac{KBr}{Ag}$	$=1.103270$	39.104
		$\frac{KBr}{AgCl}$	$=0.63374$	39.101

TABLE 1. *Recalculation of atomic weight of potassium* ($^{12}C = 12$) – Continued

Year	Investigator	Method		Atomic weight
1929	Hönigschmid and Gaubeau [30]	$\frac{KCl}{Ag}$	$= 0.691148$	39.100
		$\frac{KCl}{AgCl}$	$= 0.520180$	39.100
1933	Baxter and MacNevin [31]	$\frac{KCl}{Ag}$	$= 0.691057$	39.090
1933	Hönigschmid and Sachtleben [32]	$\frac{KCl}{Ag}$	$= 0.69069$	39.091
		$\frac{KCl}{AgCl}$	$= 0.520132$	39.093
		$\frac{KBr}{Ag}$	$= 1.103197$	39.096
		$\frac{KBr}{AgBr}$	$= 0.633720$	39.091
1935	Johnson [33]	$\frac{KCl}{Ag}$	$= 0.691108$	39.095
1940	Baxter and Harrington [34]	$\frac{KCl}{Ag}$	$= 0.691085$	39.093
1941	McAlpine and Bird [35]	$\frac{KBrO_3}{KBr}$	$= 1.403320$	39.104
		$\frac{KBr}{Ag}$	$= 1.103193$	39.095
1957	Marinenko [36] (Recalculated data of Bates and Wickers [37])	$\frac{C_8H_5O_4K}{C_7H_6O_2}$	$= 1.673374$	39.099
		Average (overall)	=	39.095
		Average (since 1935)	=	39.097

TABLE 2. *Calculation of atomic weight of potassium from relative mass spectrometric measurements*

Year	Investigator	$^{39}K/^{41}K$	Atomic weight [a] ($^{12}C = 12$)
1934	Brewer and Kueck [38]	13.88 ± 0.4	39.098
1935	Nier [39]	13.96 ± 0.1	39.097
1936	Manley [40]	13.4 ± 0.5	39.102
1936	Bondy and Vanicek [41]	14.1 ± 0.1	39.096
1943	Cook [22]	14.12 ± 0.28	39.096
1944	Paul [42]	13.96 ± 0.6	39.097
1948	White and Cameron [43]	13.66 ± 0.1	39.100
1948	Hibbs and Redmond [44]	13.81 ± 0.15	39.099
1950	Nier [24]	13.48 ± 0.07	39.102
1951	Reuterswärd [45]	14.32 ± 0.04	39.094
1956	Reuterswärd [25]	13.57 ± 0.09	39.101
1956	White et al. [46]	13.79 ± 0.05	39.099
1958	Omura and Morito [47]	13.96 ± 0.05	39.097
1960	Kendall [23]	13.769 ± 0.029	39.099
1962	Harms et al. [15]	14.33 ± 0.06	39.094

TABLE 2. *Calculation of atomic weight of potassium from relative mass spectrometric measurements* —Continued

Year	Investigator	$^{39}K/^{41}K$	Atomic weight [a] ($^{12}C=12$)
1962	Letolle [16]	13.85 ±0.06	39.098
1962	Stauffer and Honda [48]	14.23 ±0.01	39.095
1963	Shukolyukov et al. [49]	13.96 ±0.09	39.097
1965	Schreiner and Verbeek [50]	14.19 ±0.01	39.095
1973	Barnes et al. [51]	14.015±0.014	39.097
		Average	39.098

[a] Calculated with a $^{40}K/^{41}K$ value of 0.0017343 for all investigators.

2. Experimental Procedure

2.1. Mass Spectrometry

Isotopic abundance ratios of the reference standard (Standard Reference Material 985), calibration mixes and separated isotopes were determined by solid sample, thermal ionization mass spectrometry. Two single stage, solid sample mass spectrometers (a 15 cm radius of curvature, 60° analyzer tube instrument and a 30 cm radius of curvature, 90° analyzer tube instrument) were used to obtain two independent sets of isotopic ratio measurements. Both mass spectrometers were equipped with interchangeable and nearly identical electronic components, identical thin lens "Z" focusing ion sources [52], and the same basic design of a multielement, deep-bucket faraday cage collector [52, 53, 54].

The collectors, especially designed for in-depth suppression of secondary electrons, were equipped with a tungsten ribbon (0.025 ×0.76 mm) transmission grid shadowing a series of 0.10 mm suppressor grids. The other components for each measuring circuit were a pair of vibrating reed electrometers, an expanded-scale strip-chart recorder, a voltage to frequency converter and a scaler-timer. Data acquisition was computer controlled with the 15 cm instrument interfaced to a central, time-shared computer and the 30 cm instrument interfaced to its own minicomputer. Under computer controlled operation, all phases of the ratio measurement and data reduction were programed and automatic with the exception of ranging of the vibrating reed electrometers. This was accomplished manually by programing a magnet switching delay at the end of each peak top observation which was of sufficient duration to permit manual ranging. Operators retained at all times the options for digital, expanded scale recorder or simultaneous digital-recorder measurements.

Absolute isotopic abundance studies of uranium [54] established that the basic expanded-scale measuring circuit, including the multielement faraday cage collector, is linear over a ratio range 20:1 to 1:20. It was also established that for this range of isotopic ratios, a single mass dependent correction factor could be experimentally determined and applied to correct for bias effects. Corroborative support for this is provided by previous work in the atomic weight program where the isotopic ratios of a wide range of synthetic calibration mixes of the elements boron [8], chromium [5], magnesium [6], rubidium [9], and rhenium [10], were measured and compared to known values. Since most of the absolute isotopic abundance data obtained at NBS was with the expanded scale recorder, a considerable effort was made to prove the linearity of the digital measuring circuit. This was accomplished by a comparison of the digital and expanded scale recorder data obtained under simultaneous measurement conditions. Linearity of the digital circuits used in this experiment were found to be ≤ 0.02 percent.

Potassium was thermally ionized from a tantalum triple filament (0.025 × 0.76 mm) source. This filament material was selected in preference to other materials because of its poor ionization efficiency for calcium and the relative ease of reducing the potassium background ion current of a tantalum filament to 1×10^{-15} A. Prior to filament fabrication, the tantalum ribbons were boiled in ultra-high-purity water to remove all water soluble surface contaminants, rinsed in a second wash of ultra-high-purity water, and dried with a heat lamp in a clean air environment. After fabrication, the filaments were degassed in a vacuum and under a potential field. All filaments were degassed for 1 h at 4 A and then at an increased current of 4½ A for one-half hour. After minimum cooling of 30 min, the final cleaning was accomplished by a flashing procedure. This procedure consisted of a series of 1-min cycles in which the filaments were alternately pulsed with a 4 A current and then cooled for periods of 5 to 15 s. Bare filaments cleaned in this manner exhibited a potassium background ion current of $\leq 1 \times 10^{-15}$ A.

An evaluation of borosilicate glass, polyethylene, quartz, and Teflon containers over a 3-month period resulted in the selection of Teflon FEP [3] as the most acceptable for long-term storage of potassium solutions. Polyethylene containers were the least acceptable because of the relatively large amounts of material leached from some of the containers after stringent cleaning. Microgram amounts of organic or inorganic impurities on the sample filaments with 10–15 μg of potassium, changed the isotopic fractionation pattern of a high purity potassium chloride standard from a significantly decreasing $^{39}K/^{41}K$ ratio to a nearly con-

[3] A commercial material is identified in this paper in order to adequately specify experimental procedure. Such identification does not imply recommendation or endorsement by the National Bureau of Standards.

stant or increasing ratio with time [55]. Thus, a "dirty" standard, independent of the source of the impurities, showed a bias when compared to the same high purity standard analyzed under identical conditions. The deleterious effects of impurities on the accuracy of potassium isotopic measurements is well documented [22, 23, 25, 50, 55, 56]. The Teflon FEP containers were cleaned for a prolonged period of 1 week in hot, ultra-high purity (1 + 1) nitric acid [57], rinsed with ultra-high purity water, leached for 1 week in hot, ultra-high purity (1 + 1) hydrochloric acid, rinsed with ultra-high purity water and dried in a Class 100 clean air environment. The containers were then filled with ultra-high purity (1 + 1) hydrochloric acid, capped and stored in a clean air environment until needed. Prior to adding potassium solutions, the containers were thoroughly rinsed with ultra-high purity water.

Quartz tubing was used to make the pipets which were used to transfer solution from sample storage containers to the filaments. The quartz tubing was cleaned by heating in nitric acid (1 + 1) for 48 h, rinsed several times in warm high purity water, boiled in ultra-high purity nitric acid (1 + 1), rinsed in warm ultra-high purity water, and dried in a clean air environment by heat lamps. Immediately before transferring solution for analysis, additional cleaning was accomplished by flushing with high purity hydrochloric acid (1 + 49), rinsing with ultra-high purity water, and conditioning with an expendable aliquot of the sample to be analyzed. The effects of environmental contamination on cleaned filaments and pipets were minimized by careful handling and storage in a Class 100 clean air environment.

Potassium was deposited on the sample filaments as dilute hydrochloric acid solutions (1 + 49) of potassium chloride at a concentration of 2.5 mg of potassium per ml. One drop, 5 μl for MS #1 and 10 μl for MS #5, were evaporated to dryness on each sample filament with heat lamps and electrical currents which were adjusted as follows: 1.0 A for 10 min; 1.2 A for 5 min; and 1.5 A for 5 min. The heat lamps and electrical currents were turned off and the filaments allowed to cool 5 min before removal from the clean air environment. Sample filament alinement and spacing criteria required positioning these filaments the maximum distance of approximately 0.5 mm from the edges of the ionizing filament. This type of open spacing was used to reduce the effects of radiant heat by the ionizing filament.

Potassium ions were measured at a constant accelerating voltage of 3.8 kV by varying the magnetic field via a temperature compensated, Hall effect controller. For the mass spectrometric analysis, the ionizing filament was maintained at 1250 °C (direct pyrometer reading) and the sample filament currents were initially adjusted to 0.6 A. At specified times of 5 and 10 min into the analysis, the K^+ ion current was adjusted to 5×10^{-11} A and 1.0×10^{-10} A, respectively. No further adjustments were made until the ion current exhibited a growth pattern. Failure to produce an ion current growth pattern within 25 min after starting the run was sufficient cause for termination and rejection of the analysis. Under ion current growth conditions, the sample filament currents were adjusted to yield intensities of 1.5×10^{-10} A and 2.0×10^{-10} A at specified times of 15 and 20 min into the analysis. No further adjustments were normally required. The ratio measurement which was started after 40 min of heating was made in the sequence of $^{39}K/^{41}K$, $^{41}K/^{40}K$, $^{39}K/^{41}K$. While the two operators did not select or use the same parameters, such as sample size, sample mounting, heating pattern, and signal intensity, rigid standardization was maintained on each mass spectrometer. Isotopic fractionation was observed and, under normal conditions, the $^{39}K/^{41}K$ decreased ≤ 0.2 percent during the 45 min ratio measuring period. The effects of secondary electrons were observed in the vicinity of the ^{40}K base and were due primarily to the 10^{-10} A ^{39}K ion current. Reducing the x-axis opening into the collector with a baffle removed the large ^{39}K ion beam from the collector plates when the ^{40}K ion beam was focused on the faraday cage. This procedure was successfully used on both instruments to minimize the effects of secondary electrons. However, as collector plates were coated with a thin layer of potassium, suppression of secondary electrons became uncontrollable. It was necessary to remove the collector, thoroughly clean all surfaces and replace the tungsten transmission grids with virgin ribbon. This cleaning procedure was necessary and essential after approximately 50 analyses. Efforts to clean the tungsten transmission grids were unsuccessful and, under such conditions, deterioration of secondary electron suppression was rapid and unacceptable within 20 analyses. Contributions from the ^{39}K tail at the ^{40}K mass position were not detectable on the 30 cm instrument but were $\leq 1 \times 10^{-15}$ A on the 15 cm instrument. This tailing effect limited the accuracy of $^{40}K/^{41}K$ measurements with the digital system.

Although memory was not detected when the ^{39}K and ^{41}K separated isotopes were analyzed in an alternate pattern on the same source, or when analyzed in a similar pattern with natural or isotope dilution samples, it was known that significant amounts of potassium were deposited on the ion source during an analysis. Since K^+ ions contributed from residual potassium can be a source of significant error, the ion source was removed from the mass spectrometer, disassembled, and thoroughly cleaned before analysis of each separated isotope, the equal atom calibration mix, and the reference standard and remaining calibration mixes. All tools and associated sample mounting apparatus were also cleaned with each source cleaning. The clean ion source was first degassed for at least 1 h with a bare set of filaments and then conditioned for 90 min with a sample of the approximately isotopic abundance to be analyzed.

2.2. Purification of the Separated Isotopes

Electromagnetically separated ^{39}K and ^{41}K isotopes in the form of potassium chloride were obtained from the Isotopes Division, Oak Ridge National Laboratory

of the Union Carbide Nuclear Company. The ^{39}KCl and the ^{41}KCl were designated series 107401 and 149401, respectively. The certificates of analysis which accompanied each sample included a semiquantitative spectrographic analysis which showed that zinc could be present at the 0.2 percent level and several other elements, including aluminum, cadmium, cobalt, chromium, and nickel could be present up to the 0.5 percent level. To reduce these impurities to a level low enough so that they could not cause a significant error in the determination of the potassium, the separated isotope samples were further purified. The purification method used which was based on the crystallization of potassium perchlorate had been previously found by this laboratory to be effective for removing cationic and anionic impurities from rubidium chloride with the exception of potassium and cesium which cocrystallized with the rubidium [9]. The effectiveness of this purification procedure for potassium, in which potassium perchlorate is crystallized, was first tested by the purification of natural potassium chloride to which 1,000 ppm of 21 common elemental impurities had been added. The results of the analysis of the purified material by spark source–isotope dilution analysis is shown in table 3. Only sodium and iron were detected at the 10-ppm level and most of the other elements were at the low ppm level. The purification method does not separate rubidium or cesium.

Each separated isotope sample was purified as follows: The potassium chloride (about 3.5 g) was dissolved in 50 ml of 0.02*N* HCl in a Teflon-FEP beaker. The solution was filtered through a close textured filter paper that had been previously washed with 200 ml of 5*N* HCl into a Teflon-FEP beaker. The filtrate was diluted to 100 ml, and 6 ml of high-purity perchloric acid were added. The precipitated $KClO_4$ was dissolved by covering the beaker with a Teflon cover and heating the solution to near boiling. Potassium perchlorate was crystallized by removing the cover and allowing the solution to concentrate to about 35 ml. The solution was allowed to cool to room temperature and then to about 5 °C by placing it in the refrigerator overnight. The crystallized potassium perchlorate was recovered from the solution by filtering it through a fine porosity polyethylene filter. After the $KClO_4$ was washed with a cold 95 percent ethanol solution, it was returned to the Teflon beaker and the crystallization process was repeated except that only 2 ml of perchloric acid were added. The recrystallized $KClO_4$ was again caught on the polyethylene filter and washed with cold 95 percent ethanol. The purified material was dried by passing clean air over the $KClO_4$.

TABLE 3. *Spark source-isotope dilution mass spectrographic analysis of purified natural potassium chloride*

Element	Concentration μg/g	Element	Concentration μg/g
Al	0.6	Mo	5
Ba	1	Na	10
Bi	0.3	Ni	4

TABLE 3. *Spark source-isotope dilution mass spectrographic analysis of purified natural potassium chloride* —Continued

Element	Concentration μg/g	Element	Concentration μg/g
Ca	1	Pb	1
Cd	2	Se	6
Co	3	Sn	4
Cr	2	Sr	0.1
Cu	2	Te	2
Fe	11	Tl	0.4
Mg	1	Zn	0.4
Mn	1		

The purified $KClO_4$ was transferred back to the Teflon beaker and dissolved in 150 ml of hot water. This solution, while still hot, was passed through a cation exchange column containing 50 ml of AG50X8 resin, 100–200 mesh which is a strongly acidic cation exchange resin. (The polyethylene and resin were previously cleaned with 800 ml of 5*N* HCl.) The column was washed with 100 ml of water to completely remove perchloric acid from the column and the potassium was eluted with 200 ml of 5*N* HCl. The eluate containing the potassium was caught in the original Teflon beaker and evaporated to dryness.

The residue of potassium chloride was transferred to a 15 cm×1 cm×1 cm platinum boat. The boat was transferred to a quartz tube furnace and the boat and contents were ignited under oxygen at 550 °C for 2 h to oxidize the organic residue from the column. (To avoid any possibility of cross isotopic contamination, the ignitions were performed in new separate quartz tubes which had never been exposed to potassium.)

Calculations based on the starting weights of ^{39}KCl and ^{41}KCl and the weights of the corresponding purified salts showed about 95 percent of the potassium was recovered in each case.

The acids and water used during these purifications were produced at NBS by subboiling distillation [57] and have been shown to be extremely low in trace cation contamination. Apparatus such as beakers, columns, and filters were vigorously cleaned with high-purity acid.

2.3. Preparation and Analysis of the Separated Isotope Solutions

The 3.7 g of purified ^{39}KCl were dissolved in about 50 ml of (1+49) HCl, transferred to a tared 250 ml Teflon-FEP screw cap bottle and diluted to about 190 ml with (1+49) HCl. The 3.3 g of purified ^{41}KCl were dissolved in about 50 ml of (1+49) HCl, transferred to a tared 500 ml Teflon-FEP screw cap bottle and diluted to about 350 ml with (1+49) HCl. The bottles and contents were weighed to ±0.2 mg and the preliminary potassium concentration were calculated. The solution of ^{39}KCl was designated "K39" and the solution of ^{41}KCl was designated "K41".

Samples of the "K39" and "K41" solutions were analyzed for impurity elements by isotope dilution-spark source mass spectrometry [57]. Samples equivalent to about 100 mg of K were spiked with

10^{-7} g of ^{109}Ag, ^{137}Ba, ^{44}Ca, ^{111}Cd, ^{53}Cr, ^{65}Cu, ^{54}Fe, ^{113}In, ^{26}Mg, ^{62}Ni, ^{206}Pb, ^{82}Se, ^{117}Sn, ^{86}Sr, ^{125}Te, ^{203}Tl, and ^{67}Zn. Most of the potassium matrix was removed by crystallization of potassium perchlorate and concentration of the solution to about 0.2 ml. The liquid was removed from the crystallized $KClO_4$ by decantations and concentrated to about 0.05 ml by evaporation. Each solution was then evaporated to dryness on high purity gold wires and analyzed by spark-source mass spectrometry. In addition to these elements, Al, Bi, Co, Mo, and Mn were estimated by comparison to other nuclides. In addition, Rb and Cs, which are not removed by the purification procedure were determined by thermal ionization mass spectrometry by spiking with ^{87}Rb, measuring the $^{85}Rb/^{87}Rb$ ratio and comparing the ^{132}Cs to ^{87}Rb. The results of the analysis for impurities are shown in table 4. No element was detected at a level high enough to cause a significant error in the assay procedure, that is greater than 100 $\mu g/g$.

TABLE 4. *Impurities in potassium separated isotopes*

Element	"K39" $\mu g/g$[a]	"K41" $\mu g/g$[a]
Al[b]	1.5	0.5
Ba	0.6	.09
Ca	.4	.3
Cd	.3	.09
Cr	.4	.5
Cs	.1	.1
Cu	.3	.1
Fe	.8	1.2
Mg	.2	0.2
Na[b]	1	1.4
Ni	0.1	0.06
Pb	.09	.03
Rb	.3	.4
Sn	1	.01
Sr	0.04	.01
Te	.06	.05
Tl	.1	.05
Zn	.5	.09

[a] Essentially all of the values represent upper limit values.
[b] Compared to ^{26}Mg.

2.4. Assay of Separated Isotope Solutions

The bottles containing the potassium separated isotope solutions were shaken to thoroughly mix the solution and the screw cap closures were replaced with prepunctured polyethylene stoppers. Four weighed portions of about 15 g for the "K39" solution and about 30 g for the "K41" solution, equivalent to about 4 mmol of K, were withdrawn from each solution in the following manner. A 16-cm platinum needle was inserted through the prepunctured polyethylene stopper. A 20-ml polyethylene hypodermic syringe was attached to the Kel-F hub of the needle and the desired amount of solution was withdrawn. The syringe was then disconnected from the hub and the tip was capped with a Kel-F hub. Any static charge that might be present on the plastic syringe was dissipated by wiping it with a damp lintless towel and the syringe and contents were weighed on a semimicrobalance to ± 0.02 mg. The solution was then delivered into a Teflon-FEP beaker and the syringe was again capped, wiped and weighed. The weight of the sample was determined from the weights of the syringe before and after delivery of the sample. Since about 30 ml of the "K41" solution were required to produce a 4-mmol sample, two loadings of the 20-ml syringe were weighed for each assay sample. Two assay samples were withdrawn from each solution before the calibration samples were withdrawn and two samples were withdrawn after the calibration samples to insure that no change in concentration occurred during this time interval (about 6 h).

Each sample was then assayed as follows: Two ml of (1 + 1) $HClO_4$ was added to the weighed portion of the separated isotope solution. The solution was heated to dissolve the precipitated potassium perchlorate, $KClO_4$, and evaporated to constant volume at about 85 °C. The temperature of the hot plate was then raised to about 110 °C to volatilize the excess perchloric acid. The beaker and contents were cooled to room temperature, 15 ml of water were added and the solution was heated until the crystallized $KClO_4$ dissolved. The solution was again evaporated and any excess perchloric acid was removed by heating at about 110 °C. These evaporations freed the $KClO_4$ from chloride and occluded perchloric acid.

The recrystallized potassium perchlorate was again dissolved in 15 ml of water by heating and the solution was evaporated until only about 1 ml of solution remained with the crystallized $KClO_4$. (This was estimated by weighing the beaker and contents.) After cooling to room temperature, 4 ml of perchloric acid were added and the beaker and contents were cooled to about 5 °C in a refrigerator for 16 h (overnight).

The crystallized potassium perchlorate was transferred with cold (5 °C) 95 percent ethanol to a tared 15 ml fine porosity borosilicate glass filtering crucible. As much of the salt as possible was transferred by scraping the sides of the beaker with a Teflon "policeman" and washing the salt into the crucible with cold ethanol. The filtrate and original beaker were reserved for the determination of dissolved and untransferred potassium.

The filtering crucible and contents were dried at 110 °C for 2 h and at 300 °C for 4 h, cooled in a desiccator, and then transferred to the case of a microbalance and allowed to stand for several hours. The crucible and contents were then weighed to ± 0.002 mg. A buoyancy correction for the glass crucible was made by averaging three empty tare crucibles. The air weight of the $KClO_4$ was then determined and converted to vacuum weight using 2.522 for the density of $^{39}KClO_4$ and 2.557 for the density of $^{41}KClO_4$. These densities were calculated by assuming that they are proportional to the density of natural $KClO_4$ in the same relationship as their molecular weights. For simplicity of calculations, the vacuum weight of the potassium perchlorate was converted to millimoles of potassium using the calculated atomic weight for potassium and 1973 atomic weight values for chlorine and oxygens. The formula

594-051 O - 76 - 4

TABLE 5. *Assay—potassium separated isotope solutions*

Solution	Sample	Weight $KClO_4$ K g	$KClO_4$ K mmol	Filtrate K mmol	Total K mmol	Weight sample g	Conc. sample mmol
"K39"	1	0.517358	3.737737	0.007600	3.745337	14.52021	0.257939
	2	.543999	3.930210	.005786	3.935996	15.25967	.257934
	3	.531849	3.842430	.004935	3.847365	14.91381	.257973
	4	.522707	3.776382	.003977	3.780359	14.65616	.257936
						Average =	.257946
						s.d. =	.000018
"K41"	1	0.514726	3.666247	0.006539	3.672786	30.03932	0.122266
	2	.492306	3.506555	.005527	3.512082	28.72888	.122249
	3	.487376	3.471440	.006114	3.477554	28.44437	.122258
	4	.498044	3.547426	.005187	3.552613	29.05879	.122256
						Average =	.122257
						s.d. =	.000008

weights used were 138.4148 for $^{39}KClO_4$ and 140.3959 for $^{41}KClO_4$.

The beaker in which the precipitation was performed was thoroughly washed with hot water and the washings were combined with the filtrate. The "K39" solutions were spiked with about 15 μmol of ^{41}K and the "K41" solutions were spiked with about 15 μmol of ^{39}K for determining soluble and untransferred potassium by isotope dilution mass spectrometry. The spiked solution was mixed, 1 ml of nitric acid was added and the solution was evaporated to constant volume at about 85 °C. A few ml of water was added and the solution was evaporated to dryness at a higher temperature. The residue was taken up in 5 ml of water and passed through a column containing 3 ml of AG50X8 cation exchange resin. After washing the column with 20 ml of H_2O, the potassium was eluted with 20 ml of 5*N* HCl. The eluate was evaporated to dryness and taken up in 0.3 ml of (1+49) HCl and the $^{39}K/^{41}K$ ratio was determined by thermal ionization mass spectrometry. The potassium found by isotope dilution was added to the potassium from the gravimetric determination to yield the total potassium in the sample. The concentration was then calculated by dividing this value by the weight of the sample. Table 5 shows the results of these determinations.

This method of determining the concentration of potassium solutions was previously tested on solutions containing known amounts of potassium. Six solutions were prepared from SRM 999 which is certified to contain 52.435 ± 0.004 percent potassium by weight in the approximate concentration of the separated isotope solution. Four samples containing from 3.5 to 5.0 mmol of potassium were withdrawn from each solution and the potassium concentrations were determined as described.

Comparison of the calculated and measured concentrations of the six solutions showed that: (a) the concentration of potassium determined by this method agreed to within 0.01 percent of the calculated potassium concentration, (b) systematic errors were negligible, and (c) the analyses were of equal precision.

From these analyses and the analyses of the separated isotope solutions, the standard deviation of an individual measurement of the concentration of a potassium solution was computed to be 0.000017 mmol/g (24 degrees of freedom). The uncertainty of the concentration at the 95 percent confidence level is computed to be 0.000018 mmol/g for the "K39" solution and 0.000008 mmol/g for the "K41" solution.

2.5. Isotopic Analysis of Separated Isotopes

Two aliquots of each separated isotope were utilized for mass spectrometric analysis. One aliquot was withdrawn from each separated isotope solution before blending of the first calibration mix and the other immediately after finishing the last calibration mix. Each of the premixing separated isotope solutions was analyzed eight times and each of the postmixing solutions was analyzed two times for a total of 10 analyses per instrument. A comparison of the observed isotopic ratios of these solutions revealed no significant contamination during preparation of the calibration mixes.

Exclusive of variable isotopic fractionation between analyses, the major sources of error in determining the isotopic composition of highly enriched separated isotopes are memory, contamination, filament background and nonlinearity of the measuring circuit. Memory effects were minimized by thorough cleaning and conditioning of the ion source for analysis of each separated isotope. The ^{39}K background contribution of the bare degassed filaments was confirmed to be 1×10^{-15} A by mass spectrometric analysis. A selected number of these filaments were removed from the mass spectrometer and a known quantity, either 10 μg or 25 μg, of potassium separated isotope was immediately deposited on each sample filament. When analyzed, the effect of natural potassium was much larger than could be accounted for by a nominal 1×10^{-15} A filament background. This "threshold effect," where a small amount of sample on the filament surface is necessary to obtain an accurate measure of filament blank, was observed when the ionizing filament was used for a single analysis or when used for as many as four different analyses with four different sets of sample filaments. The effect of filament blank on the $^{39}K/^{41}K$ ratios of the separated isotopes was approximately

0.002 percent and 0.05 percent for ^{39}K and ^{41}K, respectively.

Bias due to RC response of the measuring circuit was minimized by delaying a minimum of 30 s to allow the system to stabilize after magnetically switching peak tops. Continuous monitoring of ^{39}K on the faraday cage produced a condition in which the $^{39}K/^{41}K$ ratio decreased more than could be accounted for by the isotopic fractionation associated with the heating pattern. Removing the ^{39}K ion current from the collector for less than 5 min produced a recovery to the initially observed $^{39}K/^{41}K$ ratio. This change was in the same direction and, in most cases, of the same magnitude as that obtained from isotopic fractionation. The maximum change observed, including isotopic fractionation, for a normal analysis in which ^{39}K was continuously focused on the faraday cage was 0.5 percent. A most likely cause of this condition, secondary electrons, was investigated with negative results. The number and position of collector suppressor magnets, increased suppressor voltage on collector plates and two different thoroughly cleaned collectors on two different mass spectrometers did not have any significant effect. A nonlinear response of a component of the measuring circuit because of continuous and prolonged exposure to 10^{-10} A ion currents was also a likely cause but could not be proven. Although this effect was not detected for any other sample, precautions were taken to avoid prolonged or continuous monitoring of 10^{-10} A ion currents, to limit ratio measurements to less than 10 min, and to defocus the ions from the collector for 5 min between each measurement cycle within an analysis.

Corrected isotopic compositions of the separated isotopes are reported in table 6. The uncertainties are limits of error which are larger than the calculated 95 percent confidence limits and which include additional components for nonlinearity and the effects of a natural potassium filament blank.

TABLE 6. *Isotopic composition of separated potassium isotopes*

Separated isotope		Isotopic composition (atom percent)
"K39"	^{39}K	99.9765 ± 0.0004
	^{40}K	0.0014 ± .0001
	^{41}K	.0221 ± .0004
"K41"	^{39}K	0.8186 · 0.0020
	^{40}K	.0004 ± .0001
	^{41}K	99.1810 ± .0020

The uncertainties are based on minimum errors for the ratio determinations. The calculated 95 percent confidence limits are well below the minimum error statement.

2.6. Preparation of the Calibration Samples

Six calibration samples were prepared by mixing weighed portions of the "K39" and "K41" solutions to produce five calibration samples with $^{39}K/^{41}K$ ratios that approximated natural potassium and varied over a range of 4 percent. A sixth calibration sample was prepared with a $^{39}K/^{41}K$ ratio of 1. The portions were withdrawn from the bottles and weighed in the manner previously described. To eliminate any possibility of change in concentration of the isotope solutions with time, the portions for the calibration samples were withdrawn from the bottles at the same time the samples for determining the potassium concentrations were withdrawn.

TABLE 7. *Composition of potassium calibration samples*

Sample No.	Isotope solution	Weight solution g	^{39}K mmol	^{41}K mmol	$^{39}K/^{41}K$ ratio
1	"K39"	6.74034	1.738235	0.0003842	14.13808
	"K41"	1.01137	0.001012	.1226344	
2	"K39"	7.49182	1.932031	.0004271	13.91228
	"K41"	1.14244	0.001143	.1385274	
3	"K39"	7.07292	1.824002	.0004032	13.94269
	"K41"	1.07620	0.001077	.1304954	
4	"K39"	7.19697	1.855994	.0004103	13.67965
	"K41"	1.11621	0.001117	.1353469	
5	"K39"	7.25150	1.870055	.0004134	13.55556
	"K41"	1.13500	0.001136	.1376252	
6	"K39"	2.45747	.6337456	.0001401	0.989239
	"K41"	5.32666	.0053309	.6458880	

Table 7 shows the calculated isotopic composition of the calibration samples. The isotopic ratio of each calibration sample was calculated from the isotopic analysis of the separated isotopes and the mmol of potassium from each separated isotope solution.

Each calibration sample was thoroughly mixed by stirring and evaporated to dryness on a hot plate. The calibration samples were taken up with (1+49) HCl so that 1 ml of solution contained 2.5 mg of K.

2.7. Isotopic Analysis of the Calibration Mixes and the Reference Standard

Two complete and independent sets of analyses of the calibration mixes and the reference standard were made, one on MS #1 by Operator I and the other on MS #5 by Operator II. Each set consisted of 18 analyses of the calibration mixes and 18 analyses of the standard. Exclusive of the equal atom calibration mix which was analyzed on a clean source, a simple alternating pattern of standard and calibration mix was maintained until three analyses per calibration mix were obtained. Four solutions of the high purity potassium chloride standard were prepared and stored in specially cleaned Teflon bottles. Three of these samples were representative of different positions of the bulk material and the fourth was a composite of the first three. The composite sample was processed through an ion exchange column to duplicate the treatment of the separated isotopes during the purification procedure.

Operator I utilized the digital system to determine

TABLE 8. *Determination of correction factors*

Calibration sample No.	$^{39}K/^{41}K$ Ratio			Correction factor [a]		
	Operator I (digital)	Operator II (digital)	Operator II (recorder)	Operator I (digital)	Operator II (digital)	Operator II (recorder)
1	14.2879	14.2723	14.2709	0.989590	0.990583	0.990684
2	14.0525	14.0432	14.0378	.990097	.990666	.991050
3	14.0871	14.0766	14.0749	.989825	.990475	.990598
4	13.8221	13.8088	13.8024	.989769	.990636	.991098
5	13.6940	13.6838	13.6797	.989966	.990617	.990917
6	0.999965	0.998973	0.998859	.989391	.990250	.990367
Mean value of correction factors =				[b] 0.989849	[b] 0.990595	[b] 0.990869

[a] These correction factors are calculated using the individually determined compositions of the separated isotopes to compute the isotopic ratio of each calibration sample.

[b] Values of calibration sample No. 6 were not used in calculating the averages, but were included in the computation of the uncertainty in the ratio determination.

TABLE 9. *Observed isotopic ratios of reference standard*

Bottle No.	Operator I		Operator II	
	$^{39}K/^{41}K$ Digital	$^{39}K/^{41}K$ Recorder	$^{39}K/^{41}K$ Digital	$^{39}K/^{41}$ K Recorder
B-2	13.99743		13.98520	13.98286
B-6	13.99798		13.98952	13.98477
B-11	13.99840		13.98805	13.98590
Composite	13.99826		13.98951	13.98653
Average	13.99802		13.98807	13.98502
	$^{41}K/^{40}K$ Digital	$^{41}K/^{40}K$ Recorder	$^{41}K/^{40}K$ Digital	$^{41}K/^{40}K$ Recorder
B-2	573.363	574.204	575.301	573.987
B-6	573.307	573.289	576.027	574.090
B-11	573.921	573.653	575.135	573.571
Composite	573.852	573.851	575.648	574.453
Average	573.611	573.749	575.528	574.025

NOTE.—The value for each bottle is the average of five analyses.

the potassium isotopic ratios of all samples and also simultaneously recorded the data by expanded scale recorder. Of the strip chart recorder data by Operator I, only the $^{41}K/^{40}K$ ratio was calculated with the intent of providing a rigorous evaluation of the linearity of the digital system. Operator II utilized the digital and expanded scale recorder in a simultaneous mode of operation to measure the isotopic ratios of all samples. Two sets of measurement by Operator II, the set of digital measurements by Operator I, and the $^{41}K/^{40}K$ recorder measurements by Operator I were submitted to a statistician for analysis.

3. Results and Discussion

Table 8 summarizes the analysis of the calibration mixes and the calculation of correction factors. Calibration mixes one through five formed the point calibration for determining the correction factors. Analysis of equal atom mix (No. 6) yielded correction factors slightly different from the averages on both instruments. This calibration mix was excluded in calculating the average correction factors but was included in determining the uncertainty in the ratio measurement.

The average values for the observed isotopic ratios of four subsamples of the reference standard are given in table 9. The agreement between subsamples indicates that the Teflon sample containers were adequately cleaned or that any impurities leached from the containers did not affect the isotopic analysis. Organic contributions from the ion exchange column purification were also too small to significantly affect the isotopic ratios. The $^{41}K/^{40}K$ ratio as determined by Operator II on the digital system is biased high with respect to the recorder data on the same instrument. This bias is due to a slight amount of ^{39}K tail at the ^{40}K mass position on the 15 cm instrument. The digital system takes the linear average of two points on opposite sides of the ^{40}K peak to determine the baseline, but the tail contribution is nonlinear. This type correction is more accurately determined from the recorder spectra. The precision of the $^{39}K/^{41}K$ ratio measurements are approximately the same for both operators using either digital or expanded scale re-

TABLE 10. *Determination of corrected isotopic ratios*

	$^{39}K/^{41}K$			$^{41}K/^{40}K$		
	Observed $^{39}K/^{41}K$	Correction factor	Corrected $^{39}K/^{41}K$	Observed $^{41}K/^{40}K$	Correction factor	Corrected $^{41}K/^{40}K$
Digital I	13.99802	0.989849	13.85593	573.611	1.005128	576.552
s.d. =	0.00022	.000114	0.00141 (8 d.f.)	0.160	0.000051	0.163 (8 d.f.)
Digital II	13.98807	.990595	13.85651	575.528	1.004747	578.260
s.d. =	0.00102	.000070	0.00195 (8 d.f.)	0.198	0.000035	0.199 (8 d.f.)
Recorder II	13.98502	.990869	13.85732	574.025	1.004608	576.670
s.d. =	0.00081	.000114	0.00161 (8 d.f.)	0.182	0.000057	0.163 (8 d.f.)
		Mean =	13.85662 ± [a]0.00627		Mean =	576.6 ± [a]2.0
Uncertainty Components:						
95 percent confidence limits on ratio determination			±0.00267			±1.88
Bounds due to possible systematic error in composition of separated isotopes			±0.00119			±0.05
Bounds due to possible systematic error in chemical analysis			±0.00241			±0.10

[a] Digital I and Recorder II were used as the two independent determinations to calculate the means and uncertainty component due to ratio determination.

corder measurements. The two complete sets of measurements by Operator II do not satisfy the criteria for two independent determinations. Satisfaction of this criteria requires each set of analyses to be different in all respects from sample loading through the ratio measurement. Therefore, the digital measurements of Operator I and the recorder measurement of Operator II were used as two independent determinations from which the absolute isotopic ratios, the isotopic compositions, and the atomic weight were calculated. The absolute isotopic ratios are summarized in table 10.

The calculation of the atomic weight of the reference standard is summarized in table 11. Each uncertainty component is at least as large as the 95 percent confidence limit. For the $^{40}K/^{41}K$ ratio measurement of the standard and the isotopic ratios of the separated isotopes, the statistically calculated 95 percent confidence limits are smaller than the limiting error of the instrument. For this condition an uncertainty component larger than the calculated 95 percent confidence limit, but equivalent to the limiting error of instrument for the analytical conditions of the measurement, is used. The overall limit of error is the sum of the uncertainty components due to the isotopic composition of the separated isotopes, the chemical assay and mixing of the separated isotopes, and the mass spectrometric ratio measurement.

An extensive survey of terrestrial potassium by

TABLE 11. *Summary calculations of the atomic weight of potassium in Standard Reference Material 985*

Value	Uncertainty Components			
	Overall limit of error [a]	Mass spectrometric analytical error	Possible systematic error in composition of separated isotopes	Possible systematic error in chemical analysis
Atomic weight = 39.098304	± 0.000058	± 0.000025	± 0.000011	± 0.000022
Nuclidic masses ($^{12}C = 12$)				
$^{39}K = 38.9637089$	± 0.0000008			
$^{40}K = 39.9640001$	± 0.0000008			
$^{41}K = 40.9618270$	± 0.0000011			
Atomic percent				
$^{39}K = 93.25811$	± 0.00292	± 0.00130	± 0.00053	± 0.00109
$^{40}K = 0.011672$	± 0.000041	± 0.000038	· 0.000001	· 0.000002
$^{41}K = 6.73022$	± 0.00292	± 0.00130	± 0.00053	± 0.00109
Isotopic ratios				
$^{39}K/^{41}K = 13.85662$	± 0.00627	0.00267	± 0.00119	± 0.00241
$^{40}K/^{41}K = 0.0017343$	± 0.0000061	± 0.00000564	± 0.00000015	± 0.0000003

[a] The overall limit of error is the sum of the 95 percent confidence limits and the terms covering effects of known sources of possible systematic error.

Garner et al. [56] found no major isotopic abundance variations among approximately 70 mineral samples of different geological origins and geographic locations. Particular attention was given to include samples which might be expected to show isotopic variations or which had been previously reported to show significant isotopic variations. The average value of the minerals is biased approximately 0.03 percent higher than the $^{39}K/^{41}K$ of the reference standard, SRM 985. This difference is attributed to an altered fractionation pattern rather than to real differences in isotopic abundance between the minerals and reference standard. The alteration in fractionation pattern of the minerals is produced by the relative small amounts of organic and/or inorganic impurities which are not removed by the chemical separation and purification procedure.

Based on this survey, the atomic weight of terrestrial potassium is calculated to be 39.09830 ± 0.00019. The error limits include an additional component of ± 0.000136 to cover uncertainties in the terrestrial mineral survey data resulting from possible natural isotopic variations and bias introduced by the chemical purification procedure. The reported isotopic variations of lunar potassium [51, 58] were treated as a special case and are not covered by the error limits for terrestrial potassium.

We are indebted to: Hsien H. Ku for statistical analysis; W. R. Shields, former Section Chief, for his advice and efforts in initiating the project; W. A. Bowman, III, for maintenance support; Carrie A. Garfink for filament fabrication and assistance in reduction of strip chart recorder data; Joy J. Shoemaker and Josephine Ledford for skillful manuscript preparation.

4. References

[1] Shields, W. R., Garner, E. L., and Dibeler, V. H., J. Res. Nat. Bur. Stand. (U.S.) **66A** (Phys. and Chem.) 1–3 (Jan.–Feb. 1962).
[2] Shields, W. R., Murphy, T. J., Garner, E. L., and Dibeler, V. H., J. Am. Chem. Soc. **84**, 1519–1522 (1962).
[3] Shields, W. R., Murphy, T. J., and Garner, E. L., J. Res. Nat. Bur. Stand. (U.S.) **68A** (Phys. and Chem.) 589–592 (Nov.–Dec. 1964).
[4] Catanzaro, E. J., Murphy, T. J., Garner, E. L., and Shields, W. R., J. Res. Nat. Bur. Stand. (U.S.) **68A** (Phys. and Chem.) 593–599 (Nov.–Dec. 1964).
[5] Shields, W. R., Murphy, T. J., Catanzaro, E. J., and Garner, E. L., J. Res. Nat. Bur. Stand. (U.S.) **70A** (Phys. and Chem.) 193–197 (March–April 1966).
[6] Catanzaro, E. J., Murphy, T. J., Garner, E. L., and Shields, W. R., J. Res. Nat. Bur. Stand. (U.S.) **70A** (Phys. and Chem.) 453–458 (Nov.–Dec. 1966).
[7] Catanzaro, E. J., Murphy, T. J., Shields, W. R., and Garner, E. L., J. Res. Nat. Bur. Stand. (U.S.) **72A** (Phys. and Chem.) 261–267 (May–June 1968).
[8] Catanzaro, E. J., Champion, C. E., Garner, E. L., Marinenko, G., Sappenfield, K. M., and Shields, W. R., Nat. Bur. Stand. (U.S.), Spec. Publ. 260–17, 70 pages (Feb. 1969).
[9] Catanzaro, E. J., Murphy, T. J., Garner, E. L., and Shields, W. R., J. Res. Nat. Bur. Stand. (U.S.) **73A** (Phys. and Chem.) 511–516 (Sept.–Oct. 1969).
[10] Gramlich, J. W., Murphy, T. J., Garner, E. L., and Shields, W. R., J. Res. Nat. Bur. Stand. (U.S.) **77A** (Phys. and Chem.) 691–698 (Nov.–Dec. 1973).
[11] Barnes, I. L., Moore, L. J., Machlan, L. A., Murphy, T. J., and Shields, W. R., Absolute Isotopic Abundance Ratios and the Atomic Weight of a Reference Sample of Silicon, J. Res. Nat. Bur. Stand. (U.S.) **79A** (Phys. and Chem.) No. 6. (Nov.–Dec. 1975).
[12] Wapstra, A. H., and Gove, N. B., Nuclear Data Tables **9**, 265–301 (1971).
[13] Cameron, A. E., Anal. Chem. **36**, 23A–35A (1963).
[14] Brewer, A. K., J. Amer. Chem. Soc. **58**, 365–370 (1936).
[15] Harms, G., Blanc, G., Espagno, L., and Blanc, D., Comptes Rendus **255**, 3203–3204 (1962).
[16] Letolle, R., Comptes Rendus **254**, 2205–2206 (1962).
[17] Letolle, R., Comptes Rendus **257**, 3996–3998 (1963).
[18] Schreiner, G. D. L., and Verbeek, A. A., Proc. Roy. Soc. **A285**, 423–429 (1964).
[19] Lebadev, V. I., Prokofyev, L. M., Kirillov, A. S., Tarasov, A. V., Geokhimiya **10**, 1255–1257 (1966).
[20] Verbeek, A. A., and Schreiner, G. D. L., Geochim. Cosmochim. Acta **31**, 2125–2133 (1967).
[21] Schreiner, G. D. L., and Welke, H. J. H. F. D., Geochim. Cosmochim. Acta **35**, 719–726 (1971).
[22] Cook, K. L., Phys. Rev. **64**, 278–293 (1943).
[23] Kendall, B. R. F., Nature **186**, 255–256 (1963).
[24] Nier, A. O., Phys. Rev. **77**, 789–793 (1950).
[25] Reuterswärd, C., Arkiv Fysik **11**, 1–54 (1956).
[26] Wichers, E., J. Am. Chem. Soc. **74**, 2447–2450 (1952).
[27] Richards, T. W., and Staehler, J. Am. Chem. Soc. **29**, 623–639 (1907).
[28] Richards, T. W., and Müeller, E., J. Am. Chem. Soc. **29**, 639–656 (1907).
[29] Hönigschmid, O., and Gaubeau, J., Z. Anorg. Allgem. Chem. **163**, 93–164 (1927).
[30] Hönigschmid, O., and Gaubeau, J., Z. Anorg. Allgem. Chem. **177**, 102–108 (1928).
[31] Baxter, G. P., and MacNevin, W. M., J. Am. Chem. Soc. **55**, 3185–3190 (1933).
[32] Hönigschmid, O., and Sachtleben, R., Z. Anorg. Allegem. Chem. **213**, 365–376 (1933).
[33] Johnson, C. R., J. Phys. Chem. **39**, 781–789 (1935).
[34] Baxter, G. P., and Harrington, C. D., J. Am. Chem. Soc. **62**, 1836–1837 (1940).
[35] McAlpine, R. K., and Bird, E. J., J. Am. Chem. Soc. **63**, 2960–2965 (1941).
[36] Marinenko, G., Talanta **16**, 1339–1340 (1969).
[37] Bates, R. G., and Wichers, E., J. Res. Nat. Bur. Stand. (U.S.) **59**, 9–17 (July 1957).
[38] Brewer, A. K., and Kueck, P. D., Phys. Rev. **46**, 894–897 (1934).
[39] Nier, A. O., Phys. Rev. **48**, 283–284 (1935).
[40] Manley, J. H., Phys. Rev. **49**, 921–924 (1936).
[41] Bondy, H., and Vanicek, V., Z. Physik **101**, 186–192 (1936).
[42] Paul, W., Z. Physik **124**, 244–257 (1948).
[43] White, J. R., and Cameron, A. E., Phys. Rev. **74**, 991–1000 (1948).
[44] Hibbs, R. F., and Redmond, J. W., Y–290, AECI–24 (1949).
[45] Reuterswärd, C., Ark. Fysik **4**, 203–205 (1952).
[46] White, F. A., Collins, T. H., and Rourke, F. M., Phys. Rev. **101**, 1786–1791 (1956).
[47] Omura, I., and Morito, N., J. Phys. Soc. Japan **13**, 659 (1958).
[48] Stauffer, H., and Honda, M., J. Geophys. Res. **67**, 3503–3512 (1962).
[49] Shukolyukov, Yu. A., Tolstikhin, I. N., and Varshavskaya, E. S., Geokhimiya **4**, 373–375 (1964).
[50] Schreiner, G. D. L., and Verbeek, A. A., Proc. Roy. Soc. **A285**, 423–429 (1965).
[51] Barnes, I. L., Garner, E. L., Gramlich, J. W., Machlan, L. A., Moody, J. R., Moore, L. J., Murphy, T. J., and Shields, W. R.,

Proceedings of the Fourth Lunar Science Conference. Geochim. Cosmochim. Acta Suppl. 4. **2**, 1197–1207 (1973).
[52] Shields, W. R., (Ed.), Nat. Bur. Stand. (U.S.) Tech. Note 426, 53 pages (Sept. 1967).
[53] Shields, W. R., (Ed.), Nat. Bur. Stand. (U.S.) Tech. Note 277, 99 pages (July 1966).
[54] Garner, E. L., Machlan, L. A., and Shields, W. R., Nat. Bur. Stand. (U.S.) Special Publication 260–27, 150 pages (April 1971).
[55] Garner, E. L., Machlan, L. A., Gramlich, J. W., Moore, L. A., Murphy, T. J., and Barnes, I. L., 7th IMR Research Symp., Gaithersburg, MD, Oct. 7–11, 1974. NBS Spec. Publ. 422, U.S. Government Printing Office, Washington, D.C. 20402 (In press).
[56] Garner, E. L., Goldich, S. S., Gramlich, J. W., Machlan, L. A., and Murphy, T. J., Absolute Isotopic Composition of Terrestrial Potassium (In preparation).
[57] Kuehner, E. C., Alvarez, R., Paulsen, P. J., and Murphy, T. J., Anal. Chem. **44**, 2050–2056 (1972).
[58] Garner, E. L., Machlan, L. A., and Barnes, I. L., Proceedings of the Sixth Lunar Science Conference (In press).

(Paper 79A6–869)

JOURNAL OF RESEARCH of the National Bureau of Standards—A. Physics and Chemistry
Vol. 79A, No. 6, November–December 1975

Absolute Isotopic Abundance Ratios and the Atomic Weight of a Reference Sample of Silicon

I. L. Barnes, L. J. Moore, L. A. Machlan, T. J. Murphy, and W. R. Shields*

Institute for Materials Research, National Bureau of Standards, Washington, D.C. 20234

(August 27, 1975)

Absolute values have been obtained for the isotopic abundance ratios of a reference sample of silicon using electron impact mass spectrometry. Samples of known isotopic composition prepared from nearly isotopically pure separated silicon isotopes were used to calibrate the mass spectrometers. The resulting absolute $^{28}Si/^{30}Si$ ratio=29.74320±0.00747 and the $^{29}Si/^{30}Si$ ratio=1.50598±0.00086 which yield atom percents of $^{28}Si = 92.22933 \pm 0.00155$, $^{29}Si = 4.66982 \pm 0.00124$ and $^{30}Si = 3.10085 \pm 0.00074$. The atomic weight calculated from this isotopic composition is 28.085526 · 0.000056. The indicated uncertainties are overall limits of error based on 95 percent confidence limits for the means and allowances for the effects of known sources of possible systematic error. A study of natural $^{28}Si/^{30}Si$ ratio variations reported in the literature extends the estimated uncertainty in the atomic weight of natural silicon to ±0.00039.

Key words: Absolute ratios; atomic weight; isotopic abundance; silicon.

* Present address: Teledyne Isotopes, Timonium, Maryland 21200.

1. Introduction

The Analytical Spectrometry Section of the National Bureau of Standards is conducting a long term program of absolute isotopic abundance ratios and atomic weight determinations using thermal ionization mass spectrometry. Previous elements studied include silver [1],[1] chlorine [2], copper [3], bromine [4], chromium [5], magnesium [6], lead [7], boron [8], rubidium [9], rhenium [10], and potassium [11]. This present work extends the study to silicon and demonstrates an expansion of the technique to include electron impact mass spectrometry.

Interest in the atomic weight of silicon was stimulated by the long-term project of the NBS Institute for Basic Standards to replace the kilogram as a standard of mass. Mass is the remaining triumvir of the *m–k–s* measurement system whose definition is expressed in terms of an artifact physical unit—the platinum-iridium 1-kg mass that resides in Paris. The meter and second have been redefined as multiples of measurable natural phenomena.

As a milestone in achieving this goal, a high purity silicon crystal of high lattice perfection was selected as a candidate for the measurement of its unit cell dimensions, density and atomic weight, with desired measurement uncertainties for each of these at the parts-per-million level or less. Since silicon in nature consists of a mixture of three stable and nonradioactive isotopes (^{28}Si, ^{29}Si, ^{30}Si), the uncertainty of the relative proportions of these masses immediately became the limiting error in the precise characterization of the silicon crystal.

As a secondary objective, the atomic weight of silicon could also be combined with the crystal parameter measurements by the IBS to permit a new and direct redetermination of Avogadro's Constant [12].

Finally, also unanswered was the question of whether the atomic weight of the silicon crystal had been distorted during the zone refining purification process.

To achieve these objectives a project was begun to determine the absolute silicon isotope abundance ratios and, hence, the atomic weight of a reference sample of silicon, with an intermediate goal of ≤10 parts-per-million (ppm) uncertainty in the atomic weight.

To obtain absolute isotopic ratios from the observed or relative measurements made on a mass spectrometer it is necessary to calibrate the instrument using samples of accurately known isotopic ratios of the element

[1] Figures in brackets indicate the literature references at the end of this paper.

under study. These synthetic isotopic standards, prepared from chemically pure and very nearly isotopically pure separated isotope, provide a bias or fractionation correction (calculated isotope ratio-observed isotope ratio) which when applied to the observed isotope ratio of the reference sample being calibrated allow an absolute ratio to be calculated for this sample. The atomic weight can then be calculated from the absolute isotopic abundances and the atomic masses reported by Wapstra and Gove [13].

Prior to 1948 the accepted atomic weight of silicon was 28.06 based on the work of Baxter et al. [14] measuring the ratios $SiCl_4$:4 Ag and $SiBr_4$:4 Ag. Based on the isotopic ratios measured by White and Cameron [15] and others the value 28.086 ± 0.001 was accepted [16] but the error limits were expanded to ± 0.003 [17] based on the report of the variations of silicon isotopes by Allenby [18].

2. Experimental Procedure

2.1. Mass Spectrometry

Isotope ratio measurements were made on a 60° extended flight path 15 cm (6 inch) mass spectrometer. The mass spectrometer was equipped with a "Z" focusing thin lens source [19] (see below). The collector was a deep bucket Faraday Cage type equipped with a 50 percent transmission grid shadowing a series of electron suppression grids [20]. The measuring circuit consisted of two state-of-the-art vibrating reed electrometers with provisions for automatic range switching. The output of the measuring system was fed into both an expanded scale recorder [21] and a digital system consisting of a voltage to frequency converter and a precision scaler-timer. In general both systems were used redundantly. The digital system and the range switching systems were under computer control.

Mass measurements were made by magnetic field switching. The magnetic field was controlled and changed with the use of a gaussmeter-controller. Source and collector slits were arranged so that complete resolution of each of the masses of interest was obtained.

The electron impact source used was similar to the thermal emission source normally used in our laboratory except that the shield was replaced with an electron impact section consisting of a tungsten filament, impact chamber or "cage" and an electron trap. The trap plate was provided with an external electrical circuit so that it could be continuously heated to about 300 °C which reduced the background to negligible levels.

The sample gas was admitted to the impact region through a short section of Teflon [2] tubing from a leak of the type described by Shields [22].

[2] Certain commercial products are identified in order to adequately specify the experimental procedure. In no case does such identification imply recommendation or endorsement by the National Bureau of Standards, nor does it imply that the products identified are necessarily the best available for the purpose.

The operating parameters of the source were as follows:

Electron energy	50	eV
Accelerating potential	4780	V
Emission current	85	μA
Trap current	80	μA
Filament current	3.0	A

The various samples of reference materials and of separated isotopes prepared as described below were processed for analysis using essentially the system described by Reynolds and Verhoogen [23] in which solid barium fluosilicate ($BaSiF_6$) was heated to produce BaF_2 and gaseous SiF_4. The silicon tetrafluoride was collected and introduced into the mass spectrometer to become the source of the SiF_3^+ ions which were measured.

The vacuum system used for the preparation of the SiF_4 was constructed of nickel and copper tubing instead of the glass system used by Reynolds and Verhoogen since it was believed that the glass itself might be the source of small amounts of water which might lead to the formation of SiF_2O^+, SiF_2HO^+ and $SiF_2H_2O^+$ ions as noted by them (see below).

The sample was placed in a 3/4-inch nickel tube approximately 30 cm long which was attached to a vacuum line through a "Dalton" fitting with an aluminum gasket. The vacuum line constructed of 5/8-inch copper tubing contained a U-tube trap which was cooled with a mixture of dry ice-ethanol during processing of the sample. The silicon tetrafluoride gas was collected in a nickel sample tube cooled with liquid nitrogen.

In a typical sample preparation cycle a new sample tube was placed on the vacuum system evacuated to a pressure of $< 10^{-5}$ Pa (10^{-7} torr), the trap cooled, a tube furnace placed around the sample container and the tube baked at a temperature of 700 °C for 1 hr. The furnace was then turned off and the tube was allowed to cool to room temperature. The tube was removed from the system and 100 mg of the $BaSiF_6$ was added. The tube was reattached to the system and evacuated with a sample collecting tube attached to the system. When a pressure of $< 10^{-5}$ Pa (10^{-7} torr) was reached the U-tube trap was cooled and liquid nitorgen placed on the sample collecting tube. At this point the vacuum system was valved off, the furnace turned on and the sample heated to 410 °C (±5 °C measured with a calibrated chromel-alumel thermocouple) at a rate of approximately 7°/min. Previous experiments had shown that at a temperature of 400 °C the sample had completely decomposed and the SiF_4 produced was quantitatively removed and collected. This was substantially in agreement with the results of Reynolds and Verhoogen. After a period of 10 min at 410 °C the furnace was turned off and allowed to cool to below 200 °C after which the main vacuum system valve was opened and the system pumped out for 15 min to remove any other gases in the system not held at liquid nitrogen temperature in the sample collecting tube. The sample

collecting tube valve was closed, the liquid nitrogen removed and the tube was allowed to warm to room temperature after which it was connected to the mass spectrometer inlet manifold.

During subsequent analyses of the gas the sample collection tube was always cooled in a dry ice-ethanol bath to ensure that no water vapor would enter the spectrometer. Examination of the mass region of interest and for seven or eight mass units both above and below showed no sign of interfering peaks.

One further precaution was observed during sample preparation to ensure that no inadvertant isotopic contamination could occur. A number of sample tubes, sample collection tubes, and vacuum manifold U-traps were constructed, marked and tagged. A separate set was used for the preparation of each different sample.

2.2. Purification of Separated Silicon Isotopes

The final goal of achieving stoichiometric assays of the enriched isotopes at the 0.01 percent precision and accuracy level is strongly dependent on the chemical purity of each isotope. The enrichment of the ^{28}Si and ^{30}Si isotopes was done by electromagnetic separation at Oak Ridge National Laboratory (Union Carbide Nuclear Company). Collection of each high energy separated Si ion beam was effected with a graphite faraday cup. Thus the removal of the separated isotope from the graphite cup resulted in a material, as received at NBS, that was a mixture of SiO_2, SiC and graphite. The silicon 28 was designated sample 900390 and consisted of 4.452 g of mixed SiO^2 and SiC along with some graphite from the collector. The silicon 30 was designated sample 900490 and consisted of 200 mg of the same type mixture.

The ^{28}Si separated isotope sample was transferred to a 100 ml FEP-Teflon beaker and the silicon dioxide along with any silicon metal present in the material was dissolved by adding 16 g of 50 percent sodium hydroxide solution and diluting to 50 ml. The solution was digested overnight on a hot plate at about 80 °C and filtered through a close textured filter paper. The insoluble residue and filter paper were washed with water, transferred to a platinum crucible and the paper and residue were ignited over a Meeker burner. About 25 percent (1 g) of the original material remained and was assumed to be silicon carbide.

The filtrate was split into two equal portions and each portion was diluted to 500 ml in Teflon beakers. Each portion was passed through a strongly acidic cation exchange column to remove sodium and other cations. The columns were constructed from polystyrene and were approximately 33 cm long and of 2.5 cm inside diameter. They were filled to a height of 25 cm with Bio-Rad AG50 × 8, 100–200 mesh, cation exchange resin. The eluates were caught in Teflon beakers. Each column was washed with about 150 ml of water to completely remove the silicic acid, $H_2{}^{28}SiO_3$, from the column. The eluates and washings were then evaporated to dryness on a hot plate and the resulting hydrated silica, $^{28}SiO_2 \cdot xH_2O$, was transferred to a 50-ml platinum crucible.

The 1 g of ^{28}SiC insoluble residue resulting from the filtration of the sodium hydroxide solution was decomposed by sodium carbonate fusion. About 5 g of sodium carbonate was added to a 20-ml platinum crucible and about 50 mg of the ^{28}SiC was added. The crucible was covered with a platinum cover and heated over a Meeker burner at moderate heat to fuse the Na_2CO_3 and react with the ^{28}SiC. After a few minutes the heat was raised to the full Meeker burner temperature for about 5 min. The crucible and contents were then cooled, the cover removed, a second 50 mg portion of ^{28}SiC added, and the Na_2CO_3 fusion repeated. This procedure was repeated until the entire sample of ^{28}SiC had been added and fused. One gram of Na_2CO_3 was added to the original platinum crucible and fused to react with any remaining ^{28}SiC. The sodium carbonate melts were dissolved in about 400 ml of H_2O in a 500-ml Teflon beaker. The solution was titrated with (1 + 4) HCl to PH 5–6 (as determined by pH indicating paper), the CO_2 expelled by rapid stirring, and the solution was made alkaline with dilute sodium hydroxide to about pH 9. The solution was then passed through a cation exchange column as described for the sodium hydroxide solution of the soluble silica. The eluate was caught in a Teflon beaker, evaporated to dryness and the resulting hydrated silica was transferred to the platinum crucible that contained the previously separated silica. The crucible was then covered with a platinum cover and ignited in an electric muffle furnace at 800 °C for several hours. The total recovered $^{28}SiO_2$ weighed 4.185 g equivalent to 1.952 g of ^{28}Si.

The ^{30}Si separated isotope mixture was taken into solution in a manner similar to the ^{28}Si procedure except on a reduced scale because of the smaller sample size. The total sample was transferred to a 100-ml FEP-Teflon beaker and the silicon dioxide and silicon metal were dissolved by adding 2 g of 50 percent sodium hydroxide and diluting to 50 ml. After overnight digestion on a hot plate at about 80 °C, the solution was filtered through a close textured filter paper. The insoluble residue and filter paper were washed with H_2O, transferred to a platinum crucible, and ignited over a Meeker burner. About 50 percent (97 mg) of the original material remained and was assumed to be ^{30}SiC.

The filtrate containing the sodium hydroxide soluble (silicon was passed through a strongly acidic cation exchange column constructed from polypropylene and containing about 35 ml of Bio-Rad AG50 × 8 resin, 100–200 mesh. The column was washed with 70 ml of water to completely remove the silicic acid, $H_2{}^{30}SiO_3$, from the column and the eluate and washings were evaporated to dryness. The residue was transferred to a 10-ml platinum crucible and ignited to $^{30}SiO_2$ over a Meeker burner.

The silicon carbide insoluble residue resulting from the filtration of the sodium hydroxide solution was decomposed by sodium carbonate fusion in the same manner as the ^{28}SiC except that only 1 g of Na_2CO_3 was used. Any ^{30}SiC remaining in the original platinum crucible was dissolved by fusion with 0.2 g Na_2CO_3. The sodium carbonate melts were dissolved in about

100 ml of H_2O in a Teflon beaker. The solution was titrated with (1+4) HCl to pH 5–6 (as determined by pH indicating paper), the CO_2 was expelled by rapid stirring, and the solution was made alkaline with dilute sodium hydroxide solution to about pH 9. This solution was then passed through the same cation column as the sodium hydroxide fraction and the column was washed with about 70 ml of H_2O. The eluate and washings were caught in a Teflon beaker, evaporated to dryness, and the residue was transferred to the platinum crucible that contained the previously separated $^{30}SiO_2$. The crucible was then covered with a platinum cover and ignited to an electric muffle furnace at 1000 °C for ½ h. The $^{30}SiO_2$ recovered weighed 0.1814 g equivalent to 87.8 mg of ^{30}Si.

Throughout these procedures, the utmost care was used to prevent contamination of the isotopes with natural silicon. All of the beakers, ion-exchange columns ion-exchange resins and filter papers were cleaned with dilute high-purity hydrofluoric acid before use. All of the chemical reagents were selected for low silicon content. For example, the total system blank for the purification of the ^{30}Si isotope amounted to 4 μg of natural silicon or about 0.0003 percent of the ^{30}Si.

2.3. Preparation and Analysis of the Separated Isotope Solutions

The 4.18 g of purified $^{28}SiO_2$ was transferred to a 250-ml Teflon beaker and dissolved in a mixture of 130 ml of water and 30 ml of high-purity 48 percent hydrofluoric acid at room temperature. The solution was transferred to a tared 500-ml Teflon bottle and diluted to approximately 300 g with water containing 30 ml of concentrated hydrofluoric acid to give a solution containing approximately 0.18 mmol/g of $H_2{}^{28}SiF_6$ in 3N hydrofluoric acid. This solution was designated "Si–28".

The 0.181 g of purified $^{30}SiO_2$ was transferred to a 100-ml Teflon beaker and dissolved in a mixture of 35 ml of water and 7 ml of 48 percent hydrofluoric acid at room temperature. The solution was transferred to a 125 ml tared FEP-Teflon bottle and diluted with water to approximately 55 g to give a solution approximately 0.05 mmol/g of $H_2{}^{30}SiF_6$ in 3*N* hydrofluoric acid. The solution was designated "Si–30".

Samples of the "Si–28" and "Si–30" were analyzed for impurity elements by isotope-dilution spark source mass spectrometry. Samples equivalent to about 5 mg of silicon were spiked with 10^{-7} g of ^{109}Ag, ^{137}Ba, ^{44}Ca, ^{111}Cd, ^{53}Cr, ^{65}Cu, ^{54}Fe, ^{41}K, ^{26}Mg, ^{97}Mo, ^{62}Ni, ^{206}Pb, ^{123}Sb, ^{82}Se, ^{117}Sn, ^{86}Sr, ^{125}Te, ^{203}Tl, ^{67}Zn. After the addition of 0.5 ml of perchloric acid to each sample, the silicon matrix was volatilized as SiF_4 by evaporation to a small drop of perchloric acid. The drop was transferred to a pair of gold wires, evaporated onto the wires, and the deposit was analyzed by spark source mass spectrometry .

In addition to the elements determined by isotope dilution, Al, As, Na, and Sb were estimated by comparison to isotopes of other elements. Table 1 shows the result of these analyses. The results showed that there was no significant difference in the purity of the two isotope solutions at a level that could interfere with the assay method for silicon which was based on the gravimetric determination of Cs_2SiF_6. The principal interferences are the elements that form insoluble fluosilicates such as the alkalies and alkaline earths.

In addition to the elements reported in table 1, tungsten was detected in the "Si–30" solution. Subsequent analysis of $Cs_2{}^{30}SiF_6$ from the assay using a ^{183}W spike showed that the tungsten concentration was negligible at less than 3 ppm.

2.4. Assay of the Separated Isotope Solutions

Four weighed portions each containing about 10 mg of silicon, were withdrawn from each separated isotope solution in the following manner. A 10-cm platinum needle was inserted through a No. 2 polyethylene stopper and used to replace the cap in the bottle. A 10-ml polyethylene hypodermic syringe with the plunger covered with a thin sheet of Teflon was attached to the Kel-F hub of the needle and the desired amount of solution was withdrawn. The syringe was then disconnected from the hub and the tip was capped with a Kel-F cap. Any static charge that might be present on the plastic syringe was dissipated by wiping it with a damp lintless towel. The syringe and contents were weighed on a semimicrobalance to ±0.02 mg. The solution was then delivered from the syringe into a 50-ml Teflon-FEP beaker and the syringe was again capped, wiped and weighed. The weight of the sample was determined from the weight of the syringe before and after delivery of the sample. Two assay samples were withdrawn from each solution before and after

TABLE 1. *Analysis of silicon isotopes*

Element	"Si–28" ppm	"Si–30" ppm
Ag	7	2
[a] Al	5	3
[b] As	3	2
Ba	0.5	1
Ca	5	3
Cd	1	4
Cr	10	30
Cu	4	4
Fe	18	26
K	1	7
Mg	1	1
Mo	3	20
[c] Na	[e] 30	[e] 50
Ni	2	7
Pb	1	2
[d] Sb	21	7
Se	3	0.2
Sn	1	5
Sr	0.2	0.3
Te	0.5	1
Tl	1	1
Zn	1	8

[a] Versus ^{26}Mg
[b] Versus ^{82}Se
[c] Versus ^{41}K
[d] Versus ^{117}Sn
[e] Value not significantly different from blank.

withdrawing the calibration samples to ensure that no change in concentration had occurred during this time interval (about 3 h).

Each weighed portion was then assayed as follows: The "Si–28" solutions were diluted to approximately 6 ml with 1*N* HF. The "Si–30" aliquots were 6 ml so no further dilution was required. A weighed aliquot of CsCl solution (100 mg CsCl/g) was added to the separated isotope assay solution in an amount to give approximately 10 percent excess of the stoichiometric amount required to yield cesium fluosilicate, Cs_2SiF_6. Twenty grams of acetone were added to the beaker, the solution was covered and stored in a plastic box with an open beaker of acetone to prevent excessive loss of acetone from the assay solution. After allowing the solution to stand at least 48 h (the "Si–28" solution stood for 5 days) it was filtered through a weighed 15-ml Munroe crucible and washed with approximately 20 ml of a 90 percent acetone/10 percent water (v/v) solution. (The filtrate and washings were transferred back to the original beaker and reserved for the determination of dissolved and untransferred silicon.) The crucible and contents were dried for 2 h at 110 °C, allowed to cool in a desiccator, transferred to the case of a microbalance and allowed to stand for at least 1 h. The crucible and contents were weighed to ±0.002 mg. A combination blank and buoyancy correction was made by averaging three crucibles that had been used to filter blank samples carried through the procedure. The drying, cooling and weighing were repeated until constant weight was reached. The air weight of the Cs_2SiF_6 was then determined and converted to vacuum weight using a Chemical Rubber Handbook (54th edition) value of 3.372 as the density of the salt. The micromoles of silicon present in the salt were determined using a calculated atomic weight for silicon and 1973 atomic weight values for the other two elements. The formula weights used were 407.7782 for $Cs_2\,{}^{28}SiF_6$ and 409.7463 for $Cs_2\,{}^{30}SiF_6$.

The filtrate from the precipitation of the cesium fluosilicate was transferred to the original beaker and about 15 ml of water was added to insure that any untransferred salt was dissolved. The acetone was removed by evaporating the solution to approximately 15 ml.

The solution was transferred to a 100-ml FEP-Teflon beaker and 40 g of boric acid solution (5 g/100 ml) and 4 g of molybdic acid solution (25 g of ammonium molybdate tetrahydrate dissolved in 200 ml of H_2SO_4 (1+9) and diluted to 250 ml with water) were added. After mixing, the pH of the solution was adjusted to 1.7–1.8 with NH_4OH (1+1). After allowing the solution to stand for 10 min, 4 g of tartaric acid solution (25 g/100 ml) was added. The solution was mixed and 4 g of reducing solution (27 g of sodium bisulfite, 2 g of sodium hydroxide and 0.5 g of 1-amino 2-napthol 4-sulfonic acid dissolved in 250 ml of water and filtered through a close-textured paper) was added. The solution was transferred to a 100-ml volumetric flask, filled to the mark with water and thoroughly mixed. The absorbancy was measured on a spectrophotometer at 650 nm using a 2-cm cell with water in the reference cell. The micromoles of silicon were calculated from a curve plotted by carrying known amounts of silicon through the same procedure. The silicon found was added to the silicon from the gravimetric determination to yield the total silicon in the sample. Table 2 shows the results of these analyses.

This method of determining the concentration of silicon solutions was previously tested on solutions containing known amounts of silicon. Two solutions were prepared from high purity silicon, SRM 990. Three sets of four samples each containing from 320 to 420 μmol of silicon were withdrawn from each solution and the silicon concentrations were determined as described above. Comparison of the calculated and measured concentrations showed biases of −0.017 and −0.032 percent for the two solutions. The silicon was dissolved in diluted HNO_3 and HF and there was apparently a greater loss of Si as SiF_4 from one solution than the other. The concentration determined for each solution was internally consistent with concentrations of 0.107778 ± 0.000012 and 0.106541 ± 0.00001 μmol/g for 12 determinations on each solution.

Pooling the results of the "Si–28" separated isotope solutions with the results of the six sets described

TABLE 2. *Concentration of silicon isotope solutions*

Solution	Sample No.	Weight solution g	Silicon		Total silicon μmol	Conc. solution μmol Si/g
			From ppt μmol	From sol μmol		
"Si–28"	1	2.20065	390.482	0.182	390.664	177.522
	2	2.08974	370.552	.332	370.884	177.479
	3	2.03935	361.606	.379	361.985	177.500
	4	2.09052	370.763	.283	371.046	177.490
Average						177.498
"Si–30"	1	6.64491	355.205	0.374	355.579	53.5115
	2	6.27097	335.154	.387	335.541	53.5070
	3	6.62758	354.344	.242	354.586	53.5016
	4	6.63155	354.524	.317	354.841	53.5080
Average						53.5070

above yields a value of 0.0000126 μmol/g for the standard deviation of an individual measurement.

2.5. Isotopic Analysis of Separated Isotopes

The quantities of "Si–28" and "Si–30" were transferred as the barium compound and decomposed to SiF_4 as described above. Because of the very large ratios these compounds were measured using a 30 cm radius mass spectrometer which was otherwise identical to the 15 cm radius used for the remaining measurements. The results of these measurements are given in table 3.

TABLE 3. *Measurements of the separated isotopes*

	Silicon-28	
Sample No.	$^{28}Si/^{29}Si$	$^{28}Si/^{30}Si$
1	15500	45040
2	15450	43890
3	15740	46690
Average.....	15563	45207
S.D.....	155	1407
	Silicon-30	
Sample No.	$^{30}Si/^{29}Si$	$^{30}Si/^{28}Si$
1	71.81	883.4
2	71.50	888.8
3	71.29	879.4
Average.....	71.53	883.9
S.D.....	0.26	4.7

2.6. Preparation of Calibration Samples

Three calibration samples were prepared by mixing weighed portions of the "Si–28" and "Si–30" solutions. One mixture was within 0.25 percent of the observed natural $^{28}Si/^{30}Si$ ratio of 29.7 and the other two mixtures bracketed the natural ratio by 2 percent. The portions were withdrawn from the bottles and weighed in the manner previously described for the assay of the solution. To ensure that there had been no change in concentration of an isotope solution with time, the portions for the calibration samples were withdrawn from the bottles between the samples taken for assay.

Table 4 shows the concentration of the calibration samples calculated from the isotopic analysis of the separated isotopes and the micromoles of silicon from each separated isotope solution as determined from the assay and weight of solution taken.

Each calibration sample was thoroughly mixed and a weighed aliquot of $BaCl_2$ solution (100 mg $BaCl_2$/g) was added in an amount to give a 1 percent excess of the stoichiometric amount required to yield barium fluosilicate, $BaSiF_6$. The solution was evaporated to dryness at low heat (~80 °C) on a hot plate. Each sample was evaporated separately to avoid any possibility of cross-contamination.

2.7. Measurement of the Relative Ratios of the Reference Material

To determine the relative, or uncalibrated, isotopic abundances of the reference material, SRM 990 samples were prepared as described above and the isotopic ratios measured. To ensure that no instrumental memory effects were observed a careful background scan of the measured region was made before the introduction of each sample. No sample was examined if the mass 85 position showed a detectable signal of more than 3×10^{-15} A. Sufficient sample was introduced to give a total silicon beam intensity of 3×10^{-11} A and the ratios measured in a pattern of 10 $^{28}Si/^{29}Si$ ratio measurements, 20 $^{30}Si/^{29}Si$ ratios and 10 $^{28}Si/^{29}Si$ ratios. Additional sample was then introduced to give a signal intensity of 7×10^{-11} A and the ratio measurement repeated. After this the pattern was repeated at signal intensities of 3×10^{-10} A and 7×10^{-11} A. In no case did the ratios show a change outside of experimental error for each of the four different runs on each sample. The results of the relative measurements of the reference samples are shown in table 5.

2.8. Comparison of the Isotopic Ratios of the Calibration Mixes and the Reference Sample

In the measurements of the isotopic ratios of gases such as silicon tetrafluoride using electron impact ionization sources the problem of memory is nearly always encountered. Although large and efficient vacuum systems help alleviate the problem the gas molecules adsorb on components of the source and are released with the introduction of subsequent samples causing an unpredictable alteration of the isotopic composition of the sample. To eliminate these effects the so-called "constant" background or interpolative

TABLE 4. *Composition of silicon calibration samples*

Sample No.	Isotope solution	Weight solution g	^{28}Si μmol	^{30}Si μmol	Isotope ratio $^{28}Si/^{30}Si$
1	"Si–28"	9.41413	1.6708450	0.0000369	30.389838
	"Si–30"	1.04286	0.0007393	.0549688	
2	"Si–28"	9.47683	1.6819732	0.0000372	29.149102
	"Si–30"	1.09454	0.0008074	.0576929	
3	"Si–28"	9.16645	1.6268861	0.0000360	29.815019
	"Si–30"	1.03502	0.0007635	.0545556	

TABLE 5. *Determination of relative ratios of reference sample (SRM 990)*

Determination No.	28/29	30/29
1	19.74689	0.665180
2	19.74790	.664296
3	19.73678	.664621
4	19.74046	.663930
5	19.73318	.663806
6	19.73143	.663284
7	19.74364	.664562
8	19.74626	.664026
9	19.73565	.664692
10	19.73730	.664650
11	19.73281	.664752
12	19.74000	.664753
Average	19.73936	.664379
S.D.	0.00577	.000526
Composition (Atom %)		
28 92.22389		
29 4.67208		
30 3.10403		
28/30 = 29.71099		
29/30 = 1.50517		

method was chosen for these measurements. The interpolative method which has been in use by the nuclear fuels industry for many years has been described in detail by Smith et al. [24] and by Rodden [25]. It consists essentially in the analysis of accurately known standards and samples in a prescribed and carefully timed pattern which permits the calculation of the precise ratio difference between samples and standards regardless of the actual isotopic ratios measured. The samples may be given accurate values through the differences measured and the known values of the standards. In this case two of the prepared synthetic mixes (A and B) were chosen with compositions slightly above and below the composition of the standard. The three samples were prepared in separate sample containers to contain exactly the same quantity of gas (within ±0.5 percent) and the three containers were attached to the mass spectrometer and were analyzed in the following manner. Sample A was introduced into the instrument to give a total silicon ion beam of 3×10^{-11} A. The ion beam was allowed to stabilize for exactly 2 min (all times given were controlled to ±1 s) after which 10 ratio measurements were made. The pump on the sample manifold was then opened and the system allowed to evacuate for 5 min after which the sample X was introduced as above. These measurements were repeated in the order $A-X-B-B-X-A-A-X$ . . . until a minimum of 10 $A-X-B-B-X-A$ cycles were completed. From each cycle a ratio of differences may be calculated as

$$R_D=\frac{R_X-R_A}{R_B-R_A}$$

where R_X = average reading for sample entries
R_A = average reading for low standard entries
R_B = average reading for high standard entries

and the standard related to the known values for the standards through

$$K_X=R_D(K_B-K_A)+K_A.$$

It is also possible to correct for a small amount of residual bias by use of an end point measurement. For this the standards are substituted for the unknown sample in a sequence $A-A-B-B-B-B-A-A$ and the reverse from which the end point bias may be calculated as:

$$R_{DA}=\frac{R_{XA}-R_A}{R_B-R_A}$$

$$R_{DB}=\frac{R_{XB}-R_A}{R_B-R_A}.$$

If no bias exists R_{DA} will be equal to zero and R_{DB} equal to 1. Normally this is not the case and the ratio of differences, R_D is corrected as:

$$R_{D(\text{corrected})}=\frac{R_D-\bar{R}_{DA}}{\bar{R}_{DB}-\bar{R}_{DA}}$$

The value of K_X, the true isotopic ratio of the sample corrected for residual bias may then be calculated from the formula given for K_X above. When this value of the true $^{28}Si/^{30}Si$ ratio is obtained a correction factor for the filament bias may be calculated using that and the observed ratio. This may be used to correct all other measured values to a "true" scale.

In addition to the above sequence another synthetic mix (C) had been prepared with isotopic ratios nearly identical to the reference material. This sample could be directly compared using the same timing program as given above in a $C-X-C-X$ . . . sequence. The values of X, the true $^{28}Si/^{30}Si$ ratio in the reference and the correction factor obtained are shown in table 6.

As a test of the validity of the above system this third mix C was substituted for the reference material X, in a $A-C-B-B-C-A-A-$ . . . sequence. The value for the $^{28}Si/^{30}Si$ ratio calculated from this measurement agreed with that known from the chemical preparation to within 0.001 percent.

TABLE 6. *Summary of filament correction factor calculation*

1. From comparison of mixes 2, 4 and SRM 990
   $R_{D(\text{corrected})}$ = 0.48115
   S.D. = 0.00428
   True $(^{28}Si/^{30}Si)_{990}$ = 29.74608
2. From comparison of mix 5 and SRM 990
   Ratio $\frac{(^{28}Si/^{30}Si)_{990}}{(^{28}Si/^{30}Si)_5}$ = 1.002512
   S.D. = 0.000260
   True $(^{28}Si/^{30}Si)_{990}$ = 29.74031
3. Average true value = 29.74320
4. Correction factor = $\frac{29.74320}{29.71099}$ = 1.001084
5. Correction factor/mass unit = 1.000542
6. True $(^{29}Si/^{30}Si)_{990}$ = 1.50598

3. Results and Discussion Calculation of Reference Sample Atomic Weight

Using the corrected or true values for the isotopic ratios determined for the reference sample and the values of the nuclidic masses given by Wapstra and Gove [12] the atomic weight of this reference sample may be calculated. The summary of the calculations are shown in table 7.

As mentioned above Allenby reported a variation in the $^{28}Si/^{30}Si$ ratios of 1.4 percent within the samples he analyzed. Reynolds and Verhoogen however, found only a maximum variation of 0.3 percent in materials very similar to those analyzed by Allenby. In an attempt to resolve this discrepancy Tilles [26] analyzed a large variety of samples including a number of both biological and meteoric origin. His results agreed very well with those of Reynolds and Verhoogen but extended the maximum range slightly to 0.53 percent. Tilles suggested that laboratory fractionation in the sample preparation system used by Allenby may have been the cause of the larger variation noted by him. In view of the excellent agreement between the results of Tilles and Reynolds and Verhoogen and the much larger variety of samples analyzed it seems that a maximum variation in nature of 0.5 percent is most probable.

The authors are indebted to P. J. Paulsen who performed the spark source mass spectrometric analysis of the reference material and of the separated isotopes and to Hsien H. Ku who provided the statistical analysis of the experimental data but also studied the experiment and provided helpful guidance.

The authors also acknowledge the help of the Division of Research US AEC (now ERDA) and the personnel of the Office of Isotope Sales, ORNL, for the use of the separated isotopes.

TABLE 7. *Summary calculations of atomic weight of a silicon reference sample*

Value	Uncertainty components				
	Overall limit of error [a]	95% L.E. on the ratio measurements	Possible bias on determination of the end point correction	Possible systematic error in composition of separated isotopes	Possible systematic error in chemical analysis
Atomic weight = 28.0855258	±0.0000555	±0.0000202	±0.0000097	±0.0000073	±0.0000183
Nuclidic masses [12] ($^{12}C = 12$)					
$^{28}Si = 27.9769286$					
$^{29}Si = 28.9764969$					
$^{30}Si = 29.9737722$					
Atomic percent					
$^{28}Si = 92.22933$	± 0.00383	±0.00155	±0.00063	±0.00047	± 0.00118
$^{29}Si = 4.66982$	± .00218	±0.00124	± .00026	± .00019	± .00049
$^{30}Si = 3.10085$	± .00205	±0.00074	± .00036	± .00027	± .00068
Isotopic ratios					
$^{28}Si/^{30}Si$ 29.74320	±0.02101	±0.00747	±0.00373	±0.00278	±0.00703
$^{29}Si/^{30}Si$ 1.50598	± .00119	± .00086	± .00009	± .00007	± .00047

[a] The overall limit of error is the sum of the 95 percent confidence limits for the ratio determinations and terms covering effects of known sources of possible systematic error.

4. References

[1] Shields, W. R., Garner, E. L., and Dibeler, V. H., J. Res. Nat. Bur. Stand. (U.S.) **66A** (Phys. and Chem.) 1–3 (Jan.–Feb. 1962).

[2] Shields, W. R., Murphy, T. J., Garner, E. L., and Dibeler, V. H., J. Am. Chem. Soc. **84**, 1519–1522 (1962).

[3] Shields, W. R., Murphy, T. J., and Garner, E. L., J. Res. Nat. Bur. Stand. (U.S.) **68A** (Phys. and Chem.) 589–592 (Nov.–Dec. 1964).

[4] Catanzaro, E. J., Murphy, T. J., Garner, E. L., and Shields, W. R., J. Res. Nat. Bur. Stand. (U.S.) **68A** (Phys. and Chem.) 593–599 (Nov.–Dec. 1964).

[5] Shields, W. R., Murphy, T. J., Catanzaro, E. J., and Garner, E. L., J. Res. Nat. Bur. Stand. (U.S.) **70A** (Phys. and Chem.) 193–197 (March–April 1966).

[6] Catanzaro, E. J., Murphy, T. J., Garner, E. L., and Shields, W. R., J. Res. Nat. Bur. Stand. (U.S.) **70A** (Phys. and Chem.) 453–458 (Nov.–Dec. 1966).

[7] Catanzaro, E. J., Murphy, T. J., Shields, W. R., and Garner, E. L., J. Res. Nat. Bur. Stand. (U.S.) **72A** (Phys. and Chem.) 261–267 (May–June 1968).

[8] Catanzaro, E. J., Champion, C. E., Garner, E. L., Marinenko, G., Sappenfield, K. M., and Shields, W. R., Nat. Bur. Stand. (U.S.), Spec. Publ. 260–17, 70 pages (Feb. 1969).

[9] Catanzaro, E. J., Murphy, T. J., Garner, E. L., and Shields, W. R., J. Res. Nat. Bur. Stand. (U.S.) **73A** (Phys. and Chem.) 511–516 (Sept.–Oct. 1969).

[10] Gramlich, J. W., Murphy, T. J., Garner, E. L., and Shields, W. R., J. Res. Nat. Bur. Stand. (U.S.) **77A** (Phys. and Chem.) 691–698 (Nov.–Dec. 1973).

[11] Garner, E. L., Murphy, T. J., Gramlich, J. W., Paulsen, P. J., and Barnes, I. L., Absolute Isotopic Abundance Ratios and the Atomic Weight of a Reference Sample of Potassium, to be published in J. Res. Nat. Bur. Stand. (U.S.), **79A** (Phys. and Chem.) No. 6. (Nov.–Dec. 1975).

[12] Deslattes, R. D., Henins, A., Bowman, H. A., Schoonover, R. M., Carrol, C. L., Barnes, I. L., Machlan, L. A., Moore, L. J., and Shields, W. R., Phys. Rev. Lett. **33**, 463–466 (1974).
[13] Wapstra, A. H., and Gove, N. B., Nuclear Data Tables **9**, 265–301 (1971).
[14] Baxter, G. P., Weatherill, P. F., and Scripture, E. W., Jr., Proc. Am. Acad. Arts Sci. **58**, 245–268 (1923).
[15] White, J. R., and Cameron, A. E., Phys. Rev. **74**, 991–1000 (1948).
[16] Cameron, A. E., and Wichers, E., JACS **84**, 4175–4197 (1962).
[17] Atomic Weights of the Elements—1969, Pure Appl. Chem. **21**, 93–107 (1970).
[18] Allenby, R. J., Geochim. Cosmochim. Acta **5**, 40–48 (1954).
[19] Shields, W. R., (Ed.), Nat. Bur. Stand. (U.S.) Tech. Note 426, 53 pages (Sept. 1967).
[20] Shields, W. R., (Ed.), Nat. Bur. Stand. (U.S.) Tech. Note 277, p. 8 (July 1966).
[21] Shields, W. R., (Ed.), Nat. Bur. Stand. (U.S.) Tech. Note 277, p. 10 (July 1966).
[22] Shields, W. R., U.S. Patent 2,956,771 (1960).
[23] Reynolds, J. H., and Verhoogen, J., Geochim. Cosmochim. Acta **3**, 224–234 (1953).
[24] Smith, R. L., Shields, W. R., and Tabor, C. D., US AEC Report GAT–1711 Rev. 1 (1956).
[25] Rodden, C. J., (Ed.), Selected Measurement Methods for Plutonium and Uranium in the Nuclear Fuel Cycle, 2nd ed. U.S. Atomic Energy Commission (1972).
[26] Tilles, D., J. Geophys. Res. **66**, 3003–3013 (1961).

(Paper 79A6–870)

594-051 O - 76 - 5

JOURNAL OF RESEARCH of the National Bureau of Standards—A. Physics and Chemistry
Vol. 79A, No. 6, November–December 1975

Absolute Determination of the Electrochemical Equivalent and the Atomic Weight of Zinc I. Method, Apparatus, and Preliminary Experiments

George Marinenko

Institute for Materials Research, National Bureau of Standards, Washington, D.C. 20234

and

The American University, Washington, D.C. 20016

and

Robert T. Foley

The American University, Washington, D.C. 20016

(August 28, 1975)

The use of a specially designed coulometer and a high accuracy coulometric circuit resulted in the accurate measurement of the electrochemical equivalent and atomic weight of zinc. The experimental conditions to make possible the final precise and accurate measurements were established. These include a study of mechanical losses from the anode during the electrolysis and the corrosion of zinc in various media used in the determination. The effects of both of these sources of error may be controlled. Mechanical losses are minimized when an amalgamated electrode is used; corrosion, when an amalgamated electrode is used in an air free system. An electrolyte, 25 wt. percent NH_4Cl and 3 molal $ZnCl_2$, was used in these determinations. This report presents the account of research which was prerequisite to subsequent accurate determination of the electrochemical equivalent and the atomic weight of zinc.

Key words: Atomic weight; coulometry; electrochemical equivalent; zinc atomic weight.

1. Introduction

The 1967 Report of the International Commission on Atomic Weights states that today virtually all data upon which atomic weights can be based are furnished by mass spectrometric measurements of "absolute" isotopic composition [1].[1] This observation of the Commission can be viewed in two ways. The first view is that the "state-of-the-art" of mass spectrometry has attained a level of sophistication unmatched by other methods potentially useful for the determination of atomic weights. The second view is that scientists in other areas of accurate measurement lack the incentive to involve themselves in this exacting yet significant work. Perhaps both factors are responsible for the existing situation. In any case the state of affairs is not very desirable. Determination of the constants of nature should be performed by a variety of methods, since it is clear that each method will invariably have some (though they may be extremely small) systematic errors. Determination of physical constants by several independent methods will, at least in principle, avoid some of these errors.

Prior to this work the accepted value of the atomic weight of zinc was 65.37 ± 0.03 [1, 2]. The above value was based on combining weight ratios of $ZnCl_2$/2 Ag [3], $ZnCl_2$/2AgCl [3], $ZnBr_2$/Zn [4], and $ZnCl_2$/Zn [5]. Two mass spectrometric determinations of the isotopic abundances [6, 7] yielded a significantly different value for the atomic weight of zinc but since they were conducted without "absolute" calibration of the instruments the Commission recommended retaining the chemically determined value [1]. Zinc, which has five naturally occurring isotopes, presents a formidable problem for "absolute" calibration of mass spectrom-

[1] Figures in brackets indicate the literature references at the end of this paper.

eters. Five separate Zn isotopes of considerable isotopic purity (99.9 percent of better) would be required. Moreover, a high precision method would also be required for analysis of these isotope solutions and subsequent preparation of known, requisite isotope mixtures for calibration of mass spectrometers [8–15]. The largest number of isotopes handled in this manner thus far in the determination of atomic weights is four. This was done for chromium [14].

Thus, at the start of this investigation there existed a divergence in the reported values for the atomic weight of zinc. It was important that this divergence be resolved since for many of the other elements the uncertainties in the atomic weights are of the order of 0.001, or one order of magnitude less than that of zinc.

The suitability of electrochemical methods for the determination of atomic weights was implied in the original work of Faraday, and the explicit utilization of Faraday's laws for the determination of atomic weights was recognized very early in the development of quantitative electrochemistry. Thus, for example Laird and Hulett state [16]:

> *"Faraday's law, that a definite quantity of electricity is associated with one gram equivalent of any ion, is, as far as we know, strictly accurate, probably as accurate as the law of conservation of mass. There is evidence that not even as small a quantity of electricity as 10^{-16} coulomb passes from an electrolyte to and electrode without a corresponding chemical change taking place . . . "*

Using electrolytic deposition of Cd in series with a silver coulometer, Laird and Hulett were able to obtain precise Cd/Ag ratios, and by using the accepted value for the atomic weight of silver they calculated the atomic weight of cadmium. A similar approach was used by Gladstone and Hibbert earlier [17] for the determination of Zn/Ag and Zn/Cu ratios, and consequently, the atomic weight of zinc. Unfortunately, we now know that silver deposition coulometers and copper coulometers, though precise, are not accurate due to the variation of the amount of occluded mother liquor in the deposit. This aspect of silver deposition coulometers has been discussed by Hamer [18]. A more direct approach to the determination of the electrochemical equivalent is through the use of absolute current and time measurement, employed by Craig and coworkers [19] in the determination of the electrochemical equivalent of silver and the Faraday and by Marinenko and Taylor in the determination of electrochemical equivalents of benzoic acid and oxalic acid [20].

The difference between chemical values for the atomic weight of zinc (65.37) and the value obtained mass spectrometrically (65.39) is of the order of 0.03 percent. The atomic weight obtained by the electrochemical method was expected to have an uncertainty of 0.003 percent, one order of magnitude smaller than the existing uncertainty in the atomic weight of zinc. The significance of such an improvement in a constant of nature, as important as an atomic weight, is self-evident.

The earlier published paper [25] contains only a small fraction of data obtained in this research. This paper and the following [26] contain a complete account of the research conducted with the objective of determining accurately the electrochemical equivalent and the atomic weight of zinc.

This first paper describes the method, apparatus, and certain critical preliminary experiments which provided the basis for the determinations. The experimental study of the material treatment, electrode fabrication and handling, corrosion in air as well as in electrolyte solutions is described below.

2. Experimental Procedures

2.1. The Method

The method used involved the determination of the zinc dissolved anodically during the passage of a constant electrical current through the following electrochemical cell:

$$\mathrm{Zn(Hg)\,|\,ZnCl_2\ (3\ m.\ aq).\ NH_4Cl\ (25\ wt\ \%.\ aq)\,|\,Zn(Hg).}$$

The anodic reaction is

$$\mathrm{Zn(Hg) \rightarrow Zn^{++} + Hg + 2}e; \qquad (1)$$

and the accompanying cathodic reaction is simply the reverse of reaction (1):

$$\mathrm{Hg + Zn^{++} + 2}e \rightarrow \mathrm{Zn(Hg).} \qquad (2)$$

In such a cell the composition of electrolyte remains unaltered throughout the whole experiment.

The passage of two Faradays of charge through the cell dissolves 1 mole of zinc from the zinc amalgam anode and deposits it on the cathode. The coulometric circuit employed in this work insures the passage of charge through the cell with 0.0002 percent accuracy. The coulometer used in this work is described in detail in a later section. A weighed zinc amalgam anode is suspended in the coulometer. A mercury pool cathode is located at the bottom of the coulometer. A ground glass flat joint in the coulometer is provided for insertion of a porous membrane filter which is used in some experiments to establish the existence or the absence of any significant fall-off of the material from the anode in the course of its electrochemical dissolution. The electrolyte is deaerated and a nitrogen atmosphere is maintained in the coulometer throughout the experiment.

Zinc anodes are weighed by substitution on a 20 g-capacity microbalance. The uncertainty of the mass measurement process (standard deviation) is 3×10^{-6} g.

A constant current of known magnitude is passed through the coulometer for a precalculated period of time sufficient to produce a desired change in mass of the anode, approximately equal to the mass of a single weight in the calibrated set of weights. After termination of electrolysis, the zinc anode is carefully

removed from the coulometer, washed first in 0.1 molar NH_4Cl solution and then in hot distilled water, dried and reweighed. Appropriate corrections for the effects of buoyancy of air are applied. Thus the charge to mass ratio can be readily computed.

2.2. Coulometric Circuit

The work described here was performed by constant current coulometry. In coulometry the following parameters are measured: electric charge consumed in performing electrochemical conversion and mass of substance involved. Since

$$Q=\int_0^t i\,dt$$

and $i=$ constant, the integral reduces to

$$Q=it$$

Thus the measured electrical parameter, requiring accurate control, is current. In addition it is necessary to measure accurately the time in the course of which the electrical current flows through the coulometric electrolysis cell. The schematic diagram of the coulometric circuit is shown in figure 1.

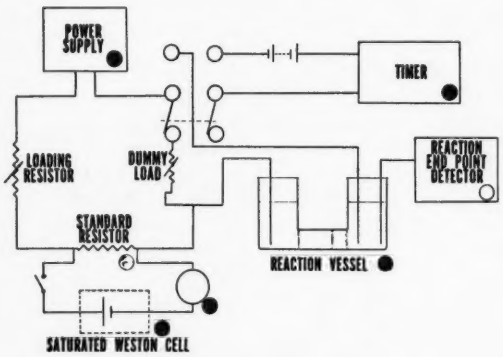

FIGURE 1. *The schematic diagram of the coulometric circuit.*

The circuit consists of a high precision constant current power supply, an accurate current comparison system, the necessary current stabilization resistors, the timing circuit and the coulometric reaction vessel, the electrolysis cell.

Power Supply. The instrument used in this work to power the coulometric circuit is a Princeton Applied Research regulated dc constant voltage and constant current power supply, Model TC–602CR.[2] In the constant current mode of operation its output can be varied from 0 to 2 A, provided the resistance of the external load (the coulometric circuit) does not exceed the value limited by the maximum voltage output capability of the power supply, namely 60 V. Thus the power supply can control accurately a constant current of 1 A with external loading up to 60 Ω.

The output current is selected by means of a five-place stepwise Kelvin-Verley divider with an additional continuously variable vernier slidewire, resulting in 0.0001 percent adjustable resolution in the output. The long-term stability of the output of the power supply (the constancy of current) is on the order of 0.001 percent per 8 h as determined by the manufacturer and verified experimentally in our laboratory. The load regulation (from no load to full load) and the line regulation (for 10% line voltage fluctuations) is 0.0001 percent. The ripple component (at any load) i.e., the combined effects of all ac components appearing in the output, is less than 50 μV rms. This, of course, means that it is highly desirable to operate the power supply into a load of such magnitude that virtually full capability of the power supply to generate a given value of the current is utilized.

For this reason, as is indicated on the circuit diagram, an auxiliary variable loading resistance is incorporated into the coulometric circuit.

To minimize the time of recovery of the power supply to the preselected current value when the coulometer switch is turned on, a second set of resistors simulating the resistance of the coulometer, is inserted into the circuit. It is labeled "dummy load" on the schematic circuit diagram. Thus, the power supply always operates into essentially the same load, with the exception of the time of flight of the coulometer switch at the start and at the end of the experiment. This switching time is on the order of 0.02–0.03 s.

Current comparator. The most commonly used method for accurate current measurement is a comparison method in which Ohm's law is utilized in its exact form. By Ohm's law

$$i=\frac{1}{R}V \qquad (10)$$

i.e., the current flowing in an electrical circuit is proportional to the applied voltage and $1/R$ is the proportionality constant. Thus, if one passes a current through an accurately calibrated resistor and measures accurately the voltage drop across that resistor one can readily compute the value of current. The most direct way of making an accurate current comparison is to make it of such magnitude that the iR drop across the standard resistor, through which this current flows, is virtually equal to the voltage of a standard cell (in our case a saturated Weston cell). The difference between the iR drop and the voltage of the standard cell is measured by means of a high input impedance null detector. The high impedance of the null detector is a prerequisite condition for such a measurement since otherwise appreciable current can flow in the comparator circuit at such times when an imbalance exists between the iR drop and the voltage of the stand-

[2] Certain commercial materials and equipment are identified in this paper in order to adequately specify the experimental procedure. In no case does such identification imply recommendation or endorsement by the National Bureau of Standards, nor does it imply that the material or equipment identified is necessarily the best available for the purpose.

ard cell. The passage of current through the standard cell is of course not permissible. If current is passed through the cell it becomes polarized and its emf departs from its equilibrium value. Following polarization, standard cells require long periods of time to recover to the equilibrium state and in fact permanent damage to the cells due to polarization is not uncommon [21].

For these experiments a Leeds and Northrup electronic d-c null detector model 9834 was used. Its input impedence is $4 \times 10^4 \Omega$. Thus if the imbalance between the iR drop across the standard resistor and the emf of the standard cell (~ 1.018 V) is 0.1 percent (10^{-3} V) the current in the comparator circuit will be $2.5 \cdot 10^{-8}$ A or 0.025 μA which is negligible. Furthermore, immediately after a mismatch between the iR drop and the standard cell voltage is noticed the output of the power supply is adjusted until a perfect balance is achieved (within 1 μV). The accurate value of current is computed from the calibration values of the standard resistor and the emf of the saturated standard Weston cell. National Bureau of Standards (NBS) type calibrated standard resistors were used in all experiments. Their resistance values are known to ± 0.0001 percent. Since the resistor wire in NBS standard resistors is manganin its temperature coefficient near 25 °C is about 0.0005 percent per °C. In order to insure accurate current measurement, standard resistors were kept in an oil bath, thermostated to better than 0.1 °C thus insuring accuracy in the resistance value of better than 0.0001 percent [22].

Saturated Weston cells have a much larger temperature coefficient (at 35 °C it is on the order of 0.005 % per °C). Consequently they were maintained in an air thermostat, the temperature of which was maintained constant near 35 °C within 0.01 °C, again insuring better than 0.0001 percent accuracy in the value of the emf of the standard cell [21]. Thus the value of the current in all experiments was known to better than 0.0001 percent.

Timer. Since the laboratory in which experiments were conducted has a 100 kHz standard frequency outlet, the accuracy of which is better than 1 part in 10^{12}, the simplest way to measure the time was to scale the frequency between the time that the current is diverted to flow through the coulometer and the time that it is turned off (diverted to flow through the dummy resistance). This provided 10^5 counts on the scaler per second, or the resolution of time interval to the nearest 10 μs.

Mass Measurement. A 20-gram capacity Mettler microbalance was used for all mass measurements. To make mass measurements of the highest accuracy substitution weighing must be performed. The standard deviation of the mass measurement operation, established over a number of years in this laboratory amounts to 3×10^{-6} g.

2.3. The Coulometer

The final design of the coulometer was achieved after many trial attempts with various designs. The coulometer (fig. 2) consists of four segments. The lower part is the cathode cup containing a ground glass flat surface to mate with the second part and a platinum contact sealed into the side. The original intent was to use the lower cup for the gravimetric determination of zinc, deposited cathodically into the mercury pool. Unfortunately, cathodic deposition and weighing of zinc for the purpose of determining the electrochemical equivalent was not sufficiently quantitative to produce significant results. One of the reasons is growth of zinc dendrites, which are difficult to handle, wash and weigh with a high degree of accuracy.

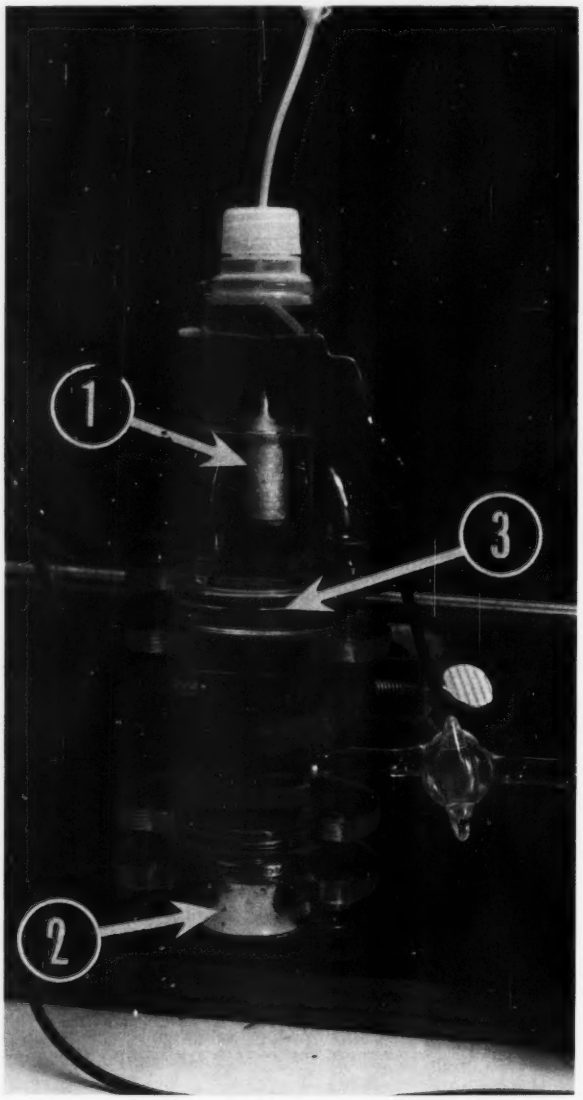

FIGURE 2. *Coulometer for the determination of the atomic weight of zinc.*

1 – zinc amalgam anode; 2 – mercury pool cathode; 3 – ground glass flat joint.

The second segment of the cell contains stopcock provisions in order to allow drainage of the electrolyte above that point. The upper surface of the second segment is the flat ground glass surface designed to mate with the third segment of the cell. This arrangement enables one to insert a previously weighed filter between the ground glass surfaces during assembling of coulometer. Filters are used to establish the existence or the absence of any material flaking from the anode.

The third segment contains provisions for a platinum hang wire upon which the zinc anode is suspended, making an electrical contact with the constant current circuitry.

Finally, the uppermost segment of the cell is a cut-down polyethylene cap with a friction fitted polyethylene tube insert. This tube enables deaeration of the electrolyte in the cell and subsequent passage of the high purity nitrogen over the electrolyte in order to reduce spontaneous corrosion of zinc.

In the upright design coulometer used in this work, a Millipore filter was inserted between the second and third segments of the cell. Thus the deposit could be accumulated directly upon the filter. By opening the stopcock in the second segment of the cell one could easily drain the electrolyte through the Millipore filter, wash it as many times as required, disassemble the cell, dry and reweigh the filter. Thus the amount of deposit on it could be determined.

Another advantage of the coulometer used in this work is that the path length of the current in the electrolyte is relatively short as compared with the coulometer of Craig and coworkers [19] and therefore the resistance of the cell is quite low (the resistance of the cell filled with electrolyte was about 10 Ω). This allows passage of relatively large currents (e.g., 1 A) without any appreciable heating of the cell and without the requirement of having a power supply with a large voltage output.

2.4. The Problem of Anodic Fall-Off

The Millipore filter incorporated in the final improved design of the coulometer was intended to cope with the problem of undissolved material falling from the zinc anode during the passage of current. This addition to the coulometer came about in the following way. The initial experiment involved the use of a pure zinc anode. No precautions were taken to keep the air out of the cell. The passage of 101 mA current through the cell for a sufficient period of time dissolved 5.274 mmol of zinc to produce a 345.6 mg change in the mass of the zinc anode (corrected to the mass in vacuum). It was noted at the time that a significant amount of particulate matter was flaking from the anode. The precipitate was collected and weighed. The weight of this deposit was 1.0 mg.

Using the value for the mass difference based only on the weight of anode before and after the experiment the computed atomic weight is 65.52. This value is much too high and can be explained reasonably well by the weight loss due to flaking of the material from the anode. If one applies the correction on the basis of the collected particulate material (1.0 mg) the change in mass of the anode becomes 344.6 mg and the corrected atomic weight is 65.33. This latter value is in closer agreement with the then recognized value (65.37).

It is not the numerical value obtained in this experiment but rather the observable flaking effect which is of significance. Since the amount of flaking is about 0.3 percent the anode material cannot be used in this form for accurate atomic weight determination. The experiment described above was repeated using a zinc anode amalgamated with high purity mercury. The apparent surface area of the electrode was 13 cm^2. Here again the coulometer was operated in the air atmosphere.

Seven experiments were performed using a current of 101 mA. The obtained data are summarized in table 1.

TABLE 1. *Anodic dissolution of the amalgamated zinc, (code 3)**

Experiment No.	Approximate change in the mass of the anode, g	Calculated* atomic weight of Zn
1	2.79	65.3951
2	3.29	65.3981
3	1.35	65.3957
4	2.62	65.3923
5	6.81	65.3937
6	2.52	65.3940
7	8.07	65.4032
Mean		65.3960
Standard deviation		0.0037
95% Confidence interval for the mean		0.0014

*No precautions were taken to exclude air from the cell, thus the results obtained here are biased by the amount proportional to the corrosion current in air saturated electrolyte. The area of the anode was ~ 13 cm^2.

The results of these experiments must be taken only as indicative and not definitive as far as the obtainable accuracy of the atomic weight of zinc is concerned. The experiments described later will in fact show that the presence of air in the electrolyte produces an undesirable effect as it increases the rate of spontaneous corrosion of zinc amalgam. Thus, the values obtained here are biased by the amount proportional to the corrosion current.

Under the experimental conditions used here no *visible* flaking of the material from the anode took place. The reproducibility of the results and the agreement of the computed value of the atomic weight with the accepted value were sufficient to warrant further serious effort to be made in improving the procedure and testing the accuracy of the results.

The absence of visible flaking does not necessarily prove that it does not take place. A more convincing proof of the nonexistence of flaking could be offered if the electrolyte were filtered after electrolysis and the amount of solid residue produced in the course of the electrolysis determined by weighing. This in fact was

done in the determination of the electrochemical equivalent of silver and the value of the Faraday by Craig and coworkers [19]. They utilized an anodic silver coulometer, similar in principle to the one employed in this work. The anodic coulometer was chosen in favor of the cathodic silver deposition coulometer because it obviates mother liquor occulsion errors. At the same time it requires collection and weighing of material which flakes off in the course of the dissolution of the silver anode. In the case of silver, flaking off is quite significant (but not as significant as in the case of unamalgamated zinc). Craig et al. [19] took great care in transferring the contents of the anode compartment into Pyrex filtering crucibles, filtering it and determining the weight of the sediment. This procedure is rather time consuming and requires a great deal of manipulative practice and skill.

It therefore seemed desirable to design a coulometer which would eliminate the need for material transfer. Since no visible flaking from the amalgamated zinc anode took place it was suspected that perhaps particle size in this case is extremely small. It would therefore be desirable to filter the anolyte through a high efficiency filter. Membrane filters with 0.8 μ pore size were used. Before the electrolyte was introduced into the coulometer it was filtered into a suction flask through the same type of a filter used in the coulometer. This was done to insure that no appreciable amount of solid could be introduced by the electrolyte. Therefore any increase in the mass of the filter in the coulometric cell must of necessity be attributed to the solid material flaking from the anode (located above the filter).

The lower part of the cell was filled with the electrolyte prior to the placement of the preweighed filter upon the ground glass surface. After the filter is satisfactorily seated upon the flat glass surface and adheres to the electrolyte beneath without any visible gas bubbles, the upper structure of the cell is put in place. The remaining part of the cell is then assembled, appropriately clamped, and the upper part filled with the electrolyte to the desired level.

Following the passage of the preselected amount of electric charge through the coulometer the electrolyte is drained through the stopcock. About 200 ml of 0.1 *M* NH_4Cl solution is used to wash the filter followed by about 400 ml of hot distilled water. The cell is then disassembled, the filter is dried at 50 °C in a drying oven for 1 h, set into a disiccator (in which humidity was maintained at 50 percent) for 4 h, then weighed.

In these experiments a second filter was placed in the cell, beneath the first one in a sandwich form. It served as a control filter. This was necessary because the mass of a filter varies from time to time depending on handling, extent of rinsing, etc. The use of a control filter minimizes the experiment-to-experiment variation.

The two filters used in the described experiments weighed approximately 0.70 g each. The data obtained in these experiments are given in table 2. In the experiments in which current was passed through the coulometer the mean change of the mass of zinc anodes per experiment was 4.17 g.

TABLE 2. *Filtration of electrolyte after anodic dissolution of Zn*

Experiment No.	Change in mass of Zn(Hg) anode oxidized at 500 mA*	Normalized change of mass (g) of top Millipore filter
1	—**	+ 0.000011
2	1g (5800 s)	− 0.000041
3	—**	− 0.000044
4	—**	− 0.000042
5	4g (23200 s)	+ 0.000049
6	—**	− 0.000156
7	2g (11600 s)	+ 0.000038
8	4g (23200 s)	− 0.000145
9	—**	+ 0.000070
10	4g (23200 s)	− 0.000008
11	10g (58000 s)	+ 0.000068
Mean.....	.....	− 0.000018

*The electrolysis time is given in parenthesis.
**No current was passed through the cell, i.e., a blank experiment.

The changes in the mass of the membrane filter, (Δm_f), are independent of the passage of charge and there appears to be no relationship between the mass of zinc dissolved and Δm_f. For example, in experiment 11 the mass of dissolved zinc is 10 g and $\Delta m_f = +68$ μg, which is almost the same as in experiment 9 ($\Delta m_f = +70$ μg), in which no coulometric dissolution of zinc was performed. The mean value of Δm_f per gram of zinc dissolved (based on experiments 2, 5, 7, 10, and 11) is 1.6 μg.

For the purpose of statistical evaluation of the results and for making the comparison between the blank experiments and the experiments in which coulometric dissolution of zinc was performed it is more useful to compute the mean value of the change of mass of the filter per experiment. The overall mean Δm_f per experiment including both the blank experiments and the coulometric experiments is -18 μg (table 2). For coulometric experiments only, the mean value of Δm_f is -7 μg per experiment. For experiments (1, 3, 4, 6, 9) the mean Δm_f is -32 μg per experiment.

The pooled standard deviation for the Δm_f per experiment on the basis of the two sets of data (the blank experiments and the coulometric experiments) is $s = 81$ μg. Using this value of s in conjunction with the 6 coulometric experiments the uncertainty in the mean change of mass of the filter per experiment is $s/\sqrt{n} = 38$ μg. On this basis the mean value of Δm_f does not produce a significant error.

Thus using the mean value of the mass of dissolved Zn (4.17 g) and assigning the above computed uncertainty to the change of mass of the filter (38 μg) one can safely conclude that within the limits of the uncertainty of the measurement the amalgamated zinc anodes undergo electrochemical dissolution without any detectable fall-off of material in the course of electrolysis. These data justified abandoning any further attempts to measure the material fall-off.

2.5. The Electrolyte

The electrolyte used in final experiments was 25 wt percent $NH_4Cl + 3$ molal $ZnCl_2$. The choice of these particular concentrations was not arbitrary. The optimum electrolyte for the coulometric experiments should meet several criteria: (a) it must nave low resistivity; (b) it must have sufficient concentration of Zn^{++} to satisfy cathodic demand for deposition of Zn^{++} at large currents (up to 1 ampere); (c) it must dissolve $ZnCl_2$ without any hydrolysis to $Zn(OH)_2$. Criterion (c) is satisfied by using NH_4Cl as the electrolyte. The presence of a large concentration of $ZnCl_2$ fulfills criterion (b). Finally the actual choice of the specific concentrations was dictated by the resistivity data [23]. Tabulated data [23] show that 25 wt percent NH_4Cl is virtually a saturated solution and its resistivity is the lowest; thus this is its optimum concentration.

2.6. Electrode Construction

Rectangular or cylindrical pieces of zinc were used for fabrication of electrodes. Cylindrical pieces were obtained either by transverse cutting of commercial zinc (which frequently comes in the shape of cylindrical rods) or the rods obtained during vacuum or air fusion of various zinc samples in Vycor tubes. Rectangular specimens were obtained by cutting originally large ingots of zinc on a mill with a tungsten carbide tool. After cutting, pieces of zinc were cleaned by etching in 1:1 Ultrex[3] HNO_3. An approximately 2-mm diameter hole was drilled in the upper surface of the electrode to a depth of about 5 mm, figure 3. A snugly fitting Cu wire coated on the end with a film of solder was inserted into the hole. A soldering gun was applied to the Cu wire unit the solder just softened and then removed quickly. This treatment provided for a reliable electrical contact between Cu and Zn. The upper surface of the electrode along with about ½ of the Cu wire lead were coated with epoxy cement and permitted to harden. The lower segment of the electrode was then cleaned again by partial immersion into 1:1 HNO_3. Subsequently the zinc surface was amalgamated with high purity Hg by immersion. The electrode was then suspended in a specially designated and coded spot of an electrode storage-box made of Lucite. Each electrode was cleaned in 0.1 *M* NH_4Cl and washed with hot distilled water just prior to its use in the experiment.

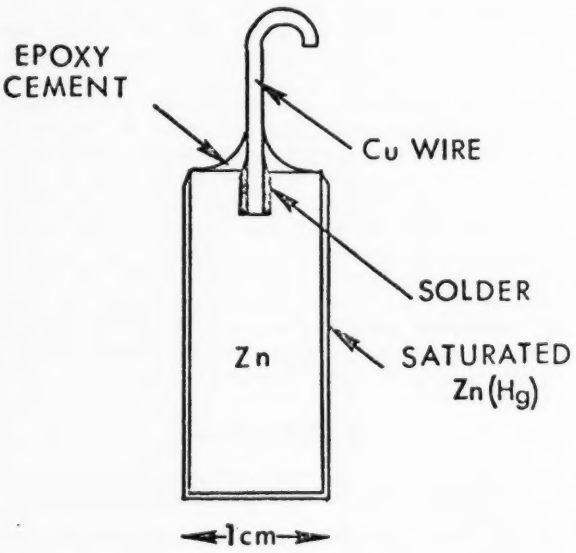

FIGURE 3. *Construction of Zn (Hg) anode.*

[3] Ultra-high purity material from J. T. Baker Chemical Co.

2.7. Stability of Zinc and Zinc Amalgam Anodes in Different Media

In order to conclude that the change in mass of the anode is caused by the passage of electric current one must first of all prove that the mass of the anode is in fact invariant when such current is not passed through the system. Or, one must establish the stability of anodes in the media to which they will be exposed and determine to what extent the observed changes will affect the finally determined value of the atomic weight of zinc.

Zinc and zinc amalgam anodes of the same geometric configuration as used in the final experiments were investigated for stability in different media. These media are those in which the electrodes will reside in the course of the final experiments: (1) 0.1 *M* NH_4Cl; (2) 25 wt percent $NH_4Cl + 3m$ $ZnCl_2$; (3) distilled water; (4) air.

Eight electrodes, 10 cm^2 in area, were fabricated in the same manner as the electrodes used in the final experiments. Four of these electrodes were amalgamated using dilute Ultrex HNO_3 and high purity mercury, rinsed in 0.1 *M* NH_4Cl and hot distilled water, dried in air for 15 min and then weighed. The remaining four electrodes were left nonamalgamated. One of each kind of electrode was immersed into NH_4Cl or $NH_4Cl + ZnCl_2$ solution or distilled water by suspending it on a support wire above a beaker containing the solution and left immersed for the desired period of time. Following the desired exposure time the electrodes were removed, washed in hot distilled water and reweighted in the manner described above. The electrodes suspended in air were first dipped into 0.1 *M* NH_4Cl solution then washed with hot distilled water, dried and weighted.

The rate of mass changes of Zn(Hg) and pure Zn electrodes during the exposure to the different media are shown in table 3.

The interpretation of these tabular data leads to several conclusions.

Firstly, in all media the rate of corrosion of Zn(Hg) electrodes is lower than that of pure Zn electrodes.

TABLE 3. *The rate of mass change of Zn(Hg) and Zn per unit area*

Medium	Rate of mass change per unit area $\mu g\ cm^{-2}\ h^{-1}$*	
	Zn(Hg)	Zn
NH_4Cl (0.1*M*)	−2.5	−7.7
NH_4Cl (25 wt percent) + 3 molal $ZnCl_2$	−1.7	−8.0
Distilled water	+1.6	+2.6

*The estimated uncertainty in these measurements is 0.5 $\mu g\ cm^{-2}\ h^{-1}$.

Secondly, the rate of corrosion of Zn(Hg) electrodes is lower in a NH_4Cl solution containing 3 molal $ZnCl_2$ than in a NH_4Cl solution alone. This can occur for two reasons: (a) the addition of Zn^{++} (the corrosion product) by the law of mass action decreases the driving force of the reaction; (b) corrosion of Zn(Hg) involving oxygen will be decreased, since the increase of the ionic strength of solution decreases the solubility of oxygen in aqueous solutions [24]. Hence, a decrease in the rate of corrosion results.

Thirdly, the rate of corrosion of nonamalgamated zinc remains virtually the same in the two electrolytes ranging from −7.7 in NH_4Cl solution to −8.0 $\mu g\ cm^{-2}\ h^{-1}$ in $NH_4Cl + ZnCl_2$ solution. On the other hand the rate of corrosion of amalgamated zinc is −2.5 and −1.7 $\mu g\ cm^{-2}\ h^{-1}$ in the above two solutions respectively. Thus, the lower solubility of oxygen in the solution of higher ionic strength has no effect on the rate of corrosion of nonamalgamated zinc. What is more important in this case is the slight decrease of pH due to hydrolysis of $ZnCl_2$, which in fact accelerates the rate of corrosion. The pH of the NH_4Cl solution was 4.70 while the pH of the 25 wt percent NH_4Cl + 3 molal $ZnCl_2$ was 3.72. From table 3 it is clear that in NH_4Cl and $NH_4Cl + ZnCl_2$ solutions the constancy of weight of Zn(Hg) electrodes is a factor of 3 to 4 greater than that of nonamalgamated electrodes. Using Faraday's law and taking the atomic weight of zinc as 65.4, the computed corrosion current density, J_{corr}, for amalgamated zinc in 25 wt percent $NH_4Cl + 3$ molal $ZnCl_2$ (the electrolyte which was selected for final experiments) is 1.3×10^{-3} mA cm^{-2}. It must be kept in mind, however, that this corrosion current is obtained with air-saturated solutions. When solutions are deaerated and an inert atmosphere is maintained above them a corresponding decrease of the corrosion current on the Zn(Hg) surface is observed.

The corrosion in NH_4Cl solution was measured because it was used as one of the wash solutions for the electrodes in the final experiments. In the course of 5–10 min of washing time no significant weight loss is encountered. Using a 10 cm^2 electrode as a typical example and assuming 15 min wash time in 0.1 *M* NH_4Cl solution the total anticipated weight loss will be about 6 μg.

Distilled water was tested for the same reason as the 0.1 *M* NH_4Cl solution. It is used for the final rinsing of electrodes. As one would expect, both Zn and Zn(Hg) electrodes gain weight upon immersion into distilled water due to formation of water insoluble hydrated ZnO. The rate of formation of ZnO is somewhat greater (by about a factor of 2) on a pure Zn surface than on Zn(Hg).

On examining the weight change data for the electrodes stored in air it became quite apparent that within the experimental error the weight loss is not a function of exposure time. Since the weight loss itself results from the dissolution of ZnO, formed on the electrode surface during exposure to air, one must conclude that the oxide film thickness on electrodes, stored in air, reaches a constant value (parabolic behavior). The limiting value (after 264 h of exposure) is 16.0 $\mu g\ cm^{-2}$. A 28-h exposure produces 10.9 $\mu g\ cm^{-2}$ of ZnO, indicating that the limiting value is approached asymptotically. Final experiments in which the weighing operation required approximately 2 h substantiated this value. The amount of ZnO formed in the course of weighing of electrodes in the final experiments was found to be 9.1 $\mu g\ cm^{-2}$.

It is interesting to note that in distilled water the formation of hydrated ZnO on Zn(Hg) (the weight gain) is much greater than in air. The decrease in the rate of formation of ZnO with time, however, is perceptible.

3. Conclusions

In principle, an electrochemical method should provide the requisite accuracy for the determination of the atomic weight of such elements as zinc, i.e., elements whose anodic behavior is such that they may be incorporated into a coulometric cell. Such operations as the accurate measurement of current, time, and mass pose no problem. Two practical problems, however, the fall-off of anode material during the passage of current, and the corrosion of the zinc anode required investigation in some depth. The incorporation of a membrane filter into the coulometric cell made possible measurements that show that anode fall-off is negligible during a typical coulometric experiment when an amalgamated zinc electrode is used. The corrosion of the amalgamated zinc anode is primarily a function of the concentration of air in the electrolyte. Deaeration of the electrolyte reduces this corrosion effect below the level of significance in the conducted coulometric experiments. This study paved the way for subsequent accurate determination of the electrochemical equivalent and the atomic weight of zinc, as described in the companion paper [26].

4. References

[1] International Commission on Atomic Weights, Comptes Rendus XXIV IUPAC Conference, Prague, 4 to 10 Sept. 1967, pp. 130–141.

[2] Cameron, E. A., and Wichers, E., J. Am. Chem. Soc., **84**, 4175 (1962).

[3] Hönigschmid, O., and von Mack, M., Z. anorg. und Allgem. Chem., **246**, 363 (1941).

[4] Baxter, G. P., and Grose, M. R., J. Am. Chem. Soc., **38**, 868 (1916).

[5] Baxter, G. P., and Hodges, J. H., J. Am. Chem. Soc., **43**, 1242 (1921).

[6] Leland, W. T., and Nier, A. O., Phys. Rev., **73**, 1206 (1948).
[7] Hess, D. C., Inghram, M. G., and Hayden, R. J., Phys. Rev., **74**, 1531 (1948).
[8] Shields, W. R., Craig, D. N., and Dibeler, V. H., J. Am. Chem. Soc., **82**, 5033 (1960).
[9] Shields, W. R., Garner, E. L., and Dibeler, V. H., J. Res. Nat. Bur. Stand. (U.S.) **66A** (Phys. and Chem.), No. 1, 1–3 (Jan.–Feb. 1962).
[10] Shields, W. R., Murphy, T. J., Garner, E. L., and Dibeler, V. H., J. Am. Chem. Soc., **84**, 1519 (1962).
[11] Shields, W. R., Murphy, T. J., and Garner, E. L., J. Res. Nat. Bur. Stand. (U.S.), **68A** (Phys. and Chem.), No. 6, 589–592 (Nov.–Dec. 1964).
[12] Catanzaro, E. J., Murphy, T. J., Garner, E. L., and Shields, W. R., J. Res. Nat. Bur. Stand. (U.S.), **68A** (Phys. and Chem.), No. 6, 593–599 (Nov.–Dec. 1964).
[13] Shields, W. R., Goldich, S. S., Garner, E. L., and Murphy, T. J., J. Geophys. Res., **70**, 479 (1965).
[14] Shields, W. R., Murphy, T. J., Catanzaro, E. J., and Garner, E. L., J. Res. Nat. Bur. Stand. (U.S.), **70A** (Phys. and Chem.), No. 2, 193–197 (Mar.–Apr. 1966).
[15] Catanzaro, E. J., Murphy, T. J., Garner, E. L., and Shields, W. R., J. Res. Nat. Bur. Stand. (U.S.), **70A** (Phys. and Chem.), No. 6, 453–458 (Nov.–Dec. 1966).
[16] Laird, J. S., and Hulett, G. A., Trans. Am. Electrochem. Soc., **22**, 385 (1913).
[17] Gladstone, J. H., and Hibbert, W., J. Chem. Soc., **55**, 443 (1889).
[18] Hamer, W. J., J. Res. Nat. Bur. Stand. (U.S.), **72A** (Phys. and Chem.), No. 4, 435–439 (July–Aug. 1968).
[19] Craig, D. N., Hoffman, J. I., Law, C. A., and Hamer, W. J., J. Res. Nat. Bur. Stand. (U.S.), **64A** (Phys. and Chem.), No. 5, 381–402 (Sept.–Oct. 1960).
[20] Marinenko, G., and Taylor, J. K., Anal. Chem., **40**, 1645 (1968).
[21] Hamer, W. J., Standard Cells. Their Construction, Maintenance, and Characteristics. Nat. Bur. Stand. (U.S.), Monogr. **84**, 42 pages (June 1968).
[22] Thomas, J. L., Precision Resistors and Their Measurement, Nat. Bur. Stand. (U.S.), Circ. **470**, 35 pages (Oct. 1948).
[23] Hodyman, C. D., and Holmes, H. N., eds., Handbook of Chemistry and Physics, Chemical Rubber Publishing Co., Cleveland, Ohio, 1943, p. 1867.
[24] Mancy, K. H., and Jaffe, T., Analysis of Dissolved Oxygen in Natural and Waste Waters, U.S. Department Health, Education and Welfare, Cincinnati, Ohio, 1966.
[25] Marinenko, G., and Foley, R. T., J. Res. Nat. Bur. Stand. (U.S.), **75A** (Phys. and Chem.), No. 6, 561–564 (Nov.–Dec. 1971).
[26] Marinenko, G., and Foley, R. T., J. Res. Nat. Bur. Stand. (U.S.), **79A** (Phys. and Chem.), No. 6, 745–757 (Nov.–Dec. 1975).

(Paper 70A6–871)

JOURNAL OF RESEARCH of the National Bureau of Standards—A. Physics and Chemistry
Vol. 79A, No. 6, November–December 1975

Absolute Determination of the Electrochemical Equivalent and the Atomic Weight of Zinc II. Final Determination

George Marinenko

Institute for Materials Research, National Bureau of Standards, Washington, D.C. 20234

and

The American University, Washington, D.C. 20016

and

Robert T. Foley

The American University, Washington, D.C. 20016

(August 28, 1975)

A new, successful approach to the determination of atomic weights of suitable elements has been demonstrated in this research. An absolute constant-current coulometric method was employed for the determination of the electrochemical equivalent and the atomic weight of zinc. The effects of possible sources of systematic error were investigated and appropriate corrections applied. The newly determined values of the two constants are 0.3387958 mg C^{-1} and 65.3771 respectively. The uncertainty in the atomic weight of zinc was reduced by more than an order of magnitude. The publication of partial data resulted in the revision of the value of the atomic weight of zinc by the International Union of Pure and Applied Chemistry.

Key words: Atomic weight; coulometry; electrochemical equivalent; zinc atomic weight.

1. Introduction

The nature of the problem of determining the electrochemical equivalent and the atomic weight of zinc and the general outline of the approach taken to achieve the objective have been reported in Part I of this publication [1].[1] The present paper includes the final measurements performed under what were considered to be optimum conditions as well as the conclusions drawn from these results.

In brief the research entailed accurate determination of the electrochemical equivalent of zinc by oxidizing zinc from the Zn^0 to the Zn^{++} state and measuring the electrical charge associated with a given mass change of the zinc amalgam anode. The number of moles of zinc dissolved was computed from the magnitudes of the electrolysis current and the time, employing Faraday's law. Partial results of such an approach have already been published [16].

Perhaps the most significant part of any determination of a constant of nature is in assessing the inaccuracy of the determined value. In the case of ordinary analytical determinations of major constitutents the accuracy of the analysis at a 0.1 percent level can be proven rather readily through the use of chemical standards. Clearly, for the determination of a physical constant no such standard exists. As a result one must resort to some other means of testing the accuracy. One method of testing the accuracy of the determined physical constant is to vary the experimental parameters over a wide range, preferably more than one order of magnitude, and determine whether or not this variation of parameters has any effect on the determined value. In the case of the determination of the electrochemical equivalent of Zn the following parameters were varied and their effects were investigated: the absolute value of the current, the mass of dissolved zinc, the charge passed through the coulometer, the area of the electrode, the current density, the electrolysis time, the origin of the material, the purity of the material, the nature of the pretreatment of the

[1] Figures in brackets indicate the literature references at the end of this paper.

material (such as vacuum fusion or fusion in air). Variation of additional parameters, such as experiment sequence, arose naturally out of unavoidable lapses of time between sequential operations.

1.1. Materials

To evaluate the magnitude of the effects of the material source, its purity and treatment on the electrochemical equivalent of zinc, determined by the anodic dissolution of zinc metal from the saturated zinc amalgam, a number of materials from different sources were used. The following identifies each material by its code as used in the data table and, on the basis of the available data, gives as complete a description of each as possible.

High purity zinc (*code 4*). This is a high purity standard research material which is issued by the National Bureau of Standards as SRM 682. The material was prepared from a special lot of high-grade electrolytic zinc, purified by vacuum distillation, zone-refining and degasification.

The overall assessment of impurities (NBS certificate) indicates that this material is 99.9999 percent Zn. This clearly does not apply to the surface of the material, since the exposure of Zn to air leads immediately to oxide formation. This aspect will be discussed below.

In preparation of the electrodes the material was cut on a mill using a tungsten carbide tool.

Intermediate purity zinc (*code 6*). The National Bureau of Standards issues this material as SRM 683. This material was prepared from a high grade electrolytic zinc in a manner similar to that for high purity zinc (code 4).

The certificate of analysis of this material is available from the National Bureau of Standards. The sum of all other elements which were detected is less than 30 ppm. On the basis of impurity analyses the purity of this material is 99.997 percent Zn. The handling of the material and electrode preparation were the same as for material code 4.

Intermediate purity zinc (*code 105*). This is essentially the same material as material code 6 except that it is in pellet form (SRM 728). It was fused in Vycor[2] tubes into rod shaped electrodes. Fusion was conducted in vacuo. Estimated starting purity of the material on the basis of impurity analyses is 99.997 percent.

Intermediate purity zinc (*code 205*). With the exception of fusion, which was conducted in air, this material is the same as code 105 material.

Melting point standard zinc (*code 3*). This material was produced by the New Jersey Zinc Company, Palmerton, Pennsylvania and issued by the National Bureau of Standards as SRM 43g. It is in the form of rods which were cut directly into appropriate size segments for electrode fabrication.

Melting point standard zinc (*code 107*). This is one of the first zinc samples issued by NBS. The date of issue of this material is unspecified. The certificate is signed by the late NBS Director S. W. Stratton, which would date it back to 1923 or before. It was vacuum fused prior to electrode fabrication.

Commercial zinc (*code 2*). On the basis of impurity data for this material (Fisher Scientific Certified ACS grade zinc lot No. 781161) it is estimated to be 99.99 percent pure. The reported impurity content includes 0.003 percent Fe and 0.005 percent Pb. The rod-shaped material was cut and fabricated directly into electrodes.

Commercial zinc (*code 102*). This is the same material as described under code 2 but melted under vacuum for degassing and then used in electrode fabrication.

Commercial zinc (*code 1*). This material is sold by Baker and Adamson in the shape of cylindrical rods. The assay indicated by the distributor is 99.9 percent. The material contains less than 0.01 percent Fe and less than 0.01 percent Pb. It was also used in its original form for fabrication of electrodes.

Commercial zinc (*code 101*). This is the same material as described under code 1 but degassed under vacuum, similarly to material 102.

Zincs from other worldwide sources. A word of caution seems appropriate here. The origin of manufactured zinc does not necessarily prove that local zinc ores were exclusively used in each case. However, sampling from several worldwide sources is definitely shown. Materials coded 109, 110, and 111 are commercial grade zincs produced in Peru, Yugoslavia, and Italy respectively. They were also vacuum fused. Material 108 was obtained from the Electrolytic Zinc Company of Australasia Ltd. The manufacturer's evaluation of its purity is 99.995 percent. It was also vacuum fused.

Chemicals. All the reagents used were of the highest commercially obtainable purity. The mercury used in all experiments was a triple distilled material produced by the Bethlehem Apparatus Company, Inc. On the basis of the weighable residue test it contains impurities at the 1 part in 10 million (0.00001 percent by weight) level.

1.2. Procedure

The fabricated and amalgamated electrodes were washed in 0.1 *M* NH_4Cl, hot distilled water, air dried and weighed on a 20-g capacity Mettler microbalance. As the anode was readied for the experiment, the coulometer was filled with 25 wt percent NH_4Cl + 3 molal $ZnCl_2$ and deaerated by purging with water pumped nitrogen. Purging was performed by lowering the polyethylene tube, mounted in the cell top, into the electrolyte and permitting nitrogen to flow through it.

Prior to delivery into the coulometer the electrolyte was stored in a scrubbing tower over saturated zinc amalgam. Nitrogen, presaturated with water vapor by passage through the solution of the same composition

[2] A commercial product and company names are identified in this paper, in order to adequately specify the experimental procedure. In no case does such identification imply recommendation or endorsement by the National Bureau of Standards, nor does it imply that such a product is necessarily the best available for the purpose.

as the electrolyte, was continuously flowing through the stock electrolyte solution, stored in the tower. Thus, even before delivery into the coulometer the electrolyte was deaerated. The storage of the electrolyte over the saturated zinc amalgam was chosen to remove any impurities which are more easily reducible than zinc.[3]

After the Zn(Hg) anode had been weighed accurately it was suspended in the coulometer on the platinum support wire. The wire, in turn, was connected to the anode lead of the coulometric circuit. The upper surface of the suspended electrode, where epoxy resin was used to seal the suspension lead, was always above the solution-atmosphere interface. The area of the electrode cited in the data tables is that part of the apparent geometric area of the anode which was submerged into the electrolyte. Following the placement of the electrode into the coulometer the cell top was replaced, the polyethylene tube carrying the nitrogen pulled up so that the nitrogen could flow over the solution and the coulometer-timer switch thrown into the "on" position. After the expiration of the desired time interval the coulometer switch was turned off, the electrode removed, washed and dried and reweighed by the substitution method, using calibrated standard weights. The mass difference was always compensated by the standard weights within 10 mg. Differences smaller than 10 mg were observed on the optical scale of the balance. On the basis of the densities of air, Zn, and the materials from which the standard weights are fabricated (1–20 g stainless steel; 50–500 mg Ta; 1–20 mg Al) corrections were applied to the observed weight loss of the anode, converting it to the mass in vacuum. The amount of charge passed through the coulometer was computed from the values of the time interval of electrolysis (measured with an accuracy of 10 μs or 0.0001 percent whichever is greater) and the magnitude of the current, based on the values of the standard resistor employed and the emf of the saturated Weston cell.

2. Measurements

Nine sets of measurements were performed; the data for all nine sets, arranged according to the ordinal number of the experiment and the set number, are given in table 1. The data assembled in this table includes only the measurments on degassed materials. Column 4 of table 1 gives only an approximate current value and column 5 an approximate electrolysis time for correlation purposes. Accurately measured values of these parameters for each experiment were used in the computation of the charge, shown in column 7 of the same table. The electrode area (column 6) is an estimate of the apparent geometric area of the anode, immersed in the electrolyte during the electrolysis. The mass change of Zn(Hg) anodes (mass in vacuum) is presented in column 8.

The experiments with unprocessed material (no vacuum fusion) and material fused in air were intentionally incorporated and performed within the same experimental scheme as the experiments with degassed materials to make them equivalent, as much as possible. The data from these experiments, with materials containing dissolved gases, however, were extracted along with their ordinal numbers, compiled into a separate table (table 2) and processed as a separate entity, for reasons which will be discussed later.

Out of 150 final experiments, four (experiment numbers 58, 63, 99, 104) differed so far from the mean value that they were excluded from the data treatment as outliers according to Grubbs [2]. The choice of experiments was such as to shed some light on the possible errors which could be encountered. First of all, experiments designated as Set 8 (experiment numbers 139–150) were conducted to investigate the effect of material origin on the electrochemical equivalent of zinc. Secondly, six different levels of electrolysis current were used (including zero current as one level) covering six orders of magnitude from 0 to 1.0 A, although for the final calculation of the electrochemical equivalent, only three current levels are used in essence, viz., 0.1, 0.5, and 1.0 A. The electrolysis times required to improve precision of data at lower current levels are obviously prohibitive, and consequently only a few data points were obtained in this region. Thirdly, the electrolysis time ranged from 0 to 79000 s, again covering a range of six orders of magnitude. The electrode area was varied from 0.5 to 10 cm^2. The charge, passed through the cell, ranged from 0 to 29500 C. The mass of dissolved zinc ranged from a few micrograms to 10 g—a six orders of magnitude range. Material purity ranged from 99.9999 to 99.9 percent Zn. Finally, degassed materials, unprocessed materials, and air-fused materials were incorporated into the experimental scheme.

3. Treatment of Data

The simplest way of treating the electrochemical equivalent data is to assume a linear equation of the following form

$$W = kQ \tag{1}$$

where W is the mass difference in the electrode before and after electrolysis (mg) and Q is the charge passed through the coulometer (coulombs). Clearly the slope of such a plot, k, is the electrochemical equivalent in mg C^{-1}.

W and Q are measured experimental quantities which determine the value of k. The method of least squares was employed, using the OMNITAB FIT

[3] It is quite clear that if Cu^{++}, for example, were present in the electrolyte it would spontaneously undergo the following reaction in the coulometer

$$Zn(Hg) + Cu^{++} \rightarrow Zn^{++} + Cu\,(Hg)$$

thus causing an error in the mass of Zn(Hg) anode equal to

$$\text{wt percent Cu} \times \frac{\text{At wt Zn}}{\text{At wt Cu}}.$$

The removal of such impurities from the electrolyte prior to the delivery into the coulometer, by the sacrificial use of Zn (Hg), eliminates this source of error.

TABLE 1. *Final data on the determination of the electrochemical equivalent of zinc with degassed materials*

Exp. No.	Set No.	Material code	Current A	Electrolysis time, s	Electrode area, cm^2	Charge C	Mass of dissolved Zn, g
16	0	4	0.5	1160	1.5	590.382	0.200030
17	0	4	.5	2320	1.5	1180.743	.400023
18	0	105	.5	5800	4	2951.781	1.000048
20	0	101	.5	5800	7	2951.830	1.000196
21	0	101	0.5	5800	5	2951.800	1.000213
22	0	101	.5	290	5	147.615	0.050067
28	0	105	.5	116	5	59.066	.020087
30	0	4	.5	116	0.5	59.082	.019969
32	0	105	0.5	580	5	295.179	0.099982
36	1	4	.5	580	2	295.200	.100087
37	1	4	.5	580	1	295.195	.100098
38	1	4	.5	580	2	295.134	.100045
39	1	4	0.5	1160	2	590.303	0.200089
40	1	4	.5	58	2	29.564	.010059
41	1	4	.5	5800	2	2951.845	1.000064
42	1	4	.5	6	2	2.952	0.000942
43	1	6	0.5	5800	2	2951.845	1.000193
44	1	9	.5	29	2	14.784	0.005030
45	1	4	.5	2900	2	1475.913	.500031
46	1	4	.5	12	2	5.898	.001922
47	1	6	0.5	4060	2	2066.302	0.700096
48	1	4	.5	11600	2	5903.599	2.000038
49	1	4	.5	1450	2	738.010	0.250126
50	1	6	.5	290	2	147.564	.050010
51	1	4	0.5	29	2	14.790	0.005041
52	1	4	.5	29	2	14.830	.005026
53	2	4	1.0	10	2	10.308	.003523
54	2	4	1.0	2900	2	2951.791	1.000068
55	2	6	1.0	7250	2	7379.408	2.500127
56	2	4	1.0	290	2	295.143	0.099934
57	2	4	1.0	290	2	296.109	.100347
59	2	6	1.0	3	2	3.054	.001095
62	3	6	1.0	11600	4	11806.958	4.000194
64	3	4	1.0	2900	2	2951.767	0.999974
65	3	102	1.0	2900	4	2951.798	1.000076
66	3	102	1.0	5800	7	5903.484	1.999961
67	3	102	1.0	10150	7	10331.044	3.500364
68	3	107	1.0	5800	7	5903.474	2.000184
69	3	107	1.0	14500	7	14758.654	5.000353
70	3	107	1.0	30	3	30.539	0.010552
71	3	101	1.0	5800	7	5903.570	2.000219
72	3	4	1.0	30	2	30.513	0.010325
73	3	107	1.0	31	3	31.403	.010688
74	3	107	1.0	30	5	30.352	0.010301
75	3	4	1.0	30	2	30.759	.010296
76	3	101	1.0	17400	8	17710.343	6.000210
77	3	4	1.0	290	2	295.162	0.100018
78	3	107	1.0	290	5	295.213	0.100054
79	3	101	1.0	1450	8	1475.930	.500107
80	3	4	1.0	145	2	147.586	.050021
81	4	101	0.1	5800	5	590.324	.200049
82	4	107	0.1	5800	7	590.331	0.200039
83	4	4	.1	2900	1.5	295.162	.099965
84	4	101	.1	*1800	5	0.050	.000078
85	4	107	.1	58000	7	5900.507	1.998978

TABLE 1. *Final data on the determination of the electrochemical equivalent of zinc with degassed materials*—Continued

Exp. No.	Set No.	Material code	Current A	Electrolysis time, s	Electrode area, cm^2	Charge C	Mass of dissolved Zn, g
86	4	4	0.1	5800	1	592.898	0.200861
87	4	101	.1	18700	5	1903.308	.644818
88	4	4	.1	100	1	10.201	.003482
89	4	6	.1	35000	5	3541.969	1.200063
90	4	101	0.1	*3600	5	1.017	0.000393
91	4	4	.1	*4500	1	1.026	.000293
92	4	101	.1	*16900	5	1.022	.000387
93	4	4	.1	*69300	1	1.023	.000373
94	4	4	0.1	*3600	1	1.013	0.000315
95	4	101	.1	*6300	5	1.026	.000353
96	4	101	.1	*52200	5	1.023	.000432
97	4	4	.1	*1800	5	1.022	.000411
98	5	101	0.0	7200	6	0.0	0.000036
100	5	4	.0	1800	2	.0	.000028
101	5	107	.0	3900	6	.0	.000015
102	5	101	.0	1800	6	.0	.000016
103	5	4	0.0	19800	9	0.0	0.000118
105	5	107	.0	2700	6	.0	.000135
106	5	101	.0	5700	6	.0	.000153
107	5	4	.0	12000	9	.0	.000089
108	5	4	0.0	2700	9	0.0	0.000054
109	5	4	.0	45900	1	.0	.000092
110	5	4	.0	1800	7	.0	.000044
111	5	2	.0	4800	1	.0	.000027
112	5	4	0.0	4500	10	0.0	0.000079
113	5	4	.0	19500	10	.0	.000113
114	5	4	.0	12600	10	.0	.000067
115	5	4	.0	18000	2	.0	.000173
116	5	4	0.0	54000	9	0.0	0.000062
117	5	4	.0	79200	9	.0	.000157
118	5	4	.0	0	5	.0	.000038
119	5	4	.0	0	5	.0	.000107
120	5	4	0.0	0	2	0.0	0.000019
121	5	4	.0	0	2	.0	.000004
122	5	101	.0	0	7	.0	.000102
123	5	101	.0	0	7	.0	.000079
124	5	6	0.0	0	5	0.0	0.000058
125	5	2	.0	0	4	.0	.000017
126	6	4	.01	1000	9	10.1775	.003551
127	6	4	.01	1000	2	10.1776	.003558
128	6	107	0.01	5000	6	50.8878	0.017314
129	6	101	.01	*4500	5	40.7102	.013873
130	6	4	.01	6500	2	66.1539	.022518
131	6	4	.01	43764	9	445.4066	.150919
132	6	107	0.01	1650	5	16.7932	0.005742
133	6	107	.01	4500	8	45.7987	.015604
134	6	107	.01	13500	5	137.3959	.046566
135	7	101	.0001	8430	8	0.8430	.000271
136	7	4	0.0001	19500	2	1.9449	0.000700
137	7	101	.0001	14000	10	1.4000	.000555
138	7	4	.0001	60100	10	6.0100	.002269
139	8	4	.5	11600	10	5903.631	2.000151
140	8	4	0.5	23200	10	11807.189	4.000181
141	8	4	.5	29000	10	14758.990	5.000361
142	8	108	.5	53200	10	27075.126	9.173009
143	8	108	.5	11600	10	5903.587	2.000192

594-051 O - 76 - 6

TABLE 1. *Final data on the determination of the electrochemical equivalent of zinc with degassed materials*—Continued

Exp. No.	Set No.	Material code	Current A	Electrolysis time, s	Electrode area, cm^2	Charge C	Mass of dissolved Zn, g
144	8	109	0.5	11600	8	5903.596	2.000202
145	8	109	.5	11600	8	5903.590	2.000132
146	8	110	.5	11600	8	5903.631	2.000135
147	8	110	.5	11600	8	5903.595	2.000092
148	8	111	0.5	11600	6	5903.615	2.000178
149	8	111	.5	11600	6	5903.658	2.000189
150	8	4	.5	58000	10	29517.796	10.000693

*In these experiments electrolysis time is the total time elapsed between the immersion of the electrode into electrolyte and its removal from the coulometer ($t = t^{I} + t^{II}$). Part of this elapsed time (t^{I}) was under condition $i=0$, while the remainder of time $\left(\frac{Q}{i} = t^{II}\right)$ under the condition when $i>0$. This latter current is indicated in column 4. These values were not included in the least squares fitting of the individual sets of data.

TABLE 2. *Final data on the determination of the electrochemical equivalent of zinc with materials not subjected to vacuum fusion*

Exp. No.	Set No.	Material code	Current A	Electrolysis time, s	Electrode area, cm^2	Charge C	Mass of dissolved Zn, g
1	−1	1	0.5	11600	4	5903.604	2.000357
2	−1	1	.5	11700	8	5954.507	2.017550
3	−1	1	.5	41500	8	21120.554	7.156331
4	−1	2	.5	5750	3	2926.352	0.991514
5	−1	2	1.0	5800	3	5903.488	2.000106
6	−1	2	1.0	11600	15	11806.968	4.000604
7	0	2	0.5	11600	10	5903.608	2.000179
8	0	1	.5	11600	4	5903.615	2.000363
9	0	1	0.5	17400	8	8855.445	3.000217
10	0	3	.5	40600	10	20662.469	7.001076
11	0	2	.5	11600	3	5903.629	2.000290
12	0	2	.5	5800	2	2951.827	1.000226
13	0	1	0.5	57990	21	29512.774	9.999688
14	0	3	.5	17400	16	8855.369	3.000898
15	0	3	.5	11600	3	5903.568	2.000192
19	0	2	.5	1160	2	590.405	0.200099
23	0	2	0.5	1160	2	590.369	0.200075
24	0	205	.5	5800	3	2951.754	1.000296
25	0	3	.5	1160	2	590.379	0.199828
26	0	2	.5	116	3	59.026	.019914
27	0	3	0.5	116	3	58.990	0.020001
29	0	205	.5	8700	3	4427.722	1.500478
31	0	2	.5	580	3	295.154	0.099989
33	0	3	.5	580	3	295.185	.100011
34	0	3	.5	17400	7	8855.384	3.000889
35	0	3	.5	15000	7	7379.436	2.500424
60	3	2	1.0	1450	1	1475.945	0.500156
61	3	1	1.0	2900	7	2951.747	1.000334

program [3] and NBS UNIVAC 1108 computer facility. It seemed reasonable, however, to fit the data to the equation of a more general form

$$W = k_1 Q + k_2. \qquad (2)$$

If k_2 in eq (2) has a value different from zero, a process or processes other than the passage of the measured charge must be responsible for the mass change of the anode. It was known, from the preliminary studies discussed earlier [1], that two processes occur

on the zinc surface immersed in the electrolyte: (1) zinc oxide formed on Zn(Hg) between the time that the electrode is cleaned and the time it is immersed into the coulometer (i.e., during drying and weighing period) dissolves; (2) zinc metal corrodes spontaneously. Therefore, having found a statistically significant intercept, k_2, in eq (2), it appeared desirable to reconsider the data treatment and introduce the necessary parameters into the equation to make it describe the behavior of this system as completely as possible in terms of these physically significant parameters rather than combining their average effect into a single empirical constant, k_2.

The primary parameter which determines the weight loss of the anode is, of course, the amount of charge, Q, passed through the coulometer. Thus k_1Q should be the first term in the new modified equation. The weight loss of anode due to the dissolution of ZnO will obviously be proportional to the surface area of the electrode, a, if one hypothesizes that the zinc amalgam surface is covered relatively uniformly with ZnO. Thus k_2a should be another term in the equation. In the spontaneous corrosion of Zn(Hg) both the area of the electrode, a, as well as the time of electrolysis, t, play an important role. Thus weight loss due to corrosion should be represented by a variable of these two coupled parameters.

A number of model equations were tested to establish the most accurate representation of the experimental data. Some representative test equations along with the computed fitting coefficients are shown in table 3.

TABLE 3. *Test equations for electrochemical oxidation of* Zn

(1) $W = k_1Q$	$k_1 = 0.33880104 + 0.00000131$
(2) $W = k_1Q + k_2a$	$k_1 = 0.33879579 \pm 0.00000129$ $k_2 = 0.0091 \pm 0.0012$
(3) $W = k_1Q + k_2a + k_3t$	$k_1 = 0.33879539 \pm 0.00000133$ $k_2 = 0.0084 \pm 0.0013$ $k_3 = (4.67 \pm 4.02) \times 10^{-10}$
(4) $W = k_1Q + k_2a + k_4(at)$	$k_1 = 0.33879540 \pm 0.00000137$ $k_2 = 0.0085 \pm 0.0014$ $k_4 = (-4.62 \pm 5.50) \times 10^{-11}$
(5) $W = k_1Q + k_2a + k_5J$	$k_1 = 0.33879586 \pm 0.00000129$ $k_2 = 0.0093 \pm 0.0012$ $k_5 = -0.0165 \pm 0.0270$

W mass of Zn dissolved, mg (milligrams).
Q charge passed, C (coulombs).
a apparent surface area of Zn anode, cm^2.
t time of coulometric experiment, s.
J current density, A cm^{-2}.
k_1 electrochemical equivalent of zinc, mg C^{-1}.

The physical significance of k_1 and k_2 is as follows: k_1 is the electrochemical equivalent of zinc; k_2 represents the weight of ZnO formed on the surface of zinc amalgam exposed to air in the course of 1–2 h.

Fitting the data of table 1 to the two-parameter equation (2) gave the following values for the fitting coefficients:

$$k_1 = 0.33879579 \pm 1.29 \times 10^{-6} \text{ mg C}^{-1}$$
$$k_2 = 0.00914 \pm 1.21 \times 10^{-3} \text{ mg cm}^{-2}$$

The cited uncertainty is the standard deviation of the respective coefficients. The least-squares fit of table 1 data to a one-parameter test equation (1), neglecting k_2, yields a different value of the primary coefficient:

$$k_1 = 0.33880104 \pm 1.31 \times 10^{-6} \text{ mg C}^{-1}.$$

The inclusion of k_2 into the equation changes the value of k_1 by 0.0015 percent, thus affecting the atomic weight of zinc only by 0.00098.

4. Discussion of the Results

4.1. The Effects of Variables

A least-squares fit of the experimental data to a two-parameter equation does not necessarily constitute the accurate description of the coulometric behavior of the system. It must be shown that other variables in the system have no effect on this function. The most direct way to approach this problem is to examine the dependence of the residuals $(W_i - W)$ on the value of each varied parameter. W_i is the observed change of mass of zinc anode and W is the mass change computed from the least-square fit.

If a given variable, V_j, affects the results, then the residuals $(W_i - W)$ can be described as some function of that variable i.e.,

$$(W_i - W) = f(V_j). \tag{30}$$

Again using a linear relationship as the first approximation, subject to further refinement if warranted, one can write

$$(W_i - W) = k_j(V_j) \tag{31}$$

and fit the data to this equation by the method of least squares. If k_j does not reach statistical significance at the desired confidence level, the residuals and the original function itself may be taken as independent of that variable V_j. (See for example Mandel [4].)

Not all of the varied parameters are easily adaptable to the least squares data treatment. Material pretreatment (degassing) is one such parameter. It can be experimentally realized and verbally described, but the quantification of treatment cannot be performed very readily. One possible way of quantifying this parameter would have been to analyze the material for the total gas content after each treatment. The determination of gases in zinc is in itself a formidable problem and was not undertaken. It was decided to resort to the cause (treatment) and the observable effect approach. Similarly, the origin of material (e.g., Australia, Peru, etc.) cannot be readily quantified, and therefore one is again forced to resort to the statistical testing of observable differences between

different unquantifiable groups of data for significance.

4.2. Effect of Gases in Zn

One parameter, mentioned above, which can not be quantitatively inco.porated into the linear equation describing the electrochemical behavior of Zn(Hg) is the effect of gases (oxygen) dissolved in the metal. It was therefore tested on three distinctly different groups of materials.

Two experiments (No. 24 and No. 29) performed with the air-fused material yielded the following values of the fitting coefficients:

$$k_1 = 0.3388235 \pm 3.2 \times 10^{-6} \text{ mg C}^{-1}$$

$$k_2 = 0.0107 \pm 1.5 \times 10^{-3} \text{ mg cm}^{-2}.$$

To make this solution feasible by the method of least squares the data of experiments 24 and 29 were combined with the "zero current" data, shown as set No. 5 in table 1.

Using the values of k_1 for materials subjected to different treatments the apparent values of the atomic weight of zinc were computed from Faraday's law and are shown in table 4.

It is quite clear from these data that the atmosphere in which molten zinc solidifies has a significant effect on the apparent electrochemical equivalent of zinc. The atomic weight of zinc computed on the basis of data for air-fused materials is about 0.02 percent higher than for vacuum fused materials.

TABLE 4. *Apparent atomic weight of zinc as a function of material treatment*

Material treatment	Apparent atomic weight
Air Fused Zn	65.3932
Unfused Zn	65.3823
Degassed Zn*	65.3771

* In addition to the vacuum fused commercial materials, this data includes the unfused high purity Zn (code 4) and the intermediate purity Zn (code 6). The latter two materials were deoxygenated by the manufacturer, as indicated in the corresponding certificates of analysis.

The commercial grade zincs without any *a priori* processing yield a 0.008 percent higher value of the electrochemical equivalent than the same materials subjected to vacuum fusion. This can be explained by the presence of gases, notably oxygen, in the commercial material which are removed under vacuum fusion conditions.

4.3. Effect of the Apparent Surface Area of the Electrode

It has been already shown that the apparent electrode surface area has a significant effect, resulting from the dissolution of ZnO formed on the surface of the amalgam during exposure to air. The magnitude of this effect is obtained by solving for the coefficient k_2 in eq (2). Three sets of data were used to obtain the three solution for k_2. The data of all coulometric measurements with degassed samples were used to obtain one solution. The data on unprocessed materials (table 2) were used to obtain the second solution. Finally the data of "zero current" set No. 5 (experiments 98–125) were used to obtain the third, independent soultion. The constants obtained in these three treatments are given in table 5 in the above described sequence. The mean value of the coefficient k_2 is 0.0102 ± 0.0040 mg cm^{-2}.

TABLE 5. *Three independent solutions for the coefficient* k_2

Solution No.	k_2, mg cm^{-2}	$\bar{s}$	Degrees of freedom
1	0.0079	0.0017	90
2	.0121	.0087	26
3	.0107	.0015	25
Mean.....	0.0102	0.0040	

4.4. Effect of Origin of Material

Another parameter which is not easily quantifiable in the sense of permitting the least-squares treatment of data is the geographic origin of the material. Here again the data can only be compared by testing the difference for significance. Experiment numbers 139 through 150 were performed as the final set of data [16]. Only the data of this set for high purity zinc (code 4) were used in the intercomparison. If all measurements on this material were used, the pooled standard deviation would have been overwhelmingly dependent on the high purity zinc data.

On the basis of data presented in table 6, there

TABLE 6. *Atomic weight of zinc determined by coulometry for materials of different origins* [16]

Experiment No.	Origin of material	Atomic weight of zinc
139	Canada	65.3759
140	Canada	65.3761
141	Canada	65.3782
142	Australia	65.3783
143	Australia	65.3778
144	Peru	65.3786
145	Peru	65.3764
146	Yugoslavia	65.3761
147	Yugoslavia	65.3751
148	Italy	65.3784
149	Italy	65.3783
150	Canada	65.3791
Mean.....	.....	65.3773_6

Pertinent Statistical Data.

Standard deviation of a single determination $s = 0.00134$.

Standard deviation of the mean $s/\sqrt{n} = 0.00039$.

Two sided 95 percent confidences interval for the mean based on 11 degrees of freedom $ts/\sqrt{n} = \pm 0.00086$.

appears to be no significant difference between the atomic weight values for materials of different origins even at the 10 percent level of significance. The published results of mass spectrometric investigations [5, 17] also indicate no significant differences in the isotopic composition of zinc.

4.5. Effect of Impurities

To investigate the effect of Zn purity on the coulometrically determined atomic weight the data obtained for material 4, high purity zinc (99.9999%), material 6, intermediate purity zinc (99.997%), material 109, Australian zinc (99.995%) and material 101, a commercial vacuum fused material (99.9%), were intercompared. (Table 7.)

TABLE 7. *Effect of purity of* Zn *on the determined atomic weight*

Material code	Purity, percent	Atomic weight of zinc
4	99.9999	65.3770
6	99.997	65.3774
109	99.995	65.3760
101	99.9	65.3768

Pooled standard deviation $s = 0.0013$.

A mere inspection of these data, clearly demonstrates that three orders of magnitude range of purity of the material has no significant effect on the determined atomic weight. This is not inconsistent with our understanding of the metallic impurity effect. The elements generally present as impurities in Zn are Pb, Cu, Fe, Ag, and Cd. Since Zn is more active than any of these elements, it would be expected that zinc would be oxidized preferentially and the impurities left in the amalgam.

4.6. Other Parameters

In addition to the three above-discussed parameters (gases in Zn, purity and origin), quantification of which for the purpose of the least-squares treatment was not possible, there were a number of variable parameters in the experiments which can be quantified and their effects can be easily tested. To perform the test for significance, the residuals (i.e., $W_i - \bar{W}$), obtained for each experiment in the fit of table 1 data to eq (2) in table 3 were least-square fitted as a linear function of each of the variable parameters. The coefficients for each of these parameters, k, their respective standard deviations, $\bar{s}_k$, and $k/\bar{s}_k$ ratios are given in table 8.

Clearly there is no evidence that any of these tested parameters have an effect on the electrochemical equivalent, or the atomic weight of zinc. This conclusion can be made on the basis of the last column in the ratio of coefficient of each fitted parameter to the standard deviation of that coefficient. The test for significance indicates that there exists no dependence between the residuals of the final fit and the tested parameters.

TABLE 8. *Effect of variable parameters*

Variable	Coefficient k	Standard deviation of k, $\bar{s}_k$	$k/\bar{s}_k$
Charge, Q	-5.39×10^{-10}	16.60×10^{-10}	-0.32
Time, t	1.65×10^{-10}	7.33×10^{-10}	0.23
Current, i	2.34×10^{-5}	2.83×10^{-5}	0.83
Current density, J	-5.31×10^{-5}	5.4×10^{-5}	-0.98
at product	-1.38×10^{-11}	10.42×10^{-11}	-0.13

5. Summary of Findings

1. In the preliminary studies [1] it was found that the zinc amalgam electrodes are more stable than the unamalgamated electrodes. Zinc amalgam electrodes show no perceptible fall-off of material in the course of electrolysis.

2. The presence of oxygen (air) in the electrolyte has a significant effect on the rate of spontaneous corrosion of zinc. This in turn affects the experimentally determined electrochemical equivalent and the atomic weight of zinc. For this reason air was removed from the electrolyte by purging with nitrogen. A nitrogen atmosphere was maintained in the coulometer in all final determinations of the electrochemical equivalent of zinc.

3. On the basis of current density-potential studies it was established that even at current densities as high as several amperes per square centimeter the oxidation of zinc proceeds at 100.000 percent current efficiency. This was verified further by the coulometric experiments conducted at current densities ranging from 10^{-5} to 1.0 A cm^{-2}, which show no relation between the current density and the measured electrochemical equivalent of zinc.

4. Commercial grade zincs without any prior processing yield a higher measured electrochemical equivalent (on the order of 0.008%) than the same materials subjected to vacuum fusion. This is explained by the presence of oxygen in the commercial material which is removed under vacuum fusion. Air-fused zinc samples yielded an even higher value than the unprocessed Zn (0.02 %).

5. The geographic origin of material has no apparent effect on the measured electrochemical equivalent of zinc.

6. The presence of metal impurities does not have any significant effect on the measured electrochemical equivalent and the atomic weight of zinc.

7. Other investigated parameters which have no apparent effects as shown by the residual analysis of the least-squares fit include: current in the 10^{-4} to 1.0 A range; electrolysis time, up to 7×10^4s; amount of charge passed through the cell, up to 3×10^4C; mass of dissolved Zn, up to 10 g.

8. Only the electrode area, a, is the parameter which must be included in the final equation for the electrochemical equivalent of Zn. The effect of electrode

area arises from the disolution of ZnO formed on the surface of Zn(Hg) during the handling of the electrode in air.

The final least-squares fit, therefore, includes all data in table 1 since all samples of Zn used in these experiments were deoxygenated and the correction for the surface ZnO was applied by using the electrode area as one of the parameters in the equation.

9. The resulting equation is:

$$W = 0.338,795,79\ (\pm 0.000,001,29)\ Q + 0.009,1\ (\pm 0.001,2)a$$

where W is the mass of zinc dissolved (in milligrams), Q is the charge (in coulombs) and a is the electrode area (in cm^2). Subsequent fit of the residuals as a function of a and Q shows no significant correlation. Therefore the assumption that the first order equation, with respect to these two variables, is appropriate and is accepted by us as valid. The uncertainty figures for the coefficients in the above equation represent the deviations of the means based on 116 degrees of freedom.

10. As a final check on the imprecision measure calculated from the least-squares fit of all the data in table 1, we could compute the electrochemical equivalent for each of the six sets (0, 1, 2, 3, 4, 8) and take the average of these six values. The spread among these values would include variabilities due to sets, if any, and allow a more conservative estimate of the uncertainty of the value determined. The low current values, set numbers 6 and 7, were not included in this calculations because of their inherent imprecision. The results are given in table 11. The unweighted average is 0.33879491, agreeing very well with the least value for all the data points, but the standard error of the average (.00000435) is larger by a factor of four. It was decided that the final value of the electrochemical equivalent should be the value using all the data (to allow for better estimation of the effect of areas of electrodes). Its uncertainty, however, should be estimated in the conservative way, i.e., a 95 percent confidence interval for the mean using the standard error calculated from the six sets with five degree of freedom, or:

$$0.33879579\ (\pm 0.00001120).$$

Thus for Zn the determined molar mass is equal to:

$$\text{Molar mass of Zn} = 0.338,795.79\ \text{mg C}^{-1} \times 96,484.56\ \text{C mol}^{-1}(e) \times 2\ \text{mol}\ (e)/\text{mol (Zn)} \times 10^{-3}\ \text{g mg}^{-1}$$

$$= 65.37707 \pm 0.00216\ \text{g/mol (Zn)}$$

where the uncertainty is the 95 percent confidence interval.

There is a distinction between the molar mass and atomic weight. The latter is a dimensionless quantity numerically equivalent to molar mass. Thus the mean value of the atomic weight of Zn based on 118 final coulometric measurements under the optimum condition is 65.3771 ± 0.0022.

The two-sided 95 percent confidence interval for the mean, ± 0.0022, reflects adequately the uncertainty in this value due to the random sources of error. The accuracy of the result, however, depends not only on the random error of measurement, but also on the biases which could exist in the various stages of the measurement process and in the constants which are employed in the calculation of the results. An assessment of the magnitude of these sources of error must be made and incorporated into the uncertainty statement.

5.1. Assessment of Errors

In addition to the random error of measurement some systematic errors can be encountered which are not revealed in the statistical treatment of data.

The uncertainty in each standard weight can be as large as 3 μg. The average weight of zinc dissolved in the final coulometric experiments is 1 g. Thus this source can contribute as much as 0.0003 percent error.

Electrical current measurements can be biased systematically (due to uncertainty in the standard resistor, saturated Weston cell and comparator error) by 0.0004 percent.

The timer was never found to have an error as great as 0.0001 percent. For the purpose of estimation of error it is assumed that it can be off by as much as 0.0001 percent.

The Faraday, which is used for final computation of the atomic weight, has 0.27 C $mol^{-1}(e)$ uncertainty [6]. This corresponds to 0.00028 percent.

It would appear highly unlikely for all of these errors to be of the same sign. In fact a root-mean-square (rms) estimate of the possible combined effect would be appropriate and realistic. The overall rms estimate of the possible systematic error is 0.0006 percent (or 0.00040 in the atomic weight of Zn). Thus, the total error in the atomic weight of zinc, consisting of the sum of the random error contribution and possible systematic error estimate is 0.0026.

The new, accurate value of the atomic weight of zinc presented here is:

$$65.3771 \pm 0.0026.$$

5.2. Comparison With Previous Work

Only one earlier published research paper, that of Gladstone and Hibbert [7], describes work that is directly comparable with the research reported here. They also used Zn(Hg) anodes, made from sheet zinc. Three important features set apart the experiments of Gladstone and Hibbert from those conducted in this research: (1) commercial zinc, not subjected to degassing, was used by Gladstone and Hibbert while both types of materials were used here; (2) the charge consumed in the electrochemical reaction was measured by Gladstone and Hibbert by means of a silver deposition voltameter (coulometer) while the absolute cur-

rent and time measurements were employed in this work; (3) the experiments reported in [7] were conducted without the exclusion of air while an inert atmosphere (N_2) was maintained in the coulometer used in this research.

It is desirable to analyze these differences and establish what effects they would produce in the final measured value of the atomic weight.

The first of these differences, the effect of gases in commercial zinc, was investigated directly. The difference between the atomic weight for the untreated material and the vacuum fused material is 0.00521 (or 0.00976%), the untreated material being the one which yields the higher value.

Secondly, the use of a Ag deposition coulometer invariably entails some occlusion errors. This aspect of the cathodic silver coulometer was treated in some detail by Hamer [8]. Hamer arrives at a value of 0.0102 ± 0.0014 weight percent as the mean error of the Ag deposition coulometers. Consequently, an error of this magnitude is probably incorporated into the results reported in [7] and propagated into the value for the atomic weight of Zn computed by Gladstone and Hibbert.

Finally, the presence of air in the electrolyte has a pronounced effect on the rate of spontaneous corrosion of zinc amalgam. This error again was no doubt affecting the work reported in reference [7] while it was minimized in the final experiments reported in this research by the use of deaerated electrolyte and the maintenance of an inert atmosphere in the coulometer. The average current density employed in the experiments of Gladstone and Hibbert [7] was 94 $mA \cdot cm^{-2}$. From the studies of corrosion of Zn(Hg) in air saturated electrolyte, conducted here, the corrosion current density is found to be $J_{corr} = 1.37 \times 10^{-3}\ mA \cdot cm^{-2}$. Thus the error from this source is on the order of 0.0015 percent. This estimate, however, may involve a somewhat questionable extrapolation. Gladstone and Hibbert used $ZnSO_4$ electrolyte while $NH_4Cl + ZnCl_2$ were used here.

Since reference [7] gives no data on the surface area of the anodes it is not possible to make any corrections for ZnO, formed on the surface during drying of electrodes, which dissolves when the electrodes are immersed in the electrolyte. Moreover, in reference [7], electrodes were washed in alcohol and then dried at 40 °C, which probably accelerates the rate of oxidation of Zn(Hg).

The mean value of the Ag/Zn weight ratio reported in reference [7] is 3.298 ± 0.001. Using 107.93 as the atomic weight of silver Gladstone and Hibbert computed the atomic weight of Zn as 65.44. Using the presently accepted value for the atomic weight of silver, 107.868, the above value becomes 65.414. To this value the sum of all the above discussed corrections must also be applied. The total correction is −0.0197 percent. Thus the value of the atomic weight of zinc based on the data of Gladstone and Hibbert, corrected for known possible sources of error, is 65.40 ± 0.02. A copper coulometer, operated in series with a Zn and Ag coulometer, gave a Zn/Cu weight ratio of 1.0322, yielding 65.58 as the atomic weight of zinc. As pointed out by the authors themselves, the combining weight ratio 1.0322 is too high, thus this value contributes little to the the information on the atomic weight of zinc. The only inference which can be made is that the Cu coulometer gives an error of about $+0.3$ percent in the charge integration.

The above computed value of the atomic weight of Zn 65.40, based on the Ag/Zn ratio, is not in very good agreement with our final value (65.3771). The difference is on the order of 0.033 percent. It must be remembered, however, that no information is given regarding the material used in the work reported in reference [7]. If one supposes that the zinc was fused in air to form sheets which were then fabricated into the electrodes then the Zn atomic weight value obtained should be corrected for the effect of oxygen in the metal by a much greater amount than estimated above. Using the data of this research this additional correction is 0.011. Thus the Gladstone and Hibbert's value becomes 65.39 ± 0.02. Now the values are consistent within the experimental uncertainty.

Most of the results on the atomic weight determinations prior to 1910–1915 have been collected, analyzed and evaluated critically by Clarke [9, 10]. Since at the time Clarke did his reevaluation many of the atomic weights were not known accurately, and since the atomic weight scale has changed from the chemical atomic weight scale (based on oxygen = 16 exactly) to the unified C^{12} scale,[4] the values obtained by Clarke must be recalculated for the purpose of meaningful comparison.

It is rather fortunate that in science certain measured quantities remain truly invariant. Such constants are usually dimensionless ratios. The combining weight ratios are in this select group of constants. Even if the standard weights used in the measurements are inaccurate, as long as the same weights are used in the determination of the ratio, and the comparison method itself is flawless, the ratio is accurate.

Usually this latter condition, the flawlessness of the method, is the one which is difficult to realize.

Clarke arrived at the following group of combining weight ratios and his assessment of the uncertainties:

(1) ZnO:Zn $= 100:80.349 \pm 0.00065$
(2) $ZnSO_4$:ZnO $= 100:50.413 \pm 0.0020$
(3) H_2O:Zn $= 100:366.319 \pm 0.088$
(4) $2CO_2$:ZnO $= 100:93.169 \pm 0.012$
(5) H:Zn $= 100:6507.9 \pm 0.0036$
(6) 4Ag:K_2ZnCl_4 $= 100:66.111 \pm 0.0023$
(7) 2Ag:$ZnBr_2$ $= 100:104.38 \pm 0.0007$
(8) 2AgBr:$ZnBr_2$ $= 100:59.962 \pm 0.0004$
(9) Au:Zn $= 197.2:65.436 \pm 0.0087$

The data used for the intercomparison must be judiciously selected. It is quite clear that all of the

[4] One mole of substance is now defined to contain as many entities (atoms, molecules, electrons, etc.) as there are atoms in exactly 12 g of C^{12} isotope.

combining weight ratio data, given above, are not equivalent in reliability. Ratios (3), (4) and (5) should be ignored because the gasometric methods can be hardly considered accurate in view of the fact that real gases do not obey the ideal gas law, and, in general, volume measurements on real gases are susceptible to many errors. Ratio (6) can also be discarded because K_2ZnCl_4 is a compound of questionable stoichiometry. The calculated atomic weights of Zn based on the remaining 5 combining weight ratios are given in table 9. The agreement of the mean of these 5 ratios 65.384 ± 0.016, and the value found in this research is well within the assigned uncertainty bounds.

In addition to Clarke's collection more recent data are also available on the determination of the atomic weight of Zn.

Baxter and Grose [11] determined $Zn:Br_2$ ratio by preparing pure $ZnBr_2$, depositing Zn from weighed samples of $ZnBr_2$ into a mercury cathode, then weighing the deposit. Their value of $Zn:Br_2 = 0.409063$. Using 79.904 for the atomic weight of Br the calculated atomic weight of Zn becomes 65.3715.

TABLE 9. *Atomic weight of zinc based on selected combining weight ratios*

Ratio No.	Atomic weight of Zn
1	65.418
2	65.392
7	65.377
8	65.376
9	65.359
Mean	65.384 ± 0.016

Baxter and Hodges [12] determined the ratio $Zn:Cl_2 = 0.92195$ by the same method as [11]. Using 35.453 for the atomic weight of Cl the calculated atomic weight of Zn is found to be 65.3718.

Hönigschmid and von Mack [13] also utilized $ZnCl_2$ in their determinations, but titrated Cl with Ag^+. Their $ZnCl_2/2AgCl$ ratio is 0.475424, yielding the value 65.3698 for the atomic weight of Zn.

Using the relative isotope abundance values, determined by Leland and Nier [14] and by Hess et al. [5], as well as Mattauch's [15] data on mass defects for the five Zn isotopes, the atomic weight of zinc can be readily computed.

The summary data of these most recent determinations of the atomic weight of Zn are given in table 10.

The mean value of the six independent determinations by previous investigators, reported in table 10, 65.3777, is in a remarkable agreement with 65.3771, the final value derived from this research.[5]

[5]This suggests that unless a method has been proven to be accurate it is desirable to resort to as many different, judiciously selected, independent methods as possible. Nature will in turn cooperate by distributing errors randomly so that the mean value of these many, less accurate methods, will be a better approximation of the true value than any one particular determination.

TABLE 10. *Most recent data on the atomic weight of zinc*

Method	Source (reference)	At. wt. of Zn
Zn/Br_2	[11]	65.3715
Zn/Cl_2	[12]	65.3718
$ZnCl_2/2AgCl$	[13]	65.3698
ZnI_2 Mass spectr.	[14]	65.3873
Do.	[5]	*65.3911
Do.	[5]	**65.3744
Mean		65.3777

* Electrolytic Zn.
** Zn produced by chemical reduction.

TABLE 11. *Analysis of data by sets*

Set No.	Number of measurements	Current, A	K_1, mg C^{-1}	Standard error of K_1
0	9	0.5	0.33880890	0.00001644
1	17	.5	.33878853	.00000957
2	6	1.0	.33879535	.00000675
3	18	1.0	.33879872	.00000510
4	8	0.1	.33877785	.00000997
8	12	.5	.33880008	.00000200

Mean	0.33879491 mg · C^{-1}
Standard error of the mean	0.00000435 mg · C^{-1}
95 percent confidence interval	$\pm$ 0.00001120 mg · C^{-1}

6. Conclusion

Based on the publication of partial results of this research [16] the IUPAC Commission on Atomic Weights has published [18] a new value, 65.38 ± 0.01, for the atomic weight of Zn.

The new, more accurate value of the atomic weight of zinc, determined by an absolute coulometric method in this research is

$$65.3771 \pm 0.0026.$$

7. References

[1] Marinenko, G., and Foley, R. T., J. Res. Nat. Bur. Stand. (U.S.) **79A**, (Phys. and Chem.), No. 6, (1975).
[2] Grubbs, F. E., Technometrics **11**, 1 (1969).
[3] Hilsenrath, J., Ziegler, G. G., Massina, C. G., Walsh, P. J., and Herbold, R. J., OMNITAB–A Computer Program for Statistical and Numerical Analysis, Nat. Bur. Stand. (U.S.), HandB 101, 285 pages (Mar. 1966).
[4] Mandel, J., The Statistical Analysis of Experimental Data (Interscience Publishers, New York, 1964) pp. 185–192.
[5] Hess, D. C., Inghram, M. G., and Hayden, R. J., Phys. Rev. **74**, 1531 (1948).
[6] Cohen, E. R., and Taylor, B. N., J. Phys. Chem. Ref. Data **2**, No. 4, 741 (1973).
[7] Gladstone, J. H., and Hibbert, W., J. Chem. Soc. **55**, 443 (1889).
[8] Hamer, W. J., J. Res. Nat. Bur. Stand. (U.S.), **72A** (Phys. and Chem.), No. 4, 435–439 (July–Aug. 1968).
[9] Clarke, F. W., The Constants of Nature Part V. A Recalculation of the Atomic Weights, Third edition, Smithsonian Institution Publication, Washington, D.C., (1910), pp. 223–234.
[10] Clarke, F. W., The Constants of Nature Part V. A Recalculation of the Atomic Weights, Fourth revised and enlarged edition, Government Printing Office, Washington, D.C., 1920, pp. 179–187.

[11] Baxter, G. P., and Grose, M. R., J. Am. Chem. Soc. **38,** 868 (1916).
[12] Baxter, G. P., and Hodges, J. H., J. Am. Chem. Soc. **43,** 1242 (1921).
[13] Hönigschmid, O., and von Mack, M., Z. anorg. and Allgem. Chem. **246,** 363 (1941).
[14] Leland, W. T., and Nier, A. O., Phys. Rev., **73,** 1206 (1948).
[15] Mattauch, J. H. E., Thiele, W., and Wapstra, A. H., Nucl. Phys., **67,** 1 (1965).
[16] Marinenko, G., and Foley, R. T., J. Res. Nat. Bur. Stand. (U.S.), **75A** (Phys. and Chem.), No. 6, 561–564 (Nov.–Dec. 1971).
[17] Rosman, K. J. R., Geochim. et Cosmochim. Acta, **36,** 801 (1972).
[18] IUPAC Commission on Atomic Weights, Pure and Applied Chemistry, **30,** 639 (1972).

(Paper 79A6–872)

JOURNAL OF RESEARCH of the National Bureau of Standards—A. Physics and Chemistry
Vol. 79A, No. 6, November–December 1975

The Use of Synchrotron Radiation as an Absolute Source of VUV Radiation

D. L. Ederer, E. B. Saloman, S. C. Ebner, and R. P. Madden

Institute for Basic Standards, National Bureau of Standards, Washington, D.C. 20234

(September 10, 1975)

Synchrotron radiation has been used as a standard source to calibrate spectrographic instruments at the National Bureau of Standards (NBS). Conceptually it is straightforward to apply the calculable continuum distribution of synchrotron radiation to problems requiring a source of known irradiance if the electron energy, the radius of the electron orbit, and the beam current are known. In practice many factors affect the accuracy of such a calibration, such as temporal and spatial variations in the electron beam, uncertainties in the orbital radius and maximum energy of the orbiting electron beam. These sources of error are discussed and the method of calibration on SURF–I is specified. A storage ring synchrotron radiation facility (SURF–II) is now operational at NBS. The calibration techniques developed for SURF–I are applied to SURF–II with anticipated improvements in calibration accuracy. For SURF–I the incident flux was determined with an accuracy of 15 percent while for SURF–II we anticipate accuracies of about 7 percent.

Key words: Irradiance; radiometry; spectrometer calibration; standard source; synchrotron radiation; vacuum ultraviolet.

1. Introduction

The need for vacuum ultraviolet (vuv) source and detector standards has been growing steadily during the past decade with the requirements of space physics, aeronomy, and plasma physics setting the pace. Reliable detector transfer standards have been developed [1, 2][1] for use over a wavelength range from 200 to 2500 Å. While detector-transfer-standard systems cover a broad spectral range in the vuv, source standards are not as well developed.

The simplest calibration method is the substitution of a calibrated standard for the unknown in an existing system. This makes source standards the standards of choice in calibrating other sources. The use of detector standards for this purpose requires independent knowledge of the monochromator optical system efficiency. On the other hand, detector standards are the standards of choice for calibrating other detectors.

Several sources have been devised [3–15] for use as standards in the vuv, however the 1000 to 3000 Å spectral range is where the most intense development has taken place. Among the various proposed sources synchrotron radiation [3–6] has appeared especially attractive. In addition, the radiation from wall-stabilized arcs [7, 8], transition radiation [9, 10], and discharge lamps [11, 12] have also been demonstrated as feasible sources which can be characterized sufficiently well to be used as standards. Branching ratio techniques [13–15] have also proven useful in certain situations.

The characteristics of these different sources are given in table 1 for comparison. It is clear that the features pertaining to each source serve to specialize its use. The best choice must be made with a given experiment in mind. For example, while both the synchrotron and wall-stabilized arc are possible standard sources, one would be drawn to the use of a synchrotron at wavelengths less than 1200 A, the lithium fluoride cutoff, simply because an expensive differential pumping system is unnecessary. On the other hand if a filled optical system is a more important criterion than high intensity, one would use a transition radiation source which in addition to its greater divergence is also more portable than either a synchrotron or a wall-stabilized arc. While for the 1600 to 2600 Å spectral range a deuterium lamp [12] is the simplest to use. All the sources mentioned except the synchrotron have cutoffs above 500 Å. At wavelengths less than 500 Å the synchrotron remains the only effective candidate for a continuum calibration source.

Wall-stabilized arcs and sources of synchrotron radiation are considered absolute sources since their radiation is a known function of their operating parameters. Both, unfortunately, are rather immobile and require some means of transferring the calibration to

[1] Figures in brackets indicate the literature references at the end of this paper.

TABLE 1. *Characteristics of vuv standard sources*

Source	Synchrotron radiation	Wall-stabilized arc	Transition radiation	Cerenkov radiation	Branching ratio technique	Discharge and deuterium lamps
Relative (R) or absolute (A) standard	A	A[b], R	A	A	A	R
Line (L) or continuous (C) source	C[a]	C	C	C	L	L, C
Wavelength range (Å)	> 0.1	1300–3600	> 500	> 1200	900–3000[c]	> 304[d]
Maximum intensity	Bright[f]	Bright	Dim[g]	Dim	Intermediate	Intermediate
Scalable in intensity?	Yes	Limited[e]	Yes	Yes	Limited	Limited
f Number	Small (f/500)	Small	Large (f/10)	Large	Large	Large
Polarized?	Yes	No	Yes	Yes	No	No
Vacuum in source	High	Poor	High	High	Poor	Poor
Physical size	Massive	Large	Small	Small	Small	Small

NOTES:
[a]Adjustable wavelength distribution; storage ring very stable.
[b]Only hydrogen arc is absolute.
[c]Usable only at selected wavelengths; subject to absorption effects; portable.
[d]Usable only at selected wavelengths; good as transfer standard; portable.
[e] Over factor of ten.
[f]About 10^{16} photons s Å · Sr.
[g]About 10^{10} photons s Å · Sr.

the unknown source. Transition radiation sources and the deuterium lamp have been suggested [9, 10, 12] for this purpose in the vuv.

Transferring a calibration from a standard source in one laboratory to an unknown source in a second laboratory effectively involves the calibration of two spectrometers, one at the laboratory housing absolute-transfer standards and the other in the field where the transfer standard is compared with the unknown source. There are significant advantages in an alternate approach; namely to directly calibrate the spectrometer that is to be used for determining the radiance of the unknown source. If the calibration is made on a before-after basis, any changes in sensitivity can be interpolated, and errors resulting from a double transfer are eliminated. This method requires direct illumination (no auxiliary mirrors) of the spectrometer by both standard and unknown sources. When NASA encouraged us to establish a source calibration facility at the National Bureau of Standards "Synchrotron Ultraviolet Radiation Facility" (NBS–SURF) for the Skylab program we took the approach outlined above, namely, calibrate a spectrometer to be used as a transfer standard. We used synchrotron radiation as the absolute standard source because the required calibration range, 200 to 1200 Å, was beyond the range of all other sources. The use of synchrotron radiation to calibrate a spectrometer above 500 Å has recently been reported [16].

The basic assumption of our calibration method is that the intensity distribution of synchrotron radiation is a calculable quantity. Once this assumption is granted, it is straightforward conceptually to apply the calculable continuum distribution of synchrotron radiation to problems requiring a source of known irradiance provided the electron energy, the radius of the electron orbit, and the beam current are known. In practice many factors affect the accuracy of such a calibration and this paper will discuss the steps taken at NBS to attain a successful calibration. In the following sections the measurements required to determine the parameters necessary for the calibration will be presented. Systematic errors, their sources and cure, will be a topic of discussion, as will some special problems that arise due to the peculiar characteristics of the radiation source. While this paper will deal primarily with synchrotoron radiation that arises from the periodic acceleration of electrons in a synchrotron, some time will be devoted to the application of synchrotron radiation from a storage ring to spectrometer calibrations because the NBS synchrotron (SURF–I) has now been converted into an electron storage ring (SURF–II).

2. The Synchrotron as a Primary Radiation Standard

We must first discuss the validity of the fundamental assumption involved in using synchrotron radiation as an absolute source standard: that the photon flux distribution in both wavelength and angle is an exactly calculable quantity. In the following paragraphs ample evidence has been given to justify this basic assumption. The reader is referred to several excellent reviews [17–19] of the historic development of the use of synchrotron radiation for a more detailed account of

the characteristics of the radiation and for other applications of it.

In their classic paper Tomboulian and Hartman [3] suggested that synchrotron radiation could be used as an absolute radiation standard because of the calculability of the radiant energy wavelength distribution. This suggestion arose as a result of their experiments that compared measured synchrotron radiation intensity with the calculated intensity distribution. Their experiments covered different wavelength regions, from the quartz ultraviolet to the vacuum ultraviolet, as well as both radiation from monoenergetic electrons and electrons accelerated over a full machine cycle. They measured the angular distribution of the radiation at several wavelengths and electron energies. The result of this extensive study demonstrated the classical theory was appropriate to the description of synchrotron radiation.

Nine years later Codling and Madden [4] reported measurements of the polarization properties of the radiation in the visible and also used radiometric techniques to measure the beam current. A year later a group [5] at DESY (Deutsches Elektronen-Synchrotron) compared the relative intensity distribution as a function of photon energy and azimuthal angle relative to the orbital plane. In this case the electron energy varied between 4 GeV and 6 GeV and the photon energy extended between 20 keV and 300 keV. Their results substantially confirmed the measurements of Tomboulian and Hartman [3] at lower electron and photon energies, namely, that the measurements were in agreement with calculations to within the experimental error of order 10 percent.

Lemke and Labs [6], working at DESY, explored the possibility of using synchrotron radiation as a fundamental radiometric standard in the wavelength region 2200 to 5500 Å. They compared the spectral radiance from the synchrotron with that of a standard lamp. From this comparison they were able to measure the relative spectral distribution for their geometry as well as independently determining the circulating electron current. Applying the appropriate polarization correction (synchrotron radiation is highly polarized in the orbital plane) they obtained a relative spectral distribution that agreed with the computed flux within 2 percent. Their optical measurement of the circulating current was consistent with an independent direct measurement of the beam current to within the 15 percent limit of experimental error of this direct technique. These experiments have shown the measurements to be consistent with the calculations of the flux over a broad spectra range for accelerated electrons over a wide energy range. At the Glasgow University synchrotron, Key [20] made a very careful relative flux determination between 3500 Å and 6000 Å by comparing the radiance from the electron beam with the radiance from a standard lamp. This comparison yielded coincidence to $\pm$ ½ percent between the relative measured spectral distribution and the predicted spectral distribution.

In 1969 Pitz [11] used synchrotron radiation as a primary standard to calibrate mercury, xenon, and deuterium transfer standard lamps in the wavelength range 1500 to 2700 Å. Later a mercury lamp and a deuterium lamp traceable to one calibrated by Pitz was compared to a wall-stabilized hydrogen arc [21]. Discrepancies were found to be about 10 percent between 1650 Å and 2550 Å. Between 2550 Å and 2700 Å, the long wavelength limit of the calibration, the deviations were as great as 25 percent. Whether these discrepancies were due to aging of the lamp or some other source is not clear, however evidence points to a lamp change rather than something faulty with the synchrotron radiation flux determination. More recently a comparison [22] between a wall-stabilized arc and synchrotron radiation has been made through the use of deuterium lamp and xenon lamp transfer standards at a wavelength near 1650 Å. The resulting calibrations agreed to $\pm$20 percent at low arc currents and $\pm$5 percent at the higher currents. The authors concluded that the discrepancies were consistent with errors expected from the synchrotron calibration and the wall-stabilized arc calibration.

From these measurements the validity of the fundamental assumption underlying the use of synchrotron radiation as an absolute standard seems to be well founded. Not only have direct measurements of the spectral distribution confirmed the calculable nature of synchrotron radiation but independent calibrations of transfer standards with synchrotron radiation and with the wall-stabilized arc have also been found consistent.

3. Method

It is conceptually straightforward to apply the calculable continuum distribution of synchrotron radiation to spectrometer calibration since the efficiency, $\epsilon(\lambda)$, of the spectrometer at wavelength λ, is given by:

$$\epsilon(\lambda)=\frac{F(\lambda,\Delta\Omega)}{R(\lambda,\Delta\Omega)}, \tag{1}$$

where $F(\lambda,\Delta\Omega)$ is the flux incident on the entrance aperture of the spectrometer which subtends a solid angle $\Delta\Omega$ located at some angle θ with respect to the orbital plane, and $R(\lambda,\Delta\Omega)$ is the response of the instrument to the incident flux. In order to understand the problems involved in the use of synchrotron radiation and to compute the quantity $F(\lambda,\Delta\Omega)$ it is necessary to delve into the properties of the radiant flux emitted by this source.

3.1. Properties of Synchrotron Radiation

The radiation emanating from centripetally accelerated electrons is confined along the direction of motion due to relativistic effects. The average divergence angle of the radiation is m_0c^2/E where m_0 is the electron rest mass and E is the instantaneous energy of the electrons. Since $E \gg m_0c^2$, the radiation from most

machines is confined to an angle of a few milliradians above and below the orbital plane. Because of the electron orbital motion the radiation is uniform in the orbital plane and at a given energy and radius is a function only of the azimuthal angle. A schematic view of the radiation pattern is shown in figure 1.

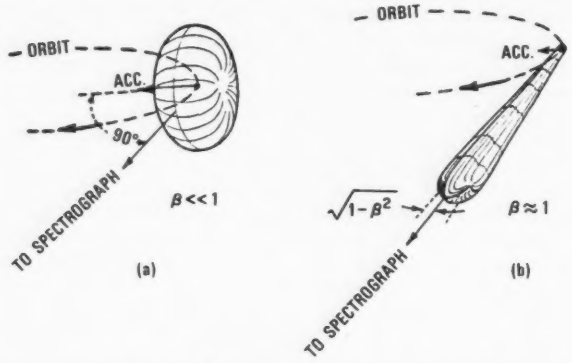

FIGURE 1. *Angular radiation patterns for orbiting electrons of greatly different energies.*

(a) Nonrelativistic energy, showing the typical dipole pattern: (b) Very relativistic energies, showing that the dipole pattern has been greatly warped around to the forward direction of the electron (from ref. [3]).

This rather narrow distribution presents the first problem for spectrometer calibration since most other sources, whose radiance is to be determined through the use of the calibrated spectrometer, have a much different angular distribution. In addition the radiation from the synchrotron source will often not fill the entrance solid angle of the instrument.

The power radiated by monoenergetic, accelerated electrons is a continuum which has the form [23, 3]

$$P(E,R,\theta,\lambda)=\frac{4e^2cR}{3\lambda^4}\,\gamma^{-4}\,(1+X^2)^2 \left[K_{2/3}^2(\xi)+\frac{X^2}{1+X^2}K_{1/3}^2(\xi)\right] \qquad (2)$$

where $P(E, R, \theta, \lambda)$ is the power in ergs per second per radian per electron per angstrom, $\gamma = E/m_0c^2$, and $\xi = (2\pi R/3\lambda)\,\gamma^{-3}\,(1+X^2)^{3/2}$ with $X=\gamma\theta$. The quantity R is the orbital radius and θ is the azimuthal angle with respect to the orbital plane while e and c are the electron's charge and the speed of light respectively. The quantities $K_{2/3}(\xi)$ and $K_{1/3}(\xi)$ are modified Bessel functions of the second kind. This the fundamental equation that is used to compute the flux incident upon the entrance aperture of a spectrometer. For a storage ring where the instantaneous energy E is a constant it is only necessary to integrate eq (2) over the entrance aperture solid angle to obtain the flux per electron at wavelength λ. However, for many accelerators (of which SURF–I, the old NBS–180 MeV synchrotron was an example) the energy of the electrons varies as they are periodically accelerated from zero to maximum energy. In this case eq (2) must be integrated over the time variation of the electron energy as well. Figure 2 shows the angular

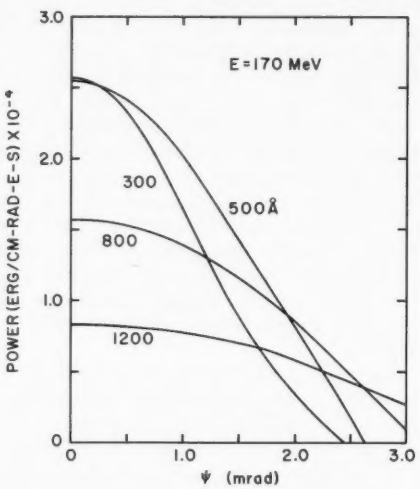

FIGURE 2. *Angular distribution of synchrotron radiation at several wavelengths for accelerated electrons with a maximum energy of 170 MeV.*

variation of the flux for accelerated electrons at several wavelengths. Equation (2) was integrated numerically for a time variation of the electron energy given by $E(t)=E_{\max}\sin\omega t$. Typical operating conditions for the NBS synchrotron were chosen, namely $E_{\max}$=170 Mev, $R=83.4$ cm, and $\omega=2\pi/T=2\pi 60$ s^{-1}. The ordinate defines the power $P(E_{\max},\theta,\lambda)$ in ergs per second per centimeter per radian of azimuthal angle per electron. The quantity $P(E_{\max},\theta,\lambda)$ is given by

$$P(E_{\max}\theta,\,\lambda)=\frac{1}{T}\int_{E(t_1)}^{E(t_2)} P(E,\,R,\,\theta,\,\lambda)\,dE(t). \qquad (3)$$

The limits of integration $E(t_1)$ and $E(t_2)$ are the instantaneous electron energies at t_1 (chosen to be zero, the beginning of the acceleration cycle) and t_2=5.57 ms the time when the radio frequency accelerating voltage was turned off. It may be seen from figure 2 that in the wavelength region between 100 Å and 2000 Å the angle at which the flux is smaller by a factor of two is typically a few milliradians.

The power $P(E_{\max},\,\theta,\,\lambda)$ given by equation (3) was numerically integrated over a round spectrometer aperture (0.836 cm^2 area) located 13.26 m from the tangent point of the orbiting electrons. This was the size of the aperture used for the calibration of a Wadsworth spectrometer. The flux $P(E_{\max},\,\lambda)$ in photons/sec-Å-e passing through this aperture for two values of the maximum electron energy, $E_{\max}$, is shown in figure 3. Notice that the flux is almost constant between 400 Å and 1000 Å for $E_{\max}$ equal to 170 MeV (curve A) while the magnitude of the flux at these wavelengths is greatly reduced for 140 MeV

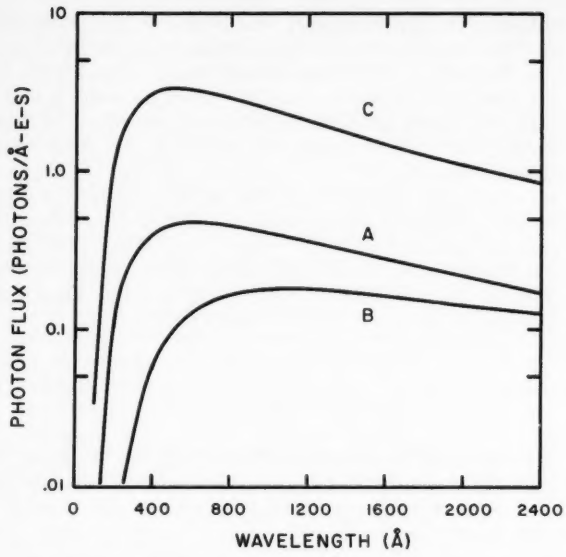

FIGURE 3. *Flux passing through a round aperature of solid angle equal to* 4.8×10^{-7} *strad as a function of wavelength.*

Curve A: Accelerated electron whose energy equals 170 MeV. Curve B: Accelerated electrons whose maximum energy is 140 MeV. Curve C: Monoenergetic electrons of energy 170 MeV.

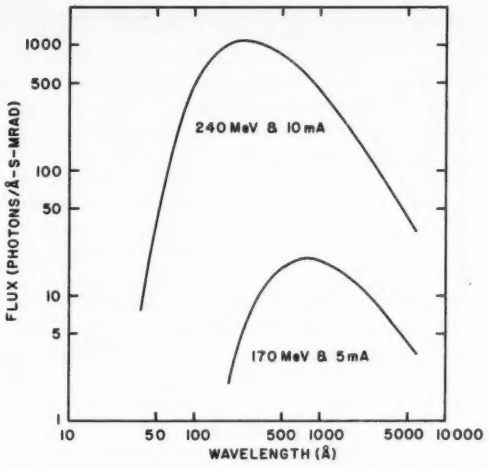

FIGURE 4. *Photon flux versus wavelength for (A) a monoenergetic 240 MeV, 10 ma beam of electrons—typical performance expected for SURF–II and (B) an accelerated 5 ma beam of 170 MeV maximum energy electrons—typical performance of SURF–I.*

Multiply ordinate by 1.1×10^{6}.

electrons (curve B). In fact, this great variation in the flux can be used to determine the instrument's response to second order radiation [24]. Curve C in figure 3 is the flux for monoenergetic electrons of 170 MeV energy obtained by just integrating equation (2) over the aperture. Notice that for the monoenergetic electrons the peak intensity in the spectral distribution is shifted to shorter wavelengths and the flux per electron is significantly greater than for accelerated electrons of the same peak energy averaged over the acceleration cycle. This difference is due both to the duty cycle of the cyclic accelerator and to the fact that the electrons, emit most of their radiation when their instantaneous energy $E(t)$ is nearly equal to E_{max}. The contrast between the two curves A and C emphasizes one of the advantages of using a storage ring for a calibration, namely, for the same number of electrons in the beam, the ring will emit about seven times more radiation than the synchrotron.

In figure 4 we show a comparison between accelerated 170 MeV electrons at an instantaneous current of 5 mA (typical of SURF–I operation) and 240 MeV monoenergetic electrons at a current of 10 mA (expected for initial SURF–II operation). Higher flux and the availability of shorter wavelengths make SURF–II a superior calibration source. In addition temporal variation in the radiation from the storage ring is a slowly varying monotonically decreasing function, due to the fact the electron beam lifetime is of the order of an hour, rather than the few milliseconds obtained in a sinusoidally run synchrotron. The fluctuations in the radiation due to variations in the injected current occurs on the order of hours, rather than every few milliseconds. These are powerful arguments for the use of a storage ring in spectrometer calibration. Other arguments favoring storage rings will be discussed later.

If the entrance aperture is large enough to accept the full vertical angular distribution of the radiation, eq (2) can be integrated over the azimuthal angle θ to yield the flux distribution for monoenergetic electrons:

$$P(E, \lambda) = \frac{3^{5/2}}{16\pi^2} \frac{e^2 c}{R^3} \gamma^7 G(y). \tag{4}$$

Similarly for electrons whose energy is given by $E(t) = E_{max} \sin(\omega t)$ eq (2) can be integrated over angle and averaged over one fourth the energy cycle to yield [3]:

$$P(E_{max}, \lambda) = \frac{3^{5/2}}{8\pi^3} \frac{e^2 c}{R^3} \gamma^7 L(y). \tag{5}$$

In eq (4) and eq (5) the quantities $G(y)$ and $L(y)$ are universal scaling functions independent of the electron energy and orbital radius. The quantity $y = \lambda_{c/\lambda}$. The critical wavelength λ_c is given in the following equation:

$$\lambda_c = \frac{4}{3} \pi R \gamma^{-3}.$$

These two functions are plotted in figure 5. The simple functional form of eq (4) and eq (5) are conveniently used with the figure 4 to estimate (since the vertical acceptance angle of the experiment is initially unknown) the flux available to an experimental ap-

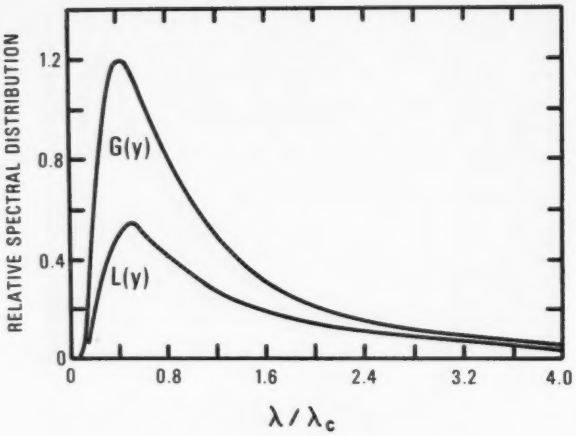

FIGURE 5. *Universal photon distribution functions for the total angular flux distribution.*

$G(y)$, the distribution function for monoenergetic electrons, and $L(y)$, the distribution function for accelerated electrons. The dimensionless quantity y defining the abscissa scale is equal to $\lambda/\lambda c$, where λc is defined in the text.

paratus from a specific machine. A rather tedious computation and integration is thus reduced to a "back of the envelope" calculation.

3.2. Determination of the vuv Irradiance

The vuv irradiance $F(\lambda, \Delta\Omega)$ incident on the spectrometer is given by:

$$F(\lambda, \Delta\Omega) = n_e \int_{\Delta\Omega} P(E_{\max}, \theta, \lambda) d\Omega \qquad (6)$$

where $F(\lambda, \Delta\Omega)$ is the number of photons per Å-s passing through the spectrometer aperture subtending a solid angle $\Delta\Omega$ measured from the tangent point. The quantity $P(E_{\max}, R, \theta, \lambda)$ was described in the preceeding paragraphs for both monoenergetic and periodically accelerated electrons. $P(E, \theta, \lambda)$ depends on the experimentally determined quantities R, the radius of the electron orbit and, $E_{\max}$, the maximum electron energy, in a straightforward way. The quantity n_e may be measured by using an induction technique [6] or it can be determined from the synchrotron radiation [4] itself. A particularly elegant technique [25] may be used in the case of photomultiplier calibrations using a storage ring. A reasonably small number of electrons (about 100) is allowed to circulate in the ring. As the electrons are lost from orbit one by one, the decrease in visible emission due to the loss of one electron is noted and from this the exact total number of electrons may be readily obtained. Note with this method the absolute amount of radiation need not be measured. This technique will be available for use at SURF–II. In another method, the radiation is allowed to fall on a suitable calibrated detector. The number of electrons is determined by dividing the measured flux by the flux of synchrotron radiation a single electron radiates to the detector. At SURF–I the spectral interval used for absolute measurement of the synchrotron flux was a 100 Å wavelength band around 5150 Å because an irradiance standard could be used to calibrate a silicon photodiode-filter combination in this band. The visible region of the spectrum was also chosen because for $\lambda >> \lambda_c$ (for 170 MeV electrons accelerated at SURF–I $\lambda_c = 940$ Å) the radiated power is approximately independent of the electron energy and proportional to $\lambda^{-7/3}$. Thus small fluctuations in the energy have a negligibly small effect on the determination of the number of electrons in orbit. Thus the number of electrons is given simply by

$$n_e = \frac{F(\lambda_0, \Delta\Omega)}{P(E, \lambda_0)}. \qquad (7)$$

Explicitly writing the integrations over the variation of the detector sensitivity $R(\lambda)$, the filter transmission $T(\lambda - \lambda_0)$ and the radiated power from the synchrotron we have

$$F(\lambda_0, \Delta\Omega) = \frac{n_e}{2\pi} \int_{\Delta\Omega} \int_{\lambda_1}^{\lambda_2} \int_{E(t_1)}^{E(t_2)} P(E, R, \theta, \lambda) T(\lambda - \lambda_0) R(\lambda) dt d\lambda d\Omega \qquad (8)$$

which reduces to

$$F(\lambda_0, \Delta\Omega) = n_e P(E_{\max}, \lambda_0) \frac{\Delta\Omega}{2\pi} A \qquad (9)$$
$$= K V_F$$

under the following simplifying assumptions: (a) that $P(E, R, \theta, \lambda) \approx P(E, R, \lambda)$ (the variation of $P(E, R, \theta, \lambda)$ over the aperture is about 0.1 percent over a 1 cm diameter aperture 13.26 meters from the tangent point); (b) the gate time used for determining $F(\lambda_0, \Delta\Omega)$ is short enough so that $P(E, R, \theta, \lambda) \approx P(E_{\max}, R, \theta, \lambda)$ and (c) the filter is sharp enough so that $P(E_{\max}, \lambda) = P(E_{\max}, \lambda_0) \quad (1 + a(\lambda - \lambda_0))$. Under these assumptions the quantity A is a simple calculable factor while K is the detector sensitivity where F watts input to the detector-filter amplifier combination produces a response of V_F volts. The quantity K is determined by the detector system response to an irradiance standard. Thus

$$K V_S = \int_{\lambda_1}^{\lambda_2} \int_{\Delta\Omega'} S(\lambda, \theta) T(\lambda - \lambda_0) d\Omega d\lambda \qquad (10)$$

which reduces to

$$K V_S = S(\lambda_0) \Delta\Omega' B \qquad (11)$$

if the standard spectral irradiance $S(\lambda, \theta)$ is constant over the solid angle $\Delta\Omega'$ and if the filter has a narrow enough bandpass so that $S(\lambda, \theta) = S(\lambda_0) \ (1 + b(\lambda - \lambda_0))$. The quantity B is eq (11) a calculable factor like A in eq (9). Substituting eq (11) into eq (9) we have

$$n_e = C\frac{S(\lambda_0)}{P(E_{max}, \lambda_0)}\frac{V_F}{V_S} \quad (12)$$

with $C = 2\pi B\Delta\Omega'/(A\Delta\Omega)$ a calculable quantity containing the solid angle factors and the results of integrating eq (8) and eq (10) under the assumptions listed in the preceeding paragraphs.

This approach is valid for both accelerated and monoenergetic electrons. Although the case of an accelerated beam was used as an example, the form of eq (12) is the same for monoenergetic electrons. (The most important difference is that for accelerated electrons one must measure the instantaneous number of electrons since the power averaged over one acceleration cycle is used to compute the flux incident on the spectrometer.) The determination of the number of circulating electrons by this method is essentially reduced to a problem of measuring a voltage ratio. The sources of error intrinsic to this method will be discussed in later paragraphs.

The vuv irradiance incident on the spectrometer can be given in terms of eq (6) and eq (12):

$$F(\lambda, \Delta\Omega) = C\frac{S(\lambda_0)}{V_S}\frac{V_F}{P(E_{max}, \lambda_0)}P(E_{max}, \lambda). \quad (13)$$

The spectral irradiance incident on the spectrometer is known in terms of calculated quantities and a measured voltage ratio.

Calculations evaluating $P(E_{max}, \lambda)$ were carried out to a accuracy of better than 1 percent. For monoenergetic electrons, because the integration over the time variation of the electron energy is eliminated, the accuracy of the calculation is an order of magnitude greater than the uncertainty in the flux due to uncertainties in the electron energy. Determining the response of the instrument, $R(\lambda, \Delta\Omega)$, is the next task.

3.3. Positioning of Spectrometer

To determine the flux on the spectrometer, the spectrometer must be aligned at a known angle with respect to the orbital plane of the radiating electrons. In addition, any temporal variation of the inclination of the orbit must be determined since the irradiance is a strong function of the azimuthal angle θ.

Two types of spectrometers have been calibrated at SURF–I: A grazing incidence monochromator [26] and a Wadsworth [27] spectrometer using photographic detection. The instrument to be calibrated, S, (see fig. 6) was installed behind the calibrated detector, C, aperture assemble, A, and an alignment procedure was undertaken with the aid of the visible radiation from the orbiting electrons. The visible radiation was also used to check the effectiveness of the baffling system in eliminating reflections. Since the light beam is almost parallel (average divergence is 3 mrad) and about 1 cm in diameter it is impossible to fill the grating of many spectrometers. Therefore, provisions were made to scan the beam over the grating by moving the instrument. It is not necessary to make absolute flux measurements during these scans but only measurements relative to the point of calibration on the grating. For this procedure synchrotron radiation was used for convenience rather than out of necessity. At the storage ring radiation facility, SURF–II, two ports with a direct view of the beam will be provided for instrument calibration. However, at the present time the user must supply his own test chamber to house the instrument to be calibrated.

Synchrotron radiation is highly polarized with the most intense component of polarization lying in the orbital plane. To test the instrument response to this polarization, provisions were made to rotate each instrument about the grating pole. For the grazing incidence monochromator the axis of rotation was coincident with a line drawn from the grating pole to the center of the entrance slit. For the Wadsworth mounting the instrument rotated about an axis passing through the grating pole perpendicular to the rulings. To preserve the geometry of illumination under rotation it was important to align the axis of rotation with the axis of symmetry of the beam. By using the visible radiation from the synchrotron it was possible to make these adjustments without evacuating the instrument chamber. Therefore the alignment procedure could be carried out in a straightforward convenient manner.

At SURF–I the position of the orbital plane could be determined and instruments could be aligned with the plane so that the beam and the optic axis are coincident. The position of the orbital plane was determined by scanning in the vertical direction a grazing incidence monochromator set at a short wavelength (about 200 Å) and oriented so that its entrance slit was horizontal. The position where the maximum output from the monochromator occurs defines the position of the orbital plane. The monochromator was left in this position and the movable aperture, A, was scanned vertically to determine the upper and lower slit occultation positions. Setting the aperture at the average of the upper and lower slit occultation positions aligns its center with the center of the entrance slit. The aperture is set on the orbital plane, the entrance slit of the instrument for calibration is then aligned with the aperture and the optic axis can be aligned with the synchrotron radiation beam by centering the radiation transmitted through the entrance slit on the grating.

Unfortunately, during the course of a day's operation at SURF–I thermal gradients in the magnet produced beam motions of up to one milliradian. Such a motion can produce a large variation in the flux illuminating the optical elements of an instrument. As an example, in figure 7 the variation in output flux from a special torroidal grating monochromator at a wavelength of 188 Å correlates very closely with the temporal variation of the position of the beam illuminating the torroidal grating. Notice that a motion of 0.26 mrad produces a flux variation of 7 percent. A beam motion monitor described in the next section was devised to

594-051 O - 76 - 7

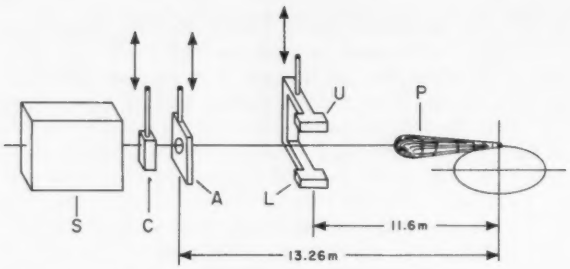

FIGURE 6. *Schematic diagram of spectrometer calibration apparatus.*

Synchrotron radiation P, illuminates detectors U and L in the beam motion monitor and the calibrated aperture A. Radiation passing through A illuminates either the spectrometer S or the calibrated detector-filter (C).

track this beam motion in addition to providing intensity monitoring during calibration. By monitoring the beam motion it was possible to determine that the beam always moved in one direction, that the greatest motion occurred during the first hour or so of operation, and finally that the daily motion of the beam was regular. A calibration could be carried out when the beam was positioned within acceptable limits.

Beam motion was a potential source of systematic error and a needless complication to the calibration procedure. The conversion of the NBS synchrotron into a storage ring will virtually eliminate beam motion because (a) there will be no eddy current heating in the magnet and (b) the only other important source of heat, the power dissipated in the magnet excitation coils, has been eliminated by water cooling the coils. Consequently, spectrometer calibration at SURF–II will be much more accurate and straightforward.

4. Parameter Measurement and Their Uncertainties

4.1. Measurement of the Electron Current and Beam Position

This basic monitoring system consisted of a detector-filter combination which was calibrated periodically with an irradiance standard and a pair of detectors used both as a beam motion monitor and as an intensity monitor during the spectrometer calibration when the calibrated detector-filter was removed from the beam. The geometrical layout is shown schematically in figure 6. The beam motion monitor was located in front of the calibration aperture 11.6 meters from the tangent point. The central portion of the beam of radiation passed between the monitor diodes to reach the calibration aperture (A). The beam was then allowed to enter either the calibrated detector-filter (C) or the spectrometer (S). The two diodes serving as the beam motion monitor (U,L) were separated by an angle of 3.3 mrad. Nicol prism polarizers placed in front of these detectors were adjusted to view the component of the beam polarized perpendicular to the orbital plane.

Each detector was displaced symmetrically about the orbital plane and viewed radiation for which the

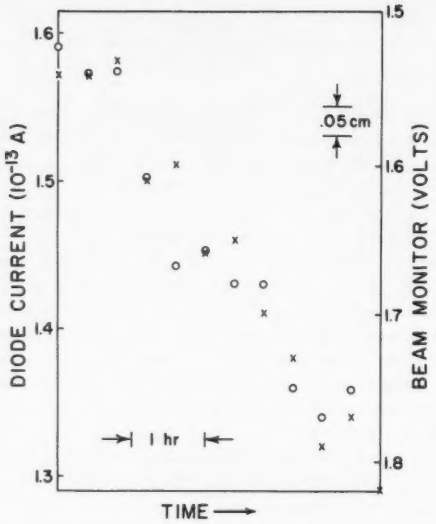

FIGURE 7. *Output from the beam motion monitor (BMM) shown as 0 and the output of a diode shown as* x *versus time.*

The diode measures the vuv flux diffracted by a grating illuminated directly by the synchrotron radiation beam.

intensity varied linearly with angle. This is illustrated in fig. 8. Thus if the beam moved upward slightly the signal in the upper detector (U) would decrease an amount proportional to the beam motion and the signal in the lower detector (L) would increase by about the same amount (assuming the sensitivity of the detectors

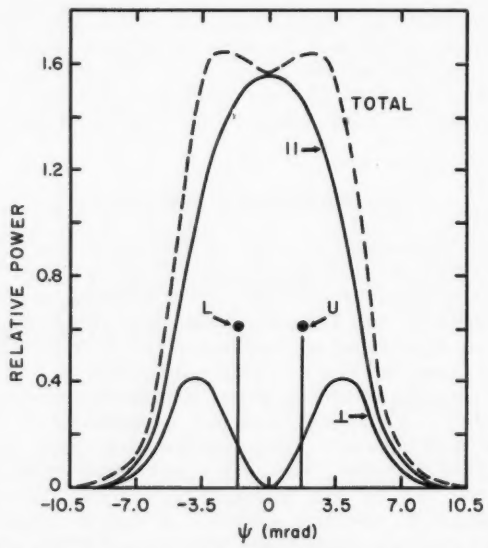

FIGURE 8. *Angular distribution of the synchrotron radiation showing the total angular distribution of the flux as well as the component of the flux polarized parallel* (||) *and perpendicular* (⊥) *to the orbital plane.*

The angular position of the upper (U) and lower (L) beam motion monitors is shown.

are the same). Thus the beam motion, $\Delta\phi$, is proportional to the fractional change of the signal level in the detectors. To first order the beam displacement $\Delta\phi = K(U-L)/(U+L)$, assuming that the sensitivity of the detectors is adjusted equal. The output from the upper detector (U) and the lower detector (L) were amplified and manipulated so that the sum $(L+U)$ and difference $(L-U)$ were obtained. Using the $(L-U)$ signal as the numerator input and the $(L+U)$ signal as the denominator input to a quarter-square analogue dividing circuit, the output ratio $R=\frac{L-U}{L+U}$ was proportional to the beam position. A block diagram of the electronic circuitry of the beam motion is shown in fig. 9a. The monitor was calibrated by moving the

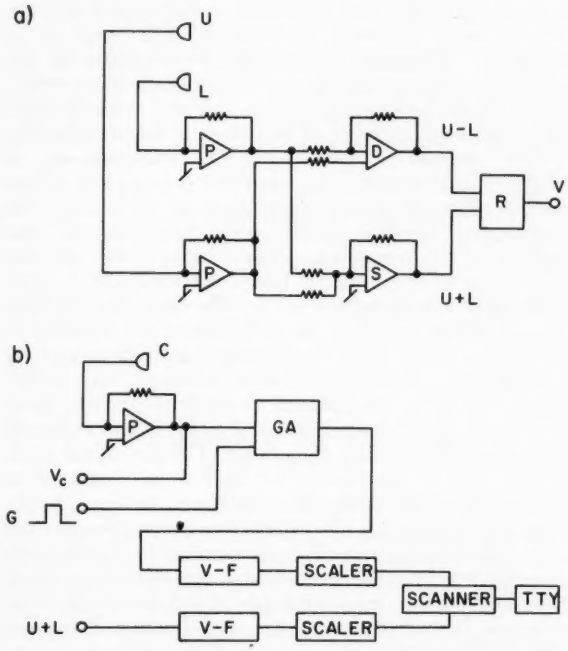

FIGURE 9. *(a) Schematic of the electronic circuitry of the beam motion monitor.*

Photocurrents from U and L are converted to voltages by P. The sum and difference of these voltages are generated in the amplifiers S and D respectively. The output of S and D is the input for a quarter square divider R, which provides the ratio $(U-L)/(U+L)$.

(b) Schematic of the electronic circuitry used to transfer calibration from calibrated detector to U + L.

Photocurrent from calibrated detector-filter combination C is converted to a voltage by P. The output of P or a calibration V_c is the input of a gated amplifier GA whose output is digitized along with $U+L$, the sum signal from the beam motion monitor. The signals $U+L$ and GA are counted on scalers, scanned and printed on a teletype.

detectors some distance and noting the signal change in R. The calibration curve is shown in fig. 10. The sum signal $(L+U)$ to first order is independent of beam position and was used as an intensity monitor during actual spectrometer calibrations to determine the temporal variation in n_e while R monitored the change

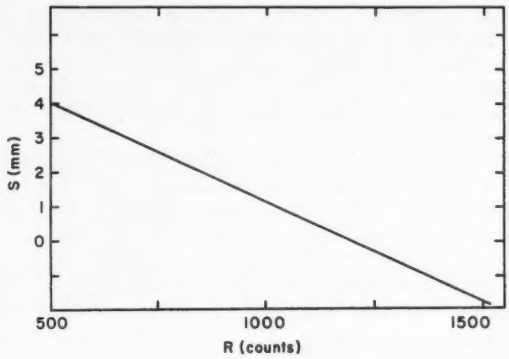

FIGURE 10. *The position (S) of the beam motion monitor (BMM) versus the output of ratio* R *of the BMM.*

in beam position. The calibrated detector-filter system provided the absolute measurement of n_e.

An improved system for locating the orbital plane will be used at SURF–II. A pair of open xuv diodes covered with thin carbon foil filters (transmitting between 40 and 250 Å) will be placed above and below the orbital plane. The short wavelength is used to minimize the divergence of the synchrotron radiation beam (see fig. 2) so as to obtain maximum sensitivity. The two diodes will be mounted on a rotatable plate allowing their positions to be interchanged. Thus the position of the orbital plane can be determined as the height at which an interchange of the diodes produces no change in the ratio of the signals from the diodes. This system is expected to be a big improvement over that used on SURF–I.

The temporal stability of the sensitivity of the calibrated detector-filter system and the monitor detectors was sufficient so that it was adequate to calibrate the detector-filter system with an irradiance standard just before and just after the actual spectrometer calibration took place. In a similar manner the calibration was transferred to the monitor diodes sometime during the calibration. Figure 9b shows schematically the measuring system used with the calibrated detector-filter system. The instantaneous voltage is measured by putting the output of the photodiode amplifier (which is fast enough to track the time variation of the light during the acceleration cycles) into a linear gate that is synchronized to the repetition frequency of the accelerator. A peak-reading voltmeter is used to measure and suitably average the voltage pulses that are proportional to n_e. The width and position of the gate input to the gated linear amplifier is suitably chosen so that the light output in the visible is approximately constant over that portion of the acceleration interval. For the accelerated electrons the complicated integral over the time variation of the electron energy is replaced by a small correction factor amounting to a few percent of the value of flux obtained for monoenergetic electrons of energy E_{max}. This numeric simplification is offset to some extent by more complicated electronics. For stored monoenergetic electrons it is unnecessary to use a gated amplifier, an ordinary

digital voltmeter or other suitable recording device can be used to measure the voltage, and, moreover, no correction is necessary because the electron energy is constant. Because of these factors, n_e can be determined much more accurately for stored electrons than for accelerated electrons.

Two types of spectrometers have been calibrated at SURF–I a grazing-incidence monochromator [26] and a Wadsworth [27] spectrometer using photographic detection. For the monochromator it was easy to use the same visible detector gate for gating the output of the monochromator. For the spectrograph, n_e was assumed constant over the acceleration cycle. This assumption was tested and will be discussed in the section 4.3.

The NBS irradiance standard used to calibrate the filter-detector system was too intense to be used at the calibration distance (1 meter). To achieve the signal level appropriate to the synchrotron (nW/nm), the calibration was carried out with the lamp located at distances between 25 m and 40 m. Thus the validity of the inverse square law was assumed in order to scale the intensity from the lamp calibration distance (1 m) to the detector calibration distance (25 m–40 m). We determined that the measurements over the 25 m–40 m path were consistent with the inverse square law to ±1.0 percent, the uncertainty level of the measurements. Reproducibility of the measurements with respect to the realignment, lamp current adjustment, detector orientation, etc. was ±2 percent. Lamp calibration was tested by comparing the working irradiance standard with another standard. The intensity of the working standard derived from the comparison deviated less than 2 percent from its specified value. Combining these sources of errors in quadrature, the quantity $S(\lambda_0)$ in eq 12 could be determined with a probable error of 3 percent. In table 2 we have listed the sources of the errors that contribute to the uncertainty of n_e. Combining all these errors in quadrature we find that n_e can be determined with a probable error of 6 percent.

Possible sources of systematic errors that pertain to the determination of n_e were investigated such as the assumption that the standard lamp was a point source (implying the validity of the inverse square law), the possibility that the detector interference filter was not properly blocked, or the presence of reflected radiation sources either at the synchrotron or the lamp calibration hall. From an analysis of these possible sources of errors and other tests, we estimate that sources of systematic errors might contribute a 5 percent uncertainty to the measurement of n_e.

TABLE 2. *Sources of errors contributing to the uncertainty in the determination of the number of electrons, n_e, in SURF–I.*

Source of Error	Magnitude of error
Transfer of calibration to beam motion monitor	3%
Determination of change in detector efficiency	3%
Correction factor for accelerated electrons	1%
$S(\lambda_0)$	3%
C	1%
$P(E_{max}, \lambda_0)$	1%
V_F	1%
V_S	1%
Probable error of n_e =	6%

A storage ring (SURF–II) is now the source of synchrotron radiation at NBS. Using improved techniques and fewer transfers with SURF–II, the uncertainty in the measurement of n_e should be reduced by at least a factor of two to a probable error of 3 percent. By further testing and cross checking we expect to reduce the systematic error by the same amount. It is very clear that the increased stability both in time and in space achieved at SURF–II will result in an excellent calibration facility for wavelengths in the vuv. Furthermore with the low intensity electron counting method mentioned section 3.2 the error is zero since the total number of electrons is known exactly.

The method of positioning the spectrometer at SURF–I was described in the early paragraphs of this section. The estimated uncertainty in positioning the instrument on the orbital plane according to that method is ±3 mm at a distance 13.26 m from the tangent point or ±0.2 mrad. Beam motion monitor drift and other uncertainties associated with the monitor system would increase the positioning uncertainty to ±4 mm or ±0.3 mrad. To estimate the error caused by misaligning a spectrometer with respect to the orbital plane, the flux that passed through a circular aperture 1 cm in diameter, located a specified angle off the orbital plane, was calculated. The fractional error in the flux determination for such a misalignment is shows as a function of wavelength in fig. 11. As expected the greater the misalignment the greater the error. However, for displacements of up to 0.4 mrad the error is less than 10 percent for wavelengths greater than 200 Å. For misalignments of 0.8 mrad the error exceeds 10 percent only for wavelengths less than 600 Å. This strong dependence of the error on wavelength is due, of course, to the highly collimated nature of synchrotron radiation, particularly the fact that short wavelength radiation is more tightly collimated than longer wavelength radiation (see fig. 2). Therefore, as the aperture is displaced with respect to the orbital plane, the shorter wavelength radiation becomes occulted first while the longer wavelength radiation, due to its broader angular distribution, is relatively unimpeded. By confining the alignment error to ±4 mm, (0.3 mrad) at SURF–I the fractional error in intensity is limited to something less than 5 percent at 200 Å decreasing to about 0.5 percent at 1200 Å.

At the SURF–II calibration facility the position of orbital plane will be known to high precision by means of the orbital plane locator described in section 4.1. Therefore errors introduced bacause of uncertainties in the beam position will be negligibly small.

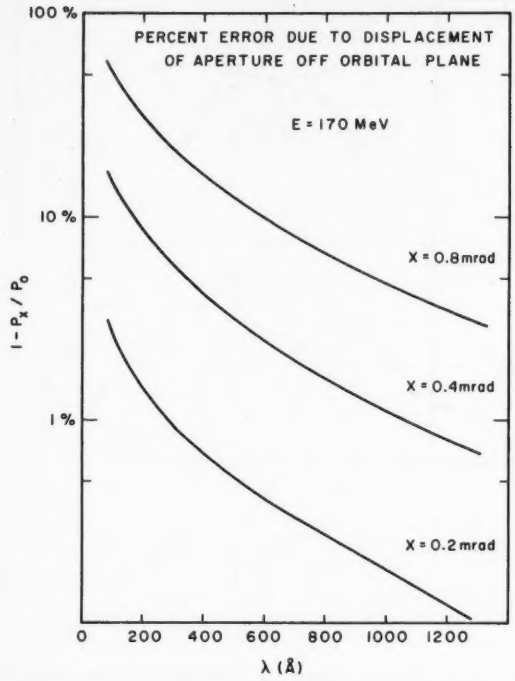

FIGURE 11. *The percent error due to the displacement of aperture A in figure 7 by the indicated angle* X *from the orbital plane.*

The curves were calculated for accelerated electrons whose maximum energy was 170 MeV.

4.2. Uncertainty in the Orbital Radius of the Electrons

The magnet geometry at SURF–I and SURF–II is such that the electrons travel in very nearly circular orbits. Thus R, the orbital radius, is simply related to the rf accelerating frequency ν_0 (known to a few parts-per-million). However in practice, since the beam executes small betatron oscillations about the equilibrium orbit, knowledge of the value of R is limited by the extent of these horizontal oscillations which typically have an radial amplitude of a few mm. However since the oscillations result in an instantaneous radius that is equally likely to be larger or smaller than the equilibrium radius, errors in flux determinations tend to cancel. The beam also executes betatron oscillations in the vertical plane which smear the angular distribution somewhat. The extent of this smearing has been computed [28] and while the sum of the intensity due to both polarizations changes very little from the distribution of radiation by a point source of electrons, the magnitude of individual polarization components is affected somewhat. The effect is very small in SURF–I because the observations [4] of both polarization components deviated only slightly from distribution expected for a point source. For the spectrometer calibrations achieved on SURF–I a point source was assumed and the flux distribution was computed accordingly. We estimate that this assumption contributes an error of less than 1 percent to the total flux calculations. Also the beam rather than being 100 percent polarized in the orbital plane is about 95 percent polarized. The response of a spectrometer to both planes of polarization while an important test does not affect the accuracy of the instrument calibration for unpolarized radiation since the average response to both orientations is used. However to properly determine the amount of polarization an instrument introduces to unpolarized radiation the degree of polarization of the radiation on the instrument should be measured.

4.3. Determination of E, the Electron Energy

In its early life the synchrotron supplying radiation for SURF–I was used for the production of gamma rays. The maximum energy of the electrons accelerated in this synchrotron was determined, at that time, both from the threshold energy for the production of π^0 mesons and from the kinematics of the reaction $h\nu + C^{12} \rightarrow p + B^{11}$. An integrating fluxmeter measured the ac magnetic field at a point away from the electron orbit, to which the energy calibration of the nuclear reaction could be attached (since $E_{max} \propto B_{max}$). This fluxmeter was also used to measure the maximum electron energy when the synchrotron became the radiation source for SURF–I. At the time of calibration the maximum energy of the electrons was known to 0.6 percent.

At SURF–I measurements were made to test the assumption made in section 3.1 that (a) the electron energy varied sinusoidally and (b) that the number of electrons captured, n_e, was constant over the acceleration cycle. A grazing incidence monochromator was set at 212 Å. The output pulses from this monochromator were accumulated in a multichannel analyzer (MCA) whose sweep was synchronized with the acceleration cycle of the synchrotron. The analyzer display, shown as open circles in fig. 12, represents the instantaneous intensity (averaged over many machine cycles) as a function of time. The dwell time for each channel is 50 μs. The vertical aperture of the apparatus to the 212 Å radiation was large enough so that all of the radiation entered the monochromator. The solid line represents the flux integrated over all azimuthal angles and normalized to the peak of the time distribution. The flux was calculated for an electron energy variation proportional to sin $(2\pi 60t)$. The time scale has an arbitrary zero so that the maximum count rate, which corresponded to the maximum electron energy, occurred at $t = 2.2$ ms rather than $t = 4.17$ ms. Note the step at 3.6 ms, about 1.4 ms after the maximum count rate. The rf voltage is turned off at this time because the electrons can no longer be maintained in a stable orbit as the magnetic field decreases. From a comparison of the calculated curve with the observations it is quite plain that the electron energy is proportional to sin $2\pi 60t$. If the number of electrons captured per cycle were not constant then the data in fig. 12 would not fit the symmetrical calculated curve. As a by-product of the measurement we may note that

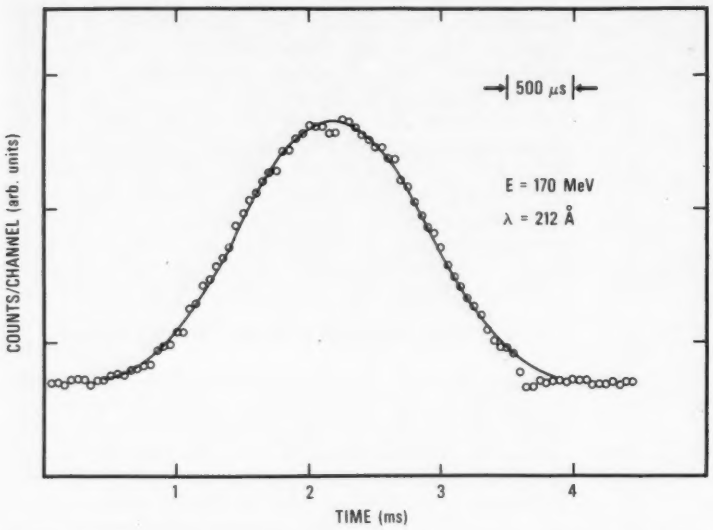

FIGURE 12. *Photon flux per 50 μs channel dwell time versus time (zero displaced) shown as 0.*

The flux was integrated over many cycles at 212 Å for electrons accelerated to a maximum energy of 170 MeV. The solid line is the calculated photon flux.

if the maximum energy were much greater than 170 MeV, the full width at half maximum of the distribution would be somewhat wider since the electrons would radiate at 212 Å sooner, broadening the time distribution. However, this is not a very sensitive electron energy indicator because for an electron whose peak energy is 170 MeV a 10-MeV variation in energy produces only a 7 percent variation in the full width at half maximum of the time varying light flux at 200 Å. Nonetheless, the observations are consistent with a maximum electron energy of 170 MeV with an uncertainty of ±5 MeV. As a further consistency check the accuracy of maximum electron energy changes was tested by another experiment. As before the output of the monochromator at 212 Å was recorded by a MCA synchronized to the acceleration cycle of the synchrotron. The maximum electron energy was first set at 170 MeV and the signal was integrated for a time determined by integrating the light flux in the visible to some predetermined level. The maximum energy was then set at 160 MeV and the integration was carried out using the multichannel analyzer until the visible light integration reached the same level as before. Since the visible flux is very nearly independent of energy (the flux at 5150 Å for 160 MeV electrons is only about 2 percent less than the flux at 5150 Å for 170 MeV electrons), an equal number of electrons contribute to the time distribution for $E_{max} = 170$ MeV as for $E_{max} = 160$ MeV (once the 2 percent correction is made). As these curves are normalized to the same number of electrons, the instantaneous flux radiated by electrons when their energy is E should be the same independent of the eventual maximum energy. If $E_{max} = 170$ MeV the flux radiated by these electrons at 160 MeV should equal the flux radiated by electrons at their maximum energy when $E_{max} = 160$ MeV.

In figure 13 the 170 MeV data is shown as dots while the 160 MeV data (normalized to the same total number of electrons) is shown as solid squares. The large tic on the abscissa indicates the time when electrons whose maximum energy is 170 MeV have an instantaneous energy of 160 MeV. A horizontal line indicating the instantaneous flux radiated by 160 MeV electrons guides the eye to the data where the maximum electron energy is 160 MeV. The correspondence between the data is quite clear. Two short horizontal lines, one above and the other below the data for which the maximum electron energy was 160 MeV, indicate the instantaneous flux radiated by electrons of energy 158 MeV and 162 MeV. From figure 13 we see a change of electron energy of 2 MeV produces a rather large change in intensity at this wavelength. From this data we infer that the probable error in the energy change of 10 MeV was about 0.2 MeV.

To determine the systematic error introduced by the quoted uncertainty in the maximum energy (0.6%), the percent change in flux for an electron energy change of 1 MeV (0.6%) at 170 MeV is plotted as a function of wavelength in figure 14. Notice as the wavelength increases the photon flux change is much less sensitive to changes in the electron energy. At 200 Å such an uncertainty in energy results in a 9 percent uncertainty in the photon flux. This uncertainty decreases monotonically to 1 percent at a wavelength of approximately 2000 Å.

At the SURF–II storage ring a great deal of effort has been expended to measure the (now dc) magnetic field at the orbit to 0.1 percent. A highly accurate

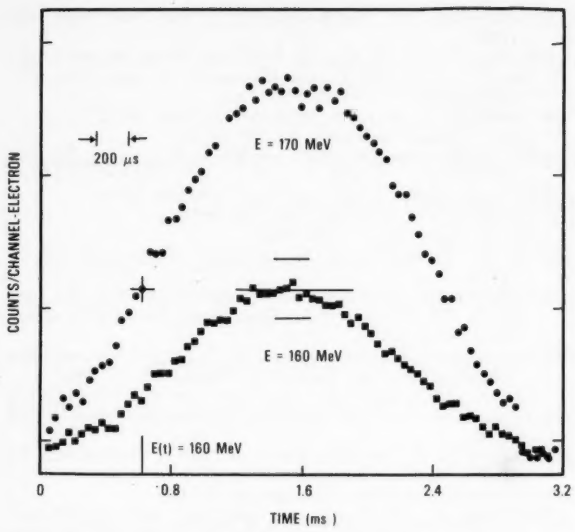

FIGURE 13. *Instantaneous photon flux normalized to the same total beam current for two maximum energies:* $E_{max} = 170$ *MeV and* $E_{max} = 160$ *MeV.*

Vertical line on abscissa denotes time when electrons with $E_{max} = 170$ MeV have an energy of 160 MeV. The horizontal lines indicate the maximum flux expected if $E_{max} = 162$ MeV or if $E_{max} = 158$ MeV.

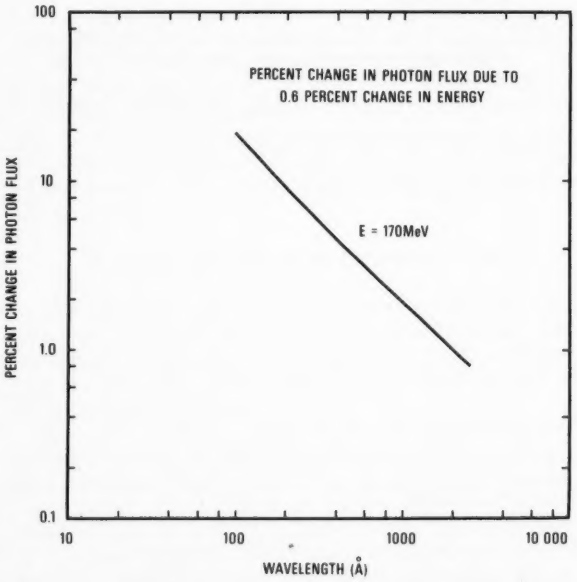

FIGURE 14. *Percent change in photon flux emitted by accelerated electrons with* $E_{max} = 170$ *MeV due to a 0.6 percent change in electron energy.*

Hall probe (calibrated by the NBS magnetic field calibration group to 0.1%) is inserted at a point on the electron orbit. Because an active probe would interfere with the electron beam, the orbital field calibration was transferred to the Hall probe field monitor located away from the electron orbit.

With the magnetic field and hence the electron energy known to this accuracy, radiometric uncertainties will be much less, as is indicated in figure 15. In this figure we show as a function of wavelength the flux change, passing through an aperture subtending an angle 2 mrad centered on the orbital plane and 1 mrad along the orbit, that is due to a change in electron energy of 0.1 percent. The flux change for 200 MeV *monoenergetic* electrons is shown in the top curve while the bottom curve represents the flux change for 240 MeV *monoenergetic* electrons. With the electron energy known to this accuracy, it is possible to keep the uncertainties in photon flux less than 5 percent for all wavelengths greater than 40 Å, the practical short wavelength limit of our storage ring. Now instead of being one of the major sources of systematic error, especially at shorter wavelengths, the uncertainty in the energy introduces one of the smaller errors into the calibration process.

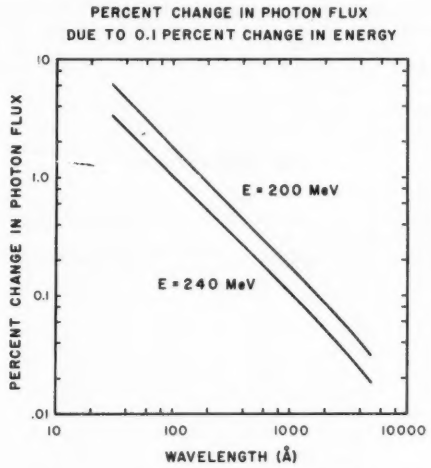

FIGURE 15. *Percent change in photon flux emitted by monoenergetic electrons with the energies shown for a 0.1 percent charge in the electron energy.*

The uncertainty of 0.1 percent is that expected at SURF-II.

5. Summary

In this report we have dealt with the use of synchrotron radiation as an absolute irradiance standard in the vacuum ultraviolet in general. In addition, we detailed the calibration procedures devised at the NBS-SURF-I facility for several spectrometer calibrations. General sources of systematic errors were identified and their importance was studied relative to SURF-I. Improved calibrations are anticipated at the NBS storage ring (SURF-II) based mainly on better energy determination of the monoenergetic electrons, higher spatial and temporal beam stability due to the storage ring operation and finally, a more accurate determina-

tion of the circulating current. Table 3 is a final summary of the sources of errors for SURF–I and SURF–II and the role they play in the overall accuracy of a calibration.

TABLE 3. *Sources of errors in the use of synchrotron radiation as an absolute source*

Error source	Type[a]	Magnitude of error	
		SURF–I	SURF–II
Determination of n_e	*R*	6%	3%
	S	6%	3%
Electron energy calibration	*S*	8%–1%[b]	5%–0.04%[c]
Electron energy variation	*R*	8%–1%[b]	Negligible[d]
Orbital radius	*S*	< 2%	< 1%
Uncertainty in beam position	*S*	5%–0.5%[b]	< 1%
Finite source size	*S*	< 1%	< 1%
Precision of calculated model	*S*	< 4%	< 1%
Total	*R*	11%–6%	3%
	S	< 10%	< 6%

[a] *R* designates random errors and *S* designates systematic errors.
[b] The first value is the uncertainty at 200 Å and the second value is the uncertainty at 2000 Å.
[c] The first value is the uncertainty at 40 Å and the second value is the uncertainty at 2000 Å.
[d] A readout of electron energy will be available.

6. References

[1] Canfield, L. R., Johnston, R. G., and Madden, R. P., Appl. Opt. **12**, 1611 (1973).
[2] Saloman, E. B., and Ederer, D. L., Appl. Opt. **14**, 1029 (1975).
[3] Tomboulian, D. H., and Hartman, P. L., Phys. Rev. **102**, 1423 (1956).
[4] Codling, K., and Madden, R. P., J. Appl. Phys. **36**, 380 (1965).
[5] Bathow, G., Freytag, E., and Haensel, R., J. Appl. Phys. **37**, 3449 (1966).
[6] Lemke, D., and Labs, D., Appl. Opt. **6**, 1043 (1967).
[7] Boldt, G., Space Sci. Revs. **11**, 728 (1970).
[8] Ott, W. R., Fieffe-Prevost, P., and Wiese, W. L., Appl. Opt. **12**, 1618 (1973).
[9] Böhm, W., and Labs, D., Appl. Opt. **10**, 2021 (1971).
[10] Van Raan, A. F. J., Physica **65**, 566 (1973).
[11] Pitz, E., Appl. Opt. **8**, 255 (1969).
[12] Ott, W. R., and Wiese, W. L., Optical Engineering **12**, 86 (1973).
[13] Zaidel, A. N., Malyshev, G. M., and Shreider, E. Ya., Zh. Tekh. Fiz. **31**, 129 (1961) [Eng. trans. Soviet Phys.-Tech. Phys. **6**, 93 (1961)].
[14] Gladushchak, V. I., and Shreider, E. Ya., Opt. i Spektroskopia **14**, 815 (1963) [Eng. Trans., Opt. Spectr. **17**, 75 (1964)].
[15] Mumma, M. J., and Zipf, E. C., J. Opt. Soc. Am. **61**, 83 (1971).
[16] Rusbüldt, D., and Thimm, K., Nucl. Instrum. Methods **116**, 125 (1974).
[17] Godwin, R. P., Springer Tracts in Modern Physics Vol. **51** (Berlin: Springer-Verlag (1969)).
[18] Codling, K., Rep. Prog. Phys. **36**, 541 (1973).
[19] Madden, R. P., Synchrotron Radiation and Applications, Chapter in X-Ray Spectroscopy, Ed., L. Azaroff (McGraw-Hill, 1974) pp. 338–378.
[20] Key, P. J., Metrologia **6**, 97 (1970).
[21] Ott, W. R., and Bartoe, J. D., J. Opt. Soc. Am. **62**, 1372 (1972).
[22] Struck, D., and Wende, B., J. Opt. Soc. Am. **62**, 96 (1972).
[23] Schwinger, J., Phys. Rev. **75**, 1912 (1949).
[24] Saloman, E. B., Appl. Opt. **14**, 1391 (1975).
[25] Fairchild, T., private communication.
[26] Higgins, James, Salter, R., and Heroux, Leon, private communication.
[27] Bartoe, John, and Bruckner, Keith, private communication.
[28] Zhukovskii, V. Ch., and Shishanin, O. E., Opt. i Spektroskopia **31**, 857 (1971) [Eng. Trans., Opt. Spectr. **31**, 465 (1971)].

(Paper 79A6–873)

JOURNAL OF RESEARCH of the National Bureau of Standards—A. Physics and Chemistry
Vol. 79A, No. 6, November–December

Corrections to Paper Entitled "Third Virial Coefficient for Air-Water Vapor Mixtures"

R. W. Hyland and E. A. Mason*

Institute for Basic Standards, National Bureau of Standards, Washington, D.C. 20234

(August 28, 1975)

This note points out errors in the values of the third virial coefficients for pure water vapor which appeared in a 1967 paper by Hyland and Mason. The errors arose while converting from the units of Goff and of Keyes to the desired units of (liter/mole)^2. The consequences of the errors are outlined, and it is shown that there is no effect on the primary results of the paper, namely, in the preferred values of the third interaction virial coefficient for air-water vapor mixtures, C_{aww}.

Key words: Chemical association; Lennard-Jones potential parameters; third interaction virial coefficients; virial coefficients; water vapor-air mixtures.

1. Introduction

In 1967 Hyland and Mason [1] [1] published a paper in which a third interaction virial coefficient for air-water vapor mixtures, C_{aww}, was derived. In that paper, a computational error was committed while converting the third virial coefficients for pure water, C_{www}, from the units of Goff [2] and Keyes [3] to the desired units of (liter/mole)^2. This note points out the consequences of that error.

2. Error Source, and Consequences

The incorrect values of C_{www} appear in the last two columns of table 1 of [1]. The proper values would be obtained by subtracting the squares of the corresponding second virial coefficients. The revised version of table 1 is given below.

The errors were propagated into the first two columns of table 2 of [1], which gives values for B_{ww_2}, into equations (21a, b) and (24b, c), and finally into the C_{aww} values of table 3 based on eqs (24b, c). The revised version of table 3 is given below. The appendix to this note indicates the changes necessary to correct the text, and points out that the C_{aww} values which appear in table 3 (revised) are not significantly different from those given in table 3 of [1].

The viscosity-based values of C_{aww}, which are the preferred values, and their stated uncertainties, are the same in both versions of table 3. Obviously results in reference [1] depending on the incorrect values of C_{www} must be ignored.

TABLE 1. *(Revised) Experimental values of the second and third virial coefficients of water vapor; extropolated values in parentheses*

Temp.	$-B_{ww}$ cm^3/mol			$-C_{www}$ liter^2/mol^2	
	Goff [4]	Keyes [8]	Ave.	Goff [4]	Keyes [8]
°C					
0	(1834)	1854	1844	(61.1)	90.4
10	1510	1520	1515	(32.4)	47.0
20	1265	1266	1266	(18.1)	26.0
30	1074	1070	1072	(10.5)	15.1
40	924	917	920	(6.34)	9.03
50	803	794	798	(3.93)	5.63
60	705	695	700	2.51	3.58
70	625	613	619	1.64	2.38
80	558	546	552	1.09	1.62
90	501	489	495	0.738	1.13
100	(453)	441	447	.506	0.793

3. Appendix 1

In reference [1] the paragraph ending page 222, and the paragraph below eq (20b) could be rewritten by substituting the value -0.89 liter/mol for the -1.11 value, -0.57 liter/mol for the -0.79 value, and -0.73 liter/mol for the -0.95 value.

The paragraph containing eqs (21a, b) would be rewritten as follows:

Empirical curve fitting with B_{ww2}, matching at the adjusted limit of -0.73 liter/mol, leads to the parameters

* Present address: Brown University, Providence, R.I. 02912.

[1] Figures in brackets indicate the literature references at the end of this paper.

$$t^* = 1.1,\ \sigma_{ww_2} = 3.45\ \text{Å},\ \frac{\epsilon_{ww_2}}{k} = 380\ \text{K}. \quad (21a)$$

TABLE 3. *(Revised) Calculated values of the third interaction virial coefficient* C_{aww} *based on the parameters of eqs (24) and (25)*

Temp.	$-C_{aww}$, litter²/mol²					
	Virial			Viscosity*	Limits	
	Eq (24a)	Eq (24b)	Eq (24c)	Eq (24d)	Eq (25a)	Eq (25b)
°C						
0	0.152	0.137	0.123	0.203	0.062	0.549
10	.117	.105	.094	.156	.047	.424
20	.092	.082	.074	.123	.037	.332
30	.073	.064	.058	.098	.029	.266
40	.058	.052	.047	.080	.024	.216
50	.048	.042	.038	.065	.019	.178
60	.040	.034	.031	.054	.016	.148
70	.034	.028	.026	.046	.013	.123
80	.028	.024	.021	.039	.011	.105
90	.024	.020	.018	.033	.009	.090
100	.021	.017	.015	.028	.008	.077

*Best estimates.

Within the limits specified by eqs (20a, b), the parameters cannot be adjusted to force the fit through the Goff-based value of −0.57 liter/mol at 100 °C. By adjusting the parameters as far as possible, we obtain

$$t^* = 0.98,\ \sigma_{ww_2} = 3.58\ \text{A°},\ \frac{\epsilon_{ww_2}}{k} = 380\ K, \quad (21b)$$

which leads to a value of B_{ww_2} of −0.62 liter/mol at 100°C.

The reader can obtain the relationships corresponding to eqs (24b, and 24c) of [1] leading to the C_{aww} values appearing in columns 3 and 4 of table 3 (revised). The magnitudes are roughly 13 percent greater than the corresponding values appearing in table 3 of [1], and, in any event, are not the preferred values.

4. References

[1]. Hyland, R. W., and Mason, E. A., Third Virial Coefficient for Air-Water Vapor Mixtures, J. Res. Nat. Bur. Stand. (U.S.), **71A** (Phys. and Chem), No. 3, 219–224 (May–June 1967).

[2]. Goff, J. A., Standardization of Thermodynamic Properties of Moist Air, Heating, Piping and Air Conditioning (Journal Section), **21**, 118 (1949).

[3]. Keyes, F. G., The Thermodynamic Properties of Water Substance from 0° to 150 °C, J. Chem. Phys. **15**, 602 (1947).

(Paper 79A6–874)

JOURNAL OF RESEARCH of the National Bureau of Standards — A. Physics and Chemistry
Vol. 79A, No. 6, November-December 1975

Publications of the National Bureau of Standards*

Citations with Selected Abstracts

J. Res. Nat. Bur. Stand. (U.S.), **79A** *(Phys. and Chem.),* No. 5 (September-October 1975), SD Catalog No. C13.22/sec.A:79/5.

Surface films on polyoxymethylene single crystals, J. E. Breedon and P. H. Geil.

On the origin of the amorphous component in polymer single crystals and the nature of the fold surface, J. D. Hoffman and G. T. Davis.

Some thermodynamic properties of bromobenzene from 0 to 1500 K, J. F. Masi and R. B. Scott.

Relativistic effects on line strengths for transitions in the hydrogenic isoelectronic sequence, S. M. Younger and A. W. Weiss.

The enthalpies of combustion and formation of 2,2′-dichlorethyl sulfide, W. H. Johnson.

Barothermal theory of two devices for measuring absorption coefficients, H. S. Bennett.

J. Res. Nat. Bur. Stand. (U.S.), **79B** *(Math. Sci.),* Nos. 1 and 2 (January-June 1975), SD Catalog No. C13.22/sec.B:79/1&2.

Ideal elements for perturbed Keplerian motions, A. Deprit.

Generalized or adjoint reciprocity relations for electroacoustic transducers, A. D. Yaghjian.

The diophantine equation $p^2x^4 + 3px^2y^2 + y^4 = z^2$, p an odd prime, T. N. Sinha.

A condition for the diagonalizability of a partitioned matrix, C. R. Johnson and M. Newman.

Linearly independent sets of isotropic Cartesian tensors of ranks up to eight, E. A. Kearsley and J. T. Fong.

Maximal network flows, matroids and matchings, F. Minieka.

A note on the metrizability of spaces with countably based closed sets, R. R. Sabella.

Charge profiles in parallel-plate ionization chambers, G. F. Leal Ferreira, L. Nunes de Oliveira, and B. Gross.

J. Res. Nat. Bur. Stand. (U.S.), **79B** *(Math. Sci.),* Nos. 3 and 4 (July-December 1975), SD Catalog No. C13.22/sec.B:79/3&4.

Two submatrix properties of certain induced norms, C. R. Johnson.

Properties of neighboring sequences in stratifiable spaces, R. R. Sabella.

Maximin facility location, P. J. Slater.

Similarity of partitioned matrices, R. R. Feinberg.

On the dimension group of classical physics, C. H. Page.

Complete elliptic integrals resulting from infinite integrals of Bessel functions. II, S. Okui.

SP260, 1975-76 Edition. **Catalog of NBS Standard Reference Materials 1975-76 Edition,** R. W. Seward, Nat. Bur. Stand. (U.S.), Spec. Publ. 260-1975-76 catalog, 90 pages (June 1975) SD Catalog No. C13.10:260-1975-76 cat., $1.50.

Key words: analysis; characterization; composition; General Materials; properties; Research Materials; Standard Reference Materials.

This Catalog lists and describes the Standard Reference Materials (SRM's), Research Materials (RM's), and General Materials (GM's) currently distributed by the National Bureau of Standards, as well as many of the materials currently in preparation. SRM's are used to calibrate measurement systems and to provide a central basis for uniformity and accuracy of measurement. The unit and quantity, the type, and the certified characterization are listed for each SRM, as well as directions for ordering. The RM's are not certified, but are issued to meet the needs of scientists engaged in materials research. RM's are issued with a "Report of Investigation," the sole authority of which is the author of the report. The GM's are standardized by some agency other than NBS. NBS acts only as a distribution point and does not participate in the standardization of these materials. Announcements of new and renewal SRM's, RM's, and GM's are made in the semi-annual supplements of this Catalog, SRM Price List, and in scientific and trade journals.

SP260-52. **Standard reference materials: Thermal conductivity and electrical resistivity standard reference materials: Tungsten SRM's 730 and 799, from 4 to 3000 K,** J. G. Hust and P. J. Giarratano, Nat. Bur. Stand. (U.S.), Spec. Publ. 260-52, 47 pages (Sept. 1975) SD Catalog No. C13.10:260-52, $1.05.

Key words: electrical resistivity; high temperature; Lorenz ratio; low temperature; standard reference materials; thermal conductivity; thermopower; tungsten.

A historical review of the development of thermophysical Standard Reference Materials, SRM's, is given and selection criteria of SRM's are listed. Thermal conductivity and electrical resistivity data for arc cast and sintered tungsten are compiled, analyzed, and correlated. Recommended values of thermal conductivity (SRM 730) and electrical resistivity (SRM 799) for these lots of tungsten are presented for the range 4 to 3000 K. These values are based on low temperature NBS measurements and higher temperature measurements by participants of the AFML-AGARD project. The uncertainty of the thermal conductivity values below ambient is 2 percent and rises to 5 percent between ambient and 2000 K. Above 2000 K the uncertainty rises to a maximum of about 8 percent. The uncertainty of the electrical resistivity values is 2 percent over the entire temperature range.

SP305. Supplement 6. **Publications of the National Bureau of Standards 1974 catalog. A compilation of abstracts and key word and author indexes,** B. L. Hurdle, Ed., Nat. Bur. of

**Publications with prices and SD Catalog numbers may be purchased directly from the Superintendent of Documents, U.S. Government Printing Office, Washington, D.C. 20402 (foreign: one-fourth additional). Microfiche copies of the above, plus paper copy and microfiche versions of NBS Interagency Reports (NBSIR's), may be purchased from the National Technical Information Service (NTIS), Springfield, Va. 22161. Prices are subject to change. Reprints from the NBS Journal of Research and non-NBS publications may often be obtained directly from the authors.*

Stand. (U.S.), Spec. Publ. 305 Suppl. 6, 523 pages (June 1975) SD Catalog No. C13.10:305 Suppl. 6, $6.80.

Key words: abstracts, NBS publications; key words; publications.

This supplement to Special Publication 305 Supplements 1 through 5 of the National Bureau of Standards lists the publications of the Bureau issued between January 1, 1974 and December 31, 1974. It includes an abstract of each publication (plus some earlier papers omitted from Special Publication 305 Supplement 4), key-word and author indexes; and general information and instructions about NBS publications.

Miscellaneous Publication 240 (covering the period July 1, 1957 through June 30, 1960) and its supplement (covering the period July 1, 1960 through June 30, 1966), Special Publication 305 (covering the period July 1966 through December 1967) and Special Publication 305 Supplement 1 (covering the period 1968-1969), Special Publication 305 Supplement 2 (covering the period 1970), Special Publication 305 Supplement 3 (covering the period 1971), Special Publication 305 Supplement 4 (covering the period 1972), Special Publication 305 Supplement 5 (covering the period 1973) remain in effect. Two earlier lists, Circular 460 (Publications of the National Bureau of Standards, 1901 to June 1947) and its supplement (Supplementary List of Publications of the National Bureau of Standards, July 1, 1947 to June 30, 1957) are also still in effect.

SP407. **59th National conference on weights and measures 1974,** S. J. Edgerly, Ed., Nat. Bur. Stand. (U.S.), Spec. Publ. 407, 284 pages (June 1975) SD Catalog No. C13.10:407, $3.75.

Key words: digital indicators; drained weight; laws and regulations; metrication; metric conversion; net weight; package control; petroleum products; scales; survey; temperature compensation; uniformity; weights and measures.

This is a report of the proceedings (edited) of the Fifty-Ninth National Conference on Weights and Measures, sponsored by the National Bureau of Standards, held in Washington, D.C., July 7-12, 1974, and attended by state, county, and city weights and measures officials, the Federal Government, business, industry, and consumer organizations.

SP415. **Biomaterials.** Proceedings of a Symposium held in conjunction with the Ninth Annual Meeting of the Association for the Advancement of Medical Instrumentation, New Orleans, April 19-20, 1974, E. Horowitz and J. L. Torgesen, Eds., Nat. Bur. Stand. (U.S.), Spec. Publ. 415, 109 pages (May 1975) SD Catalog No. C13.10:415, $1.75.

Key words: biocompatibility; biomaterials; blood protein; ceramic implants; implantable electrodes; metallic implants; nerve prosthesis; synthetic implants; thromboresistance.

This volume is based on papers presented at the Symposium on Biomaterials, held in conjunction with the Ninth Annual Meeting of the Association for the Advancement of Medical Instrumentation, New Orleans, LA, April 19-20, 1974. It provides a review of special topics in biomaterials research selected to focus attention on some noteworthy achievements. The topics covered include plasma-polymerized polymers and their application in biomedicine; biocompatibility of ceramic materials and their application both as inert coatings for synthetic implants and as porous materials for bone repair; the selection of metallic implant materials through engineering and medical considerations; in vitro testing of thromboresistance; adsorption of blood proteins on synthetic substrates; a prosthesis for nerve regeneration; and properties of fibrous biomaterials.

SP429. **Proceedings of the 7th Annual Conference of the National Conference of States on Building Codes and Standards,** S. A. Berry, Ed., Nat. Bur. Stand. (U.S.), Spec. Publ. 429, 129 pages (Sept. 1975) SD Catalog No. C13.10:429, $1.95.

Key words: ASHRAE 90-P; building codes; mobile homes; NCSBCS.

The National Conference of States on Building Codes and Standards had its formal beginning in Wisconsin in 1967. Its formation represented a response by the States to recommendations for intergovernmental reforms in the area of building codes, prepared by the Advisory Commission on Intergovernmental Relations. The formative meeting held in Wisconsin was a direct outgrowth of an earlier exploratory meeting, involving several States, called by the National Bureau of Standards. At this meeting, the States represented discussed the idea of a national organization of the States similar to the National Conference of Weights and Measures, assisted by the National Bureau of Standards, leading to a cooperative solution regarding the multiple problems in the entire building regulatory system.

The Governor of Wisconsin issued an invitation to the States to gather in Wisconsin to address the problem, to develop an organization which could effectively respond to this national need, and to consider the offer of assistance of the National Bureau of Standards. Sixteen States attended this meeting and unanimously agreed to the formation of the NCSBCS and to accept the secretariat role of the National Bureau of Standards.

The Conference is structured to develop many technical and general recommendations in the field of comprehensive building code administration and its programs explore the entire system of this important segment of governmental regulatory service.

The secretariat of the National Conference of States on Building Codes and Standards located in the Office of Building Standards and Codes Services, Center for Building Technology, National Bureau of Standards, Washington, D.C. 20234.

NSRDS-NBS3, Section 5. **Selected tables of atomic spectra. A: Atomic energy levels—Second edition. B: Multiplet tables. N I, N II, N III,** C. E. Moore, Nat. Stand. Ref. Data Ser., Nat. Bur. Stand. (U.S.), 3, Sec. 5, 67 pages (May 1975) SD Catalog No. 13.48:3/Sec.5, $1.80.

Key words: atomic energy levels, N I, N II, N III; multiplet tables, N I, N II, N III; nitrogen spectra, N I, N II, N III; spectra, N I, N II, N III; wavelengths, nitrogen spectra N I, N II, N III.

The present publication is the fifth Section of a series being prepared in response to the persistent need for a current revision of two sets of tables containing data on atomic spectra as derived from analyses of optical spectra. As in the previous sections, Part A contains the atomic energy levels and Part B the multiplet tables. The first three spectra of nitrogen, N I, N II and N III are included. The form of presentation is described in detail in the text of Section 1.

NSRDS-NBS55. **Property index to NSRDS data compilations, 1964-1972,** D. R. Lide, Jr., G. B. Sherwood, C. H. Douglass, Jr., and H. M. Weisman, Nat. Stand. Ref. Data. Ser., Nat. Bur. Stand. (U.S.), 55, 15 pages (June 1975) SD Catalog No. C13.48:55, 85 cents.

Key words: cumulative property index; data compilations; National Standard Reference Data System.

A property index to data contained in publications of the National Standard Reference Data System during the period 1964-1972 is presented. Data compilations published in the NSRDS-NBS series, other publication series of the National Bureau of Standards, scientific journals, and books of commercial publishers are included. When used with the cumulative property index published annually since 1972 in the *Journal of Physical and Chemical Reference Data*, this index serves as an entry to the complete output of the NSRDS program.

BSS60. **Hydraulic performance of a full-scale townhouse drain- waste- vent system with reduced-size vents,** M. J. Or-

loski and R. S. Wyly, Nat. Bur. Stand. (U.S.), Bldg. Sci. Ser. 60, 43 pages (Aug. 1975) SD Catalog No. C13.29/2:60, $1.05.

Key words: DWV; performance testing; reduced-size vents; trap-seal retention; venting; venting criteria; vents, reduced-size.

This report describes the experimental findings of tests on a full-scale two-story plumbing system with reduced-size vents under a range of operating conditions including tests with the vent terminals closed and the building drain submerged. Results indicate that dry vent piping in 1-2 story housing units can safely be smaller than presently allowed by design without jeopardizing the trap seals. On the basis of the current investigation and from earlier work on full-scale systems of substantially different geometry, criteria for sizing reduced-size vents are given for general application to conventional 1-2 story housing units. In addition to the practical evidence in terms of acceptable trap performance, the current study provided fundamental evidence of the excessive present design criteria. For the first time measurements were obtained which relate traditional design criteria (air flow and vent pressure) to presently recommended performance criteria (trap-seal retention) under dynamic conditions. These findings indicate that the vents can be sized on the basis of 1.5 in water gage (equals 372 pascals) suction in the vent rather than the 1.0 in W.G. (equals 248.8 Pa) presently specified in the plumbing codes. Also air demands measured were significantly less than assumed in current practice for short stacks and for systems with vent networks.

BSS65. **Nonmetallic coatings for concrete reinforcing bars,** J. R. Clifton, H. F. Beeghly, and R. G. Mathey, Nat. Bur. Stand. (U.S.), Bldg. Sci. Ser. 65, 42 pages (Aug. 1975) SD Catalog No. C13.29/2:65, $1.00.

Key words: bridge decks; chloride ions; concrete; corrosion; deicing salts; epoxy coatings; organic coatings; polyvinyl chloride coatings; steel reinforcing bars.

This work was undertaken to ascertain the feasibility of using organic coatings, especially epoxies, to protect the steel reinforcing bars embedded in concrete of bridge decks from rapid corrosion. This corrosion is caused by the chloride ions from the most commonly applied deicing salts, sodium chloride and calcium chloride. Altogether, 47 different coating materials were evaluated to some extent, consisting of 21 liquid and 15 powder epoxies; 5 polyvinyl chlorides; 3 polyurethanes; 1 polypropylene; 1 phenolic nitrile; and one zinc rich coating. The chemical and physical durabilities, chloride permeabilities, and protective qualities of coatings were assessed. The bonds between coated and uncoated bars and concrete were measured by both pullout and creep tests.

The results indicate that both epoxy and polyvinyl chloride coatings, if properly applied, should adequately protect steel reinforcing bars from corrosion. However, only the epoxy coated bars had acceptable bond and creep characteristics when embedded in concrete. The powder epoxy coatings overall performed better than the liquid epoxies, and four powder epoxy coatings have been identified as promising materials to be used on reinforcing bars embedded in concrete decks of experimental bridges.

BSS71. **A proposed concept for determining the need for air conditioning for buildings based on building thermal response and human comfort,** J. E. Hill, T. Kusuda, S. T. Liu, and F. J. Powell, Nat. Bur. Stand. (U.S.), Bldg. Sci. Ser. 71, 155 pages (Aug. 1975) SD Catalog No. C13.29/2:71, $2.25.

Key words: air conditioning criteria; building thermal response; comfort indices; human comfort; predicted indoor habitability index.

Determining the need for air conditioning can be based on a wide variety of factors. To date, the only criteria that have been written and can be referenced are those of several federal organizations and many are not really criteria in the true sense of the word. They are guidelines to be used in the determination of fund allocation; in other words, provisions are made to air condition federal facilities in specific geographical locations if pertinent weather characteristics of that locality meet certain requirements. This paper presents the concept that a true criteria can be established based both on weather characteristics of the locality as well as characteristics of the building or structure under consideration.

The paper gives the details of a study showing the feasibility of such a scheme. A simulation was made of two proposed residences in several geographical localities. For the simulation, actual hour-by-hour weather data was used in conjunction with a sophisticated computer program. The results revealed for the non air-conditioned spaces, the extent and duration of undesirable indoor conditions based upon generally accepted comfort indices. The concept of a new "comfort" or "discomfort" index called Predicted Indoor Habitability Index (PIHI) is introduced. The authors indicate the way in which a criterion could be established that would be in the form of tables, indicating for a given specified building and geographical locality, whether mechanical cooling should or should not be installed.

FIPS PUB 37. **Synchronous high speed data signaling rates between data terminal equipment and data communications equipment,** G. E. Clark, Standards Coordinator, Nat. Bur. Stand. (U.S.), Fed. Info. Process. Stand. Publ. (FIPS PUB) 37, 4 pages (1975) SD Catalog No. C13.52:37, 40 cents.

Key words: data communication equipment; data processing terminal equipment; data transmission (high speed); Federal Information Processing Standards; synchronous signaling rates; teleprocessing; wide band.

This FIPS PUB announces the adoption of the American National Standard X3.36-1975, Synchronous High Speed Data Signaling Rates Between Data Terminal Equipment and Data Communication Equipment, and is the same as Federal Standard Number 1001. This standard specifies a series of signaling speeds for synchronous high speed serial data transfer.

FIPS PUB 41. **Computer security guidelines for implementing The Privacy Act of 1974,** T. C. Lowe, Standards Coordinator, Nat. Bur. Stand. (U.S.), Fed. Info. Process. Stand. Publ. (FIPS PUB) 41, 20 pages (1975) SD Catalog No. C13.52:41, 70 cents.

Key words: access controls; ADP security; computer security; Federal Information Processing Standards; information management; personal data; physical security; privacy risk assessment.

This publication provides guidelines for use by Federal ADP organizations in implementing the computer security safeguards necessary for compliance with Public Law 93-579, the Privacy Act of 1974. A wide variety of technical and related procedural safeguards are described. These fall into three broad categories: Physical security, information management practices, and computer system/network security controls. As each organization processing personal data has unique characteristics, specific organizations should draw upon the material provided in order to select a well-balanced combination of safeguards which meets their particular requirements.

TN594-10. **Optical radiation measurements: The NBS 20-, 60-, and 85-degree specular gloss scales,** J. J. Hsia, Nat. Bur. Stand. (U.S.), Tech. Note 594-10, 32 pages (July 1975) SD Catalog No. C13.46:594-10, 85 cents.

Key words: accuracy; appearance; error analysis; gloss; photometry; reflectance; scattering; spectrophotometry; specular gloss.

The 20-, 60-, and 85-degree specular gloss scales are established at NBS with an accuracy of about one half gloss unit. This is one of

many programs of the spectrophotometry group of the Optical Radiation Section of NBS directed toward improving the accuracy and assurance of spectrophotometric measurements made throughout the scientific and industrial community.

The specular gloss scales are established through a unique technique employing polarized light flux both parallel and perpendicular to the plane of incidence. General calibration equations are derived. NBS instrumentation and measurement procedures are described. Instrument calibration and error analyses are performed. Some of the analyses can also be applied to reflectance measurements in general.

TN668. **The use of National Bureau of Standards high frequency broadcasts for time and frequency calibrations,** N. Hironaka and C. Trembath, Nat. Bur. Stand. (U.S.), Tech. Note 668, 47 pages (May 1975) SD Catalog No. C13.46:668, $1.05.

Key words: dissemination; frequency; high frequency broadcasts; standard; time.

Methods to determine time or frequency by reception of NBS high frequency radio broadcasts are discussed. Results are shown for calibration of time signals to within ± 100 microseconds and calibration of frequency offset with a resolution of better than 1 part in 10^9. These results are achieved by using a systematic approach and refined measurement technique.

TN669. **The measurement of frequency and frequency stability of precision oscillators,** D. W. Allan, Nat. Bur. Stand. (U.S.), Tech. Note 669, 31 pages (May 1975) SD Catalog No. C13.46:669, 80 cents.

Key words: accurate frequency measurement; accurate time measurement; frequency; frequency stability; frequency stability analysis; models of frequency stability; picosecond time difference measurements.

The specification and performance of precision oscillators is a very important topic to the owners and users of these oscillators. This paper presents at the tutorial level some convenient methods of measuring the frequencies and/or the frequency stabilities of precision oscillators—giving advantages and disadvantages of these methods.

Conducting such measurements, of course, gives additional understanding into the performance of the given pair of oscillators involved. Further it is shown that by processing the data from the frequency measurements in certain ways, one may be able to state more general characteristics of the oscillators being measured. The goal in this regard is to allow the comparisons of different manufacturers' specifications and more importantly to help assess whether these oscillators will meet the standard of performance the user may have in a particular application.

The methods employed for measuring frequency are designed for state-of-the-art oscillators, and an effort has been made to allow for fairly simple, inexpensive, and/or commonly available components to be used in the measurement systems. The method for measuring frequency stability is basically that recommended by the IEEE subcommittee on Frequency Stability of the Technical Commitee on Frequency and Time of the IEEE Group on Instrumentation & Measurement.

TN858. **A program for survey of fire loads and live loads in office buildings,** C. Culver and J. Kushner, Nat. Bur. Stand. (U.S.), Tech. Note 858, 229 pages (May 1975) SD Catalog No. 13.46:858, $3.75.

Key words: buildings; fire loads; occupancy live loads; load surveys; structural engineering; survey techniques.

The development of a survey program for determining the fire loads and live loads in office buildings is described. Considerations involved in planning the program which is directed toward establishing the factors affecting the loads in buildings are presented. The type of data to be collected and a data collection technique which utilizes visually observed information on the characteristics of building content items to determine weight are discussed. Procedures employed to select buildings to be included in a nation-wide office building load survey being conducted by the National Bureau of Standards and a sampling plan for selecting rooms to be surveyed in these buildings are also discussed.

TN866. **Chemical kinetic and photochemical data for modelling atmospheric chemistry,** R. F. Hampson, Jr., and D. Garvin, Eds., Nat. Bur. Stand. (U.S.), Tech. Note 866, 118 pages (June 1975) SD Catalog No. C13.46:866, $1.85.

Key words: atmospheric chemistry; chemical kinetics; data evaluation; gas phase; photoabsorption cross section; photochemistry; quantum yield; rate constant.

A table of data for gas phase chemical reactions and photochemistry of neutral species is presented. Specifically, it gives preferred values for reaction rate constants, photoabsorption cross sections, and quantum yields of primary photochemical processes and also cites recent experimental work. It is intended to provide the basic physical chemical data needed as input data for calculations modelling atmospheric chemistry. An auxiliary table of thermochemi cal data for the pertinent chemical species is given in the appendix.

TN867. **Relationship of garment characteristics and other variables to fire injury severity,** L. B. Buchbinder, Nat. Bur. Stand. (U.S.), Tech. Note 867, 41 pages (June 1975) SD Catalog No. C13.46:867, $1.25.

Key words: accident patterns; apparel; apparel fires; burn injury; FFACTS; fire; flammable fabrics; flammable liquids; garment fires; garment parameters; injury severity; victim's activity; victim's reactions.

This final report on an in-depth study of apparel fire accident variables focuses on the physical parameters of fabrics and garments involved in apparel fires and the relationship between these parameters and injury severity. Interactions between accident variables are summarized and recommendations for remedial action and further research are included. Garments involved in apparel fire accidents were classified by degree of fit and amount of the body covered. Fires in which the garment configurations involved covered over half the body (the dress/shift and pants/top configurations) were shown to be associated with more extensive burn injuries than fires involving configurations covering smaller areas (loose tops, fitted pants, and loose pants). Degree of fit could not be shown to be directly related to injury severity. Within garment configuration classifications, age was shown to be a major determinant of injury severity, with victims over 65 years of age receiving a significantly higher percentage of severe burns than those in the 21-65 age group. In accidents involving loose tops, fitted pants, and loose pants the presence of flammable liquids in the accident sequence appeared to be the dominant factor in determining injury level. In addition, when accidents involved flammable liquids, (1) the fabrics involved tended to be heavier, (2) the fit of the garment at point of ignition was closer, and (3) the proportion of cellulosic/synthetic blend and 100 percent synthetic fabrics was higher than in accidents which did not involve flammable liquids. Because of the many human and physical variables shown to be associated with an apparel fire accident, the author suggests a broad fire prevention program which includes both product regulation and public education.

TN868. **Statistical analysis of extreme winds,** E. Simiu and J. J. Filliben, Nat. Bur. Stand. (U.S.), Tech. Note 868, 52 pages (June 1975) SD Catalog No. C13.46:868, $1.50.

Key words: building codes; extreme value distributions; hurricanes; probability distribution functions; reliability; risk;

statistical analysis; storms; structural engineering; wind loads; wind speeds.

With a view to assessing the validity of current probabilistic approaches to the definition of design wind speeds, a study was undertaken of extreme wind speeds based on records taken at 21 U.S. weather stations. For the purpose of analyzing extreme value data, a computer program was developed, which is described herein. The following results were obtained: (1) the assumption that a single probability distribution is universally applicable to all extreme wind data sets in a given type of climate was not confirmed, and (2) predictions of 100-year wind speeds based on overlapping 20-year sets of data taken at the same station differed between themselves by as much as 100 percent. Similar predictions for 1000-year winds differed by as much as a few hundred percent. Since wind pressures are proportional to the square of the wind speeds, errors of such magnitude are unacceptably high for structural design purposes. It is therefore suggested that while, in principle, probabilistic methods provide the most rational approach to specifying design wind speeds, it is of the utmost importance that the possible errors inherent in this approach be carefully taken into account.

TN870. **Sampling techniques for electric power measurement,** R. S. Turgel, Nat. Bur. Stand. (U.S.), Tech. Note 870, 35 pages (June 1975) SD Catalog No. C13.46:870, $1.05.

Key words: analog-to-digital conversion; digital; electricity; electric power; measurement; sampling; simulation; wattmeter.

A system is described that determines average electric power by periodically sampling current and voltage waveforms and calculating the result from digitized values of measured instantaneous currents and voltages. System performance is modeled on a digital computer to investigate the effects of noise, harmonics and sampling time errors on the result of a simulated power measurement. With 15 bit analog-to-digital conversion and 512 measured sample points an accuracy of 0.01 percent can theoretically be obtained from dc up to 5 kHz.

TN871. **Geometrical calibration of the NBS electron scattering apparatus,** S. Penner, S. P. Fivozinsky, J. W. Lightbody, Jr., L. S. Cardman, and W. P. Trower, Nat. Bur. Stand. (U.S.), Tech. Note 871, 79 pages (June 1975) SD Catalog No. C13.46:871, $1.40.

Key words: absolute cross section; beam profile; electron scattering; scattering angle; solid angle; spectrometer.

A comprehensive calibration of the geometry of the NBS electron scattering apparatus is described. A complete set of measured parameters is tabulated in this report. Combining these parameters with observed values of certain variables as described herein permits the accurate determination of the solid angle, scattering angle, and target angle for each cross section measurement made with the apparatus. The uncertainty in a cross section measurement due to the imprecision of the geometry calibrations is less than one part in 10^3.

TN872. **Computer program package for metric conversion: Reference manual,** R. K. Anderson and J. O. Harrison, Jr., Nat. Bur. Stand. (U.S.), Tech. Note 872, 145 pages (July 1975) SD Catalog No. C13.46:872, $2.10.

Key words: Caterpillar Tractor Co.; computer program; documentation; engineering drawing; General Motors Corporation; metric conversion; rounding; test problem; tolerance.

The programs in this package are designed to convert dimensions and other quantities appearing on engineering drawings from metric to U.S. customary units and vice versa. They were developed by Caterpillar Tractor Co. and General Motors Corporation. In addition to the programs themselves, the package contains documentation explaining how to get the programs running on different computers and how to use them, and test problems to permit users to verify that the programs run correctly on their own computers. The Caterpillar program converts 31 different metric units to their U.S. customary equivalents. In contrast, the General Motors programs convert in both directions but work with millimetres and inches only. The General Motors programs also use rounding conventions differing somewhat from those employed in the Caterpillar program. Both the Caterpillar and the General Motors programs are written in American National Standard FORTRAN and are suitable for use on a wide range of computers with little or no modification. The Caterpillar program is operated in batch mode while the General Motors programs are interactive.

TN875. **Interlaboratory intercomparisons of radioactivity measurements using National Bureau of Standards mixed radionuclide test solutions,** B. M. Coursey, J. R. Noyce, and J. M. R. Hutchinson, Nat. Bur. Stand. (U.S.), Tech. Note 875, 20 pages (Aug. 1975) SD Catalog No. C13.46:875, 65 cents.

Key words: environment; intercalibration; intercomparison; radioactivity; radionuclide; radiostrontium.

In 1973 the National Bureau of Standards (NBS) distributed three calibrated test solutions to interested laboratories. Two of these solutions each contained nine gamma-ray-emitting radionuclides that the participants were asked to identify and quantify. The third solution contained ^{85}Sr and ^{90}Sr-^{90}Y, and participants were asked to perform a quantitative radioactivity analysis of the mixture. The results reported by all of the participating laboratories are given here. Most of the activity values reported for the mixed gamma-ray-emitting solutions were within ±20 percent of the corresponding NBS values, but less than half of the laboratories reported ^{85}Sr and ^{90}Sr-^{90}Y activity values both of which were within ±20 percent of the NBS values.

TN876. **Exploring privacy and data security costs—A summary of a workshop,** J. L. Berg, Ed., Nat. Bur. Stand. (U.S.), Tech. Note 876, 35 pages (Aug. 1975) SD Catalog No. C13.46:876, 85 cents.

Key words: computer security; data security; privacy; privacy costs; security costs.

On February 20, 1975, the ICST hosted a one-day round-table discussion on the economic aspects of privacy and data security costs. The workshop was chaired by Gary Bearden, U.S. Civil Service Commission. The participants were Walter L. Anderson, General Accounting Office; Richard A. Eberhart, Office of the Secretary, Department of Commerce; Earl P. Bassett, Jr., Vice President, 3M Company; Robert Caravella, Federal Trade Commission; Theodore Clemence, Bureau of Census; Richard L. Nolan, Harvard Business School; Stan Halper, Coopers and Lybrand; and Larry Simonette, Peat, Marwick, Mitchell and Company. The group discussed the benefits EDP managers or data base administrators might gain from the privacy requirements, the processes for identifying direct or hidden costs, and processes for allocating costs.

TN877. **A basis for standardization of user-terminal protocols for computer network access,** A. J. Neumann, Nat. Bur. Stand. (U.S.), Tech. Note 877, 29 pages (July 1975) SD Catalog No. C13.46:877, 80 cents.

Key words: command languages; computers; man-machine systems; networks; system commands; user protocols.

A user-terminal protocol is defined which enables a user at a terminal to access computerized information systems. The basic functions such as identification, authorization, and validation are outlined and various signals and messages making up the protocol are identified. The purpose of the paper is to establish a basis for standardization and development of a unified user protocol.

TN878. **The M40 fingerprint matcher,** J. H. Wegstein, Nat. Bur. Stand. (U.S.), Tech. Note 878, 14 pages (July 1975) SD Catalog No. C13.46:878, 65 cents.

Key words: computerized fingerprint identification; fingerprint; pattern recognition.

A procedure is described for automatically determining whether two fingerprint impressions were made by the same finger. The procedure uses the x and y coordinates and the individual directions of the minutiae (ridge endings and bifurcations). The identity of the two impressions is established by computing the density of clusters of points in Δx, Δy space where Δx and Δy are the differences in coordinates that are found in going from one of the fingerprint impressions to the other.

TN879. **Fire buildup in a room and the role of interior finish materials,** J. B. Fang, Nat. Bur. Stand. (U.S.), Tech. Note 879, 49 pages (June 1975) SD Catalog No. C13.46:879, $1.10.

Key words: buildings; fire growth; flame spread; heat release; interior linings; material ignitability; performance criteria; room fires; smoke; wood crib.

A variety of wall and ceiling panels in a full-scale room corner have been exposed to a fire from a standardized wood crib, simulating the environment produced by the burning of a single item of furniture, to evaluate their contribution to room fire growth. A total of twenty room corner tests were performed using selected combinations of eight wood-base and gypsum board-base interior finish materials on the walls and ceiling. Gas temperatures and velocities, surface temperatures, heat fluxes, smoke densities, and concentrations of oxygen, carbon dioxide and carbon monoxide were measured. Ignition times of newsprint, cotton fabric and plywood in the lower part of the room were also recorded. The results of these full-scale tests were compared with laboratory tests of the ease of ignition, surface flame spread, heat release rate and smoke generation on the same materials. The maximum upper room gas temperature has been found to agree with the ignition of such indicators as newsprint and plywood, and to represent a measure of fire hazard in terms of potential involvement of all combustible contents or room flashover. A temperature range of 450 to 650 °C appears to be the boundary between limited and full involvement.

TN880. **The service concept applied to computer networks,** M. D. Abrams and I. W. Cotton, Nat. Bur. Stand. (U.S.), Tech. Note 880, 38 pages (Aug. 1975) SD Catalog No. C13.46:880, 85 cents.

Key words: computer networks; interactive computing; man-machine interaction; performance measurement; time-sharing.

The Network Measurement System (NMS) represents the implementation of a new approach to the performance measurement and evaluation of computer network systems and services. By focusing on the service delivered to network customers at their terminals, rather than on the internal mechanics of network operation, measurements can be obtained which are directly relevant to user needs and management concerns. Furthermore, the type of measurement necessary to implement this approach can be made directly, without perturbing the network system under test.

This technical note introduces the service concept and other background information necessary to understand the need for and use of the NMS. The fundamental distinction between service and internal efficiency is clarified, both in general and in the environment of computer networks. A number of different measures of service are then discussed, followed by the presentation of several models of interactive use of networks. Then, the practical aspects of gathering data and applying this information to service measurement are reviewed, leading to a presentation of the NMS as it is implemented. The note ends with a discussion of applications for the NMS.

TN881. **Critical evaluation of data in the physical sciences—A status report on the National Standard Reference Data System, April 1975,** S. A. Rossmassler, Ed., Nat. Bur. Stand. (U.S.), Tech. Note 881, 53 pages (Sept. 1975) SD Catalog No. C13.46:881, $1.10.

Key words: atomic and molecular data; chemical kinetics; colloid and surface properties; mechanical properties; nuclear data; solid state data; standard reference data; thermodynamic data, transport properties.

This is a report on the status of the National Standard Reference Data System as of April 1975. Current activities and functions of the Office of Standard Reference Data are summarized. A complete list of data evaluation projects supported by the Office of Standard Reference Data during Fiscal Year 1975 is included; this list also includes projects which received financial support during the previous fiscal year, and which are still actively involved in some aspect of data compilation and evaluation. The list of projects includes continuing data centers in the United States whose activities fall within the scope of the system, but which are not formally affiliated with it. A list of publications resulting from the Standard Reference Data program is provided.

TN882. **Criteria for the performance evaluation of data communications services for computer networks,** D. S. Grubb and I. W. Cotton, Nat. Bur. Stand. (U.S.), Tech. Note 882, 36 pages (Sept. 1975).

Key words: computer communications; computer networking; data communications; networks; performance requirements; telecommunications.

In general, when telecommunications services are used as a means of interchanging information between information processing systems, or between terminals and systems, a number of parameters determine how well that interchange is performed. This report examines the following characteristics of telecommunications services: 1. Transfer Rate; 2. Availability; 3. Reliability; 4. Accuracy; 5. Channel Establishment Time; 6. Network Delay; 7. Line Turnaround Delay; 8. Transparency; 9. Security.

These terms are all defined and their significance discussed. The effects of these factors on data communication networks are illustrated.

NBSIR 74-393. **Semi-annual report on materials research in support of superconducting machinery,** R. P. Reed, R. L. Durcholz, F. R. Fickett, P. J. Giarratano, J. G. Hust, M. B. Kasen, H. M. Ledbetter, R. P. Mikesell, E. R. Naimon, R. E. Schramm, L. L. Sparks, R. L. Tobler, and W. F. Weston, 283 pages (Oct. 1974). Order from NTIS as COM 75-10768, $8.75.

Key words: composites; elastic properties; fracture; liquid helium; mechanical properties; structural materials; superconducting machinery; thermal conductivity. .

Results of six months of study on Materials Research in Support of Superconducting Machinery (April through September, 1974) are reported to the sponsor, the Advanced Research Projects Agency of the U.S. Department of Defense. The report is divided into five sections: thermal conductivity, magnetothermal conductivity, fatigue and fracture-toughness properties, properties of advanced composites, and elastic properties. The temperature range 4 to 300 K is covered by the study. Materials studied are either being used or are candidates for use in superconducting machinery and include: aluminum alloys, composites, inconels, OFHC copper, stainless steels, and titanium alloys.

Special results of the study include: fracture-toughness and fatigue-crack growth-rate data for AISI 310, Ti-5 Al-2.5 Sn, A286 stainless steel, and Inconel 750 at 4, 76, and 300 K; initial reports of tensile testing of composites at 4 K; a second review paper on advanced-composite low-temperature behavior; magnetothermal conductivity measurements on OFHC copper and Inconel 718 indicate that, in a magnetic field, the thermal conductivity may change by 100

percent; anomalous low-temperature elastic behavior of AISI 300 series stainless-steel alloys; and thermal conductivity data for OFHC copper, Inconel 750, and Inco Low-Expansion-Alloy. These data provide considerable insight into material characteristics at extremely low temperatures, assisting in material selection and efficient design.

NBSIR 74-523. **Preparations for gage block comparison measurements,** C. D. Tucker, 14 pages (July 9, 1974). Order from NTIS as COM 75-11126, $3.25.

Key words: deburring; gage blocks, gage block comparator; linear variable differential transformer.

The methods described here for the cleaning and deburring of gage blocks can be useful to those individuals who have not established formal laboratory procedures for these operations. Many individuals may employ valid methods that vary somewhat from those employed at the National Bureau of Standards.

Many of the gage block comparators that are in use have not been periodically evaluated by the user. It is the intent of this report to set forth guidelines and procedures that may be used conveniently by metrologists to aid in obtaining more meaningful comparisons of gage blocks by the use of probe-type transducers.

NBSIR 74-597. **Piezoelectric accelerometer low-frequency response by signal insertion methods,** R. S. Koyanagi and J. D. Pollard, 33 pages (May 1975). Order from NTIS as COM 75-11069, $3.75.

Key words: accelerometer; calibration; low frequency; signal insertion; vibration.

The purpose of this study was to compare the frequency response of selected piezoelectric accelerometers using a signal insertion method to the response using traditional mechanical vibration tests. Signal insertion methods included "voltage insertion" and "change insertion" techniques. The signal is inserted in series with the electrical low-side of the accelerometer by means of a suitable series resistance. Commercially available insertion devices were used. Confidence in the use of insertion methods is increased where there is agreement between the results from insertion tests and mechanically excited tests.

NBSIR 74-614. **Mechanical tests of flammable liquid containers,** N. Halsey, A. F. Kirstein, and R. E. Snyder, 35 pages (Dec. 1974). Order from NTIS as COM 75-11013, $3.75.

Key words: consumer products; flammable liquid containers; gasoline cans; mechanical tests; product standards; safety.

Because of the concern for safety in the storage and use of gasoline and other flammable liquids around the home, this study was made to determine if standards can be established to minimize the flammable liquid hazard by controlling or standardizing the containers. Attention was focused on performance standards for stability, leakage, carrying handle strength, and pour spout strength. In general, it was found that the technology involved in existing voluntary standards for safety cans could be applied to flammable liquid containers for home use for all of the above factors except pour spout strength.

NBSIR 74-618. **US/UK joint complementary research program in building, (wind loads, water supply, fire detection), July 1973-June 1974,** C. C. Raley, I. A. Benjamin, L. S. Galowin, and R. D. Marshall, 23 pages (Oct. 1974). Order from NTIS as COM 75-11014, $3.25.

Key words: building technology; cooperation; fire safety; hydraulics; wind loads.

This is a status report of the progress achieved under the "Joint Complementary Research Program" sponsored by the Building Research Establishment (UK) and the Institute for Applied Technology (US), during the period July 1973 through June 1974. The program includes three projects: Wind Loads on Buildings, Design of Water Supply and Drainage Installations in Buildings, and Fire Detection in Buildings, each of which is discussed in the report.

NBSIR 75-641. **Performance of mobile homes data acquisition and analysis methodology,** J. H. Pielert, W. E. Greene, Jr., L. F. Skoda, and W. G. Street, 75 pages (Feb. 1975). Order from NTIS as COM 75-11209, $4.25.

Key words: construction; Hurricane Agnes; housing; mobile homes; mobile home parks; performance data; regulatory process; standards.

In a study at the National Bureau of Standards (NBS), funded by the Department of Housing and Urban Development (HUD), methods for inspecting mobile homes to identify performance problems, recording the problems and analyzing the problem data were developed. Maintenance work orders for 2881 mobile homes, a part of 12,500 provided by HUD for emergency housing in the aftermath of Hurricane Agnes, at Wilkes-Barre, Pa., were reviewed and computer coded by an interdisciplinary team of engineers. Also, performance data were obtained from State and other Federal agencies for over 967 privately owned mobile homes. A second task was the field inspection of 257 mobile homes to assist in the determination of the causes and consequences of the problems identified in the data acquisition task. Computer techniques were developed to process the data and print out problem summation tables, graphs to establish trends, compile data on obvious problems and ferret out those problems which may not be obvious. This first report documenting the data acquisition and analysis methodology will be followed by a series of reports which will present results and relate them to current standards, the regulatory and insurance processes.

NBSIR 75-651. **Procedural options to reduce the risk of injury from products installed in residences,** S. W. Stiefel, C. W. Hand, and D. W. Corrigan, 94 pages (June 1975). Order from NTIS as COM 75-11211, $4.75.

Key words: building codes; Consumer Product Safety Act; product safety; residence-related products; residential safety; safety implementation approaches; safety standards.

The Consumer Product Safety Commission's (CPSC) list of consumer products with high relative incidence of reported injuries includes many products which are integral parts of the consumer's residence, such as stairs, doors, architectural glass, furnaces and water heaters. The safety aspects of these products are influenced by on-site construction practices and design considerations which are regulated through local building codes. The problem is to identify operational methods the CPSC can employ in dealing with unreasonable hazards associated with component parts of residential units.

This report identifies, for products installed in homes, (1) the product history stages, (2) institutional groups, (3) hazard sources, and (4) countermeasures available to the CPSC. It structures relationships among these four elements for evaluating the impacts of alternative countermeasures. Current mechanisms for control of products installed in homes are presented and sixteen potential countermeasures are postulated.

NBSIR 75-661. **Strength degradation of brittle surfaces: Sharp indenters,** B. R. Lawn, E. R. Fuller, and S. M. Wiederhorn, 38 pages (May 1975). Order from NTIS as COM 75-10763, $3.75.

Key words: brittle solids; ceramic surfaces; degradation; fracture; indentation; strength.

A theory of strength loss for brittle surfaces in contact situations, developed in a previous paper for "blunt" indenters, is here extended to the case of "sharp" indenters. A prior fracture mechanics analysis of crack growth beneath ideal cone indenters serves as the basis for predetermining the prospective surface degradation of ceramic components in service. Compared to blunt indenters, severe degradation

594-051 O - 76 - 8

can occur at the lower contact loads. However, at high loads the extent of degradation becomes remarkably insensitive to indenter geometry. Essential theoretical predictions are verified by bend tests on glass slabs. The effect of indenter "sharpness" and initial specimen surface flaw state are investigated systematically, along with some secondary rate effects in the contract process. The possibility of minimizing degradation via adjustment of material parameters (including hardness) or surface condition (e.g., residual stresses, frictional properties) is briefly discussed.

NBSIR 75-673. **Development of a fire test method for flexible connectors in air distribution systems,** L. A. Issen, 31 pages (Apr. 1975). Order from NTIS as COM 75-10921, $3.75.

Key words: aluminum; ducts; fire tests; flexible connectors; furnace pressures; glass fiber; heat ventilating and air conditioning systems; high-rise buildings; optical density; steel; terminal units.

The report describes fire tests on four flexible connectors of the type used in air conditioning systems. Four flexible connectors (aluminum, felted glass fiber, steel, and woven glass fiber) were exposed to a standard ASTM E-119 fire test. The results were in agreement with previous results in which a different sized branch duct was used in the assemblies. The results indicated a need to control furnace pressures. The test results were used to develop a proposed test method for fire testing flexible connectors. This proposed test method is described in the report.

NBSIR 75-687. **Effective use of computing technology in vote-tallying,** R. G. Saltman, 140 pages (Mar. 1975). Order from NTIS as COM 75-11137, $5.75.

Key words: computer security; computing technology; election administration; public administration; state and local government; systems analysis; technology utilization; vote-tallying.

The results of a systems analysis and evaluation conducted on the role of automatic digital processing in vote-tallying are presented. Included in the report are descriptions of hardware, software, and administrative problems encountered in fourteen elections in which electronic computing technology was utilized.

Methods of assuring more confidence in the accuracy and security of the vote-tallying process are presented and described. These methods include aids to audits of calculations, physical controls over ballots and computer records, and guidelines for the use of computer programs, computer facilities, and teleprocessing. Methods of improving the election preparation process also are presented and described. These involve the development and implementation of design specifications and acceptance tests for computer programs, election equipment and supplies, and guidelines for pre-election checkout of vote-tallying systems and for assurance of management control.

Institutional factors are discussed which should be considered if improved accuracy and security controls and more effective election preparations are to be implemented. Recommendations for additional research and other activities including a possible Federal role are provided.

NBSIR 75-689. **The Shirley Highway Express Bus-on-Freeway demonstration project/a study of park-and-riding,** J. T. McQueen, G. K. Miller, and C. Harrison, 51 pages (Mar. 1975). Order from NTIS as COM 75-11190, $4.25.

Key words: bus-on-freeway operations; commuter surveys; mode choice decisions; park-and-ride; Shirley Highway; transportation planning.

The market for fixed route transit operations is not limited to travelers within walking distance of transit stops. This was demonstrated by the Shirley Highway Express-Bus-on-Freeway Project as project promoted park-and-ride operations led to sizable increases in bus patronage: Park-and-riders, commuters who traveled by auto to a bus stop and then by bus to work, greatly expanded the market for the fixed route bus service in the Shirley Highway Corridor area.

This report presents results of a study of the successful park-and-ride operation within the Shirley Highway Corridor area: Suburban fringe parking lots coupled with the high speed buses of the Shirley Highway Express-Bus-on-Freeway Project. Demographic characteristics of the park-and-riders as well as characteristics of their present park-and-ride and previous commute trips are examined. Factors important in the commuters' decisions to park-and-ride are identified. The report also describes the survey procedures used in the study.

NBSIR 75-690. **A compilation of problems related to the performance of mobile homes,** W. G. Street, W. E. Greene, J. H. Pielert, and L. F. Skoda, 86 pages (Apr. 1975). Order from NTIS as COM 75-11207, $4.75.

Key words: computer techniques; enforcement process; housing; Hurricane Agnes; mobile home parks; mobile homes; performance data; standards.

Performance of mobile homes as housing units is of broad concern to mobile home owners. This study report prepared at the National Bureau of Standards (NBS) and funded by the Department of Housing and Urban Development (HUD) presents mobile home problem data obtained from two separate data sources. The first data base for 2881 units was selected from maintenance records retained by HUD on 12,500 mobile homes used as emergency housing following the Hurricane Agnes disaster at Wilkes-Barre, Pennsylvania. The second source consisted of data for 967 privately-owned units collected from the files of various Federal, state, and private agencies responsible for regulation or consumer protection functions with regard to mobile homes. The mobile home performance problem data was processed using computer techniques to produce problem summation tables which facilitated evaluation. Although the mobile home problems experienced in various categories are highlighted in this report, no attempt was made to relate these results to current standards, regulatory or mortgage insurance (durability) processes. Analyses of this kind are planned for future reports in this series.

NBSIR 75-691. **A characterization and analysis of NBS corridor fire experiments in order to evaluate the behavior and performance of floor covering materials,** J. G. Quintiere, 89 pages (June 1975). Order from NTIS as COM 75-11015, $4.75.

Key words: corridor fire spread; energy release rate; fire induced flow; flame propagation; flashover; floor coverings; radiant heat flux.

Data is presented for four fire experiments which examine the fire propagation from a room fire to a floor covering material in a corridor. The four floor covering materials include a nylon and an olefin carpet, vinyl sheet, and red oak flooring. Limited flame spread occurred for the vinyl sheet material; however, the three other materials involved full fire propagation in the corridor. The data are analyzed to examine the factors influencing fire propagation. Included in this analysis is the rate of energy contribution from the room fire and floor covering material, the rate of flame spread, heat transfer to the floor covering, and flow interactions between the room and corridor. A review of previous related experiments is also presented.

NBSIR 75-697. **Consideration in the use of sampling plans for effecting compliance with mandatory safety standards,** V. L. Broussalian, A. J. Farrar, U. W. Lyons, C. O. Muehlhause, M. G. Natrella, J. R. Rosenblatt, R. D. Stiehler, and J. H. Winger, 58 pages (June 1975). Order from NTIS as COM 75-10920, $4.25.

Key words: quality assurance; regulation; safety standards; sampling plan; sampling scheme.

Various means available to a regulator for gaining compliance with mandatory safety standards are examined. Particular attention is given to his option of mandating a sampling plan or scheme along with the standard. It is concluded that this option as well as the others identified are all viable under suitable conditions and should be available to the regulator for his possible application on a case by case basis.

NBSIR 75-699. **The calibration of photographic edges at NBS,** R. E. Swing, 37 pages (Apr. 22, 1975). Order from NTIS as COM 75-11016, $3.75.

Key words: acutance; calibration; computer programs; microdensitometry; photographic edges; transfer function.

The method by which photographic edges made at NBS are calibrated is presented and discussed in some detail. The programs associated with the computational aspects of the analysis are listed, covered in narrative form, and their limitations and options are presented. The possible use of these edges to determine microdensitometer transfer function is discussed and limitations and relative error of all the calculations and procedures are covered in detail. Program listings are in BASIC language.

NBSIR 75-707. **Tamper-resistant television surveillance system,** O. B. Laug and K. W. Yee, 38 pages (May 1975). Order from NTIS as COM 75-11017, $3.75.

Key words: safeguards; surveillance; tamper-resistant; television.

This report describes a tamper-resistant television system. This system will be part of a larger system used for verifying compliance with certain international arms control or safeguard agreements. This work is part of a joint U.S.-Canada safeguards research program to develop and evaluate tamper-resistant, tamper-indicating techniques and instrumentation that might be applicable in safeguarding reactors or other nuclear facilities. The principal design objectives are to provide a system capable of unattended operation, data storage capacity for a period up to 90 days, and resistance to deception by insertion of false video information on the transmission line or substitution of false scenes in the camera's field of view. These objectives are accomplished by utilizing commercial high-resolution closed-circuit TV and photography coupled with a video encoding technique which permutes the luminance signal in a different pattern for each recorded picture. Motion detectors, utilizing the video signal, provide the ability to selectively record pictures when motion occurs in preselected areas, and protect the system against insertion of false scenes. The incorporation of these additional features adds comparatively little complexity to ordinary closed circuit TV while greatly increasing its effectiveness as a surveillance tool for safeguards applications.

NBSIR 75-708. **Development of a dynamic pressure calibration technique—A progress report,** C. F. Vezzetti, J. S. Hilten, and P. S. Lederer, 20 pages (June 5, 1975). Order from NTIS as COM 75-10817, $3.25.

Key words: calibration; dynamic; liquid column; pressure; sinusoidal pressure; transducer.

Work continues on the development of a method of producing sinusoidally varying pressures of at least 34 kPa zero-to-peak with amplitude variations within ± 5 percent up to 2 kHz for the dynamic calibration of pressure transducers.

Sinusoidally varying pressures of 34 kPa zero-to-peak have been produced, to date, between 40 Hz and 750 Hz by vibrating a 10-cm column of a dimethyl siloxane liquid at 36 g_n zero-to-peak. Damping of the liquid column was accomplished by packing the fixture tube with a number of smaller diameter tubes.

NBSIR 75-710. **A small-scale enclosure for characterizing the fire buildup potential of a room,** W. J. Parker and B. T. Lee, 23 pages (June 1975). Order from NTIS as COM 75-11030, $3.25.

Key words: fire growth; fire tests; flashover; room fires; scale models; thermal radiation.

A 0.76 by 0.76 m (30 by 30 inch) enclosure with a 0.61 m (24 inch) high ceiling was used to model some fires in a $3 \times 3 \times 2.4$ m ($10 \times 10 \times 8$ ft) burnout room. Temperatures, oxygen concentrations, air velocity, and conductive and radiative heat fluxes were measured. The highest average air temperature in the upper part of the room was taken as a measure of the fire buildup potential of the room. Upper air temperatures attained in the model were similar in most cases to those in the full-scale compartment. From energy balance considerations this air temperature was related to the oxygen depletion in the room and was shown to correlate well with the oxygen content of the combustion gas and air exhausting from the model and full-scale room fires.

NBSIR 75-712. **Solar heating and cooling in buildings: Methods and economic evaluation,** R. T. Ruegg, 47 pages (July 1975). Order from NTIS as COM 75-11070, $3.75.

Key words: economic optimization; HVAC systems; life-cycle cost analysis; solar energy; solar heating and cooling.

This report addresses economic issues important to the design, and evaluation of solar heating and cooling systems in buildings. It explains and illustrates with simple, but realistic examples the use of life-cycle cost analysis and benefit-cost analysis to evaluate and compare the economic efficiency of solar and conventional energy systems. It also explains the conditions for making cost-effective tradeoffs in solar system/building design. By presenting the basic methods and assessing the appropriateness of alternative assumptions, the paper provides a resource document for researchers and analysts.

NBSIR 75-713. **A file management system for a laboratory automation facility,** P. S. Shoenfeld and L. J. Kaetzel, 54 pages (June 1975). Order from NTIS as COM 75-11134, $4.25.

Key words: data acquisition; file system; laboratory automation; multiprogramming; operating system; real-time.

The National Bureau of Standards' Analytical Chemistry Division operates a centralized laboratory automation facility built around a multiprogrammed minicomputer. A file manager was developed which allows the dynamic creation and manipulation of sequential disk files. Although the system was developed for real-time data acquisition, it is a general purpose addition to the computer's operating system and may be used for a variety of applications. A new operating system function was developed to allow the queued scheduling of programs. This is used to achieve more efficient multiprogramming. A comprehensive file utility package is also provided.

NBSIR 75-714. **Report on test on a sample of non-standard size baby cribs,** R. Pierson, Jr., R. I. Beall, and J. A. Huckeba, 33 pages (June 1975). Available from the author, NBS, Washington, D.C. 20234.

Key words: baby cribs; children's furniture; product safety; product testing; safety regulations; standard development.

A sample of non-standard size baby cribs was tested for compliance with the Consumer Product Safety Commission's Proposed Regulation for Non-Standard Size Baby Cribs in order to evaluate the Proposed Regulation, especially the tests and test procedures. The test procedures were found to be easy to interpret and to carry out. This report presents the results obtained from testing the cribs for compliance with the Proposed Regulation, a detailed description of some of the hazards, and some evaluative comments on the Proposed Regulation.

NBSIR 75-715. **The implementation of a provision against**

progressive collapse, F. Y. Yokel, J. H. Pielert, and A. R. Schwab, 23 pages (Aug. 1975). Order from NTIS as COM 75-11208, $3.25.

Key words: building systems; housing systems; large-panel structures; precast concrete construction; progressive collapse; structural design; structural joints.

The design solutions used by five U.S. precast concrete housing systems to comply with a provision against progressive collapse are studied and compared. Some common characteristics of the design solutions are identified.

NBSIR 75-716. **Proceedings of procurement practices symposium, Federal, State and local, January 28-30, 1975,** T. J. Fody and J. G. Berke, 168 pages (May 1975). Order from NTIS as COM 75-11210, $6.25.

Key words: certification programs, ETIP; incentives; innovation; life cycle costing; procurement; product testing; specifications; unsolicited proposals.

The general objectives of the conference are to recommend ways to encourage information interchange and interaction between federal, state and local procurement levels and industry; to explore the use of special incentives such as life cycle costing, value incentives clauses, and unsolicited proposals as a means to promote innovation in products purchased by all levels of government; to establish the interrelationship between marketing, R&D and procurement and develop approaches to acquire the latest technology through the procurement process; to explore various product testing and evaluation efforts such as certification programs, tests by independent, company owned and association laboratories, university and government laboratories. Workshops were organized to consider procurement mechanisms, information interchange, testing and evaluation of products, and the interrelationship between marketing, R&D and procurement. Workshops were grouped as follows: (1) Procurement Incentives, (2) Interaction and Information Interchange, (3) Marketing, R&D and Government Procurement Cycles, (4) Product Testing and Evaluation, (5) Qualified Products Lists and Bid Samples, (6) Qualified Manufacturers, (7) Methods and Techniques of Contracting.

NBSIR 75-720. **Effects of electroless nickel process variables on quality requirements,** F. Ogburn and C. E. Johnson, 47 pages (Dec. 1974). Order from NTIS as COM 75-11135, $3.75.

Key words: autocatalytic nickel; electroless nickel; electroless nickel composition; electroless nickel hardness; electroless nickel properties; electroless plating; hardness of electroless nickel; nickel-phosporus alloy.

Deposition rate, phosphorus content, hardness, appearance, and metal distribution are reported for deposits from several hypophosphite type electroless nickel baths, both proprietary and nonproprietary. The baths were operated under a variety of conditions with variations of composition. Extensive data is given on the relation of deposit hardness to phosphorus content and to heat treatment at 100, 200, and 400 °C. Some data is given relative to electroless Ni-B, Ni-P-Cu, and Ni-P-Mn alloys.

NBSIR 75-723. **Aluminum branch circuit wiring in residences summary report for the Consumer Product Safety Commission January-September 1974,** J. Rabinow, 91 pages (June 1975). Order from NTIS as COM 75-10753, $4.75.

Key words: aluminum wire; consumer product safety; current cycle testing; electrical connection failure; electrical receptacles; residential wiring.

This report is a compendium of information on aluminum wiring in residences, originally prepared for the Consumer Product Safety Commission. It contains a summary of experimental research carried on at the NBS laboratories on the problems of terminating aluminum wires to screw connections as well as other pressure connectors. Since this report is an overview of the technical aspects of the aluminum wiring problem, it also contains a review by NBS staff members of available material furnished by Underwriters Laboratories and Battelle Institute. Both of these institutions are major contributors to this particular field of information.

The report also includes abstracts by NBS staff of some four volumes of testimony taken at public hearings at Washington, D.C. and Los Angeles, California during the spring of 1974. Additional information on the pertinent physical properties of aluminum, information on failure mechanisms, possible corrective actions, connector cycling tests, etc., is given in a brief literature survey and two relevant memoranda on the subject. The report concludes with a fairly extensive bibliography.

NBSIR 75-731. **A study of air-gap breakdown at 28.5 kilohertz,** F. R. Kotter, 42 pages (June 20, 1975). Order from NTIS as COM 75-11071, $3.75.

Key words: air gap; electrical breakdown; insulator flashover; lightning protection; VLF antenna; voltage breakdown.

Measurements of the electrical breakdown of both quasi-uniform and highly nonuniform-field air gaps at a frequency of 28.5 kHz are reported. Gaps between a variety of electrode geometries ranged from a few centimeters to over two meters in length.

Breakdown voltages significantly below the corresponding 60 Hz values were observed with electrodes for which appreciable prebreakdown discharges occurred, and a pattern of "anomalous" flashovers at considerably lower than the normal breakdown voltages was noted with quasi-uniform field gaps. The results obtained appear to correlate well with the data found in the literature for higher frequencies but lower voltages.

On the basis of the gap behavior observed, a prototype protective gap system designed for application to the tower base insulator assembly of a VLF (15 to 30 kHz) radio transmitter was tested and found satisfactory.

NBSIR 75-732. **NBS InterAgency transducer project—A project report,** P. S. Lederer, J. S. Hilten, and C. F. Vezzetti, 23 pages (June 27, 1975). Order from NTIS as COM 75-11022, $3.25.

Key words: calibration; dynamic, electronic flash; pnotoflash bulb; pressure; pressure transducer response; thermal transient; transducer.

The continuing development of a test method for evaluating the effects of short-duration thermal radiant-energy transients on pressure transducer performance is described. The method consists of monitoring pressure transducer output as the transducer is exposed to radiation resulting from the ignition of a photographic flashbulb or from the discharge of an electronic flash. Precision of the method is to be at least adequate for the method to serve as a first-cut screening test. During this reporting period, the following three parameters were investigated for each of three radiation sources: (1) the amount of energy per unit area available as a function of distance from the source, (2) the response of a selected transducer as a function of distance from the source, and (3) flash duration. Repeatability of the method for each source was determined. Work being performed for other agencies is also described briefly.

NBSIR 75-734. **Report on an investigation of the high speed hazards of steel belted patrol tires on police patrol cars,** J. J. Collard, 51 pages (June 1975). Order from NTIS as COM 75-11212, $4.25.

Key words: certification of steel belted radial tires; high speed radial tire hazard; radial tire failures.

Two police fatalities and one permanent disability have been

caused by catastrophic failures of steel belted radial ply tires during high speed police operations. More than 200 other failures were reported by one State highway patrol department. The report recommends that police departments use caution in selecting tires for patrol cars, and that tire manufacturers be required to provide evidence that the tires sold for police use have been tested and certified at speeds of at least 125 miles per hour.

NBSIR 75-736. **Fire research publications, 1974,** N. H. Jason, 11 pages (June 1975). Order from NTIS as COM 75-11018, $3.25.

Key words: bibliographies; building fires; construction materials; fire departments; fire tests; flame spread test; flammability tests; flammable fabrics; Operation BREAKTHROUGH; protective clothing.

"Fire Research Publications, 1974" is a supplement to the previous editions which covered the years 1969-1972 (NBSIR 73-246) and 1973 (NBSIR 74-511). Only publications prepared by the members of the Center for Fire Research (CFR), by National Bureau of Standards (NBS) personnel under contract or grant to the CFR, or by NBS personnel or external laboratories under contract or grant from the CFR are cited. Articles published in NBS house organs also are cited.

NBSIR 75-739. **Development of specifications for archival record materials,** W. K. Wilson and E. J. Parks, 19 pages (Mar. 1975). Order from NTIS as COM 75-11189, $3.25.

Key words: accelerated aging; natural aging; permanence; record materials; record papers; stability.

A specification for copies from office copying machines for permanent records has been prepared and is progressing through a standards organization. A project on the effects of 36 years of natural aging on a group of book papers of known composition was completed and reported. Work on the accelerated aging of handsheets at various relative humidities is incomplete, but data already obtained show that a low relative humidity is desirable in an accelerated aging procedure. Data on the sorption of oxygen by papermaking pulp at elevated temperatures are inconclusive.

NBSIR 75-740. **Piezoelectric polymer transducer for impact pressure measurement,** A. S. DeReggi, 39 pages (July 1975). Order from NTIS as COM 75-11127, $3.75.

Key words: calibration; construction; impact; interface; piezoelectric polymer; polymer; pressure; pressure transducer; theory; transducer.

Described are development efforts relating to the design, construction, and calibration of a piezoelectric polymer transducer for the recording of pressure transients developed over the interface between two bodies as a result of impact. A bilaminate design was selected which uses electrically poled sheets of 25-μm poly(vinylidene fluoride) as the active material. The intended primary response of the transducer is to compression in the thickness direction, which is produced by either hydrostatic or normal pressure; the transducer was also found to respond to extension in the membrane direction. Individual-sheet activity in the thickness-compression mode is approximately 15 pC/N, resulting in a bilaminate transducer pressure response of 4.5 μV/Pa(30 mV/psi). Instructions for poling sheets and for constructing transducers are given in detail. Static and dynamic methods for characterizing transducer output are described. In particular, in order to simulate field conditions in which the transducer may bend or stretch, or both, during impacts, a drop-test procedure with curved impactors has been devised and a theoretical analysis (simplified to the extent of considering the membrane-stress contribution negligible) has been developed to yield the interface pressure.

NBSIR 75-741. **Mechanistic studies of triphenylphosphine oxide-poly (ethyleneterephthalate) and related flame retardant systems,** J. W. Hastie and C. L. McBee, 45 pages (Aug. 1975). Order from NTIS as COM 75-11136, $3.75.

Key words: flame retardancy; mass spectrometry; optical spectroscopy; phosphorus; polyester.

A combination of mass spectrometric and optical spectroscopic studies has been made to establish a mechanism for phosphorus controlled flame retardancy in thermoplastics. It is shown that a vapor phase mode of flame inhibition can account for the known flame retardancy effect of triphenylphosphine-oxide in polyester substrates.

NBSIR 75-744. **Proposed implementation for development of user-terminal protocols for computer network access,** A. J. Neumann, 16 pages (July 1975). Order from NTIS as COM 75-11072, $3.25.

Key words: command languages; computer; man-machine systems; networks; system commands; user protocols.

This report summarizes activities undertaken at the National Bureau of Standards in the area of User-Terminal Protocol Standardization with support from the National Science Foundation, during the latter part of 1974 and 1975. Also discussed are present status of related standardization activities in areas of command languages, terminal keyboards, and terminology. Legal implications of standardization are indicated, and establishment of a Federal Task Group for Standardization is proposed to work under the Federal Information Processing Standards Coordinating and Advisory Committee (FIPSCAC).

NBSIR 75-747. **Building energy authority and regulations survey: State activity,** R. M. Eisenhard, 25 pages (June 1975). Order from NTIS as COM 75-11131, $3.75.

Key words: authority; building; energy; legislation; regulations; state.

Information describing the status of State regulations and authority to regulate energy use in new and existing buildings is presented in tabular form. The tables reference available information on pending bills, acts, or general authority which is embodied in a State Building Code Act. Programs relating to solar energy, insulation, and other building energy items are also listed.

NBSIR 75-748. **Power saws: A review of injury data and power saw industry survey,** V. J. Pezoldt and J. J. Persensky, 95 pages (July 1975). Order from NTIS as COM 75-11031, $4.75.

Key words: accident research; consumer products; injury data; opinion survey; portable circular saws; power saws; radial arm saws; safety; table saws.

Two activities of an investigation of power saws are described: a review of power saw injury data and two surveys of saw manufacturers' opinions concerning safety aspects of saw use and design. The injury data reviewed consisted of information from the National Electronic Injury Surveillance System and from summaries of In-Depth Investigation Reports compiled by the Consumer Product Safety Commission. The two surveys, dealing with portable circular saws and table and radial arm saws respectively, were directed toward obtaining the opinions of technical representatives of power saw manufacturers on five major areas of saw use and design, i.e., electrical safety, blade contact hazards and prevention, accidental starting, the design of various saw components and the judged adequacy of saw instruction manuals. Power saw engineers and designers recognize some problems with present saw designs, especially relating to kickbacks. Overall, however, the survey respondents believe saws to be reasonably free from hazards introduced by product design. The area in which the saw manufacturers believe the most hazards to exist is that of the operator's use of power saws. This human element in saw accidents is recognized as a major contributor to saw related injuries, but little is known about how to assure that safe practices will be followed. Areas for further study are suggested.

This column lists all outside publications by the NBS staff, as soon after issuance as practical. For completeness, earlier references not previously reported may be included from time to time.

Abrams, M. D., **A new approach to performance evaluation of computer networks,** *Proc. 1974 Symp. on Computer Networks: Trends and Applications, Gaithersburg, Md., May 23, 1974,* pp. 15-20 (Institute of Electrical and Electronic Engineers, Inc., New York, N.Y., 1974).

Key words: computer; evaluation; measurement; performance; service; utility.

Interactive conversational computing requires more appropriate measures of performance than those presently applied toward improving the efficiency of system operation. A "stimulus-acknowledgement-response" model has been conceptualized to describe the man-computer interaction. A data acquisition system called the Network Measurement Machine has been developed meeting the objective of being able to measure the delivery of computer services to any user. A set of analysis programs providing statistical summaries of workload, response, and communications utilization analysis over subsets of a conversation, such as use of specific software services, are potentially useful to systems designers and implementers. A sample application is presented with preliminary results.

Alberi, J. L., Wilson, R., Schröder, I. G., **Parity violation in neutron-capture gamma-rays,** *Phys. Rev. Lett.* **29,** No. 8, 518-521 (Aug. 21, 1972).

Key words: internucleon-force; parity-violation.

We have measured the circular polarization of γ rays from thermal neutron capture in ^{113}Cd and find a $P_\gamma = (6.0 \pm 1.5) \times 10^{-4}$ for the combined 8.51- and 9.04-MeV transitions. This value was measured using a transmission Compton polarimeter and pulse-counting technique. The value confirms the existence of parity-nonconserving terms in the internucleon force.

Ambrose, J. R., Kruger, J., **Breakdown of passive films on iron by chloride ion,** *Proc. 4th Int. Congress on Metallic Corrosion, Houston, Tex., Sept. 1969,* pp. 698-704 (National Association of Corrosion Engineers, Houston, Tex., 1972).

Key words: breakdown passivity; chloride; ellipsometry; iron; passivity; pitting.

The breakdown of passive films on iron in pH 8.4 sodium tetraborate/boric acid solution by the action of chloride ions has been studied using a combination of ellipsometric and electrochemical techniques. Two induction times associated with the breakdown process were observed. At t_1, anodic current increases due to increased ionic conduction through the film, followed at t_2 by a localized growth of thick oxide film. These induction times are influenced by chloride ion concentration, time of passive film growth, and temperature of film growth.

Growth kinetics of the passive film in the presence of chloride ion is indistinguishable from that in its absence below a potential E_a^2, that potential above which ferrous ion is not found in solution. Above this potential, breakdown occurs and film growth in the presence of chloride ion results in no limiting thickness.

The results indicate that adsorption and complete penetration by chloride ion to the metal surface is necessary to initiate pitting. When complete penetration occurs, subsequent precipitation of porous γ-FeOOH allows easy local dissolution leading to pitting. After breakdown, a lowering of potential to values below E_a^2 causes an apparent repassivation of the film as indicated by the fact that raising the potential above E_a^2 results in another incubation period before breakdown.

Argentar, H., Bowen, R. L., **Colored charge-transfer complexes from *N,N*-dimethyl-*p*-toluidine,** *J. Dent. Res.* **54,** No. 3, 588-598 (May-June 1975).

Key words: aromatic amine; charge-transfer complexes; color; dental material; methacrylate, phthalate; *N,N*-dimethyl-*p*-toluidine; ultraviolet spectroscopy.

Yellow mixtures form on adding essentially colorless *N,N*-dimethyl-*p*-toluidine (DMPT) to colorless methacrylate monomers containing phthalate, isophthalate, or terephthalate diester groups. The color-causing interactions between the amines and monomers were investigated using ultraviolet spectroscopy. Equations were derived for predicting interactions between formulation ingredients and DMPT that would lead to undesired color.

Armstrong, G. T., Domalski, E. S., **Energy from wastes,** *Report of the Conference on Thermodynamics and National Energy Problems, Warrenton, Va., June 10-12, 1974,* pp. 386-400 (National Academy of Sciences, National Research Council, Washington, D.C., 1974).

Key words: fuel from waste; incinerators; organic waste conversion; thermodynamic data for incinerators; waste utilization.

Today I am your garbageman. I hope you will consider this is an honorable estate. The problem posed by accumulating wastes of all kinds can be enormous; failure to solve it effectively can be fatal to any human community. How fortunate we would be not just to prevent it from overwhelming us, but to find a simultaneous solution to another equally grave problem. There are signs that this can be done, at least in part.

Armstrong, G. T., Domalski, E. S., Minor, J. I., Jr., **Standard combustion data for the fuel gas industry,** *Proc. American Gas Association Section Conf., Atlanta, Ga., May 8-10, 1972,* pp. D-74—D-87 (1972).

Key words: enthalpy of combustion, dry basis; enthalpy of combustion, saturated basis; enthalpy of formation, hydrocarbons, heating value; hydrocarbons; International System of Units.

Equity in the sale of natural gas or other gases for fuel purposes requires that the total calorific values be accurately known and that the same values be used throughout the industry for gases of identical properties. This paper gives the total calorific values (gross heats of combustion at constant pressure) of gaseous H_2, H_2S, CO, CH_4 and 49 selected other gaseous hydrocarbons, C_1 to C_6, in the ideal gas state at standard conditions of 60 °F and 30 in. Hg (288.71 K and 101591.3 $N \cdot m^{-2}$), on a molar basis, on a dry volumetric basis and on a water-saturated volumetric basis. Units used are $kJ \cdot mol^{-1}$, $MJ \cdot m^{-3}$, $Btu_C \cdot (scf)^{-1}$

A supplementary table is given for the total calorific values of the same substances in the ideal gas state at the slightly different standard conditions of 60 °F and 14.73 psia (288.71 K and 101559.8 $N \cdot m^{-2}$) on a dry volumetric basis and on a water-saturated volumetric basis. Units used in this table are $MJ \cdot m^{-3}$ and $Btu_{IT} \cdot (scf)^{-1}$. Total calorific values for real-gas methane are also given on the above bases. Enthalpies of combustion and molar heat capacities of crystalline carbon (graphite), and all the above named gases are given in the thermodynamic standard states at 298.15 K. Procedures for making the calculations, and necessary auxiliary data are given. Implications of the possible change of the measurement system to metric units are discussed.

Armstrong, G. T., Johnson, W. H., **Standard reference materials for combustion calorimetry,** *Proc. Third Int. Conf. on Chemical Thermodynamics, jointly with Symposium on Physicochemical Techniques at High Temperatures* (1000–4000 *K*), *Baden near Vienna, Austria, Sept.* 3-7, 1973, **VIII,** 55-72 (Abstract is found in Vol. 1, Page 148), (1973).

Key words: acetanilide; bomb calorimetry; chlorobenzoic; combustion; creatinine; fluorobenzoic; thermochemical; thianthrene.

In response to requests made over many years by international commissions on thermochemistry and national calorimetry conferences, a new series of reference materials for bomb calorimetry has been started, representing organic substances containing an element that introduces chemical complications. Investigations have been carried out on candidate substances containing fluorine, chlorine, nitrogen, sulfur and phosphorus.

The most perplexing problem for which to find a suitable decision logic is to establish criteria for the difficulty or complexity of the chemical and calorimetric problems posed by the proposed reference substance.

The compounds tested, the experimental data obtained, and the state of readiness of selected reference materials will be described.

Arp, V. D., Clark, A. F., Flynn, T. M., **Superconducting levitation of high speed vehicles,** *Transp. Eng. J.* **99,** No. TE4, 873-885 (Nov. 1973).

Key words: levitation; magnetic suspension; materials fatigue data; refrigeration; superconducting magnets; transportation.

The current status (December 1972) of worldwide research on high speed ground transportation techniques is reviewed. Particular attention is given to studies of magnetic levitation using superconducting magnets, including comparison with alternative magnetic techniques and with air suspension systems. Superconducting levitation appears to be a strong contender in the U.S. Department of Transportation hopes to select in the late 1970's the best of the possible levitation techniques for subsequent advanced development. Cryogenic engineering research needed in support of major development of a superconducting levitated system is identified.

Arvidson, J. M., Brennan, J. A., **ASRDI oxygen technology survey, Vol. VIII: Pressure measurement,** *NASA Spec. Publ.* 3092, 200 pages (Available from the National Technical Information Service, Springfield, Va. 22151, 1975).

Key words: calibration; compatibility; cryogenic; liquid oxygen; measurement; oxygen; performance; pressure; survey; transducer.

This publication is part of an oxygen safety review in progress by the NASA Aerospace Safety Research and Data Institute (ASRDI). The objectives of the review include: 1. Recommendations to improve NASA oxygen handling practices by comparing NASA and contractor oxygen systems including the design, inspection, operation, maintenance, and emergency procedures. 2. Assessment of the vulnerability to failure of oxygen equipment from a variety of sources so that hazards may be defined and remedial measures formulated. 3. Contributions to safe oxygen handling techniques through research. 4. Formulation of criteria and standards on all aspects of oxygen handling, storage, and disposal.

The special publication summarizes the current state-of-the-art in pressure measurement in the region of 50 to 150 K (the liquid state of oxygen). The report is not limited to oxygen-proved systems alone as this would have severely limited the report. The published literature available in the cyrogenic region generally is quite restricted. The survey includes information on cleaning and materials compatibility, calibration methods and descriptions of representative transducers. A summary of recommendations is presented as well as an extensive bibliography arranged by transducer type.

Baker, D. W., Koenig, A. L., **An automated prototype test system for aircraft engine fuel controls, design and operating experience,** *Proc. 13th Annual Tech. Symp., Washington, D.C., Chapter ACM, June 20, 1974,* pp. B.4.1-B.4.11 (Association for Computing Machinery, New York, N.Y., 1974).

Key words: automated test equipment; automated tests for jet engine fuel controls; computer interfacing; digital computer controlled tests; jet engine fuel control testing; minicomputer applications; minicomputer controlled tests; supervisory control; test equipment reliability.

The adjustment and calibration of the fuel control, the accessory which meters flow to the engine burners, requires long-term bench tests involving many often repeated manual operations. Minicomputer-based hardware and software systems, developed during 1968-1971, which control an existing production test stand are reviewed. The systems automating this stand, used in the rework of TF-30 engine controls, simulate engine parameters burner pressure and drive shaft speed using supervisory control. Also, metered fuel flow is measured and read out. An auxiliary panel at the test stand containing readout and input devices enables the operator to run the test. This prototype system has served as basis for two test systems, under contract and slated for production, which will automate nine stands.

Baker, D. W., Sayre, C. L., Jr., **Decay of swirling turbulent flow of incompressible fluids in long pipes,** (Proc. 1st Symp. on Flow, Pittsburgh, Pa., May 10-14, 1971), Chapter in *Flow, Its Measurement and Control in Science and Industry. Part I. Flow Characteristics,* H. W. Stoll, Ed., **1,** 301-312 (Instrument Society of America, Pittsburgh, Pa., 1974).

Key words: decay of swirling flow; helical flow; pressure differential during swirling flow; swirling flow.

The decay of swirling flow fields in steady-state flow in cylindrical, unobstructed, smooth pipes is considered from measurements made in two pipes. With water flowing in one pipe, mean point velocities and static pressures including wall pressures were measured at several stations along the pipe. With liquid hydrocarbons flowing in the other pipe, measurements were made of wall pressure and the swirling motion of the fluid, as sensed by a vaned rotor. The investigation included the pipe Reynolds number (Re) range 12,500 to 200,000 and for the vortex flows generated, the product K/MD varied from 0 to 0.9, where K is the angular momentum flux, M is the axial momentum flux, and D is the pipe i.d. Results including those of other sources show that K decreases exponentially along the pipe at a decay rate β ranging from about 2 percent per pipe diameter at Re = 200,000 to 4 percent per pipe diameter at Re = 12,500; and that data scatter and values of β for other sources demonstrate dependence of β on the inlet geometry, and possibly on K and system turbulence characteristics. Other results show the ratio of the pressure gradient along the wall during swirling flow to nonswirling flow varies primarily with the angular momentum flux. The behavior of swirling flow fields is not well known, and these facts can aid in an improved description of swirling fields in which the performance of flow measurement and control devices might be evaluated.

Ball, J. J., Keller, R. A., **Quantitative determination of gaseous nitrogen dioxide concentrations over long path lengths by selective absorption of argon ion laser emission,** *J. Air Pollut. Contr. Ass.* **25,** No. 6, 631-633 (June 1975).

Key words: absorption spectroscopy; air pollution; laser; NO_2.

An argon ion laser emits several laser lines in the visible region of the optical spectrum. The absorption coefficients of NO_2 at these laser emissions were measured in a multiple pass absorption cell. A differential technique, in which the ratio of the transmitted intensities of the argon laser emissions is measured, is described to determine the concentration of NO_2 in a polluted atmosphere over path lengths of several kilometers. Measurement of ratios eliminates interferences from particle scattering and thermal index gradients. Evaluation of the data taken in the 48 meter multipass cell indicates that concentrations of NO_2 less than one part per million could be determined in a 1 km optical path.

Bardsley, J. N., Holstein, T., Junker, B. R., Sinha, S., **Calculations of ion-atom interactions relating to resonant charge-**

transfer collisions, *Phys. Rev. A* **11,** No. 6, 1911-1920 (June 1975).

Key words: atom; collision; Cs_2^+; ion; Li_2^+; low energy; Na_2^+; pseudopotential; Rb_2^+; resonant charge transfer.

The interaction between an atom and ion of the same element leads to gerade and ungerade states of the diatomic molecular ion. The energy splittings between the gerade and ungerade states determine the cross section for resonant charge transfer. Using the JWKB approach these energy splittings are derived from the asymptotic forms of the wave functions for the isolated atom and ion. Pseudopotential calculations of the splittings are reported for Li_2^+, Na_2^+, Rb_2^+, and Cs_2^+, and are used together with previous *ab initio* and model-potential calculations to test the JWKB method. The comparison shows that the method is sufficiently reliable to facilitate accurate calculations of the cross sections for resonant charge transfer at low energies.

Barger, R. L., West, J. B., English, T. C., **Fast frequency stabilization of a cw dye laser,** *Appl. Phys. Lett.* **27,** No. 1, 31-33 (July 1, 1975).

Key words: cw dye laser; frequency stabilization; intensity stabilization.

A system is described for stabilizing a cw dye laser frequency to a high-finesse optical cavity. The length of this optical cavity is locked to a CH_4-stabilized He-Ne laser with a tunable frequency-offset technique. A very fast servo system (using an intracavity KD*P crystal), a long dye laser cavity, and the stabilized optical cavity result in an absolute frequency stability of 1 kHz for an integration time of 10^{-4} sec and 300 Hz for 300 sec. Intensity is stabilized to one part in 10^4.

Barkley, J. F., Shoenfeld, P. S., **A central laboratory automation facility,** *Amer. Lab.* **7,** No. 2, 19-20, 22, 24-25 (Feb. 1975).

Key words: analytical chemistry; computer; data acquisition; laboratory automation operating system; teleprocessor.

The Analytical Chemistry Division at the National Bureau of Standards has developed a centralized computer facility for laboratory automation, which is described in this paper. This facility consists of two major components. These are the teleprocessor, which handles all communication between the laboratory and the computer, and the computer itself. Also described are the essential system software packages including the Operating System, the File System, and the Data Acquisition System.

Bartel, T. W., Schade, P. A., **Digital processing of decay rates for reverberant sound fields,** *Proc.* 1974 *Int. Conf. on Noise Control Engineering, Washington, D.C., Sept.* 30-*Oct.* 2, 1974, pp. 61-64 (Oct. 1974).

Key words: digital processing of decay rates; digital sampling; graphics display terminal; interactive program; least-squares analysis; real-time analyzer; reverberation room; spectrum shaping.

The installation of a 64K byte minicomputer to the NBS Sound Laboratory has made the capabilities of digital processing available for application to the various types of reverberation-room measurements. The present work applies this technique to reverberant field decay rate measurements. Such measurements conducted with analog equipment are limited by the amount of time and labor required to make and process the large number of decay curves necessary to achieve precise results. Reduction of these limitations is realized by interfacing the computer to digital sampling equipment capable of processing thirty 1/3-octave bands simultaneously. Through control of the reverberation room sound source and signal-processing equipment, the computer can conduct decay measurements and apply a least-squares analysis to the stored data to compute the decay rates. The software is to be expanded into an interactive program allowing the experimenter to observe the data on a display device and insert his own decisions into the data reduction process.

Beers, J. S., Tucker, C. D., **Procedures for gage block flatness and parallelism measurement,** *J. Appl. Meas.* **2,** No. 4, 82-84 (1974).

Key words: flatness; gage blocks; interferometry; length measurement; parallelism.

Geometric properties of gage blocks are important in many length measurement applications. Methods are described for measuring the flatness of gaging faces and the parallelism between opposing gaging faces. These methods, used for many years, employ interferometers and electro-mechanical gage block comparators.

Bennett, A. J., Penn, D., **Optical properties of adsorbate atoms,** *Phys. Rev. B* **11,** No. 10, 3644-3657 (May 15, 1975).

Key words: adsorbate atom; dielectric function; electronic states; optical adsorption.

We calculate the dielectric response of adsorbate atoms on a metal surface assuming an Anderson model of the system. The dielectric function is then used to predict the change in the surface optical reflectance caused by the adsorbates. General results are obtained for substrates with one and two electron bands with and without the assumption of momentum conservation in the band-to-band optical transitions. A detailed analysis is carried out for the single-band momentum-conserving case. Here, the model is the same as that studied by Caroli and Kjollerstrom if the substrate density of states and various matrix elements are taken to be constants. However, we find an additional nonnegligible contribution omitted in their analysis. In other single-band cases, we show the wide variety of behavior which may be obtained for different parameter ranges and provide expressions to be used in data analyses.

Bennett, S. L., Lias, S. G., Field, F. H., **Ion-molecule reactions in ethane,** *J. Phys. Chem.* **76,** No. 26, 3919-3926 (1972).

Key words: ethane; gas phase kinetics; ion-molecule reactions; mass spectrometer; product ions.

The ion-molecule reactions in ethane have been investigated in a mass spectrometer at pressures from 0.1 to 5 torr and at temperatures ranging from 189 to 410 K. The major primary ions, $C_2H_4^+$, $C_2H_5^+$, and $C_2H_6^+$, react with ethane to form the respective addition ions, $C_4H_{10}^+$, $C_4H_{11}^+$, and $(C_2H_6)_2^+$. Under these conditions, the addition ions dissociate to give all the product ions which have been attributed to reactions of these primary ions in previous studies. The major product ions resulting from these dissociation reactions are the $C_3H_7^+$ and $C_4H_9^+$ ions, formed by dissociations of the $C_4H_{10}^+$ and $C_4H_{11}^+$ ions, respectively. The rate constants for disappearance of the primary ions decrease as the temperature is raised from 189 to 410 K, from 2×10^{-10} to 0.9×10^{-10} cm^3/molecule sec for the ethylene ion, from 2.5×10^{-10} to 0.5×10^{-10} cm^3/molecule sec for the ethyl ion, and from 2×10^{-10} to 0.5×10^{-10} cm^3/molecule sec for the ethane ion. There is no evidence that any of the product ions react further with ethane to give higher molecular weight addition ions under these conditions of temperature and pressure. When H_2O is added to ethane the ethylene ion is intercepted in a rapid reaction to form the $C_2H_4 \cdot H_2O^+$ complex, which reacts further with water to add a second, a third, and a fourth molecule of water.

Berger, H., **A report on the American Nuclear Society Topical Meeting "Nondestructive Testing in the Nuclear Power Industry,"** *Nucl. News* **18,** No. 1, 68, 73-74 (Jan. 1975).

Key words: electric utilities; hot cell inspection; in-service inspection; nondestructive testing; nuclear power; reactor components.

The article is a description of American Nuclear Society Topical

Meeting "Nondestructive Testing in the Nuclear Power Industry" held in Columbus, Ohio, September 23-25, 1974. Key statements and key papers in the various sessions at the 2 1/2 day meeting are discussed to give readers of the ANS journal, Nuclear News, an idea of what was presented at the meeting.

Berger, H., Motz, J. W., **A qualitative discussion of quantitative radiography,** (Proc. 2nd ASM Materials/Design Forum, Port St. Lucie, Fla., Apr. 8-11, 1974), Paper in *Prevention of Structural Failure*, T. D. Cooper, P. F. Packman, and B. G. W. Yee, Eds., No. 5, 37-47 (American Society for Metals, Metals Park, Ohio, 1975).

Key words: dimensional measurement; image enhancement; imaging methods; nondestructive evaluation; radiography; serviceability.

Quantitative aspects of radiography are described and illustrated. Radiography is a widely used method for nondestructive testing. It offers the advantage of giving an image of objects as a permanent inspection record. Voids, inclusions, and cracks in homogeneous materials and welds can be detected. The size, shape and location of discontinuities are revealed if the change in density or thickness is of the order of one percent and covers a sufficient area to be resolved by the radiographic technique. The measurement of the dimensions and depth of an object can be made and, in certain circumstances, such measurements are possible to accuracies of $\pm$ 0.001 inch.

In addition, radiography can be used effectively as an accept-reject criterion, especially in conjunction with well defined specifications and reference radiographs.

Novel radiographic methods that offer advantages in improving image contrast are briefly discussed. Included are image enhancement methods and radiography employing neutrons, monoenergetic x-radiation, or charged particles.

Bertocci, U., **Computer simulation of crystal growth on a fcc surface,** *J. Cryst. Growth* **26,** No. 2, 219-232 (Dec. 1974).

Key words: computer simulation; crystal growth; fcc crystals; roughness; surfaces.

Positive and negative crystal growth has been simulated on a (100) surface of a fcc crystal. The results show considerable similarities with the behavior of simple cubic surfaces, as far as the values of the interatomic bond energy and of the free energy for crystallization at which transition from smooth to rough surfaces occur. Growth rates are smaller, reflecting the formation of a sizable area where both deposition and removal of atoms is hindered. The surface roughness at equilibrium is similar to that obtained by computer simulation by other authors on a (100) surface of a Kossel crystal and it is close to that of a two-dimensional square lattice.

Birky, M. M., Yeh, K. N., **Calorimetric study of flammable fabrics. I. Instrumentation and measurements,** *J. Appl. Polym. Sci.* **17,** 239-253 (1973).

Key words: calorimeter; fabrics; flammability; heat of combustion; rate of combustion.

A calorimeter has been designed, calibrated, and tested to measure the total amount of heat released and the rate of heat released from the combustion of fabrics in air. Calibration of the calorimeter gave a reproducibility of $\pm$ 3 percent for total heat measurements and $\pm$ 5 percent on rate measurements. Consideration of systematic errors gives an expected accuracy of $\pm$ 7 percent for total heat and $\pm$ 10 percent for combustion rate measurements. Measurements on cotton show that 90 percent of the standard heat of combustion is released when cotton is burned in air. The rate of heat release for cotton is independent of fabric weight. The constancy of rate of heat release as determined calorimetrically confirmed the result implied by the 45° test measurements on flame spread rate. The rate and amount of heat release of other commercial fabrics and blends were also measured.

Bloss, R. L., **Evaluation testing of resistance strain gages,** *Proc. Tech. Session on Strain Gaging for Accuracy Conf., Milwaukee, Wis., Oct.* 19, 1971, pp. 1-5 (Society for Experimental Stress Analysis, Westport, Conn., 1975).

Key words: bonded resistance strain gage; combined effects; evaluation tests; fatigue; high temperature; performance characteristics.

Since it is usually impossible to determine the performance characteristics of the specific resistance strain gages that will actually be used in a test program, we must depend upon their behavior being predictable from tests that have been conducted on other gages. When resistance strain gages first became available, information about their performance was limited. The situation was further complicated during World War II when a number of organizations began producing gages, usually for their own use. A similar situation arose when the need for strain measurements at elevated temperatures induced a number of organizations to produce gages for such use. User and third party evaluation testing was instrumental in the development and characterization of the gages during these times. Today most manufacturers carry out continuing testing and evaluation programs to insure that the user can rely upon their products and to maintain and enhance their competitive positions in the field. However, the user must continue to carry out such tests when special requirements or test conditions are encountered.

A brief history of evaluation testing of bonded resistance strain gages is given, and two evaluation tests are described.

Bowen, R. L., **Adhesive bonding of various materials to hard tooth tissues. VII metal salts as mordants for coupling agents,** (Proc. Symp. on Dental Adhesive Materials, New York, N.Y., Nov. 8-9, 1973), Paper in *Dental Adhesive Materials*, H. D. Moskowitz, G. T. Ward, and E. D. Woolridge, Eds., pp. 205-221 (Prestige Graphic Services, New York, N.Y., 1974).

Key words: adhesive bonding; chelation; comonomers; coupling agents; dental materials; hard tooth tissues; metal ions; mordant.

A number of hypothetical concepts are presented to serve as a guide for experimentation. The concepts include the combined use of etching and surface-active comonomers to obtain improved adhesive bonding between polymers and hard tooth tissues, and the use of certain metal ions to augment the interaction between the coupling agents and the tooth surfaces.

Bowen, R. L., Antonucci, J. M., **Dimethacrylate monomers of aromatic diethers,** *J. Dent. Res.* **54,** No. 3, 599-604 (May-June 1975).

Key words: composites, dimethacrylates; monomers; resins; synthesis.

Crystalline aromatic diether methacrylates can be prepared from dihydric phenols or their bis(2-hydroxyethyl) derivatives by simple condensation procedures. Three solid isomers form a liquid ternary eutectic when mixed in suitable proportions.

Brauer, G. M., **Modification of soft and hard tissues,** (Proc. Symp. on Dental Adhesive Materials, New York, N.Y., Nov. 8-9, 1973), Paper in *Dental Adhesive Materials*, Moskowitz-Ward-Woolridge, Eds., pp. 180–204 (Prestige Graphic Services, New York, N.Y., Sept. 1974).

Key words: bone; chemical grafting; collagen; ratskin; surface modification; tissue surfaces.

Various techniques to modify hard and soft tissues, with the aim of enhancing adhesion, are reviewed. Treatment of enamel surfaces with acids enhances adhesion because of mechanical interlocking of resin at the enamel resin interface. Coupling agents have had some

success in promoting adhesion of tooth structure to dental restoratives.

Special emphasis is given to chemical grafting techniques to obtain covalent bonding to tissue surfaces which are investigated in our laboratory.

The grafting of monomers to soft and hard tissues so that after polymerization of the monomer the proteinaceous surface is bonded covalently to the polymer side chain, offers an attractive technique for improving surface characteristics of skin, bone or dentin. Grafting monomers containing additional functional groups that are potential reactive centers for further modification of the collagenous surfaces appears feasible. Grafting to soft tissues can be conducted in the presence of various redox systems, but grafting to bone is best accomplished with persulfate-bisulfite initiator. Modification of the tissue surface is indicated by changes in wettability, decreased water sorption and improved resistance to mold growth. Surfaces with the desired degree of hydrophil to lipophil balance to suit specific applications may be prepared. The modified surfaces could be useful as adhesion promoting liners for restorative resins.

Brown, W. E., Patel, P. R., Chow, L. C., **Formation of $CaHPO_4 \cdot 2H_2O$ from enamel mineral and its relationship to caries mechanism,** *J. Dent. Res.* **54,** No. 3, 475-481 (May-June 1975).

Key words: caries mechanism; dicalcium phosphate dihydrate; enamel mineral solubility; pyrophosphate formation.

Tooth enamel, when treated with dilute H_3PO_4 solutions, dissolved incongruently with formation of large $CaHPO_4 \cdot 2HO_2O$ crystals. Equilibrated solutions were saturated with respect to $CaHPO_4 \cdot 2H_2O$, and a mineral more soluble than well-crystallized, synthetic $Ca_5(PO_4)_3OH$, probably an impure, defective apatite. The $CaHPO_4 \cdot 2H_2O$ crystals formed at considerably higher pH values than expected because of enhanced solubility of the apatitic phase in enamel. Pyrolysis of carious enamel revealed the presence of acidic calcium phosphate presumed to be $CaHPO_4 \cdot 2H_2O$.

Cezairliyan, A., **Pulse calorimetry and transient measurement of thermal properties at high temperatures,** *Faraday Symp. Chem. Soc.*, No. 8, 7-17 (1973).

Key words: high-speed measurements; high temperature; pulse calorimetry; thermodynamics; thermophysical properties.

A system is described for the transient (subsecond) measurement of selected thermal and related properties of electrically-conducting substances in the temperature range 1500 K to the melting point of the specimen. The method is based on resistive self-heating of the specimen from room temperature to any desired high temperature in less than 1 s by the passage of an electrical current pulse through it; and on measuring and recording the experimental quantities every 0.4 ms with a full-scale signal resolution of one part in 8000. The system has been used to measure heat capacity, electrical resistivity, hemispherical total emittance, normal spectral emittance, and the melting point of selected refractory elements and alloys. The results of preliminary experiments have shown the potential application of the system to measurements of temperatures and energies of solid-solid phase transformations and heat of fusion at high temperatures.

Cezairliyan, A., Righini, F., **Measurements of heat capacity, electrical resistivity and hemispherical total emittance of two grades of graphite in the range 1,500 to 3,000 K by a pulse heating technique,** *Rev. Int. Hautes Temp. Refract.* **12,** No. 2, 124-131 (1975).

Key words: electrical resistivity; graphite; heat capacity; high-speed measurements; high temperature; thermal emittance; thermodynamics.

Measurements of heat capacity, electrical resistivity and hemispherical total emittance of Poco and pyrolytic graphites in the temperature range 1,500 to 3,000 K by a sub-second duration pulse heating technique are described. For a given graphite grade, heat capacities of different specimens were in agreement within 0.5 percent. The difference between the results of the two different grades was about 1.8 percent; the results of Poco being higher than those of pyrolytic. Electrical resistivity of the Poco graphite was about four times greater than that of pyrolytic graphite (parallel to basal planes). Hemispherical total emittance of Poco graphite was almost twice that of pyrolytic graphite.

Churney, K. L., West, E. D., Armstrong, G. T., **A cell model for isoperibol calorimeters,** *Proc. 1st Natl. Conf. on Calorimetry, Zakopane, Poland, Sept. 8-18, 1973,* pp. 1-43 (Polish Academy of Science, Institute of Chemical Physics, Warszawa, Poland, 1973).

Key words: calorimetry; energy equivalents; energy measurement; heat transfer; internal energy measurement; isoperibol calorimeters; measurement theory.

A calorimeter can be modeled as a large number of volume elements or cells in each of which the temperature may be considered uniform, and each of which can store heat and exchange heat with other cells. Application of the first law of thermodynamics to this set of cells leads to representations of the usual calorimetric equations for the energy change expressed in terms of measurable or estimatable heat capacities, heat transfer coefficients, temperatures, and work terms for the individual cells. Analysis of the results yields a framework within which most of the design and measurement problems of isoperibol calorimeters can be treated.

Clifton, J. R., Beeghly, H. F., Mathey, R. G., **Protecting reinforcing bars from corrosion with epoxy coatings,** Chapter SP 49-10 in *Corrosion of Metals in Concrete*, pp. 115-132 (American Concrete Institute, Detroit, Mich., 1975).

Key words: bridge decks; chlorides; concrete; corrosion; epoxy coatings; organic coatings; steel reinforcing bars.

This study was undertaken to ascertain the feasibility of using organic coatings, especially epoxies, to protect steel reinforcing bars embedded in concrete of bridge decks from rapid corrosion. This corrosion is caused by chloride ions from the deicing salts, sodium chloride and calcium chloride. Altogether, 47 different coatings were evaluated to some extent, of which 36 were epoxy coatings.

The results of this study indicate that some epoxy coating, if properly applied, should adequately protect steel reinforcing bars from corrosion. Epoxy coated bars had acceptable bond and creep characteristics when embedded in concrete and therefore can be used in existing bridge designs. Epoxy coated bars can also be used in other concrete structures.

Cohen, J., Edelman, S., **Polymeric pyroelectric sensors for fire protection,** *Tech. Rep. AFAPL-TR-74-16,* 27 pages (Available from the National Technical Information Service, Springfield, Va. 22151, 1975).

Key words: heat detector; optical radiation sensor; poling; polymer; polyvinyl fluoride; polyvinylidene fluoride; pyroelectric effect; relative spectral response; ultraviolet detector.

This report summarizes the results of a program to develop optical radiation sensors for fire detection using polymeric pyroelectric sensing elements. Emphasis has been placed on techniques for constructing such devices, including methods of enhancing the pyroelectric response. Materials investigated included polyvinyl fluoride (PVF) and polyvinylidene fluoride (PVF_2). Six sensors were developed and delivered to the sponsor.

Highlights reported include achievement of a value of specific detectivity, D*, of 2×10^8 cm $\cdot Hz^{1/2} \cdot W^{-1}$ and the construction of a set of sensors useful over a wavelength range extending from the ultraviolet to the infrared.

Methods of characterizing the performance of sensor elements are described.

Cooper, J. W., **Photoionization of inner-shell electrons,** Chapter 3 in *Atomic Inner-Shell Processes, Vol. 1, Ionization and Transition Probabilities,* pp. 159-199 (Academic Press, Inc., San Francisco, Calif., 1975).

Key words: atomic; inner shell; photoionization; quantum-mechanical.

This chapter of "Inner Shell Processes" (to be published by Academic Press) provides a survey of theoretical methods used in treating inner shell photoeffect. The subject is approached from a quantum-mechanical viewpoint and various approaches are related within this context.

Cotton, I. W., Meissner, P., **Approaches to controlling personal access to computer terminals,** *Proc. 1975 Symp. on Computer Networks: Trends and Applications, Gaithersburg, Md., June 18, 1975,* pp. 32-39 (IEEE Computer Society, Long Beach, Calif., 1975).

Key words: access; access control; authentication; computer networks; computer security; computer terminals; personal identification.

The advent of time-sharing and computer networking has resulted in a proliferation of computer users, many of whom are located remotely from the computer which serves them. This has been accompanied by increased opportunities for unauthorized users to gain access to computers and has focused attention on the problem of identifying and authenticating properly authorized users. The requirements of the recently-enacted Privacy Act of 1974 calls for a number of safeguards in the handling of personal information by the Federal agencies, and personal identification of personnel authorized to have access to such information is an important aspect of the implementation of this law. This paper considers the various approaches to personal identification and authentication, on the basis of things known to an individual, things possessed by an individual, and characteristics of an individual, such as appearance, handwriting, voice, fingerprints, and hand geometry.

A set of evaluation criteria is presented as a guide in selecting personal identification systems for various applications. It is pointed out that currently-available systems are vulnerable in varying degrees to erroneous recognition and circumvention, and therefore should be incorporated into a hierarchical security system which utilizes a variety of safeguards, including auditing features to provide a record of what is accessed, by whom, and for what purposes.

Cotton, I. W., **Methodologies for the cost-benefit analysis of computer graphics systems,** *Comput. & Graphics* **1,** 33-43 (1975).

Key words: computer graphics; cost-benefit analysis; cost-effectiveness; economics; performance evaluation.

This paper assesses the state of the art in cost-benefit analyses of computer graphics systems and suggests an approach for developing improved methodology. Cost-benefit analyses are distinguished from analyses of system performance in that the latter is directed at optimizing system performance at a given level of investment, while the former is directed at justifying the investment itself.

Computer graphic system design alternatives are first outlined. Then methods of analyzing the performance and costs of computer systems in general and graphic systems in particular are discussed. With this information it is shown how cost-effectiveness analyses may be performed. The next crucial step is to conduct benefit analysis, an ill-defined art. The results of benefit analysis must be combined with cost-effectiveness analysis in order to perform the desired cost-benefit analysis.

An experimental methodology is suggested for better performing benefit analyses of computer graphics systems. A more rigorous formulation of the cost-benefit procedure is then outlined. No attempt is made in this report to actually perform such an analysis.

Cotton, I. W., **Microeconomics and the market for computer services,** *Comput. Surv.* **7,** No. 2, 95-111 (June 1975).

Key words: administration of computing; computer services; management; microeconomics; pricing.

Microeconomics has much to offer the computer services manager. This article reviews some of the traditional topics in microeconomics and shows how they can be applied to the market for computer services. The topics covered include supply, demand, costs, and pricing. The most significant application of microeconomics is in setting prices—so much so that microeconomics is frequently called "price theory." Accordingly, the thrust of the article is towards providing a sound framework for the pricing of computer services.

Cotton, I. W., **Standards for network graphics communications,** *Comput.—Graphics* **1,** 45-47 (1975).

Key words: computer graphics; computer networks; graphics; networks; protocol; standards.

Common protocols provide a means for the interchange of information between dissimilar systems in a computer network. This paper discusses the background and philosophy of the common graphics protocol currently under development for the ARPANET and outlines the details of its design. Other applications for such a protocol are suggested.

Cram, S. P., Chesler, S. N., **Analytical fluidic sampling systems,** *J. Chromatogr.* **99,** 267-279 (1974).

Key words: automated systems; fluidic logic; gas chromatography; plasma chromatography; sampling.

Fluidic logic sampling systems have been developed for analytical detectors such as the plasma chromatograph and flame ionization detector. Automated systems are reported for gases and vapor-phase samples which are rapid, quantitative and reproducible. Sample modulation systems, multiplexers, parallel-to-serial converters and sequential samplers have been developed which give no leakage or cross-talk signals. Other applications in analytical chemistry are proposed.

Danos, M., Weller, H. R., **Correlation between the (d, γ_0) and (p, γ_0) cross sections in the giant dipole resonance of ^{16}O,** *Phys. Rev. C* **10,** No. 6, 2627-2628 (Dec. 1974).

Key words: giant resonance; intermediate structure; nuclear structure; particle-hole model; quasi-bound states; two-particle two-hole states.

The reaction theory of Fano is applied to the analysis of the $^{15}N(p, \gamma_0)^{16}O$ data *vis à vis* the $^{14}N(d, \gamma_0)^{16}O$ data. The result is consistent with the Gillet model which attributes the structure near 22.9 MeV in ^{16}O to a 2p-2h quasibound state.

Davis, D. D., **Calibrating crystal oscillators with TV color-reference signals,** *Electronics* **48,** No. 6, 107-112 (Mar. 20, 1975).

Key words: crystal oscillator; frequency calibrator; frequency offset; NBS traceability; phase comparison; television.

The National Bureau of Standards checks the frequency of the network television color signals and publishes the results. Here is a way to use that information to calibrate your own oscillator.

Donnay, J. D. H., Ondik, H. M., Eds., Book, **Crystal data determinative tables, Vol. 1. Organic compounds,** 999 pages (1972); **Vol. 2. Inorganic compounds,** 2106 pages (1972).

Key words: cleavage; compilation; crystal; crystal habit; crystal space group; crystal structure types; density; determination; identification; minerals; optical properties; twinning; unit cell dimensions.

This edition, which will comprise two volumes, is a thoroughly revised and updated work, containing over 24,000 entries. Some 7,500

carbon-containing crystalline compounds are given in Volume I. They are listed, within each crystal system, according to increasing values of a determinative number: *a/b* ratio in trimetric systems, *c/a* ratio in dimetric systems, cubic cell edge *a* in the isometric system. Conventional rules insure the uniqueness of crystal setting.

For each crystalline species the following properties are listed on the first line: axial ratio(s) and interaxial angles not fixed by symmetry, cell dimensions, space group or diffraction aspect, number of formula units per cell, crystal structure (whether determined), measured density, x-ray calculated density. Then come: name of the compound, synonym(s), chemical formula, literature reference, transformation matrix (when the original data had to be recast to conventional cell and setting). Additional information includes some or all of the following: crystal-structure type (if any), goniometric axial ratio(s), crystal habit, cleavages, twinning, color, optical properties, indices of refraction, optical orientation (except in the anorthic system), melting point, transition point.

Nearly all the data were obtained from original sources. "Limits of error" on numerical values are quoted from the reference. The data have been tested for self-consistency by means of computer programs. Any erratum found either in the reference or in an abstracting journal (e.g., *Structure Reports*) is specifically mentioned: erroneous values are thus identified. Editorial critical remarks point out possible errors in the literature.

Formula and name indexes enable one to learn if crystallographic information is available on any given compound, thereby providing a starting point for bibliographic searches.

Ebert, P. J., Dick, C. E., **Comments on the observation of nondivergent radiation of discrete frequencies,** *Phys. Rev. Lett. Comments* **34,** No. 24, 1537-1539 (June 16, 1975).

Key words: comment to editor; discrete; frequencies; nondivergent radiation.

A high-resolution spectroscopic study has been made of the radiation emitted in the forward direction from cylindrical targets bombarded with electrons. The discrete energy bands previously reported by Das Gupta were not observed for photon energies from 4 to 200 keV.

Ederer, D. L., Manalis, M., **Photoabsorption of the 4*d* electrons in xenon,** *J. Opt. Soc. Amer.* **65,** No. 6, 634-637 (June 1975).

Key words: atomic structure; inner shell; $N_{IV,V}$; resonance cross section profiles; spectroscopy; vacuum ultraviolet; xenon; 4d absorption.

In xenon, the cross section has been measured over the energy range 64-70 eV (194-177 Å) for two series of resonances that converge to the $4d^9 5s^2 5p^6(^2D_{5/2,3/2})$ limits. By a parametrization technique the cross-section amplitude and widths of these resonances have been obtained. The oscillator strength, averaged over the interval between resonances, and the widths of resonances in each series are essentially constant. The oscillator strength in these $4d^9 5s^2 5p^6(^2D_{5/2,3/2})np$ series is small (0.06) compared to the total continuum oscillator strength integrated over open *p* and *f* channels. The ratio of the cross section at the $4d^9 5s^2 5p^6(^2D_{5/2})$ limit to the cross section at the $4d^9 5s^2 5p^6(^2D_{3/2})$ limit had a value of 1.4(4), consistent with the ratio of the statistical weights of the $N_{IV,V}$ levels.

Evans, A. G., **Analysis of strength degradation after sustained loading,** *J. Amer. Ceram. Soc.* **57,** No. 9, 410-411 (Sept. 1974).

Key words: fracture probability; slow crack growth; strength degradation; sustained loading.

The strength degradation that occurs at sustained load, due to slow crack growth, is calculated in terms of the slow crack growth parameters. It is shown that the degradation is only significant in specimens with an initial strength marginally larger than the initial strength of the last specimen that failed at the sustained load.

Evans, A. G., Wiederhorn, S. M., Hockey, B. J., **Comments on "Dependence of Room Temperature Fracture Strength on Strain-Rate in Sapphire,"** *J. Mater. Sci. Lett.* **9,** 1367-1370 (1974).

Key words: ambient temperatures; dislocation mechanisms; fracture mechanics; sapphire; slow crack growth; thermal activation.

A recent paper attempts to explain the strain-rate dependence of the strength of sapphire filaments using a dislocation assisted slow crack growth model. We propose an alternative model which gives a quantitative prediction of the observed behavior. This model, based on fracture mechanics measurements of slow crack growth in the absence of dislocation activity, considers that the crack growth is a thermally activated bond rupture process.

Fano, U., Spencer, L. V., **Quasi-scaling of electron degradation spectra,** *Int. J. Radiat. Phys. Chem. Platzman Memorial Issue* **7,** 63-76 (1975).

Key words: charged particle penetration; dosimetry; electron slowing down; electron transport; scaling; *W*-value.

Douthat has found that plots of electron spectra calculated for different initial energies nearly coincide if a suitable choice of scaled variables is adopted for abscissas and ordinates. This paper provides a rationale for this choice of variables, reformulates the degradation equation in terms of the new variables, and shows how the trend of the solution of the transformed equation can be predicted semi-quantitatively by inspection.

Franklin, A. D., Crissman, J. M., Young, K. F., **Defect-complex reorientation processes in GdF_3-doped CaF_2,** *J. Phys. C* **8,** 1244-1266 (1975).

Key words: anelastic relaxation; calcium fluoride; defect pairs; dielectric relaxation; EPR lifetime broadening; fluorine interstitials; gadolinium ions; reorientation processes.

Measurements are reported of the temperature dependence of EPR lifetime broadening in the spectrum of Gd^{3+} ions in tetragonal sites in CaF_2 and of dielectric and anelastic relaxation in similar specimens. Concentrations ranged from 0.01 to 0.27 mol percent GdF_3, and the crystals were annealed in flowing He plus HF at various temperatures. The strongest relaxation modes (R_I) arising from pairs formed from Gd^{3+} ions plus trapped F^- interstitials could be identified in both the dielectric (T_{1u}) and the anelastic (E_g) spectra. The rate constants are $\ln \tau_0 = -32.83 \pm 0.24$ (τ_0 measured in seconds) and $Q = 0.44 \pm 0.005$ eV, and are to be associated with jumps of the F^- interstitials originating at the nearest-neighbour sites to the Gd^{3+} ions. A low-temperature relaxation ($Q \sim 0.2$ eV) was observed in the anelastic spectrum with trigonal symmetry and also in the dielectric spectrum. It was found to consist of several components. It is argued, contrary to earlier conclusions, that this relaxation is not an additional mode of the same centre giving rise to R_I. A higher temperature relaxation ($Q \sim 1.1$ eV) was seen only in the anelastic spectrum, and was approximately isotropic. It too cannot be identified on the basis of present information.

Freeman, D. H., Angeles, R. M., **The influence of hydrogen bonding upon gel permeation chromatography,** *J. Chromotogr. Sci.* **12,** 730-735 (Nov. 1974).

Key words: adsorption; gel permeation chromatography; hydrogen bonding; liquid chromatography.

Chloroform, methanol and benzoic acid are hydrogen bonding compounds that are simultaneously adsorbed and self-associated during liquid chromatography from carbon tetrachloride with polystyrene/divinylbenzene (Styragel). An equation is derived to treat the measured distribution coefficient dependence upon solute concentration. In dilute solution, chloroform and methanol exhibit the ef-

fect of adsorption without appreciable self-association. At higher concentrations methanol and benzoic acid show markedly less adsorption. This is the expected result as larger associated species are formed and then excluded sterically. The agreement between theory and experiment is better if one assumes that only the monomeric species is adsorbed. Experiments of this type are easily performed and they provide a helpful insight into the chromatographic mechanism.

Frenkiel, F. N., Klebanoff, P. S., **On the lognormality of the small-scale structure of turbulence,** *Boundary-Layer Meteorol.* **8,** No. 2, 173-200 (Mar. 1975).

Key words: boundary layer; grid; intermittency, moments; statistical properties; turbulence; velocity-gradients.

Higher-order moments of turbulent velocity gradients and their behavior with Reynolds number were measured in the nearly isotropic turbulent field generated by a square-mesh grid and in a turbulent boundary layer along a flat plate with zero pressure gradient. Hot-wire anemometry and instrumentation combining analog and digital methods were used to measure moments up to the fourteenth order. Measurements of such high-order moments required that particular attention be given to their validity. Involved herein was the evaluation of such effects as nonlinearity, averaging intervals, and the adequacy of the statistics for the tails of the probability density distributions. The results obtained are compared with those of other investigators for a variety of flow configurations in the laboratory as well as in the atmosphere. The concept of the intermittency of the small-scale structure and the theoretical approach involving lognormality of the probability density distribution of the dissipation rate are evaluated.

Fuggle, J. C., Madey, T. E., Steinkilberg, M., Menzel, D., **X-ray photoelectron satellites from adsorbed species,** *Chem. Phys. Lett.* **33,** No. 2, 233-236 (June 1, 1975).

Key words: oxygen; ruthenium; satellite; shake-up; structure; x-ray photoelectron spectroscopy.

The O 1s XPS peaks from monolayers of CO and oxygen adsorbed on the basal (001) face of a ruthenium single crystal are observed to have satellites whose position and intensity are sensitive to the chemical environment.

Gadzuk, J. W., Sunjić, M., **Excitation energy dependence of core-level x-ray photoemission-spectra line shapes in metals,** *Phys. Rev. B* **12,** No. 2, 524-530 (July 15, 1975).

Key words: asymmetric lineshapes; photoelectron spectroscopy; photoemission; x-ray edge singularities.

Creation of a deep localized hole in the process of x-ray photoemission from metals is followed by a drastic rearrangement of the surrounding electrons in the Fermi sea. This rearrangement in which low-energy electron-hole pairs are produced, in analogy with gas-phase atomic shake-up processes, gives rise to a low-energy tail in the hole spectral density with an integrable (Mahan) singularity at the energy corresponding to zero-energy pair production. When the usual (symmetric) broadening of the hole is included, the resulting hole line shape becomes a skew resonance, with the asymmetry indices growing with the strength of the electron-hole interaction. The case in which the hole potential is switched on instantaneously (the sudden or impulse limit) has been treated by Doniach and Sunjić. However, the potential switching-on time is a function of the speed at which the excited electron lea photoionization threshold value.

Garfinkel, S. B., Schima, F. J., **Ionization chamber half-life measurement of the 99-minute ^{113}In isomer,** *Int. J. Appl. Radiat. Isotop.* **26,** 314-315 (May 1975).

Key words: half-life measurement; isomeric decay; isotope $^{113}In^{m}$; radioactivity; rate of charge measurement; $4\pi\gamma$ pressure ionization chamber.

A precise determination of the $^{113}In^{m}$ half-life has been made by means of a nominal $4\pi\gamma$ pressure ionization chamber. The value obtained was 99.21 min with an uncertainty of 0.13 min which is the linear sum of the component of random error at the 99 percent confidence level and the estimated systematic errors.

Geist, J., Steiner, B., Schaefer, R., Zalewski, E., Corrons, A., **Electrically based spectral power measurements through use of a tunable cw laser,** *Appl Phys. Lett.* **26,** No. 6, 309-311 (Mar. 15, 1975).

Key words: cw dye laser; detector spectral response; electrically calibrated pyroelectric detector; radiometry; spectral irradiance; spectral radiant power density.

A new approach to radiant power measurements is described. A continuously tunable cw dye laser was used to measure the absolute spectral response of a silicon photodiode and narrow band-pass filter by comparison with an electrically calibrated pyroelectric detector. The filtered photodetector was then used to measure the spectral power density from a standard lamp that had been calibrated by the classical technique. The agreement of better than 1 percent between the two measurements is well within the uncertainties identified with each measurement individually, of the order of 1 percent. A number of advantages in the new technique are identified.

Goldberg, R. N., **Thermodynamics of hexokinase-catalyzed reactions,** *Biophys. Chem.* **3,** 192-205 (1975).

Key words: adenosine-5′-triphosphate; biochemistry; enzyme catalyzed reactions; glucose; heat measurements; *hexokinase*; metabolic processes; microcalorimetry; thermochemistry; thermodynamics.

The enthalpies of the *hexokinase*-catalyzed phosphorylation of glucose, mannose, and fructose by ATP to the respective hexose 6-phosphates have been measured calorimetrically in TRIS/TRIS · HCl buffer at 25.0, 28.5, and 32.0 °C. The effects on the measured enthalpy of the glucose/*hexokinase* reaction due to variation of pH (over the range 6.7 to 9.0) and ionic strength (over the range 0.02 to 0.25) have been examined. Correction for enthalpy of buffer protonation leads to ΔH° and ΔC_p° values for the processes: eq-D-hexose + ATP^{4-} = eq-D-hexose 6-phosphate^{2-} + ADP^{3-} + H^+. Results are $\Delta H^\circ = -23.8 \pm 0.7$ kJ · mol^{-1} and $\Delta C_p^\circ = -156 \pm 280$ J · mol^{-1} · K^{-1} for glucose, $\Delta H^\circ = -21.9 \pm 0.7$ kJ · mol^{-1} and $\Delta C_p^\circ = 10 \pm 140$ J · mol^{-1} · K^{-1} for mannose, and $\Delta H^\circ = -15.0 \pm 0.9$ kJ · mol^{-1} and $\Delta C_p^\circ = -41 \pm 160$ J · mol^{-1} · K^{-1} for fructose. Combination of these measured enthalpies with Gibbs energy data for hydrolysis of ATP^{4-} and that for the hexose 6-phosphates lead to ΔS° values for the above *hexokinase*-catalyzed reactions.

Gump, B. H., Hertz, H. S., May, W. E., Chesler, S. N., Dyszel, S. M., Enagonio, D. P., **Drop sampler for obtaining fresh and sea water samples for organic compound analysis,** *Anal. Chem.* **47,** No. 7, 1223-1224 (June 1975).

Key words: baseline studies; fresh water sampling; sampling device; sea water sampling; trace organic analysis; water pollution.

Analytical chemists have become more involved in projects concerning water pollution, environmental impact statements and hydrocarbon baseline studies. A device for obtaining replicate and representative samples of the aquatic environment under consideration is needed. A water sampler has been designed to meet this need.

Haas, S. S., Brauer, G. M., Dickson, G., **A characterization of polymethylmethacrylate bone cement,** *J. Bone J. Surg.* **57-A,** No. 3, 380-391 (Apr. 1975).

Key words: acrylic resin; cement; medical materials; orthopedic

materials; polymethylmethacrylate, self-curing; surgical bone cement; total hip replacement, cement.

Polymethylmethacrylate cement is characterized in terms of chemical composition, handling characteristics, and physical properties: the dough time, setting time, handling time, and temperature rise were found to be most affected by environmental temperature and kneading of the dough mass. As the set material ages, the residual monomer content gradually decreases and the strength increases. A volume shrinkage of up to 5 percent was observed. The porosity, which is increased by rapid mixing, may reach 10 percent. The mechanical properties of the cement approximate those of polymethylmethacrylate denture base materials. Some variability encountered in the handling qualities of the cement could be attributed only to the variability of different batches.

Haber, S., **Adaptive integration and improper integrals,** *Math. Comput.* **29,** No. 131, 806-809 (July 1975).

Key words: improper integrals; integrals; numerical analysis; numerical integration; numerical quadrature; quadrature; Riemann integral; singularities.

Let R be the class of all functions that are properly Riemann-integrable on $[0, 1]$, and let IR be the class of all functions that are properly Riemann-integrable on $[a, 1]$ for all $a > 0$ and for which

$$\lim_{a \to 0} \int_a^1 f(x)dx$$

exists and is finite. There are computational schemes that produce a convergent sequence of approximations to the integral of any function in R; the trapezoid rule is one. In this paper, it is shown that there is no computational scheme that uses only evaluations of the integrand, that is similarly effective for IR.

Hanley, H. J. M., Haynes, W. M., **The density expansion of the viscosity coefficient,** *J. Chem. Phys.* **63,** No. 1, 358-361 (July 1, 1975).

Key words: argon; correlated molecular collisions; density expansions; fluorine; oxygen; statistical analysis; viscosity coefficient.

Experimental viscosity data for gaseous argon, oxygen, and fluorine were analyzed as a function of density and temperature. Necessary conditions were applied to investigate if a given isotherm was consistent statistically with a given density function. It was found that the low temperature isotherms were consistent with the theoretically suggested density function, which involves terms logarithmic in the density. At higher temperatures, however, these logarithmic terms did not appear to be statistically significant.

Hanley, H. J. M., McCarty, R. D., Haynes, W. M., **Equations for the viscosity and thermal conductivity coefficients of methane,** *Cryogenics* **15,** No. 7, 413-417 (July 1975).

Key words: correlation; critical point; equation of state; methane; thermal conductivity; thermal conductivity coefficient; viscosity coefficient.

An equation is proposed to calculate the viscosity and thermal conductivity coefficients of methane from the dilute gas to the dense liquid. The range of validity of the equation is approximately 95-400 K for pressures up to 50 MPa (~ 500 atm). The reliabilities of the coefficients calculated are estimated at approximately 2 percent and 5 percent for the viscosity and thermal conductivity coefficients, respectively. The equation includes a contribution for the thermal conductivity enhancement in the critical region.

Hanley, H. J. M., Watts, R. O., **Molecular dynamics studies of an *m*-6-8 fluid,** *Physica* **79A,** No. 4, 351-376 (Feb. 1975).

Key words: Axilrod-Teller correction; dense liquid; excess function; hydrodynamic limit; molecular dynamics; rare gases; velocity autocorrelation function; 11-6-8 potential.

The pressure, energy and self-diffusion coefficient have been calculated for an 11-6-8 fluid using the method of molecular dynamics. A comparison with data for argon, krypton and xenon is presented. It is shown that agreement between theory and experiment for the thermodynamic properties is generally within the estimated precision of the calculated and experimental values, provided three-body and quantum corrections are included in the calculation, except when the density approaches the triple-point density. Agreement between theoretical and experimental self-diffusion coefficients is satisfactory at all densities after allowance is made for the long-time behaviour of the velocity autocorrelation function. We demonstrate that three-body forces are important in the liquid and that our estimates of such forces are very close to those suggested by Barker, Fisher and Watts.

Hanley, H. J. M., Watts, R. O., **The self-diffusion coefficient of liquid methane,** *Mol. Phys.* **29,** No. 6, 1907-1917 (June 1975).

Key words: correlation function; experimental data; hydrodynamic behavior; methane; molecular dynamics; potential function; self-diffusion coefficient; 11-6-8 potential function.

Self-diffusion coefficients of methane have been calculated over a wide density range using the method of molecular dynamics. Methane intermolecular interactions were modelled using an *m*-6-8 potential with coefficients determined from viscosity data for the dilute gas. After adding a contribution to the diffusion coefficient due to the long-time behaviour of the velocity autocorrelation function, agreement with experimental data is within the estimated errors given for both the calculated values and the experimental data.

Harrison, G. A., **The high-rise fire problem,** *CRC Critical Rev. Environ. Control* **4,** No. 4, 483-505 (Oct. 1974).

Key words: flame spread and smoke development; high-rise; human behavior; life safety; plastics.

This study focuses on life safety aspects of high-rise buildings located within the United States. A high-rise building is defined as one which exceeds 24.4 meters (80 feet) and is of a Light or Ordinary hazard occupancy classification as specified by the National Fire Codes, "Standard for Installation of Sprinkler Systems," Volume 6, No. 13, 1974. The purpose of this study is to identify and analyze the high-rise fire problems to formulate research recommendations to the Programmatic Center for Fire Research at the National Bureau of Standards.

A comprehensive review of the pertinent literature indicates that only a limited number of high-rise fire problems exist. These include increasing fuel loads and fire spread potential, smoke development and movement, life safety and occupant evacuation, and fire department operations. These specific problem areas relate to building evacuation and the vertical movement of smoke and toxic gases through a building.

A major finding of this study is that fire fatalities occurring within high-rise buildings have been few in number, historically. However, with changing construction techniques and materials, this fire experience record is subject to change. The future high-rise fire problem must be managed through the use of progressive engineering design which will keep pace with innovative high-rise building technology and interior design concepts.

Hebner, R. E., Jr., Booker, S. R., **A portable Kerr system for the measurement of high voltage pulses,** *Proc.* 1975 *IEEE Southeastcon, Charlotte, N.C., Apr.* 6-9, 1975, **1,** 3A-1-1/3A-5-1 (Institute of Electrical and Electronics Engineers, Inc., New York, N.Y., 1975).

Key words: calibration; electrical measurement; electro-optics; high voltage measurement; impulse measurement; Kerr effect; laser systems.

A portable system for the measurement of high voltage pulses based on the electro-optic Kerr effect has been constructed and

tested. This system is designed to measure microsecond risetime pulses having a duration of less than one hundred microseconds and peak values from one thousand volts to more than one hundred thousand volts.

Heinrich, K. F. J., Newbury, D. E., Yakowitz, H., **New techniques for the surface analysis of nonmetallic solids,** (Proc. 20th Sagamore Army Materials Research Conf., Sagamore Conference Center, Raquette Lake, New York, Sept. 11-14, 1973), Chapter 4 in *Characterization of Materials in Research Ceramics and Polymers* **20,** 73-102 (Syracuse University Press, Syracuse, N.Y., 1975).

Key words: contrast; electron probe microanalysis; electron spectroscopy for chemical analysis (ESCA); ion microprobe analysis; scanning electron microscopy; surface analysis.

Several modern techniques for the characterization and analysis of surfaces and shallow layers of nonmetallic materials are discussed, with particular emphasis on their relevance to technological problems. These include electron and ion probe microanalysis, scanning electron microscopy, ion scattering analysis, and secondary ion mass spectroscopy of surfaces.

Herbst, J. F., Watson, R. E., **5*f*-electron excitation energies and the Coulomb term, *U*, in the light actinide metals,** *Phys. Rev. Lett.* **34,** No. 22, 1395-1398 (June 2, 1975).

Key words: actinides; Coulomb term; energy; excitation energy; metal; 5*f* electron.

Relativistic Hartree-Fock-Wigner-Seitz band calculations have been performed for the actinide metals Ac through Am in order to estimate 5*f* excitation energies. Our calculations predict that the tetravalent state (i.e., four *s-d* conduction electrons) is favored for the lighter elements with a crossover to a trivalent ground state occurring near uranium. We find the Coulomb energy, *U*, for 5*f* electron hopping to increase from 2-3 eV at Th to 4-5 eV at Am.

Hosler, W. R., Frederikse, H. P. R., **Doped ceria for MHD-materials,** (Proc. Sixth Int. Conf. on Magnetohydrodynamic Electrical Power Generation, Washington, D.C., June 9-13, 1975), Paper in *MHD Sixth International Conference on Magnetohydrodynamic Electrical Power Generation* **II,** Conf-750601-P2, 67-76 (The Energy Research and Development Administration-Fossil Energy, Washington, D.C., 1975).

Key words: conductivity; doped ceria; high temperature; MHD electrodes; mixed ceria.

A number of ceria compositions and ceria-based mixtures show promise as electrode material in MHD generators. This paper discusses the electrical conductivity and some of the chemical stability aspects of cerium oxide, cerium-zirconium oxide, Ta doped CeO_2 and Ta doped CeO_2-ZrO_2.

Hougen, J. T., Radford, H. E., Evenson, K. M., Howard, C. J., **Analysis of the laser magnetic resonance spectrum of HO_2,** *J. Mol. Spectrosc.* **56,** 210-228 (1975).

Key words: asymmetric rotor levels; HO_2; laser magnetic resonance; rotational constants; spectral assignments; spin splitting; Zeeman spectrum.

An analysis of the previously detected laser magnetic resonance spectrum of HO_2 is carried out by (i) assigning M_J quantum numbers to each observed Zeeman line, (ii) determining the quantum numbers ($N'_{Ka'Kc'} - N''_{Ka''Kc''}$) and energies of the zero-field asymmetric rotor transitions involved, and (iii) determining the values of the zero-field spin-rotation doublet splittings in the upper and lower states of each asymmetric rotor transition. The rotational transitions obtained lie in the region 50-150 cm^{-1}, with quantum numbers $4 \leq N \leq 19$ and $1 \leq K_a \leq 4$. They are fit to an asymmetric rotor program to obtain the three rotational constants A, B, C and the three symmetric-top centrifugal distortion constants D_K, D_{NK}, D_N. The spin splittings are fit to an approximate theoretical expression involving two adjustable linear combinations of components of the spin-rotation interaction tensor ϵ. Because of the lack of spectra from other isotopic species, a unique molecular geometry cannot be derived.

Howell, B. F., Velapoldi, R. A., Travis, J. C., **Fluorescence of commercial porous high silica glasses,** *Amer. Ceram. Soc. Bull.* **54,** No. 5, 503-505, 509 (May 1975).

Key words: fluorescence; Mössbauer spectroscopy; porous glass.

Fluorescence and Mössbauer spectroscopy in conjunction with elemental analysis have been used to verify that the fluorescence which develops in commercial porous glass, sintered under reducing conditions, is due to Sn(II). The fluorescence shown by in-house-formulated, porous, high silica glass impregnated with $Sn(II)Cl_2$ and sintered under various conditions is used to substantiate this conclusion. Corrected fluorescence spectra for the Sn(II) species and isomer shifts and quadrupole splitting for various tin species in glasses are also given.

Hudson, R. P., **Conference report: European conference on temperature measurement,** *Cryogenics* **15,** 486 (Aug. 1975).

Key words: conference; temperature; thermometry.

A short report on the European Conference on Temperature Measurement (held in Teddington, London, April 9-11, 1975 at the National Physical Laboratory).

Hudson, R. P., Marshak, H., Soulen, R. J., Jr., Utton, D. B., **Review Paper: Recent advances in thermometry below 300 mK,** *J. Low Temp. Phys.* **20,** Nos. 1/2, 1-102 (July 1975).

Key words: cryothermometry; low temperature; thermometry.

The subject of temperature measurement below 0.3 K is reviewed, with particular attention paid to developments reported in the period 1970-1974. Sensors, measurement techniques, primary and secondary thermometers, and fixed points are discussed and attempts are made to assess the accuracy and relative merits of the various devices and methods.

Huebner, R. H., Celotta, R. J., Mielczarek, S. R., Kuyatt, C. E., **Apparent oscillator strengths for molecular oxygen derived from electron energy-loss measurements,** *J. Chem. Phys.* **63,** No. 1, 241-248 (July 1, 1975).

Key words: electron energy-loss; oscillator strengths; oxygen.

Oscillator strengths for O_2 from 6 to 14 eV are derived from the energy-loss spectrum of 100 eV incident electrons. Integrated f values for the Schumann-Runge bands and continuum, which span four orders of magnitude in intensity, agree well with high-resolution photoabsorption measurements. Vibrational structure superimposed on the Schumann-Runge continuum, previously assigned to the $(3s\sigma_g)^3\Pi_g$ Rydberg state, contributes less than 0.5 percent to the total oscillator strength determined for that region. These data also yield f values for discrete bands in the region between 9.5 and 14.0 eV, where line saturation problems complicate oscillator strength analysis of the optical data. An oscillator strength sum of 0.198 is obtained for all transitions below the ionization potential at 12.07 eV.

Hunt, C. M., Burch, D. M., **Air infiltration measurements in a four-bedroom townhouse using sulfur hexafluoride as a tracer gas,** *ASHRAE Trans.* **81,** Part 1, 186-201 (1975).

Key words: air exchange measurement; air infiltration measurement; building ventilation; sulfur hexafluoride tracer.

Air infiltration measurements were made in a four-bedroom townhouse by the tracer dilution method using sulfur hexafluoride (SF_6) as the tracer gas. The house was contained in an environmental chamber with control over both the inside and outside temperature,

with essentially no wind velocity. The well-known correlation between inside/outside temperature difference and infiltration rate was observed, and under conditions of negligible wind velocity the effect of sealing doors and ducts was investigated. Simultaneous use of SF_6 and He as tracer gases gave no evidence that molecular diffusion played a significant role in the measurement.

Different methods of collecting air samples for analysis were compared. SF_6 measurements were also compared with air exchange rates imposed on the house by means of a fan. Finally, the effects of poor mixing were analyzed by comparing the expected results in the case of perfect mixing with those expected in the case of air exchange without mixing and with imperfect mixing.

Hurst, W. S., **Note on the measurement of the response of oceanographic temperature sensors,** *J. Geophys. Res.* **80,** No. 18, 2663-2666 (June 20, 1975).

Key words: oceanographic temperature measurements; temperature measurement; temperature sensors; thermometry; time constant; time response.

The response times of three different types of oceanographic platinum resistance temperature sensors were measured employing the conventional rotating water container procedure. At low sensor immersion velocities (< 100 cm/s) the response was strongly dependent upon the details of the sensor insertion velocity for one sensor design. With carefully defined measurement procedures, reproducible values for the 'time constant' were obtained, but their application in data analysis must be treated with caution.

Jacox, M. E., Milligan, D. E., **The infrared spectrum of methylenimine,** *J. Mol. Spectrosc.* **56,** 333-356 (1975).

Key words: C=N bond; infrared spectrum; isotopic substitution; matrix isolation; methyl azide; methylenimine; normal coordinate analysis; photolysis; thermodynamic properties.

Eleven isotopic species of methylenimine have been prepared by the mercury-arc photolysis of methyl azide isolated in argon, nitrogen, and carbon dioxide matrices at 4 and at 14 K. Sufficient concentrations of methylenimine were obtained for identification of all of the vibrational fundamentals except the NH stretching mode. Using a recent ab initio structural calculation for this molecule, it has been possible to derive a set of valence-force potential constants which provide a satisfactory fit to all of the infrared spectroscopic data. The magnitude of the carbon-nitrogen stretching force constant is appropriate for a double bond. The temperature dependence of the thermodynamic properties of methylenimine has also been calculated.

Johnson, C. R., **Powers of matrices with positive definite real part,** *Proc. Am. Math. Soc.* **50,** 85-91 (July 1975).

Key words: field of values; Hermitian matrix; normal matrix; positive definite.

For n by n complex matrices A the following two facts are proven by elementary techniques: 1. If A^m is never normal, $m \in I^+$, then the equation $xA^m x^* = 0$ has a solution $0 \neq x \in C^n$, $m \in I^+$; 2. If $H(A) = (A + A^*)/2$ is positive definite, then $H(A^m)$ is positive definite for all $m \in I^+$ if and only if A is Hermitian.

Julienne, P. S., Krauss, M., **Predissociation of the Schumann-Runge bands of O_2,** *J. Mol. Spectrosc.* **56,** 270-308 (1975).

Key words: ab initio calculation; level shifts; line broadening; molecular oxygen; predissociation; spin-orbit matrix elements.

The predissociation line broadening in the Schumann-Runge bands of O_2 is interpreted through an ab initio calculation of the pertinent repulsive potential energy curves and spin-orbit matrix elements. The ab initio results provide an overall qualitative picture of the predissociation which is further refined through a detailed comparison of calculated level shifts and widths with experimental data. The position of the dominant repulsive curve is also deduced by a deperturbation of the level shift in the second vibrational difference. The predissociation is dominated by the $^5\Pi_u$ state crossing the $B\ ^3\Sigma_u^-$ state around 1.875 Å with a spin-orbit matrix element of 65 cm^{-1}. The $^1\Pi_u$ and $^3\Pi_u$ states have small spin-orbit matrix elements and play only minor roles in the predissociation. The calculated and experimental widths are in good agreement for low and high vibrational levels. The apparent experimental widths between $v = 5$ and 11 are shown to be inconsistent with the theoretical analysis, the difference probably being due to line blending.

Kan, P. T., Peterson, G. A., Webb, D. V., Szalata, Z. M., Fivozinsky, S. P., Lightbody, J. W., Jr., Penner, S., **Observation of electric monopole strength in the electrodisintegration of ^{3}He,** *Phys. Rev. Lett.* **34,** No. 14, 899-901 (Apr. 7, 1975).

Key words: electrodisintegration; electron scattering; inelastic electron scattering; monopole excitation; monopole strength; ^{3}He.

A broad electric monopole excitation peaking at 6.4 MeV has been observed in the breakup of ^{3}He induced by inelastic electron scattering. The monopole cross section was obtained from the observed cross section by subtracting the electric-dipole contributions converted from photodisintegration cross sections by using the virtual photon theory, and also subtracting the magnetic multipole contributions obtained from a 180° electron-scattering experiment. The extracted monopole matrix element is 2.4 ± 0.5 fm^2.

Kasen, M. B., **Mechanical and thermal properties of filamentary-reinforced structural composites at cryogenic temperatures. 1: Glass-reinforced composites,** *Cryogenics* **15,** No. 6, 327-349 (June 1975).

Key words: cryogenics; dynamic mechanical properties; glass-fiber composites; literature review; static mechanical properties; thermal properties.

Objective is to provide an understanding of the general magnitude of property values obtainable within the cryogenic temperature range, to provide a feel for the relative literature ranking of specific composite types with regard to a specific property, and to impart an understanding of the temperature sensitivity of the property of interest. A bibliography and bibliography-property cross-reference is included. This is Part I of a two-part series. Part II will consider advance composites.

Kelly, G. E., Sengers, J. V., **Droplet growth in a dilute vapor,** *J. Chem. Phys.* **61,** No. 7, 2800-2807 (Oct. 1, 1974).

Key words: aerosols; condensation; droplets; evaporation; kinetic theory; Knudsen number expansion; nucleation.

When the mass flux Γ to a liquid droplet is expanded in terms of a parameter α which is the ratio of the droplet size to the mean free path (inverse Knudsen number), one obtains a series of the form $\Gamma = \Gamma^{(0)} + \Gamma^{(1)}\alpha + \Gamma^{(2)}\alpha^2 \ln\alpha + \ldots$. As shown in a previous paper, the coefficients in this series are determined by integrals associated with sequences of successive collisions among a number of vapor molecules and the droplet. For a droplet surrounded by its pure vapor, we have calculated the coefficient $\Gamma^{(1)}$ of the first inverse Knudsen number correction to the free molecular growth rate $\Gamma^{(0)}$ assuming that the vapor molecules can be treated as hard spheres. For most nonequilibrium conditions, the ratio $\Gamma^{(1)}/\Gamma^{(0)}$ turns out to be positive, rather than negative, as heretofore was assumed in the literature. This result implies that the reduced growth rate $\Gamma/\Gamma^{(0)}$ will pass through a maximum as a function of the Knudsen number.

Kline, F. J., Lin, C. L., Peterson, G. A., Penner, S., **Inelastic electron scattering from ^{31}P,** *Nuclear Phys. A* **241,** 299-310 (1975).

Key words: electroexcitation; electron scattering; form factors; intermediate coupling; reduced transition probability; ^{31}P.

Form factors for the electroexcitation of the $3/2^+$ (1.27 MeV), $5/2^+$ (2.23 MeV), and $3/2^+$ (3.51 MeV) states in ^{31}P have been measured for momentum transfers from 0.36 to 0.80 fm^{-1} at the NBS electron scattering facility. In addition, form factors for the 2.23 MeV state in the momentum transfer range 0.74 to 1.78 fm^{-1} have been extracted from data obtained in a previous experiment. Using the DUELS distorted-wave code the $B(E2, \omega) \downarrow$ were found to be 6.0 ± 0.9, 6.9 ± 0.3, and 2.7 ± 0.3 W.u. for the 1.27, 2.23, and 3.51 MeV states, respectively. The form factors for these states, calculated using wave functions derived in an intermediate-coupling vibrational calculation, are compared with the data.

Klose, J. Z., **Mean life of the 27 887-cm^{-1} level in U I,** *Phys. Rev. A* **11,** No. 6, 1840-1844 (June 1975).

Key words: delayed coincidence; f value; imprisonment; lifetime; mean life; resonance radiation; transition probability; U I; uranium.

Measurements of the mean life of the 27 887-cm^{-1} level in U I have been made at a single vapor density using electronic excitation and a method of delayed coincidence. The lifetime values were obtained by optically detecting the decay of the 3584.9-Å resonance transition. Using branching ratios obtained from known relative f values, the average of the measured lifetimes was corrected for imprisonment of the resonance radiation, and absolute f values were derived from the corrected lifetime giving the following results: $\tau_0 = 7.3 \pm 1.1$ nsec, $f_{3585} = 0.18 \pm 0.03$, and $f_{4620} = 0.20 \pm 0.03$. The error given with each quantity is the standard deviation as determined from the dispersion of the individual measurements. A systematic error of 1 percent due to possible nonlinearities in the time scale of the system is also assigned to the results. Unaccounted for systematic errors affect only the correction in the measured lifetime, which is small compared to the statistical error. The lifetime and f values are presented in comparison with the experimental results of another group of workers.

Klose, J. Z., **Mean life of the $5p\ ^2P_{3/2}$ resonance level in Ag I,** *Astrophys. J.* **198,** 229–233 (May 15, 1975).

Key words: Ag I; f-value; imprisonment; lifetime; mean life; resonance radiation; silver; transition probability.

The mean life of the $5p\ ^2P_{3/2}$ resonance level in Ag I has been measured at two different vapor densities using electronic excitation and a method of delayed coincidence. The lifetime values, obtained by optically detecting the decay of the $5p\ ^2P_{3/2} \rightarrow 5s\ ^2S_{1/2}$ (3280.68 Å) resonance transition, increase with increasing vapor density. This vapor density dependence was interpreted as being due to the imprisonment of the 3281 Å resonance radiation. The Holstein theory of the imprisonment of resonance radiation was applied to the lifetime-versus-vapor density data to yield the following results: $\tau_0 = 6.5 \pm 0.6$ ns, $A_{3281} = 1.53 \pm 0.14 \times 10^8\ s^{-1}$, and $f_{3281} = 0.50 \pm 0.05$. The error limits were derived primarily from estimated uncertainties in the measured mean lives and possible variations in the vapor densities during the runs. Experimental results of other workers are presented for comparison with the results of the present work.

Kraft, R., **Finite difference techniques for diffusion and redistribution problems with segregation-type boundary conditions,** (Proc. AICA Int. Symp. on Computer Methods for Partial Differential Equations, Bethlehem, Pa., June 17-19, 1975), Paper in *Advances in Computer Methods for Partial Differential Equations*, R. Vichnevetsky, Ed., pp. 328-333 (AICA Dept. of Computer Science, New Brunswick, N.J., 1975).

Key words: diffusion equations; finite-difference techniques; impurity redistribution; moving boundary problems; numerical methods; partial differential equations; semiconductor technology.

Finite difference techniques and a particular computer algorithm are given for a one dimensional diffusion problem in a composite domain with time dependent domain and moving interfacial boundary. The physical problem involves the redistribution of an impurity (boron) caused by the oxidation of a semiconducting crystal (silicon). The boundary conditions at the interfacial boundary express conservation of mass and the propensity of the impurity to be dissolved in one rather than the other of the two adjacent materials (the segregation condition). The novel feature of the algorithm is its employment of the integral form of the conservation of mass boundary condition instead of the conventionally used differential form.

Kucirek, J., Melmed, A. J., **Influence of an initial (contamination) film on the determination of film properties by ellipsometry,** *J. Opt. Soc. Amer.* **65,** No. 5, 611-612 (May 1975).

Key words: ellipsometry; optics; thin films.

Computer calculations were done to evaluate the error in an ellipsometric determination of film thickness and refractive index, due to the unknown presence of a contamination film. The methods employed are described, and typical results are given.

Lambropoulos, M., Moody, S. E., Smith, S. J., Lineberger, W. C., **Observation of electric quadrupole transitions in multiphoton ionization,** *Phys. Rev. Lett.* **35,** No. 3, 159-162 (July 21, 1975).

Key words: atom; dye laser; electric quadrupole; fine structure; ionization; multiphoton; sodium.

Two flashlamp-pumped, tunable, dye lasers have been utilized to study three-photon ionization in atomic sodium. The resulting ion yield shows large peaks at laser frequencies which correspond to electric quadrupole transitions. This is the first direct observation of electric quadrupole effects in multiphoton ionization. The $3p\ ^2P_{3/2} \rightarrow 4f$ matrix element is determined, and the fine-structure splitting of the $5p$ state is measured.

Laughlin, D. E., Cahn, J. W., **Spinodal decomposition in age hardening copper-titanium alloys,** *Acta Met.* **23,** 329-339 (Mar. 1975).

Key words: age hardening; copper-titanium; Dla; metastable solvus; microstructural sequence method; nucleation; ordering; precipitation; spinodal decomposition.

The early stages of spinodal decomposition in age hardening Cu-Ti alloys have been studied by electron microscopy. The alloys (1.55, 3.08 and 5.17 w/o Ti) decomposed on the quench from solutionizing temperatures into Ti enriched and Ti lean regions. Superlattice reflections, at $1/5\{420\}_m$ positions as well as $1/2\{210\}_m$ reflections were observed in the diffraction patterns of the as quenched 5.17 w/o Ti alloy. The alloys continued to decompose when aged at elevated temperatures. A sequence of microstructures was used to show that continuous phase separation, and hence spinodal decomposition, was the mechanism of decomposition. The metastable two phase structure which formed from the spinodal process was aligned and periodic from the start of the process. The Ti enriched phase was ordered, with the $D1a(Ni_4Mo;14/m)$ structure. Reversion experiments were performed to determine the position of the coherent metastable solvus. When aging treatments were performed near this solvus, heterogeneous nucleation of the metastable phase was observed.

Laughlin, D. E., **On the imaging of composition modulations,** *J. Appl. Crystallogr.* **7,** Part 6, 635 (Dec. 1974).

Key words: composition modulations; contrast mechanism; electron diffraction; electron microscopy; lattice images; modulation images; satellites; spinodal decomposition.

A new interference contrast mechanism in transmission electron microscopy is presented and compared with the well known lattice

594-051 O - 76 - 9

imaging technique. This mechanism is termed "modulation imaging" as it may be used to study the periodic composition modulations which occur in crystalline alloys which undergo spinodal decomposition.

Lofquist, K. E., **An effect of permeability on sand transport by waves (Abstract only),** *EOS, Trans. Amer. Geophys. Union* **56,** No. 6, 370 (June 1975).

Key words: oscillatory flows; permeability; ripple; sand transport.

Permeability effects on the movement of sand in oscillatory flows are observed in laboratory experiments which approximate prototype conditions at the seabed under progressive waves. A natural sand is used, wave periods range between 3 and 14 seconds, and sand surfaces are naturally rippled. The apparatus has a symmetry which removes all effects, except those of permeability, which might cause a net movement of the sand. Onshore and offshore directions are determined by phase relationships between the horizontal flows and superposed vertical permeability flows. A positive permeability effect is found, in that the ripple profiles move in the onshore direction. The velocity of this motion is measured and described in a simple dimensionless plot. The associated net transport of sand is not observed directly but can be inferred, to an extent, form the motions of the ripple profiles. The effects of permeability sand transport are cumulative, and can be significant in coastal processes of long duration.

Ludtke, P. R., **Register of specialized sources for information on selected fuels and oxidizers,** *NASA CR*-134807, 44 pages (Available from the National Technical Information Service, Springfield, Va. 22151, 1975).

Key words: chemical reactions; combustion; cryogenic fluid safety; explosions; fires; fuels; handling; hydrogen; oxidizers; oxygen; propellants; safety information; thermodynamic properties.

This Register describes thirty-eight (38) organizations that catalog and file information in their data systems on fuel and oxidizers. The fuels include hydrogen, methane (LNG) and hydrazine-type fuels (UDMH); the oxidizers include oxygen, fluorine, flox, nitrogen tetroxide and ozone. The type of available information covers thermophysical properties, propellant systems, propellant fires-control-extinguishment, propellant explosions, propellant combustion, propellant safety, and fluorine chemistry. These organizations have assembled and collated their information so that it will be useful in the solution of engineering problems.

Malitson, I. H., Lechner, J. A., **Refractive index variance in auto headlamp glass,** *Crime Lab. Dig.* **75,** No. 5, 8-11 (July 1975).

Key words: auto headlamp glass; population; refractive index; RI variance; statistics; temperature coefficient.

The work described in this paper was designed to evaluate the refractive index (RI) variance within and between auto headlamp glass currently manufactured in the U.S.A. The purpose is to provide the criminalist with a reliable statistical data base for decision making when confronted with this type of evidence. A precision refractometer was used to measure point-to-point RI variations within the lens components of new and used lamps. At least 13 pieces of glass from each of 46 lenses were evaluated. The spread of RI for all glasses was found to be 1.475 – 1.478. From these data it was ascertained that the headlamp glass population consists of three groups: newer and older glass made by Company A and all glass made by Company B. The newer glass significantly differs by 3×10^{-3} in RI from the other two groups whose distribution of RI values overlap. This difference is many times larger than the standard deviation within each group and within a single lens. The change in RI with temperature was determined.

Manning, J. R., Stark, J. P., **General matrix equations for diffusion drift velocity in a driving force,** *Phys. Rev. B* **12,** No. 2, 549-556 (July 15, 1975).

Key words: defects in crystals; diffusion; drift velocity; driving force; matrix equations; non-cubic crystals.

From a complete-path approach in which defects are followed from the time of their creation at defect sources to the time of their destruction at defect sinks, general matrix equations are developed which relate the atom drift velocity v_k for diffusion in a driving force to simple matrices whose elements can be written by inspection. Previous equations for v_k have been restricted either to crystals and defects having high symmetry or to cases where the x components of any atom jumps were either $\pm b$ or 0. By contrast, the present equations involve no such restrictions. They apply to diffusion by interstitialcy, divacancy, and other more complex mechanisms, independent of the presence of symmetry planes, and allow calculation of diffusion drift velocities even when the individual atom jumps provide a variety of jump distances along the diffusion direction. These equations apply, for example, even when jumps to both nearest- and next-nearest-neighbor sites are allowed and to diffusion in arbitrary crystallographic directions even in noncubic crystals. The present equations can be expressed in terms of a general matrix S. The relation of S to the less general matrices S_+ and S_- defined previously for crystals having mirror symmetry planes normal to the diffusion direction is discussed.

Margulis, S. T., **A comparison of the opinions of Operation Breakthrough occupants and conventional housing occupants about their housing,** *Industrialization Forum* **6,** No. 1, 21-26 (1975).

Key words: architectural psychology; dwelling unit; federal building research; industrialized housing; occupant behavior; Operation Breakthrough; performance evaluation.

Occupants of Operation Breakthrough and of conventional housing were interviewed about their homes and on related topics. The opinions of these two groups of occupants were compared in order to determine comparability of the housing based on the opinions of their occupants. The matching of OBT and conventional housing, their occupants and their sites was relatively successful. The comparison of occupant opinions lead to the conclusion that OBT housing was favorably evaluated and that its evaluation was at least as good as if not superior to that of the conventional housing. The conclusion is discussed in the context of earlier research on industrialized housing and in terms of the goals of the Operation Breakthrough program.

Marshak, H., Soulen, R. J., Jr., **The temperature scale defined by ^{60}Co γ-ray anisotropy and noise thermometry,** Paper in *Low Temperature Physics-LT* **13,** K. D. Timmerhaus, W. J. O'Sullivan, and E. F. Hammel, Eds., **4,** 498-502 (Plenum Publishing Corp., New York, N.Y., 1974).

Key words: ^{60}Co; gamma rays; Josephson junction; noise thermometer; thermometer.

In order to establish an absolute low temperature scale we are comparing a (hcp) single crystal ^{59}Co ^{60}Co γ-ray anisotropy thermometer to a Josephson junction noise thermometer in the temperature region below 0.04 K. The temperature dependences of both thermometers are governed by independent fundamental relations. Once the parameters of each system are established, the temperatures obtained should be absolute, i.e., no previous calibration is needed, nor is any extrapolation used to determine the temperature. We have examined the possible sources of error in a single crystal Co γ-ray anisotropy thermometer. The reproducibility of the anisotropy at a fixed temperature is within the statistical uncertainty of the measurements; systematic errors arise from the uncertainty in the value of the hyperfine interaction, neglect of a possible quadrupole interaction and/or a small admixture of M3 radiation, mosaic spread of the

crystal, solid angle correction factor, effects of closure domains and domain walls, variation in background radiation, and effect of scattered γ-rays. The effects of these errors can be calculated and subsidiary experiments can be performed to check these calculations.

McCarty, R. D., **Determination of thermodynamic properties from the experimental *p-V-T* relationships,** Chapter 10 in *Experimental Thermodynamics, Vol. II –Experimental Thermodynamics of Non-Reacting Fluids*, B. Le Neindre and B. Vodar, Eds., pp. 501-526 (Butterworth and Co., Ltd., London, England 1975).

Key words: constraints; equation of state; fluid; least squares; parameter estimation; *p-V-T*; statistical weighting; thermodynamic properties.

Methods and techniques for calculating the thermodynamic properties of a fluid from a mathematical model of the *p-V-T* equation of state are given. Criteria for choosing a mathematical form for the equation of state are discussed. Numerical and statistical parameter estimation techniques presented include, linear and non-linear least squares; constraints; simultaneous use of different kinds of data; significance tests and statistical weighting. Formulas for many of the derived thermodynamic properties are also presented.

Meinke, W. W., **Characterization of solids-chemical composition,** Chapter 7 in *Treatise on Solid State Chemistry*, N. B. Hannay, Ed., **1,** 387-435 (Plenum Press, New York, N.Y., 1973).

Key words: activation analysis; characterization; chemical composition; chromatographic analysis; coulometry; electron probe microanalysis; ion-selective electrodes; mass spectrometry; polarography; spectrochemical analysis; thermal analysis; wet chemistry; x-ray fluorescence.

Determination of the chemical composition of solids, i.e., information on the identity and location of the atoms in a particular material, is essential if one is to have confidence that the material can be reproduced. In this chapter an integrated summary of pertinent information on many different analytical techniques is presented. Summaries of sensitivities and precisions to be expected using these techniques are given. Applications to specific characterization problems are discussed and examples are given from the literature, of detailed studies of a number of high purity materials which illustrate the present state-of-the-art for the characterization of practical samples.

Melmed, A. J., Stein, R. J., **Field-ion microscopy of silicon,** *Surface Sci. (Letters to Editor)* **49,** No. 2, 645-648 (Apr. 1975).

Key words: field-ion microscopy; semiconductor surface structure; silicon.

Significant advance in the state-of-the-art of silicon field-ion microscopy is described. Preliminary observations of interesting light sensitive effects are discussed. Further research is indicated.

Meshkov, S., **Current and constituent quarks,** *Proc. XVII Int. Conf. on High Energy Physics, London, England, July 1974*, pp. II-101 – II-112 (1974).

Key words: algebra of currents and quarks; constituent quarks; current quarks; hadronic structure; melosh transformation; meson spectroscopy.

In this review a summary of our attempt to establish and understand the connection between hadron spectroscopy and the algebra of currents is discussed. In addition, our present knowledge of meson structure and decays is reviewed.

Mielenz, K. D., Eckerle, K. L., **Averaging spheres without target,** *Appl. Opt.* **14,** No. 7, 1649-1651 (July 1975).

Key words: averaging spheres; diffusing effectiveness; efficiency; flux averaging; photometry; spectrophotometry.

The design of averaging spheres without internal target is described. The performance of such spheres is analyzed theoretically and tested experimentally. In a final design, an efficiency of 40 percent is achieved for visible and near-uv wavelengths. The averaging effectiveness is characterized by signal variations of the order of 1 part in 10^4 for beam displacements of several 0.1 mm.

Mountain, R. D., **A geometrical description of critical phenomena,** *J. Wash. Acad. Sci.* **64,** No. 3, 195-198 (1974).

Key words: critical phenomena; divergences at critical points; free energy surface; geometry of thermodynamic surfaces; thermodynamics.

Gibbs made extensive use of geometrical concepts in his development of thermodynamics. In this talk we examine the use of geometrical ideas to clarify our understanding of the thermodynamics of fluids in the vicinity of the critical point. The influence of Gibbs on recent developments in the study of critical phenomena is emphasized.

Murphey, W. A., Schleter, J. C., Maltese, M. D. K., **Internal control vis-a-vis diversion path analysis,** (Proc. 14th Annual Meeting of the Institute of Nuclear Materials Management, Inc., San Diego, Calif., June 20-22, 1973), *Nucl. Mater. Manage. Journal of the Institute of Nuclear Materials Management* **II,** No. 3, 232-274 (1973).

Key words: analysis; diversion of nuclear materials; diversion path analysis; internal control system characterization; nuclear materials safeguards; safeguards.

A procedure, "diversion path analysis," has been developed for systematic analysis of diversion possibilities in plants using SNM. The procedure can be applied to diversion possibilities countered by physical protection and materials balance accounting but special emphasis is given to diversion possibilities in high throughput production areas. A parallel practicality study is discussed which used plant production data and had a working diversion indication objective of 500 grams and 24 hour response for a single diversion of attractive material by a single employee without collusion given that the employee may alter any records to which he had access. Explanation of the procedure, its relation to plant internal control, relations or internal control data monitoring techniques to existing safeguards techniques and implementation implications are presented.

Murphey, W. M., Schleter, J. C., **Practicality of diversion path analysis,** (Proc. 15th Annual Meeting of the Institute of Nuclear Materials Management, Inc., Atlanta, Ga., June 19-21, 1974), *Nucl. Mater. Manage. Journal of the Institute of Nuclear Materials Management* **III,** No. III, 236-268 (1974).

Key words: analysis; diversion of nuclear materials; diversion path analysis; internal control system characterization; nuclear materials safeguards; safeguards.

Maintenance of effective safeguards requires a program for routine assessment of plant safeguards systems in terms of their capabilities to satisfy safeguards aims. Plant internal control systems provide capabilities for detection of unprevented diversion and can provide assurance that diversion has not occurred. A procedure called Diversion Path Analysis (DPA) enables routine assessment of the capabilities of internal control systems to indicate unprevented diversion and identification of safeguards problem areas in a plant. A framework for safeguards system design is also provided which will allow flexibility to accommodate individual plant circumstances while maintaining acceptable diversion detection capability. The steps of the procedure are described and the practicality of the analytical procedure is shown by referring to a demonstration test for a high throughput process where plant personnel were major participants. The boundary conditions for the demonstration case are given, along with some conclusions about the general procedure.

Nimeroff, I., Hall, W. A., **Instrumental colorimetry of retroreflective sign materials,** *Report No. FHWA-RD-75-4*, 89 pages (Available by purchase as PB239-633 from the National Technical Information Service, Springfield, Va. 22161, Jan. 1975).

Key words: colorimetry; highway signs; photoelectric tristimus colorimeters; photometry of retroreflective materials; retroreflective sign materials.

Because color-coded applications of highway signs increase, specification of colors and color tolerances are required. In order to assure that the requirements are met within specified regions, a measurement technique needs to be developed and described. To accomplish these goals the U.S. Department of Transportation contracted with the National Bureau of Standards to conduct the required studies and make the necessary recommendations. Having previously performed a study for daytime conditions, the National Bureau of Standards was competent to perform a study for nighttime conditions. The colorimetric properties of 126 samples of retroreflective materials of 7 different colors were measured with 3 telecolorimeters in simulated nighttime conditions. One spectrophotometer was used to measure color of 38 of the samples in simulated daytime conditions. The colors measured were: red, orange, brown, yellow, green, blue and silver (white). Differences of color measured by means of different telecolorimeters on the same samples were evaluated.

As a result of these studies procedures for making colorimetric and photometric measurements were developed and are included in this report. On the basis of the color measurements and their variability tentative recommendations for color boundaries were prepared and are also included in this report.

Olson, J. D., **The refractive index and Lorenz-Lorentz function of fluid methane,** *J. Chem. Phys.* **63,** No. 1, 474-484 (July 1, 1975).

Key words: critical refractive index; Fabry-Perot interferometer; Lorenz-Lorentz function; methane; rectilinear diameter law; refractive index; refractometric virial coefficients.

The refractive index of gaseous and liquid methane was measured between 95 and 300 K and to pressures of 225 bar (1 b $= 10^5$ Pa). The measurements were performed at the ^{198}Hg vapor green line, $\lambda =$ 546.2 nm, with a Fabry-Perot interferometer referred to vacuum. The refractive index data were combined with the previously measured densities of methane to calculate the Lorenz-Lorentz (LL) function. Refractometric virial coefficients were obtained from analysis of the small ($\sim 0.5\%$) maximum exhibited by the (LL) function with increasing density. B_R, the second refractometric virial coefficient, is estimated to be ~ 6.0 (cm^3/mol)^2 and is almost independent of temperature between 220 and 300 K. The critical point refractive index, $n_c =$ 1.10333, was extrapolated from a rectilinear diameter treatment of the saturated liquid and vapor results. The critical point refractive index was combined with an estimate of the critical point (LL) function to yield a critical density of methane, $\rho_c = 10.16 \pm 0.01$ mol/l.

Ottinger, C., Scheps, R., York, G. W., Gallagher, A., **Broadening of the Rb resonance lines by the noble gases,** *Phys. Rev. A* **11,** No. 6, 1815-1828 (June 1975).

Key words: line broadening; rubidium.

Normalized emission spectra of the optically excited Rb resonance lines (7800 Å, 7948 Å) have been measured in the presence of He, Ne, Ar, Kr, and Xe for about 50 Å on either side of the lines. The perturber gas pressures were in the range 100-1100 torr and the temperature was 318 K. The spectra, normalized to the total emission, are shown to be due to binary collisions. Shifts and widths of the Lorentzian cores of the lines were obtained, at pressures sufficiently low for impact theory to apply. The widths are corrected for the Rb hfs and the instrument function. Various power-law fits to the near-wing intensities are presented and compared to theoretical expectations. The red satellites reported by other authors are found to be, in the low-pressure limit, mere shoulders on the line wing for Ar and Kr, while Xe barely produces an actual peak. The measured linewidths and shifts are compared to previous measurements.

Penn, D. R., **Determination of the spin-polarized surface density of states in strongly correlated metals by field emission: Theory,** *Phys. Rev. B* **11,** No. 8, 3208-3209 (Apr. 15, 1975).

Key words: ferromagnetic transition metals; field emission; spin polarization; strongly correlated metals; surface density of states; theory.

It is shown that the combination of spin-polarization and field-emission energy distribution measurements on ferromagnetic transition metals will provide direct information about the one-dimensional surface density of states in a direction normal to the metal surface for a given spin.

Penn, D. R., **The dependence of the tunneling current on density of states in non-superconducting junctions,** *Surface Sci.* **50,** 125-136 (1975).

Key words: density of states; elastic tunneling; tunneling junctions.

The theory that the tunneling current in a non-superconducting tunnel junction depends on the densities of states of the electrodes has been known for sometime although Harrison has suggested that it is in fact not correct. In this paper Harrison's suggestion is critically discussed and the expression for the tunneling current is written in a way that emphasizes its dependence on the *surface* densities of states of the electrodes and takes into account the band structure of the oxide barrier. We find

$$J = \int_{-\infty}^{\infty} d\omega\, [f_L(\omega) - f_R(\omega)]\, \Sigma_{k\|}\, D(r_L, r_R; \omega, k_\|)\, \xi(\omega, k_\|)\, \rho_L^{\perp}(r_L, \omega, k_\|)\, \rho_R^{\perp}(r_R, \omega, k_\|)$$

where f_L, f_R are the Fermi function of the left and right hand electrodes, D is the probability that an electron tunnels from a point r_L in the barrier near the left hand electrode to a point r_R in the barrier near the right hand electrode. ξ depends on the oxide and is a slowly varying function of ω and $k_\|$, the electron momentum parallel to the electrode surfaces. $\rho_L^{\perp}(r_L, \omega, k_\|)$ is the one dimensional density of states of the left hand electrode in the direction normal to the electrode at a position r_L in the barrier for electrons of energy ω and momentum $k_\|$ and $\rho_R^{\perp}$ has a similar meaning. This expression for J reduces to that previously derived by Harrison if the electrodes as well as the oxide barrier are treated in a WKB approximation. In this limit J has no dependence on the densities of states due to cancellations from the factor ξ. Recent field emission experiments and theory have shown that the tunneling current is dependent on the electrode density of states so the expression for J given above must be used. It is suggested that the failure to observe such effects in tunnel junctions is due to imperfections in the junction and that tunneling in metal-vacuum-metal junctions or in perfected tunnel junctions will give density of states information.

Peterlin, A., **Intrinsic stress tensor of polymer solutions in laminar flow,** *Makromol. Chem. Suppl.* **1,** 453-470 (1975).

Key words: elastic dumbbell model; flow instability; flow with longitudinal gradient; flow with transverse gradient; gradient dependence of normal stress differences; gradient dependence of viscosity; hydrodynamic interaction; intrinsic stress tensor; intrinsic viscosity.

The simplified necklace or the equivalent modified elastic dumbbell model with consideration of hydrodynamic interaction among the beads and its change with coil expansion was used for the calculation of the intrinsic stress tensor in laminar flow with transverse and parallel gradient as function of the conventional gradient γ and the dimensionless gradient parameter β. The expansion of the Gaussian coil in flow first increases and then decreases the hydrodynamic interaction. As a consequence the intrinsic viscosity $[\eta]_{tr}$ of suffi-

ciently large macromolecules and the effective average hydrodynamic resistance coefficient Λ of the bead show first a decrease to a minimum and a subsequent gradually slower increase with the gradient. In laminar flow with parallel gradient this effect yields a deformational instability which may play some role in drag reduction of turbulent flow by polymer additives. Experimental evidence will have to conform or to refute these two interdependent phenomena. In the latter case, one suspects that the neglect of anisotropy of hydrodynamic interaction is the main cause of the unrealistic predictions of intrinsic hydrodynamic properties of polymer solutions.

Piermarini, G. J., Block, S., Barnett, J. D., Forman, R. A., **Calibration of the pressure dependence of the R_1 ruby fluorescence line to 195 kbar,** *J. Appl. Phys.* **46,** No. 6, 2774-2780 (June 1975).

Key words: calibration; diamond cell; fluorescence; high pressure; hydrostatic pressures; ruby.

The pressure dependence of the R_1 ruby fluorescence line has been calibrated at 25 °C against the compression of NaCl. Pressures are determined using the Decker equation of state for NaCl. The dependence is linear to 195 kbar following the equation $P_{NaCl} = 2.746(\Delta\lambda)$, where P is in kbar and $\Delta\lambda$ in Å. The uncertainty in the value of the slope, $dp/d\lambda$, expressed in terms of a 95 percent confidence interval is 2.746 ± 0.014 kbar Å^{-1}. The coefficient of the quadratic term $(\Delta\lambda)^2$ is not significantly different from zero; and the quadratic term makes indeed a negligible contribution to the fit. Taking into account the reported uncertainty associated with the Decker equation of state for NaCl, the value of the slope is 2.740 ± 0.016 kbar Å^{-1} within a 95 percent confidence interval.

Plummer, E. W., Gadzuk, J. W., Penn, D. R., **Vacuum-tunneling spectroscopy,** *Phys. Today* **28,** No. 4, 63-71 (Apr. 1975).

Key words: field emission; field ionization; ion neutralization; surface spectroscopy; tunneling.

The extension into the vacuum of the exponential tail of the wave function makes possible remarkably sensitive techniques based on field emission, ion neutralization and field ionization.

Powell, C. J., **Cross sections for ionization of inner-shell electrons by electron impact,** *Proc. 10th Annual Conf. of the Microbeam Analysis Society, Las Vegas, Nevada, Aug.* 11-15, 1975, pp. 3a-b (1975).

Key words: cross sections; electron probe microanalysis; electrons; inner-shell.

A survey has been made of available theoretical and experimental cross-section data for the ionization of inner-shell electrons by electron impact in the energy range of interest to electron probe microanalysis and to Auger-electron spectroscopy.

Prask, H. J., Trevino, S. F., Rush, J. J., **Quasielastic neutron scattering study of ammonium-ion reorientations in ammonium perchlorate,** *J. Chem. Phys.* **62,** No. 10, 4156-4160 (May 15, 1975).

Key words: activation energy; ammonium-ion dynamics; ammonium perchlorate; jump reorientations; quasi-elastic neutron scattering; residence times.

An investigation of the rotational motion of ammonium ions in NH_4ClO_4 is reported. Quasielastic neutron scattering measurements were made on a polycrystalline sample at temperatures between 66 and 150 K. The shapes and widths of the quasielastic scattering peaks as a function of momentum transfer are consistent with instantaneous reorientation about the four C_3 axes. Residence times are derived as a function of temperature yielding an activation energy of 2.3 kJ/mole and a frequency factor $1/\tau_0$ of 3.7×10^{12} s^{-1}.

Prosen, E. J., Cole, K. S., **Heat production of Arbacia eggs revisited (Extended Abstract),** *Biol. Bull.* **145,** No. 2, 450-451 (Oct. 1973).

Key words: Arbacia punctulata; calorimetry; cleavage of cells; development of cells; fertilization; growth of cells; heat production; marine eggs; metabolism; microcalorimetry.

Heat production is an important aspect of the thermodynamics and kinetics of the initiation and subsequent metabolic—and perhaps physical processes of growth. Tremendous advances in speed, sensitivity, and accuracy of heat measurements have come about from the use of modern techniques and semiconductor materials. Yet little, if anything, has been done on such simple systems as marine eggs since the 1924 measurements of Rogers and Cole.

We have repeated that work with the advanced microcalorimeter of the National Bureau of Standards (Prosen, 1973) which has been developed and used in clinical studies of enzyme reactions and bacterial growth. The instrument had been modified to accommodate a larger 3.4 ml reaction vessel to adapt it for biological work. This isothermal, heat-flow instrument measures the heat production of two solutions (0.75 ml and 1.50 ml) before and after mixing with an output signal of 0.2 volt/watt an ultimate sensitivity of 0.1 μJ/sec or 90 μcal/hr (corresponding to 0.1 μk), and with a response half-time of 2 minutes.

Since a constant-temperature room was not available it was necessary to place additional insulation around the calorimeter to limit baseline drift to 3 μW/hr or less. The original plan was to measure the heat production of several thousand *Arbacia* eggs and corresponding sperm in the separate compartments of the reaction vessel and to follow it—after fertilization by mixing—for a few hours or several cell divisions. This has been accomplished but not as yet satisfactorily since no greater than 90 percent fertilization has been achieved in the vessel. It was first found that no fertilization or development took place in the plastic reaction vessels used, although controls in glass gave over 95 percent. A glass vessel with ports sealed with paraffin also proved unsatisfactory. Finally the original plastic vessels operated properly (90% fertilization) after flushing them with sea water for several days. The vessel ports are closed with o-ring seals.

Egg and sperm counts are incomplete, but our preliminary results are as follows: (all measurements were made in natural sea water containing 0.0001 molar EDTA and pH 7.8). Unfertilized eggs gave about 0.3 μW/1000 eggs after 1 hour with a gradual drop with time. Prefertilized eggs gave about 0.6 μW/1000 eggs after 1 hour and with some small variations and a gradual drop with time. Sperm heat was also measured but results are not complete. Fertilization runs in the calorimeter gave similar heats for the unfertilized and the fertilized separate runs above and showed no burst of heat upon fertilization. Fluctuations suggest a possible correlation with stages of development.

There is no immediate explanation for the fact that these values are about twice as large as those of Rogers and Cole. However, different conditions were used and in one experiment with greater loading (50,000 eggs/ml in place of the usual 10,000 eggs/ml) we obtained their value. They used 100,000 eggs/ml. We conclude that it should not be difficult to extend the range of experiments to include measurements of fertilization and early development of a variety of marine eggs.

Raveché, H. J., Mountain, R. D., Streett, W. B., **Reply to the comment on "Monte Carlo studies of the fluid-solid phase transition in the Lennard-Jones system,"** *J. Chem. Phys.* **62,** No. 11, 4582-4583 (June 1, 1975).

Key words: coexisting densities; finite system; "flat" loop; fluid-solid phase transition; Lennard-Jones System; Monte Carlo Studies.

The issue between SRM and HV is shown to be the uncertainty in the coexisting densities obtained by the two methods and not the methods themselves.

Raveché, H. J., Stuart, C. A., **Towards a molecular theory of freezing,** *J. Chem. Phys.* **63,** No. 3, 1099-1111 (Aug. 1, 1975).

Key words: branching; freezing points; metastable fluids; nonlinear operator; pair correlation function; single particle probability density.

The subject of this article is the fluid-solid transition and, in particular, an analysis of crystallization in terms of quantities which describe the average local arrangements of molecules in a fluid. We determine whether it is possible to predict the existence of crystalline solutions for the local molecular density from a Hamiltonian which is invariant under all translations and rotations. Crystallization is studied using the singlet probability density, the pair correlation function, and the intermolecular potential energy. An integral equation is obtained for these quantities, and we pursue the existence of crystalline (i.e., periodic but nonconstant) solutions for the singlet probability which branch from the fluid (i.e., constant) solution which is the number density. The phenomenon of crystallization, that is, the existence and determination of these solutions, can then be represented as a nonlinear eigenvalue problem. The analysis is applied to hard sphere systems in one, two, and three dimensions. Crystallization to close-packed lattices is found in two and three dimensions when the isotropic media are overcompressed by amounts which depend on the structures to which the fluids crystallize. That is, the fluid persists into a portion of the metastable region. The nature of the crystalline solutions is analyzed in the neighborhood of the branching eigenvalues, and the relation between these special eigenvalues and equilibrium freezing points is discussed. The stability of these crystalline solutions is determined by comparing the values of a free energylike functional on these solutions with its value for the fluid.

Reader, J., Epstein, G. L., **Resonance lines of Cs II, Ba III, and La IV,** *J. Opt. Soc. Amer.* **65,** No. 6, 638-641 (June 1975).

Key words: barium; cerium; cesium; ionization energy; lanthanum; wavelengths.

The resonance line spectra of ions in the Xe I isoelectronic sequence, consisting of the 5 transitions to the $5p^6\ {}^1S_0$ ground state from levels with $J=1$ in the $5p^5 5d$ and $6s$ configurations, have been observed for Cs II, Ba III, and La IV. The observations were made with a sliding spark on the 10.7-m normal-incidence vacuum spectrograph at NBS. The resonance transitions from the $5p^6 6d$ and $7s$ configurations were also observed for these ions, except for that from $5p^5 6d\ {}^3P_1$ of Ba III. Several resonance transitions from higher nd and ns levels were also observed. Estimated values for the $J=1$ levels of the $5p^5 7s$ configuration of Ce V were obtained by extrapolation. The derived ionization energies in eV are Cs II 23.17(4), Ba III 35.79(6), La IV 45.95(6), Ce V 65.55(25).

Reinker, R. P., Timmerhaus, K. D., Kropschot, R. H., **Thermal conductivity and diffusivity of selected porous insulations between 4 and 300 K,** Chapter I-4 in *Advances in Cryogenic Engineering* **20,** 343-354 (Plenum Press, New York, N.Y., 1975).

Key words: cryogenic insulation; powders; thermal conductivity; thermal diffusivity.

The thermal conductivity and thermal diffusivity of selected evacuated porous insulations have been measured between 4 and 300 K to better understand the heat transport mechanisms. The thermal conductivity of both perlite and uncoated microspheres can be represented by $k = bT^3$ to within the experimental error. The conductivity of aluminum coated microspheres was found to be highly dependent upon sample history.

Roberts, R. W., Hoffman, J. D., **Reducing energy consumption in R&D labs—The NBS experience,** *Res. Manage.* **XVIII,** No. 1, 26-33 (Mar. 1975).

Key words: building energy use; conservation; energy conservation; electricity saved; fuel consumption.

The National Bureau of Standards has a major facility at Gaithersburg, Md. Over 3,000 people are housed in some 25 buildings, and rather strict temperature and humidity control must be maintained in much of the laboratory space. The climate control system uses a rather complex cool/reheat cycle to maintain proper humidity. Following a thorough analysis of the climate control system, steps were taken that reduced consumption of both electricity and fuel by 20 percent. The procedures by which these savings were realized are detailed.

Roberts, R. W., **The national/international measurement system,** *ASTM Stand. News* **2,** No. 11, 8-13 (Nov. 1974).

Key words: international measurement; measurement system; national economy; national/international measurement system.

National and international measurements are vital to our national economy. They are vital in business transactions measuring the quality of materials and goods, vital to our citizens in measuring the performance and safety of products, and vital to government for measuring compliance with national laws. This measurement "system" must have anchor points and its quality must be monitored and improved. The National Bureau of Standards was established by Congress in 1901 to accomplish that function.

Robinson, R. L., Jr., Hiza, M. J., **Solid-vapor equilibrium—A survey,** Chapter F-2 in *Advances in Cryogenic Engineering* **20,** 218-239 (Plenum Press, New York, N.Y., 1975).

Key words: binary systems; cryogenic fluids; interaction second virial coefficients; review; solid-vapor equilibria; unlike molecule interactions.

The current status of knowledge regarding solid-vapor equilibrium is reviewed. Available data are summarized for systems composed of He, Ne, Ar, Kr, Xe, H_2, N_2, O_2, F_2, CO, CO_2, CH_4, C_2H_4, C_2H_6. Currently used experimental techniques are described, including experimental difficulties. Methods for theoretical description of solid-vapor equilibrium are given. The value of solid-vapor equilibrium data is discussed, with emphasis on the information furnished regarding unlike-molecule interactions.

Rowe, J. M., Rush, J. J., Vagelatos, N., Price, D. L., Hinks, D. G., Susman, S., **Crystal dynamics of KCN and NaCN in the disordered cubic phase,** *J. Chem. Phys.* **62,** No. 11, 4551-4554 (June 1, 1975).

Key words: alkali cyanides; crystal dynamics; dispersion curves; orientation; phonons; rotational disorder; single crystal.

The lattice dynamics of KCN and NaCN in their disordered cubic phase has been studied by coherent inelastic neutron scattering and infrared reflection measurements. Acoustic phonon branches for cyanide single crystals were measured in the [001] direction, with more limited measurements taken in the [110] direction. The one-phonon scattering generally appeared as weak peaks superimposed on a large background of non-one phonon scattering, particularly as measurements were extended to higher energy. No peaks clearly assignable to optical phonons were observed in the neutron measurements but the infrared reflection spectra for polycrystalline pellets were analyzed to derive TO and LO phonon energies (at $q=0$) of 17.0 ± 0.6 and 28.5 ± 2.5 meV. These measurements (and a comparison with the rather easily measured acoustic and optical phonons in a KBr crystal of similar volume) indicate that phonons do not exist as well-characterized excitations in the cyanides at higher frequencies and finite wave vectors. The unusual character of these results is attributed to

the dynamical disorder of the cyanide ions in the fcc crystal and is compared with recent phonon measurements in the analogous fcc phase of ND_4I. The [001] transverse acoustic branches of both KCN and NaCN show unusually low frequencies below $q = 0.5$, which are consistent with recent elastic constant results and with the very large Debye-Waller factors derived from previous neutron diffraction results, and suggest further that the phase transitions in the cyanides are "driven" by a soft shear mode.

Rupp, N. W., **Dental amalgam, a plea for clinical research,** *J. Am. Acad. Gold Foil Operators* **13,** No. 1, 29-31 (Spring 1975).

Key words: creep; dental amalgam; marginal ditching.

Marginal ditching of dental amalgam restorations was related to the physical property of creep in clinical studies directed by Mahler. Because of his conclusions and similar results in other studies, a recommended revision of the ADA Specification No. 1, Alloy for Dental Amalgam, includes a creep test. This effort to improve the specification and limit the certification of alloys to those having good marginal integrity is dependent upon well planned, clinical research.

Saloman, E. B., **Unfolding first and second order diffracted radiation when using synchrotron radiation sources: a technique,** *Appl. Opt.* **14,** No. 6, 1391-1394 (June 1975).

Key words: calibrated XUV detectors; irradiance; radiometry; second order diffracted radiation; synchrotron radiation; XUV grating monochromators.

A technique is presented of using a single calibrated XUV detector for radiometric measurements of synchrotron radiation after the radiation passes through a monochromator that produces a mixture of first and second order diffracted radiation. Irradiance measurements are made with the synchrotron source operating at two different energies for the orbiting electrons. The known change in the spectral distribution produced by the electron energy change is used to calculate the flux in both first and second order. The dependence of the precision of these determinations on the two detected currents and on the detector calibration at both first and second order wavelengths is calculated. Experimental results using the National Bureau of Standards synchrotron (SURF-I) are presented, and anticipated results for the new NBS electron storage ring (SURF-II) are calculated.

Saylor, C. P., **Microscopical determination of refractive index with an error of about ±0.00001,** *Anal. Chem.* **47,** No. 7, 1114-1120 (June 1975).

Key words: identification of compounds by refractive index; micro determination of refractive index; microscope for accurate determination of refractive index; multiple prisms.

Steep optical-glass prisms in contact with the liquid being measured bend a collimated monochromatic beam. The deflected beam enters the microscope, and an image of the target forms at the back focal plane of the objective. The distance of the image from the center is proportional to the sine of the angle of deviation and rigorously related to determinable constants of the system and the refractive index of the liquid. Accuracy increases with steepness of prism, but the refractive index range served by any one is thereby reciprocally decreased. Sine of the angle of deflection, angle of the particular prism being used, and the refractive index of the prism are sufficient for direct calculation of the refractive index of the liquid. When the angle of the prisms is 72°, an accuracy of 10^{-5} is achieved. Each prism (with a numerical aperture of 0.11) can then serve a range of only 0.06 in index. This necessitates a series of prisms of selected optical properties, each serving 0.05 in index and providing a comfortable overlap. About 1 cubic millimeter of liquid is required for a full determination.

Schooley, J. F., **National measurement system temperature—A micro study,** *Nat. Conf. Stand. Lab. –Newsletter* **15,** No. 1, 26-33 (Apr. 1975).

Key words: measurement accuracy; national temperature measurement system; temperature scale; thermometer calibration; thermometer production; thermometry.

The National Temperature Measurement System is briefly described. The nature of the international temperature scale and the standard thermometers are noted, along with the accuracy levels which are possible with the letter. The "commerce" of thermometry—the producers of sensors, calibrations, and measurements as well as the major users—is outlined, with particular emphasis upon the manner in which the National Bureau of Standards interacts with and contributes to the rest of the system.

Schooley, J. F., Soulen, R. J., Jr., **Superconductive fixed points for cryogenic thermometry,** *Instrum. Technol.* **21,** No. 11, 35-39 (Nov. 1974).

Key words: superconductive transition temperatures; superconductivity; temperature; thermometric fixed points.

Research at NBS has shown that some elements exhibit very sharp and reproducible superconductive transitions. This research led to the development of a device, now offered through the Office of Standard Reference Materials, which permits ±0.001 K reproducibility at the superconductive transitions of Pb ($T_c \sim 7.2$ K), In ($T_c \sim 3.4$ K), Al ($T_c \sim 1.2$ K), Zn ($T_c \sim 0.85$ K), and Cd ($T_c \sim 0.5$ K). To extend the usefulness of the device, NBS has been examining the width and reproducibility of the superconductive transitions of Nb_3Sn ($T_c \sim 18$ K), Ir ($T_c \sim 0.1$ K), Be ($T_c \sim 0.023$ K), and W ($T_c \sim 0.015$ K) with the view of establishing these materials as additional fixed points. This article describes these superconductive fixed points.

Schooley, J. F., Soulen, R. J., Jr., **Superconductive fixed points for thermometry in cryogenics,** *Instrument Society of America International Instrumentation-Automation Conference and Exhibit, New York, N.Y., Oct.* 28-31, 1974, Paper 74-620, pp. 1-5 (1974).

Key words: fixed points; SRM 767; superconductivity; transition temperatures.

Research at the National Bureau of Standards has shown that several elements exhibit very sharp and reproducible superconductive transitions. This research led to the development of a device, now offered to the cryogenics industry through the Office of Standard Reference Materials, which permits the attainment of ±0.001 K reproducibility at the superconductive transitions of Pb ($T_c \sim 7.2$ K), In ($T_c \sim 3.4$ K), Al ($T_c \sim 1.2$ K, Zn ($T_c \sim 0.85$ K), and Cd ($T_c \sim 0.5$ K). The device is easily mounted into a cryogenic facility and the superconductive transitions are readily observed using a simple a.c. bridge circuit recently developed. Care must be taken, however, to exclude ambient magnetic fields or to correct the transitions for the field present in the laboratory. In order to extend the usefulness of the device, we have been examining the width and reproducibility of the superconductive transitions of Nb_3Sn ($T_c \sim 18$ K), Ir ($T_c \sim 0.1$ K), Be ($T_c \sim 0.023$ K), and W ($T_c \sim 0.015$ K) with the view of establishing these materials as additional fixed points.

Schramm, R. E., Reed, R. P., **Stacking fault energies of seven commercial austenitic stainless steels,** *Metall. Trans. A* **6A,** 1345-1351 (July 1975).

Key words: austenite; iron alloys; stacking fault energy, stainless steel; x-ray diffraction.

The stacking fault energies of seven commercial austenitic Fe-Cr-Ni, Fe-Cr-Ni-Mn and Fe-Mn-Ni alloys have been determined by x-ray diffraction line profile analysis. From comparison with existing data on laboratory alloys with similar compositions, it is concluded that both Ni and C increase γ while Cr, Si, Mn, and N decrease γ. Regres-

sion analysis of data produced in this study provides an expression relating γ to commercial alloy composition in terms of Ni, Cr, Mn, and Mo alloy concentrations.

Spencer, L. V., **Some comments on Fano's theorem,** *Radiat. Res.* **63,** 191-199 (1975).

Key words: cavity theory; dosimetry; Fano theorem; ionization chambers; radiation measurement; radiation transport.

Fano's proof that uniform radiation fields result when sources and interactions are strictly proportional to local density is discussed in connection with an alternative proof formulation.

Spencer, L. V., **Structure shielding against initial radiations from nuclear explosions. I. Attenuation of air secondary and fission product gamma rays,** *Nucl. Sci. Eng.* **57,** 129-154 (1975).

Key words: effects of nuclear weapons; fission product gamma rays; gamma ray penetration; initial nuclear radiations; neutron penetration; radiation shielding.

Calculations and resulting data are described which are intended for use in estimating the protection afforded by buildings against nuclear radiations emitted from a nuclear burst in the first half minute or so. The basic source configuration is that for which one assumes equal likelihood of the explosion occurring on a ring of elevation 30 deg above the horizontal, relative to a structure location on the ring axis. Source spectra and angular distributions corresponding to large distance (> 1 mile) from burst point to structure are used. As sources we discuss here only gamma rays from fission products and from neutron interactions with air molecules.

Swanson, N., Celotta, R. J., Kuyatt, C. E., Cooper, J. W., **Resonant structure in electron impact excitation of CO near threshold,** *J. Chem. Phys.* **62,** No. 12, 4880-4888 (June 15, 1975).

Key words: CO; electron excitation; energy loss spectra; resonance decay; resonant structure; threshold.

Electron impact excitation functions of numerous states in CO have been measured at 45° scattering angle with resolutions of 16-23 meV FWHM. The decay peak of the 10.04 eV resonance can be seen in the results for the $a\ ^3\Pi$, $a'\ ^3\Sigma^+$, and $A\ ^1\Pi$ vibrational levels. There was no evidence of resonant excitation of the $a'\ ^3\Sigma^+$ state near 8 eV as suggested by Newton and Thomas. Excitation functions of the $b\ ^3\Sigma^+$, $B\ ^1\Sigma^+$, $C\ ^1\Sigma^+$, $c\ ^3\Pi$, and $E\ ^1\Pi$ states, and a previously unobserved state at 11.26 eV show numerous sharp resonances in the first few eV above threshold. Energy loss spectra in the 8-14 eV loss region show peaks corresponding to known states as well as to unidentified states. No sign of the metastable state at about 9.5 eV seen by Wells, Borst, and Zipf could be detected in direct excitation, but an indirect excitation process involving the $A\ ^1\Pi$ state is consistent with the data.

Vogler, M., Dunn, G. H., **Dissociative recombination of electrons and D_2^+ to yield D(2p),** *Phys. Rev. A* **11,** No. 6, 1983-1987 (June 1975).

Key words: crossed beams; cross section; D_2^+; dissociative recombination; electron scattering; Lα radiation.

Cross sections have been measured as a function of electron energy (1.4 to 7.5 eV) for production of L_α photons from the dissociative recombination of electrons and D_2^+. Ions made in a low-pressure ion source by electron bombardment and formed into a beam are reacted at right angles with a magnetically confined electron beam. Recombination was observed by detecting L_α photons from resultant excited atoms. It was demonstrated that a large fraction of the observed light arises from cascade to the 2p state from levels of higher principal quantum number. The measured cross section is thus presented as an upper limit for formation of D(2p) in the dissociative recombination process. The results, represented approximately by the expression $\sigma(2p) < (7.6 \times 10^{-17}) E^{-1.25}$ cm^2, indicate that recombinations leading to formation of a D(2p) are a small fraction of the total recombination measured by Peart and Dolder.

Voigt, P. A., **Measurement of U I and U II relative oscillator strengths,** *Phys. Rev. A* **11,** No. 6, 1845-1853 (June 1975).

Key words: flow-stabilized arc; oscillator strength; U I; U II; wall-stabilized arc.

Relative gf values for 49 prominent U II lines and 21 of the strongest U I lines have been measured. The U II measurements were made using a wall-stabilized arc into which the uranium was introduced in the form of UF_6. The U I values were measured with a flow-stabilized arc which is essentially a free-burning arc stabilized by streaming argon around one of the electrodes which is formed from a molten ball of uranium held in a tungsten cup. Temperatures in the wall-stabilized and flow-stabilized arc were 10 500 K and 5500 K, respectively. The U I relative gf values were placed on an absolute scale employing a recent lifetime determination for the 27 887-cm^{-1} level of U I. This absolute scale was extended to the U II values by measuring the relative intensity of a U I and a U II line in the wall-stabilized arc.

Vorburger, T. V., Penn, D., Plummer, E. W., **Field emission work functions,** *Surface Sci.* **48,** 417-431 (1975).

Key words: electron energy distribution; field emission; tungsten; work function.

Field emission has proven to be a very useful technique for obtaining work function changes from single crystal planes or from the whole emitter. The inability to independently measure the electric field has limited the accuracy of field emission total current measurements for determining absolute work functions. Young and Clark's method of combining field emission energy distribution measurements and total current versus voltage measurements to eliminate the electric field as an unknown is not adequate because it does not take into account the effects of the surface density of states present in the energy distribution. In this paper we discuss a technique to overcome this problem, which involves a series of measurements taken as a function of electric field and an extrapolation to zero field. The method yields reliable values of the work function for the low index (flat) (100) and (112) planes of tungsten but not for the high index (rough) (013) and (111) faces.

Waclawski, B. J., Vorburger, T. V., Stein, R. J., **Angular dependence of uv photoelectron distributions for oxygen adsorbed on W(100),** *J. Vac. Sci. Technol.* **12,** No. 1, 301-304 (Jan.-Feb. 1975).

Key words: angular distributions; bond geometry; chemisorption; energy distributions; oxygen on (100) tungsten; surface bonds; uv photoemission.

Recent theoretical work has suggested the possibility of determining chemisorption bond geometry by the use of uv photoemission. This possibility is being investigated experimentally in an apparatus developed at NBS. The apparatus is described, and preliminary results are presented which show energy distributions as a function of emission angle for electrons photoemitted from W(100), both clean and with adsorbed oxygen. The results obtained at $h\nu = 21.2$ eV for several emission angles indicate substantial angular dependence of the photoelectron distributions, not only for the clean (100) surface, but also, more dramatically, with an oxygen adlayer.

Wang, F. W., **Viscoelasticity of dilute chain-molecule solutions: Evaluation of hydrodynamic interaction,** *J. Polym. Sci., Polym. Phys. Ed.* **13,** 1215-1231 (1975).

Key words: bead-spring model; chain molecules; chain stiffness; deoxyribonucleic acid; dilute solutions; hydrodynamic interaction; polystyrene; viscoelasticity; Zimm theory.

The viscoelastic properties of chain molecules varying in flexibility

and length have been calculated by use of the bead-spring model theory of Zimm. In the evaluation of the hydrodynamic interaction parameter, the number of springs in the bead-spring model, N, has been selected from the range in which the properties predicted by the theory are insensitive to the value of N. The results for limiting viscosity number agree with those predicted by the Yamakawa-Fujii theory of the limiting viscosity number of wormlike chains. The theory also fits the experimental data of Johnson on a sample of polystyrene of molecular weight 860,000 in theta solvents at infinite dilution. The viscoelastic properties of some moderate molecular weight deoxyribonucleic acid solutions are predicted to deviate from the non-free-draining behavior toward the free-draining behavior.

Weinstein, B. A., Piermarini, G. J., **Raman scattering and phonon dispersion in Si and GaP at very high pressure,** *Phys. Rev. B* **12,** No. 4, 1172-1186 (Aug. 15, 1975).

Key words: Gallium phosphides; high pressure; metallic phase transitions; phonon dispersion; Raman scattering; silicon.

One- and two-phonon Raman spectra of Si and GaP were measured at room temperature for pressures up to 135 kbar. An opposed diamond-anvil high-pressure cell was employed in the experiments, and its design and use for Raman scattering are described in detail. Mode Grüneisen parameters and quadratic pressure coefficients were measured for phonons at several zone-boundary critical points as well as at $q \approx 0$. In addition the general effect of pressure on large portions of the phonon dispersion near the zone edge could be inferred. In both materials zone-boundary TA modes "softened" with increasing pressure, while optical phonons shifted to higher energy. Using the high-pressure Raman data a calculation of the thermal-expansion coefficient of Si as a function of temperature (negative at low temperature) achieved fair agreement with experiment. Measured and theoretically calculated mode Grüneisen parameters are compared for several tetrahedral semiconductors. The Raman spectrum of Si was measured up to the metallic (β-Sn structure) transformation at 125 ± 5 kbar. This transition is discussed within the context of the bond-charge model.

Wiederhorn, S. M., Roberts, D. E., **Influence of normal alcohols on the abrasive wear of glass,** *Wear* **32,** 51-72 (1975).

Key words: alcohol; glass; mechanism; silicon carbide; wear.

Normal alcohols were used as cutting fluids in a study of friction and wear of soda lime silicate glass against silicon carbide. Abrasion surfaces were 600 grit silicon carbide paper and a roughened plate of hot-pressed silicon carbide. As the alcohol chain length increased, the coefficient of friction decreased. This result was attributed in part to better lubrication of the abrading surfaces by the long chain length alcohols. The wear rate and the coefficient of friction were strongly dependent on pullout of carbide grains from the silicon carbide paper. Wear on fresh abrasive paper was independent of alcohol chain length. As the paper becomes used, long chain length alcohols were more effective cutting fluids. On the silicon carbide plate, the wear rate decreased in a non-linear fashion as the alcohol chain length increased. For all conditions, the highest wear rate and coefficient of friction were obtained in water. Data are explained in terms of classical theories of friction and wear.

Wiese, W. L., Kelleher, D. E., Helbig, V., **Variations in Balmer-line Stark profiles with atom-ion reduced mass,** *Phys. Rev. A* **11,** No. 6, 1854-1864 (June 1975).

Key words: Balmer; hydrogen; ion dynamics; plasma; Stark broadening.

Calculations of the Stark broadening of hydrogen lines treat the radiating atoms and the perturbing ions as quasistatic. The present experiment represents an attempt to determine whether the possible breakdown of this approximation near the center of the line can account, at least partially, for the existing discrepancies between theoretical and experimental profiles in the core of the Balmer lines. The central regions of H_α, H_β, H_γ, and H_δ profiles have been measured in a wall-stabilized arc over a range of atom-ion relative velocities by varying the atom-ion reduced mass. The cores of all four lines exhibit a significant dependence on the reduced mass. With increasing reduced mass, the experimental profiles gradually show more structure, but still less than the theories predict. Extrapolation of the results for H_α and H_β to infinite reduced mass, i.e., to the static case, gives results that agree quite well with recent calculations.

Wu, Y. C., **On the control of thermal impact for thermal safety,** (Proc. AIAA 10th Thermophysics Conf., Denver, Colo., May 27-29, 1975), *AIAA Paper No. 75-713*, 1-11 (American Institute of Aeronautics and Astronautics, New York, N.Y., May 1975).

Key words: contact burn; heat conduction; human tissue; thermal impact; thermal potential; thermal safety.

The thermal impact exerted by a hot surface to human tissue is the rate of thermal energy delivered from it to the tissue. If the physiological reaction to the thermal impact is beyond the limit of a cell's resistance, a burn may result. Therefore, the severity of a burn is determined by two processes: physiological and physical. Once the physiological reaction to the thermal impact is determined on the basis of the severity of the burn, the thermal potential could be controlled to a safe level by means of a physical process with the aid of modern technology to provide the materials needed. It is this process that is of interest in the area of thermal safety. In the present study we wish to minimize the thermal impact of a hot surface on human tissue. An analytical solution of the linear heat conduction equation as applied to a three layer model is obtained under a given selected set of initial and boundary conditions. The parameters derived from the solution are discussed and subjected to appropriate experiments. The results verify the assumed conditions.

York, G., Scheps, R., Gallagher, A., **Continuum radiation and potentials of Na-noble gas molecules,** *J. Chem. Phys.* **63,** No. 3, 1052-1064 (Aug. 1, 1975).

Key words: molecules; noble gases; radiation; sodium.

The normalized emission spectra resulting from the perturbation of Na atoms by 1-1000 torr of noble gas have been measured in the range 10-150 nm about the 589 nm resonance line. This spectrum, due to the A-X and B-X transitions of the Na-noble gas molecules, was measured with 1.5 nm resolution. The Na, in a cell at a temperature of 417 ± 5 K, was optically pumped to the $3^2P_{1/2}$ and $3^2P_{3/2}$ states by resonance radiation. The resulting emission was measured at several Na densities to obtain the normalized emission spectra in the limit of zero radiation entrapment. Using the Franck-Condon principle, or equivalently the quasistatic theory of line broadening, and density factors, the $A^2\Pi_{1/2,3/2}$ and $X^2\Sigma_{1/2}$ state potentials for NaAr, NaKr, and NaXe have been obtained from the pressure dependence of the spectra. Continuum absorption and emission coefficients for these molecules, obtained by application of the same theories, are also presented. The analysis identifies the low pressure limit of the spectrum as due to free collision states above the angular momentum barrier. The population factors corresponding to quasibound, orbiting resonances are evaluated and used in this analysis.

JOURNAL OF RESEARCH of the national Bureau of Standards—A. Physics and Chemistry
Vol. 79A, No. 6, November–December 1975

Index to Volume 79A

January to December 1975

A

Absolute determination of the electrochemical equivalent and the atomic weight of zinc I. Method, apparatus, and preliminary experiments ... 737
Absolute determination of the electrochemical equivalent and the atomic weight of zinc II. Final determination ... 747
Absolute isotopic abundance ratios and the atomic weight of a reference sample of potassium ... 713
Absolute isotopic abundance ratios and the atomic weight of a reference sample of silicon ... 727
Absolute ratios ... 713, 727
Absorbed polymer ... 609
Absorption coefficients ... 641
Adiabatic calorimetry ... 437
Adsorbed layer ... 613
Adsorption ... 565
Amorphous component ... 613
Atomic energy levels ... 497
Atomic spectrum ... 497
Atomic weight ... 713, 727, 737, 747
Axialite ... 671

B

Barnes, I. L., Garner, E. L., Murphy, T. J., Gramlich, J. W., Paulsen, P. J., Absolute isotopic abundance ratios and the atomic weight of a reference sample of potassium ... 713
—, *Morre, L. J., Machlan, L. A., Murphy, T. J., Shields, W. R.*, Absolute isotopic abundance ratios and the atomic weight of a reference sample of silicon ... 727
Barothermal behaviour ... 641
Barothermal theory of two devices for measuring absorption coefficients ... 641
Bennett, H. S., Barothermal theory of two devices for measuring absorption coefficients ... 641
Branched polyethylene ... 437
Breedon, J. E., Geil, P. H., Surface films on polyoxymethylene single crystals ... 609
Bromobenzene ... 619

C

Calorimetry ... 425, 437, 619
Carlson, H. G., Westrum, E. F., Jr., Chang, S-S., Heat capacities of polyethylene III. One linear and one branched sample from 5 to 350 K ... 437
Cehelnik, E. D., Mielenz, K. D., Velapoldi, R. A., Polarization effects on fluorescence measurements ... 1
Cezairliyan, A., McClure, J. L., Radiance temperature (at 653 nm) of iron at its melting point ... 541
—, —, Simultaneous measurements of specific heat, electrical resistivity and hemispherical total emittance by a pulse heating technique: hafnium 3 (wt. %) zirconium, 1500 to 2400 K ... 431
—, *Righini, F.*, Thermodynamic studies of the $\alpha \rightarrow \beta$ phase transformation pulse heating technique ... 79
Chain folds ... 671, 701
Chang, S-S., Westrum, E. F., Jr., Carlson, H. G., Heat capacities of polyethylene III. One linear and one branched sample from 5 to 350 K ... 437
Chemical association ... 773
Cholesterol ... 493
Clinical standard ... 493
Coexistence boundary ... 71
Combustion ... 425, 481, 487, 561, 635
Combustion, heat of ... 493
Composite materials ... 419
Computer application ... 565
Copper ... 497
Corrections to paper entitled "Third Virial Coefficient for Air-Water Vapor Mixtures" ... 775
Correlation for the second interaction virial coefficients and enhancement factor for moist air ... 551
Coulometry ... 727, 747
Creatinine ... 425
Critical point ... 71
Crosswhite, H. M., The iron-neon hollow-cathode spectrum ... 17
Cryogenic temperature ... 437
Crystallization rate ... 671

D

Davis, G. T., Hoffman, J. D., On the origin of the amorphous component in polymer single crystals and the nature of the fold surface ... 613
Deformation ... 609
Desorption ... 565
Dichlorethyl sulfide ... 635
Differential cross section ... 415
Dimensional stability ... 545
Dirac theory ... 629
Doubly ionized copper ... 497
Dry weight determination ... 565

E

Ebner, S. C., Ederer, D. L., Saloman, E. B., Madden, R. P., The use of synchrotron radiation as an absolute source of vuv radiation ... 761
Ederer, D. L., Saloman, E. B., Ebner, S. C., Madden, R. P., The use of synchrotron radiation as an absolute source of vuv radiation ... 761
Elastic constants ... 419
Electrical resistivity ... 79, 431
Electrochemical equivalent ... 727, 747
Electron configuration ... 497
Emission anisotropy ... 1
Emittance ... 431
Enhancement factor ... 551
Enthalpies of combustion and formation of 2,2′-dichloroethyl urea ... 487
Enthalpies of combustion and formation of cholesterol [cholest-5-en-3-01 (β)] ... 493

Page

Enthalpies of combustion and formation of 2.2′-dichloroethyl sulfide... 635
Enthalpies of combustion and formation of nicotinic acid and creatinine... 425
Enthalpies of combustion and formation of ortho- and parafluorobenzoic acid... 481
Enthalpies of combustion and formation of thianthrene... 561
Enthalpy... 425, 481, 487, 493, 561, 619, 635
Entropy... 619
Equation of state... 71, 551
Equation of state for thermodynamic properties of fluids... 71
Ethane... 71
Excess thermal conductivity of N_2... 407

F

Filled polymers... 419
Fluids... 71
Fluorescence... 1
Fluorescence quantum yield... 1
Fluorescence standards... 1
Fluorimetry... 1
Fold surface... 609, 613
Foley, R. T., Marinenko, G., Absolute determination of the electrochemical equivalent and the atomic weight of zinc I. Methods, apparatus, and preliminary experiments... 727
—, —, Absolute determination of the electrochemical equivalent and the atomic weight of zinc II. Final determination... 747
Formation... 425, 431, 487, 561, 635
Formation, heat of... 493
Fractions... 701
Frolen, L. J., Ross, G. S., Homogeneous nucleation in polyethylene: molecular weight dependence... 701
—, *Hoffman, J. D., Ross, G. S., Lauritzen, J. I., Jr.*, On the growth rate of spherulites and axialites from the melt in polyethylene fractions: regime I and regime II crystallization... 671

G

Garner, E. L., Murphy, T. J., Gramlich, J. W., Paulsen, P. J., Barnes, I. L., Absolute isotopic abundance ratios and the atomic weight of a reference sample of potassium... 713
Geil, P. H., Breedon, J. E., Surface films on polyoxymethylene single crystals... 609
Gibbs energy... 619
Glass... 545
Glass-ceramic... 545
Gold decoration... 609
Goodwin, R. D., Equation of state for thermodynamic properties of fluids... 71
Gramlich, J. W., Garner, E. L., Murphy, T. J., Paulsen, P. J., Barnes, I. L., Absolute isotopic abundance ratios and the atomic weight of a reference sample of potassium... 713
Green's function... 641
Guildner, L. A., Thermal conductivity of gases. III. Some values of the thermal conductivities of argon, helium, and nitrogen from 0 °C to 75 °C at pressures of 1×10^5 to 2.5×10^7 pascals... 407

H

Hafnium... 431
Heat... 425, 481, 487, 561, 635
Heat capacities of polyethylene III. One linear and one branched sample from 5 to 350 K... 437
Heat capacity... 437, 619
Heat diffusion... 641
Heat of fusion... 619
Heat of vaporization... 619
High-speed measurements... 79, 431, 541
High temperature... 79, 541
High temperatures... 431
Hoffman, J. D., Davis, G. T., On the origin of the amorphous component in polymer single crystals and the nature of the fold surface... 613
—, *Frolen, L. J., Ross, G. S., Lauritzen, J. I., Jr.*, On the growth rate of spherulites and axialites from the melt in polyethylene fractions: regime I and regime II crystallization... 671
Hollow cathode... 17
Homogeneous nucleation... 699
Homogeneous nucleation in polyethylene: molecular dependence... 699
Hydrogen... 629
Hyland, R. W., A correlation for the second inter-action virial coefficients and enhancement factors for moist air... 551
—, *Mason, E. A.*, Corrections to paper entitled "Third Virial Coefficient for Air-Water Vapor Mixtures"... 775

I

Interaction virial coefficients... 551
Interferometry... 545
Ionization potential... 497
Iron... 17, 541
Iron-neon hollow-cathode spectrum... 17
Irradiances... 761
Isomerization... 481
Isotopic abundance... 713, 727

J

Johnson, W. H., The anthalpies of combustion and formation of acetanilide and urea... 487
—, The enthalpies of combustion and formation of cholesterol [cholest-5-en-3-01 (3β)]... 493
—, The enthalpies of combustion and formation of 2.2′-dichloroethyl sulfide... 635
—, The anthalpies of combustion and formation of nicotinic acid and creatinine... 425
—, *Prosen, E. J.*, The enthalpies of combustion and formation of ortho- and parafluorobenzoic acid... 481
—, The enthalpies of combustion and formation of thianthrene... 561
Justice, B., Precision measurements of the dimensional stability of four materials... 545

K

Kuriyama, M., On the differential cross section for x-ray inelastic scattering... 415

L

Lauritzen, J. I., Jr., Hoffman, J. D., Frolen, L. J., Ross, G. S., On the growth rate of spherulites and axialites from the melt in polyethylene fractions: regime I and regime II crystallization... 671
Lennard-Jones potential parameters... 775
Line strength... 629
Linear polyethylene... 437
Loebenstein, W. V., Unbound water content from application of adsorption theory... 565

M

Machlan, L. A., Barnes, I. L., Moore, L. J., Murphy, T. J., and Shields, W. R., Absolute isotopic abundance ratios and the atomic weight of a reference sample of silicon... 727
Madden, R. P., Ederer, D. L., Saloman, E. B., Ebner, S. C., The use of synchrotron radiation as an absolute source of vuv radiation... 761
Marinenko, G., Foley, R. T., Absolute determination of the electrochemical equivalent and the atomic weight of zinc I. Method, apparatus, and preliminary experiments... 727
—, —, Absolute determination of the electrochemical equivalent and the atomic weight of zinc II. Final determination... 747
Masi, J. F., Scott, R. B., Some thermodynamic properties of bromobenzene from 0 to 1500 K... 619
Mason, E. A., Hyland, R. W., Corrections to paper entitled "Third Virial Coefficient for Air-Water Vapor Mixtures"... 775
McClure, J. L., Cezairliyan, A., Radiance temperature (at 653 nm) of iron at its melting point... 541

Page

—, —, Simultaneous measurements of specific heat, electrical resistivity and hemispherical total emittance by a pulse heating technique: hafnium 3 (wt %) zirconium, 1500 to 2400 K..... 431
Mechanical properties..... 419
Melting..... 541
Methane..... 71
Mielenz, K. D., Cehelnik, E. D., Velapoldi, R. A., Polarization effects on fluorescence measurements..... 1
Moist air..... 551
Moisture content..... 565
Molecular weight..... 671, 701
Moore, L. J., Barnes, I. L., Machlan, L. A., Murphy, T. J., Shields, W. R., Absolute isotopic abundance ratios and the atomic weight of a reference sample of silicon..... 727
Murphy, T. J., Barnes, I. L., Moore, L. J., Machlan, T. J., Shields, W. R., Absolute isotopic abundance ratios and the atomic weight of a reference sample of silicon..... 727
—, *Gerner, E. L., Gramlich, J. W., Paulsen, P. J., Barnes, I. L.*, Absolute isotopic abundance ratios and the atomic weight of a reference sample of potassium..... 713
Mustard gas..... 635

N

Neon..... 17
Nicotinic acid..... 425
Normal spectral emittance..... 541
Nucleation theory..... 671, 701

O

On the differential cross section for x-ray inelastic scattering..... 415
On the growth rate of spherulites and axialites from the melt in polyethylene fractions: regime I and regime II crystallization... 671
On the origin of the amorphous component in polymer single crystals and the nature of the fold surface..... 613
Orthobaric densities..... 71
Oscillator strength..... 629

P

Particulate composites..... 419
Paulsen, P. J., Garner, E. L., Murphy, T. J., Gramlich, J. W., Barnes, I. L., Absolute isotopic abundance ratios and the atomic weight of a reference sample of potassium..... 713
Polarization..... 1
Polarization effects on fluorescence measurements..... 1
Polyethylene..... 437, 671, 701
Polymer crystals..... 609, 613
Poly(oxymethylene)..... 609
Potassium..... 713
Precision measurements of the dimensional stability of four mirror materials..... 545
Prosen, E. J., Johnson, W. H., The enthalpies of combustion and formation of ortho- and parafluorobenzoic acid..... 481

R

Radiance temperature..... 541
Radiance temperature (at 653 nm) of iron at its melting point..... 541
Radiometry..... 759
Real metals..... 415
Reference material..... 493
Reference standard..... 713
Regime I..... 671
Regime II..... 671
Regular folds..... 613
Relativistic corrections..... 629
Relativistic effects on line strengths for transitions in the hydrogenic isoelectronic sequence..... 629
Righini, F., Cezairliyan, A., Thermodynamic studies of the $\alpha \rightarrow \beta$ phase transformation pulse heating technique..... 79
Ross, G. S., Frolen, L. J., Homogeneous nucleation in polyethylene: molecular weight dependence..... 701

Page

—, *Hoffman, J. D., Frolen, L. J., Lauritzen, J. I., Jr.*, On the growth rate of spherulites and axialites from the melt in polyethylene fractions: regime I and regime II crystallization..... 671

S

Saloman, E. B., Ederer, D. L., Ebner, S. C., Madden, R. P., The use of synchrotron radiation as an absolute source of vuv radiation..... 761
Saturated air..... 551
Scott, R. B., Masi, J. F., Some thermodynamic properties of bromobenzene from 0 to 1500 K..... 619
Second virial coefficients..... 551
Secondary standard..... 481, 487, 561
Shear modulus..... 419
Shenstone, A. G., The third spectrum of copper (Cu III)..... 497
Shields, W. R., Barnes, I. L., Moore, L. J., Machlan, L. A., Murphy, T. J., Absolute isotopic abundance ratios and the atomic weight of a reference sample of silicon..... 727
Silicon..... 727
Simplification of van der Poel's formula for the shear modulus of a particulate composite..... 419
Simultaneous measurements of specific heat, electrical resistivity and hemispherical total emittance by a pulse heating technique: hafnium-3 ,wt %) zirconium, 1500 to 2400 K..... 431
Smith, J. C., Simplification of van der Poel's formula for the shear modulus of a particulate composite..... 419
Solid-solid phase transformation..... 79
Some thermodynamic properties of bromobenzene from 0 to 1500 K..... 619
Specific heat..... 431
Specific heats..... 71
Spectrofluorimetry..... 1
Spectrometer calibration..... 761
Spectroscopy..... 629
Spherulite..... 671
Standard source..... 761
Sulfur compound..... 561
Surface area..... 565
Surface films on polyoxymethylene single crystals..... 609
Surface free energies..... 701
Surface layer..... 609
Synchrotron radiation..... 761

T

Theory..... 415
Theory of elasticity..... 419
Thermal conductivity of Ar..... 407
Thermal conductivity of gasses III. Some values of the thermal conductivities of argon, helium, and nitrogen from 0 °C to 75 °C at pressures of 1×10^5 to 2.5×10^7 pascals..... 407
Thermal conductivity of He..... 407
Thermal conductivity of N_2..... 407
Thermochemical standard..... 487
Thermodynamic properties..... 437, 619
Thermodynamic studies of the $\alpha \rightarrow \beta$ phase transformation pulse heating technique..... 79
Thermodynamics..... 79, 431
Thianthrene..... 561
Third interaction virial coefficients..... 775
Third spectrum of copper (Cu III)..... 497
Triple point..... 619

U

Unbound water content from application of adsorption theory... 565
Use of synchrotron radiation as an absolute source of vuv radiation..... 761

V

Vacuum ultraviolet..... 761
Vapor pressures..... 71
Velapoldi, R. A., Cehelnik, E. D., Mielenz, K. D., Polarization effects on fluorescence measurements..... 1

Page

Viewing angle..... 1
Virial coefficients..... 551, 773

W

Water content..... 565
Water vapor adsorption..... 665
Water vapor-air mixtures..... 775
Wavelength standards..... 17
Wavelengths..... 497
Weakly absorbing materials..... 641
Weiss, A., Younger, S. M., Relativistic effects on line strengths for transitions in the hydrogenic isoelectronic sequency..... 629
Westrum, E. F., Jr., Chang, S-S., Carlson, H. G., Heat capacities of polyethylene III. One linear and one branched sample from 5 to 350 K..... 437

X

Page

X-ray inelastic scattering..... 415

Y

Younger, S. M., Weiss, A. W., Relativistic effects on line strengths for transitions in the hydrogenic isoelectronic sequence..... 629

Z

Zinc atomic weight..... 727, 747
Zirconium..... 79

U. S. GOVERNMENT PRINTING OFFICE : 1976 O - 594-051

NBS TECHNICAL PUBLICATIONS

PERIODICALS

JOURNAL OF RESEARCH reports National Bureau of Standards research and development in physics, mathematics, and chemistry. It is published in two sections, available separately:

• **Physics and Chemistry (Section A)**

Papers of interest primarily to scientists working in these fields. This section covers a broad range of physical and chemical research, with major emphasis on standards of physical measurement, fundamental constants, and properties of matter. Issued six times a year. Annual subscription: Domestic, $17.00; Foreign, $21.25.

• **Mathematical Sciences (Section B)**

Studies and compilations designed mainly for the mathematician and theoretical physicist. Topics in mathematical statistics, theory of experiment design, numerical analysis, theoretical physics and chemistry, logical design and programming of computers and computer systems. Short numerical tables. Issued quarterly. Annual subscription: Domestic, $9.00; Foreign, $11.25.

DIMENSIONS/NBS (formerly Technical News Bulletin)—This monthly magazine is published to inform scientists, engineers, businessmen, industry, teachers, students, and consumers of the latest advances in science and technology, with primary emphasis on the work at NBS. The magazine highlights and reviews such issues as energy research, fire protection, building technology, metric conversion, pollution abatement, health and safety, and consumer product performance. In addition, it reports the results of Bureau programs in measurement standards and techniques, properties of matter and materials, engineering standards and services, instrumentation, and automatic data processing.

Annual subscription: Domestic, $9.45; Foreign, $11.85.

NONPERIODICALS

Monographs—Major contributions to the technical literature on various subjects related to the Bureau's scientific and technical activities.

Handbooks—Recommended codes of engineering and industrial practice (including safety codes) developed in cooperation with interested industries, professional organizations, and regulatory bodies.

Special Publications—Include proceedings of conferences sponsored by NBS, NBS annual reports, and other special publications appropriate to this grouping such as wall charts, pocket cards, and bibliographies.

Applied Mathematics Series—Mathematical tables, manuals, and studies of special interest to physicists, engineers, chemists, biologists, mathematicians, computer programmers, and others engaged in scientific and technical work.

National Standard Reference Data Series—Provides quantitative data on the physical and chemical properties of materials, compiled from the world's literature and critically evaluated. Developed under a world-wide program coordinated by NBS. Program under authority of National Standard Data Act (Public Law 90-396).

NOTE: At present the principal publication outlet for these data is the Journal of Physical and Chemical Reference Data (JPCRD) published quarterly for NBS by the American Chemical Society (ACS) and the American Institute of Physics (AIP). Subscriptions, reprints, and supplements available from ACS, 1155 Sixteenth St. N. W., Wash. D. C. 20056.

Building Science Series—Disseminates technical information developed at the Bureau on building materials, components, systems, and whole structures. The series presents research results, test methods, and performance criteria related to the structural and environmental functions and the durability and safety characteristics of building elements and systems.

Technical Notes—Studies or reports which are complete in themselves but restrictive in their treatment of a subject. Analogous to monographs but not so comprehensive in scope or definitive in treatment of the subject area. Often serve as a vehicle for final reports of work performed at NBS under the sponsorship of other government agencies.

Voluntary Product Standards—Developed under procedures published by the Department of Commerce in Part 10, Title 15, of the Code of Federal Regulations. The purpose of the standards is to establish nationally recognized requirements for products, and to provide all concerned interests with a basis for common understanding of the characteristics of the products. NBS administers this program as a supplement to the activities of the private sector standardizing organizations.

Federal Information Processing Standards Publications (FIPS PUBS)—Publications in this series collectively constitute the Federal Information Processing Standards Register. Register serves as the official source of information in the Federal Government regarding standards issued by NBS pursuant to the Federal Property and Administrative Services Act of 1949 as amended, Public Law 89-306 (79 Stat. 1127), and as implemented by Executive Order 11717 (38 FR 12315, dated May 11, 1973) and Part 6 of Title 15 CFR (Code of Federal Regulations).

Consumer Information Series—Practical information, based on NBS research and experience, covering areas of interest to the consumer. Easily understandable language and illustrations provide useful background knowledge for shopping in today's technological marketplace.

NBS Interagency Reports (NBSIR)—A special series of interim or final reports on work performed by NBS for outside sponsors (both government and non-government). In general, initial distribution is handled by the sponsor; public distribution is by the National Technical Information Service (Springfield, Va. 22161) in paper copy or microfiche form.

Order NBS publications (except NBSIR's and Bibliographic Subscription Services) from: Superintendent of Documents, Government Printing Office, Washington, D.C. 20402.

BIBLIOGRAPHIC SUBSCRIPTION SERVICES

The following current-awareness and literature-survey bibliographies are issued periodically by the Bureau:

Cryogenic Data Center Current Awareness Service

A literature survey issued biweekly. Annual subscription: Domestic, $20.00; foreign, $25.00.

Liquefied Natural Gas. A literature survey issued quarterly. Annual subscription: $20.00.

Superconducting Devices and Materials. A literature survey issued quarterly. Annual subscription: $20.00. Send subscription orders and remittances for the preceding bibliographic services to National Bureau of Standards, Cryogenic Data Center (275.02) Boulder, Colorado 80302.

Electromagnetic Metrology Current Awareness Service Issued monthly. Annual subscription: $24.00. Send subscription order and remittance to Electromagnetics Division, National Bureau of Standards, Boulder, Colo. 80302.

SJRA UNIVE300UA R 1
UNIVERSITY MICROFILMS INC
ATTN SERIALS SECTION
300 NORTH ZEEB RD
ANN ARBOR MI 48106

U.S. DEPARTMENT O
National Bureau of S
Washington, D.C. 20234

OFFICIAL BUSINESS
Penalty for Private Use, $300

POSTAGE AND FEES PAID
U.S. DEPARTMENT OF COMMERCE
COM-215

SPECIAL FOURTH-CLASS RATE
BOOK

JOURNAL OF RESEARCH of the National Bureau of Standards
A. Physics and Chemistry

Vol. 79A, No. 6 Nov.-Dec. 1975

Page

Contents

On the growth rate of spherulites and axialites from the melt in polyethylene fractions: regime I and regime II crystallization. John D. Hoffman, Lois J. Frolen, Gaylon S. Ross, and John I. Lauritzen, Jr. 671

Homogeneous nucleation in polyethylene: molecular weight dependence. Gaylon S. Ross and Lois J. Frolen. 701

Absolute isotopic abundance ratios and the atomic weight of a reference sample of potassium. E. L. Garner, T. J. Murphy, J. W. Gramlich, P. J. Paulsen, and I. L. Barnes. 713

Absolute isotopic abundance ratios and the atomic weight of a reference sample of silicon. I. L. Barnes, L. J. Moore, L. A. Machlan, T. J. Murphy, and W. R. Shields. 727

Absolute determination of electrochemical equivalent and the atomic weight of zinc I. Method, apparatus, and preliminary experiments. George Marinenko and Robert T. Foley. 737

Absolute determination of the electrochemical equivalent and the atomic weight of zinc II. Final determination. George Marinenko and Robert T. Foley. 747

The use of synchrotron radiation as an absolute source of vuv radiation. D. L. Ederer, E. B. Saloman, S. C. Ebner, and R. P. Madden. 761

Corrections to paper entitled "Third Virial Coefficient for Air-Water Vapor Mixtures." R. W. Hyland and E. A. Mason. 775

Publications of the National Bureau of Standards. 777

Index to volume 79A, January to December 1975. 809

Library of Congress Catalog Card Number: 62-37059

For sale by the Superintendent of Documents, U.S. Government Printing Office, Washington, D.C. 20402. (Order by SD Catalog No. C 13.22/sec.A.79/(4)). Single copy price varies. Subscription price: $17.00 a year; $4.25 additional for foreign mailing.

UNITED STATES GOVERNMENT PRINTING OFFICE, WASHINGTON : 1975